UNIVERSITY of BRADFORD Library

University of Bradford eThesis

This thesis is hosted in Bradford Scholars – The University of Bradford Open Access repository. Visit the repository for full metadata or to contact the repository team

© University of Bradford. This work is licenced for reuse under a Creative Commons Licence.

Finite Element Modelling of Ventilated Brake Disc Hot Spotting

Jinghan TANG

Submitted for the Degree of

Doctor of Philosophy

Faculty of Engineering and Informatics

University of Bradford

2017

Abstract

Author: Jinghan TANG

Title: Finite Element Modelling of Ventilated Brake Disc Hot Spotting

Keywords: Disc brake, finite element method, hot spot, hot judder, thermal localisation, NVH

Hot spotting of automotive disc brakes is an undesired thermal localisation phenomenon, which is a challenge for numerical modelling in terms of both accuracy and efficiency especially for complex disc geometry. In this research, the aim was to develop a computationally efficient finite element (FE) approach for 2-piece pin-mounted ventilated disc hot spot prediction with acceptable accuracy enabling parametric studies to contribute to the knowledge of the complex mechanisms. A time reduction strategy for the simulations was established by incorporating an axisymmetric brake pad assumption with material scaling factor and the friction characteristics were defined by a user-subroutine. The computing accuracy and efficiency of this method were then verified by comparing with traditional FE models. 2D in-plane, 2D out-of-plane, and 3D models were performed to investigate the effects of ventilated disc hot spotting, radial hot spot/band migration, and hot spotting of realistic complex disc geometry respectively. Both 2D and 3D results were validated using experimental results based on a laboratory dynamometer and showed good correlation. The results suggested that adequate modelling of friction pair contact pressure distribution and the subsequent non-uniform heat generation is essential for hot spot simulation; speed was identified as the determinant for the number of hot spots, whereas hot spot temperature was determined by energy level. Furthermore, recommendations for vent design, pins, disc run-out, cooling, material selection, wear rate, pad length and loading distribution were given. Finally, hot spotting and hot band migration cause-effect chains were established based on the results and discussion.

Publications

Tang, J.H., Bryant, D., and Qi, H.S., 2014, *Coupled CFD and FE thermal analysis of disc brake*, EuroBrake 2014-SA-019, 13-15 May, Lille, France.

Tang, J.H., Bryant, D., and Qi, H.S., 2015, *A finite element simulation of disc brake hot band migration*, EuroBrake 2015-TEF-011, 4-6 May, Dresden, Germany.

Tang, J.H., Bryant, D., and Qi, H.S., 2015, *A numerical investigation of hot spotting origin of ventilated disc brakes*, EuroBrake 2015-NVH-009, 4-6 May, Dresden, Germany.

Tang, J.H., Bryant, D., and Qi, H.S., 2016, *A 3D finite element simulation of ventilated brake disc hot spotting*, EuroBrake 2016-SVM-025, 13-15 Jun, Milan, Italy.

Tang, J.H., Bryant, D., Qi, H.S., Whiteside, B.R., and Babenko, M., 2017, Simplified three-dimensional finite element hot-spotting modelling of a pin-mounted vented brake disc: an investigation of hot-spotting determinants, *Proceedings of the Institution of Mechanical Engineers Part D: Journal of Automobile Engineering*, 1-19

Tang, J.H., Bryant, D., and Qi, H.S., 2017, *2D Finite Element Simulation of Ventilated Brake Disc Waviness Distortions under Thermal Load*, EuroBrake 2017-SVM-010, 2-4 May, Dresden, Germany.

Acknowledgement

I would like to express my deepest appreciation to my principle PhD supervisors Dr David Bryant and Dr Hongsheng Qi for their guidance in patience, invaluable advice, excellent training and research opportunities provided, and support throughout all my life in the UK. I also would like to thank Mr Chibbuhai Mistry for his support in the practical works during the experiments as a technician in the Braking Research Centre. In addition, a thank you to Prof Andrew Day, Dr Hongsheng Qi and Dr Songdong Shao for their efforts in my PhD application and scholarship; Dr Ben Whiteside and Dr Max Babenko for support with the thermal imagery. Moreover, I would like to express my gratitude to Dr Marko Tirovic and Prof Phillipe Dufrénoy for their constructive advice towards my publications. I am also indebted to Bentley Motors Limited for their technical support in research projects and funding. Finally, I am deeply grateful to my family, especially my wife – Weiwen Song, my parents and parents in law, for their love and encouragement during my study in the UK.

Contents

Table of Figures

Table of Tables

Nomenclature

A	m^2	Contact area
A	m^2	Contact area for axisymmetric pad
A_{disc}	m^2	Surface area of the disc
A_{piston}	m^2	Piston area
A_{real}	m^2	Real contact area
A_{rad}	m^2	Area of radiation surface
b		Exponential growth rate
B_i		Biot number
c_{disc}	J/kgK	Specific heat capacity of disc
C_p	J/kgK	Specific heat capacity
C_u		Heat capacity matrix
d	m^2/s	Thermal diffusivity
$\boldsymbol{D}$		Elasticity matrix
d_h	m	Fluid dynamic diameter
E		Young's modulus
F	N	Vector of mechanical load
Fo		Fourier number
F_{piston}	N	Brake force
$\dot{h}$	m/s	Wear displacement velocity
h	m	Over-closure of contact surfaces
h_c	W/m^2K	Convective heat transfer coefficient
h_{disc}	W/m^2K	Convective heat transfer coefficient of disc
h_{eff}	W/m^2K	Effective thermal conductance
h_{ITL}	W/m^2K	Thermal conductance of interface tribo-layer
k	W/mK	Thermal conductivity

K_{wear}	m^2/N	Specific wear rate coefficient
L	m	Interface thickness
L_{disc}	m	Characteristic length of the disc
m_{disc}	kg	Mass of disc
n		Unit vector on each normal direction
p	Pa	Contact pressure
P_{piston}	Pa	Actuation pressure
P_t	%	Probability of contact in the time domain
P_{td}	%	Possibility of the vents passing through a given angular position in the disc ventilated layer during rotation
q	W/m^2	Heat flux density
q_{disc}	W/m^2	Heat flux into disc
Δq_{nodal}	W/m^2	Nodal heat flux generated in a time increment
Q	J	Thermal energy
r	m	Brake disc radius
R_i	m	Brake disc inner radius
R_o	m	Brake disc outer radius
Δs	m	Incremental slip
Δt	s	Time increment
t	s	Time
T	°C	Temperature
ΔT	°C	Temperature increment
T_0, T_{air}	°C	Environmental temperature
T_1, T_2	°C	Contact pair temperature
T_{disc}	°C	Disc temperature
T_h	m	Disc thickness

T_q	Nm	Torque
u		Transient displacement field
U_0	J/m^3	Strain energy density
U	J	Total strain energy
v	m/s	Sliding velocity
V_{disc}	m^3	Volume of disc
ΔV	m^3	Volume loss per brake application per pad
w	m	Width
Δx	m	Element size
z	m	Axial coordinates
α		Thermal expansion coefficient
γ		Heat partition ratio
δ_{disc}	m	Half thickness of the solid rotor
ε		Strain
$\boldsymbol{\varepsilon}$		Strain matrix
ε_e		Emissivity
$\boldsymbol{\varepsilon_m}$		Strain matrix under mechanical loading
ε_T		Thermal strain
$\boldsymbol{\varepsilon_T}$		Thermal strain matrix
$\Delta\varepsilon$		Strain matrix due to temperature change
θ	°	Pad arc length
μ		Coefficient of friction
ρ	Kg/m^3	Density
ρ_{disc}	Kg/m^3	Density of disc
σ_{SB}	W/m^{2}K^4	Stefan-Boltzmann constant
σ_T	Pa	Thermal stress
σ		Stress matrix
τ	Pa	Shear stress

φ	°	Angular coordinates
ω	rad/s	Rotational velocity

Abbreviations

2D	Two dimensional
3D	Three dimensional
AC	Alternating current
BPV	Brake pressure variation
BTV	Brake torque variation
CFD	Computational fluid dynamics
CMM	Coordinate measuring machine
DAQ	Data acquisition
DOE	Design of experiment
DOF	Degree of freedom
DTV	Disc thickness variation
FE	Finite element
FEA	Finite element approach
FFT	Fast Fourier transformation
HO	Higher order
IB	Inboard
IR	Infrared
LO	Lower order
MAT	Matrix file format in MATLAB
NVH	Noise, vibration, and harshness
OB	Outboard
PC	Personal computer
PSD	Power spectral density
PWD	Progressive waviness distortions
SRO	Surface run-out
TCR	Thermal contact resistance
TDMS/TDM	LABVIEW^{TM} output file format
TEDI	Thermo- elastic dynamic instability
TEI	Thermo-elastic instability

Chapter 1 Introduction

1.1 Research Background

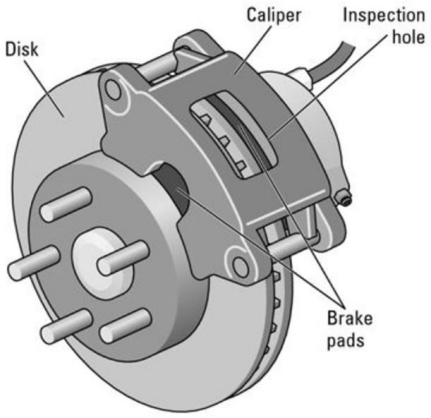

Figure 1.1 Typical disc brake system assembly (Yang, 2015)

The automotive brake system is designed to convert the kinetic energy of a moving vehicle into thermal energy and dissipated. The typical assembly of the disc brake system is shown in Figure 1.1 which comprises brake disc, brake pads, and brake calliper. During a brake application, the brake line pressure is applied to the pistons in the calliper which clamp the pads to the brake disc. Since considerable heat can be generated, disc brakes, especially ventilated disc brakes, are commonly used due to this advantage in heat dissipation performance comparing with drum brake. The thermal energy during braking can lead to thermal deformation of the brake disc. Excessive distortion of the disc is a main source of undesired automotive noise, vibration and harshness (NVH) problems and the most well-known consequence is hot judder. Hot judder is a thermally induced vibration during high speed and medium to heavy duty brake applications, which can affect both the comfort and safety of the driver. It is caused by the disc thermo-mechanical deformation, thus the frequency of vibration is related to the rotational velocity of the wheels. Hot spots are regions of high temperature (gradient) and localised areas of distortion distributed on the

disc surface during brake applications (see Figure 1.2 right). Hot spotting gives rise to brake drone. Nevertheless, hot spots can also lead to thermal cracking, brake fading and thermal fatigue phenomena (Jacobsson, 2001), which are very dangerous and should be reduced and prevented in the design of a brake system and during driving.

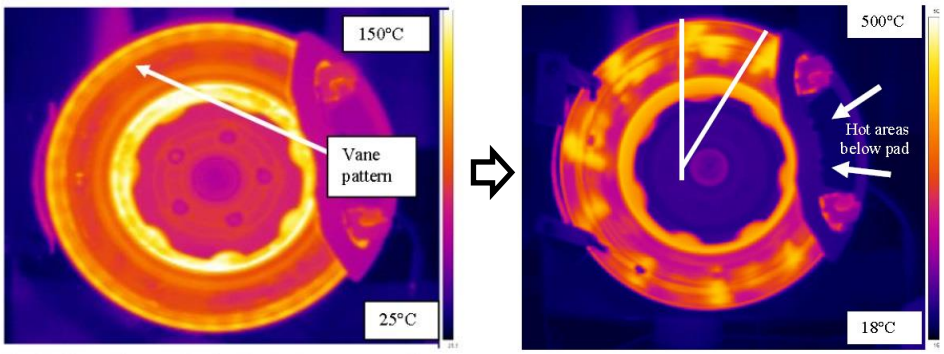

Figure 1.2 Thermal images of the hot spots developing process for a ventilated disc brake system (reproduced from Bryant et al., 2011)

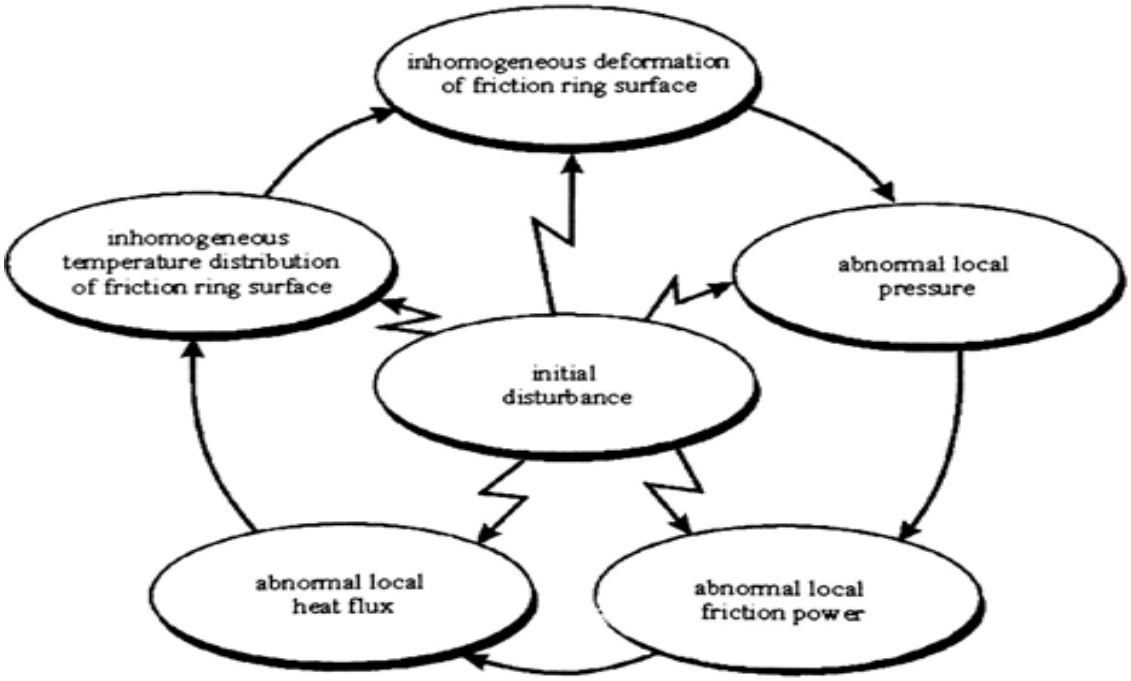

Figure 1.3 Assumptions of hot spotting development (Steffen, 2006)

Various experimental studies and analytical theories have been published in order to explain the occurrence of hot spotting over the past decades. The most famous explanation is the thermo-elastic instability (TEI) theory proposed by Barber *et al.* in 1967 which analytically predicts the generation of an initial disturbance triggered by a critical sliding velocity and corresponded to material thermal properties. The TEI theory assumed that the occurrence of hot spots is a complex thermo-mechanical localisation process which is triggered by an initial disturbance of uneven temperature, distortion, pressure, friction, or heat flux and the subsequent cause-effect chain is as shown in Figure 1.3 (Steffen, 2006). However, the accuracy of the TEI theory was challenged by the experimental results of Lee and Brooks (2003), Cho and Cho (2008) and Sardá *et al*. (2008). Other theories of hot spotting include Progressive Waviness Distortion (PWD) (Panier *et al.* 2004) and disc thermal buckling theory (Ma, 2004, Fieldhouse, 2008, Bryant, Fieldhouse and Talbot, 2011, and Yang, 2015) which explained the contribution of thermo-plastic distortions and brake disc bulk distortions to hot spotting. But the general hot spotting mechanisms and the influences of the determinants were still not fully addressed.

As indicated by Zagrodzki (2009), the TEI theory was restricted by the simplifications to the geometry and boundary conditions due to the limitations of the analytical method. Therefore, using a numerical modelling technique such as the Finite Element (FE) method to simulate hot spotting based on realistic geometry and boundaries is a natural choice. However, the previous hot spotting FE models such as Choi and Lee (2004) and Zagrodzki (2009) were limited by the modelling complexity, computing efficiency and mainly focused on 2D solid disc modelling. Therefore, it is essential that FE models are developed with acceptable computing time which can enable parametric studies that improve the knowledge and understanding of hot spotting mechanisms.

In addition, the experiments carried out by Sardá *et al*. (2008) and Bryant, Fieldhouse and Talbot (2011) showed that the distribution of hot spots was correlated with the geometry of ventilated disc which is the commonly used brake disc type. As can be seen in Figure 1.2, temperature ripples clearly showed the vent pattern and the shape of hot spots also correlated with the angle of the vents as well. The results imply that the previous solid disc simplification to the disc geometry could introduce inaccuracy to the predicted results. Thus, it was important to investigate the characteristics of hot spotting on ventilated discs which has rarely been modelled in previous FE simulations.

In summary, three main research questions are proposed in this research:

1) What is the mechanism of hot spotting, including: what are the trigger conditions; how disc waviness and bulk deformation generated and affect hot spotting; and why hot spots anti-symmetrically distributed and radially migrated?

2) How to achieve efficient modelling of hot spotting with acceptable accuracy?

3) What is the difference between ventilated disc hot spotting and the previously studied solid disc hot spotting in terms of characteristics and determinants?

1.2 Aims and objectives

Based on the research questions, the main aim of this project is to contribute to the knowledge of hot spotting mechanisms by establishing an efficient set of FE models with less computing resource demanding and high accuracy which enabled subsequent parametric studies.

To achieve the aim, the primary objectives are:

1) To identify the current state of art in hot spot research including the theories, determinants and numerical modelling methods.

2) To develop numerical hot spotting modelling techniques with effective computing efficiency and acceptable accuracy.

3) To investigate the mechanism that can cause disc waviness distortions, including thermal buckling, geometry characteristics, moving heat source and clamping forces.

4) To explore the trigger conditions of hot spotting i.e. critical speed or critical energy.

5) To evaluate the parameters of a ventilated disc that affect hot spotting including pins, vents, thickness, cooling distribution and pad length.

6) To analyse the relationship between lower order deformation and hot spots i.e. the effects of bulk deformation to hot spotting.

7) To investigate the radial migration of hot spots/bands considering disc coning and wear.

1.3 Layout of thesis

Chapter 1: The initial chapter introduces the gaps in hot spotting research and the limitations of conventional simulation methods. Then the **aims and objectives** are given.

Chapter 2: Presents a **literature review** which identifies the conventional theories, determinants and modelling methods of hot spotting. The **main research gaps** are identified.

Chapter 3: To address the research questions and achieve the desired numerical model, an **overview of the methodology** and fundamental **modelling theories of thermo-mechanical contact** are presented. The detailed **methodology** is discussed in detail for each research objectives.

Chapter 4: The **experimental studies** are presented to provide **initial investigation** of hot spotting on a full scale test rig as a **benchmark** for the further finite element modelling.

Chapter 5: The **fundamental studies** developing a time reduction strategy and presenting the establishment of the **basic assumptions** for the finite element models. The assumptions were verified by comparing the new finite element models with conventional models.

Chapter 6: The numerical simulation of **2D hot spotting models** in both in-plane and out-of-plane direction is presented. Parametric studies are performed to investigate the determinants of both **disc waviness** and **hot band migration** phenomena.

Chapter 7: To further the understanding and knowledge of hot spotting mechanisms, **3D hot spotting finite element models** are presented. More realistic geometry and boundary conditions of the 3D models enabled a **parametric investigation** on the determinants to be performed.

Chapter 8: The **discussions** based on the experimental and numerical results obtained are given to **address the research questions**. The cause-effect chains of hot spotting are proposed considering the effects of brake conditions, disc and pad geometry factors.

Chapter 9: The **Conclusions** are presented in both **theoretical and technical aspects**. The contributions to knowledge from this project and recommendations for future hot spotting studies are discussed.

Chapter 2 Literature review

2.1 Introduction

The intention of the literature review is to identify the research gaps in the conventional theories of hot spotting and current investigation methods. The literature review was proposed to improve the understanding of hot spotting mechanisms and determinants and provide an overview of the state of art in hot spotting research especially in the numerical modelling. Furthermore, some quoted literature conclusions can be used to verify the methods and results in this project. The design parameters of the disc brake system and determinants of hot spotting in this research were mainly retrieved from the literature.

2.2 Overview of hot spot and hot judder

2.2.1 *Classification of judder*

The aims of NVH research for motor vehicles are not only for improving safety (sometimes can cause an undesired driver reaction or failure of components) but also for comfort (e.g. pedal, steering wheel feel) (Jacobsson, 2001). Brake Judder can be sensed by the driver at the steering wheel, brake pedal or other surrounding structure. Abdelhamid *et al.* (2001) classified the vibration problem into two parts according to their frequency: squeal (over 1k Hz), groan and judder (less than 1k Hz). Jacobsson (2003), Yu *et al.* (2005), and Fieldhouse (2013), distinguished judder phenomena into cold judder which is caused by mechanical imperfection, and thermal judder which is caused by thermal effects. As shown in Figure 2.1, Jacobsson, (2001) summarized and classified judder according to temperature and vibrational order (order means vibration frequency per disc revolution), i.e. hot judder and cold judder, high order judder and low order judder respectively. The order of high order judder represents the number of hot spots,

normally 6-20. The typical limit of low order judder is up to 5th order.

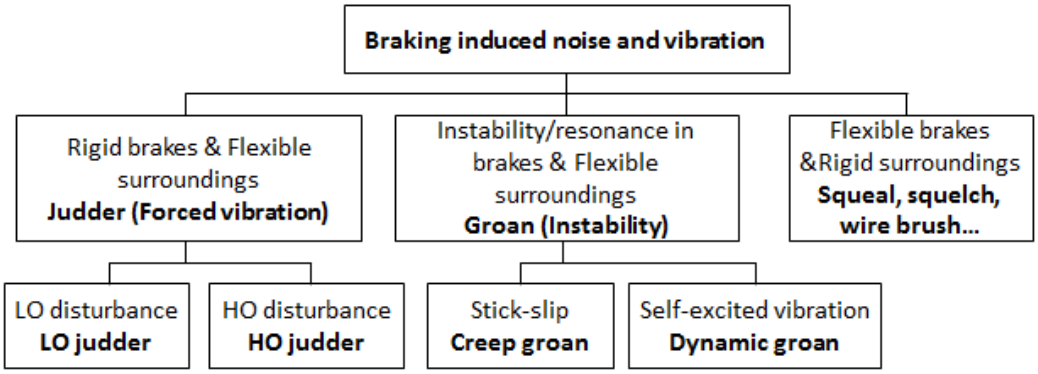

Figure 2.1 Classification of brake induced vibration (Jacobsson, 2001)

2.2.2 *Relationship between hot judder and hot spot*

Jacobsson (2003) stated that hot judder is associated with brake torque variation (BTV) and brake pressure variation (BPV) due to the rapid thermal gradients during braking which leads to thermal deformation, uneven expansion and material phase transformation. Physical effects causing BTV and BPV include geometrical irregularities, uneven wear, uneven friction films, uneven heating, uneven pressure, friction characteristics and external forces as shown in Figure 2.2. According to Ostermeyer and Graf (2013) brake torque can be calculated by:

$$T_q = r \cdot \mu \cdot p \cdot A$$

Equation 2.1

Where *r* is the effective (or mean) radius of the brake pad on the disc, μ is coefficient of friction, *p* is brake pressure and *A* is the contact surface area. The equation clearly shows that the BTV can be caused by the BPV and variations of both the effective contact radius and friction coefficient.

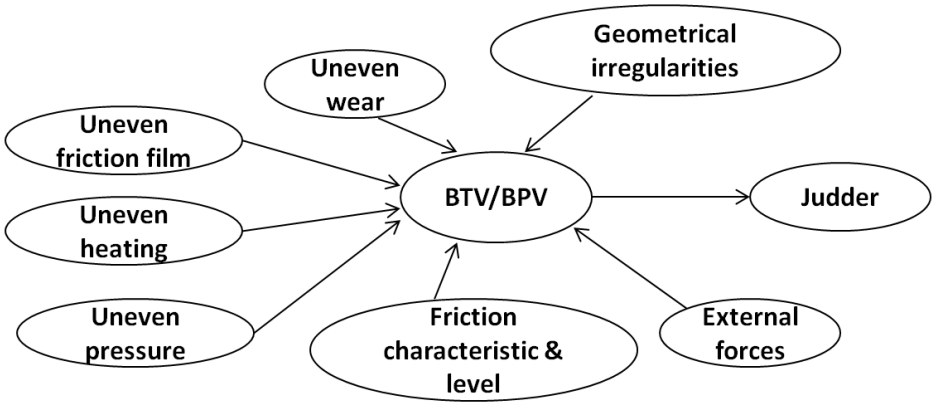

Figure 2.2 Sources of BTV and/or BPV (reproduced from Jacobsson, 2003)

In addition, hot judder was found to be significantly connected with the hot spotting. Jacobsson (2001) pointed out that the uneven heating during hot spotting can introduce disc thickness variation (DTV) through uneven disc thermal distortions and eventually causes BPV due to subsequent uneven contact pressure. Day, Tirovic and Newcomb (1991) and Tirovic and Day (1991) classified the thermal deformation of disc into bulk, macroscopic and microscopic which are associated with disc expansion/deflection, and thermal localisations (hot spotting, hot banding and surface thermal damage), and tribological characteristics (friction and wear) respectively.

Moreover, there are several other consequences of hot spotting besides judder. Regarding the metallic effects, Barber (1969) indicated hot spotting can trigger the generation of martensite permanently when the disc was heated to over 700°C and rapidly cooled. Another effect according to D'Cruz (1989) was the generation of high compressive hoop stresses on the disc surface around hot spots, which can lead to plastic flow and radial cracking. As indicated by Day, Tirovic and Newcomb (1991), hot spots can also lead to thermal fade whereby the coefficient of friction is significantly reduced due to high localised temperature.

2.2.3 *Characteristics of hot spots*

Numerous experiments have been performed by other researchers in order to identify the characteristics of hot spots such as size, temperature, duration, quantity, distribution and migration. Lamjahdy el al. (2014) stated that high thermal gradients can be observed in successive braking events, including temperature flashes, hot bands, and thermal gradients after hot banding, macroscopic hot spots, and regional hot spots. The respective images of the thermal gradients were published by Panier *et al.* (2005) and are presented in Figure 2.3. Asperity hot spots are due to discrete asperity contact and they are the only hot spot form generated when friction and wear are stable. As the duration and size are quite small, they are not directly observable (Anderson and Knapp, 1990). When the frictional heat is generated, the thermal expansion of the disc material leads to local contact pressure concentration and forms a narrow ring on the rubbing surfaces which is called hot banding. In the circumferential direction, the warping and buckling due to sufficient thermal gradients will lead out-of-phase localized macroscopic or regional hot spots. It should be noted that in this PhD thesis, the hot spots are specified as hot band and macroscopic hot spots.

Table 2.1 thermal gradients in braking (Panier et al., 2005)

Thermal gradient	Description	Dimensions	Duration	Maximum temperature
Asperities	Temperature flash	Size less than 1mm	Less than 1ms	1200°C
Hot band	Circular hot rings	Width 5 to 50mm	More than 10s	900°C
After hot band	Angular distributed gradients	Length 5 to 20mm	0.5 up to 10s	900 to 1000°C
Macroscopic hot spots	Large, high, localized thermal gradients		More than 10s	1100°C
Regional hot spots	Hot regions during cooling		More than 10s	300°C

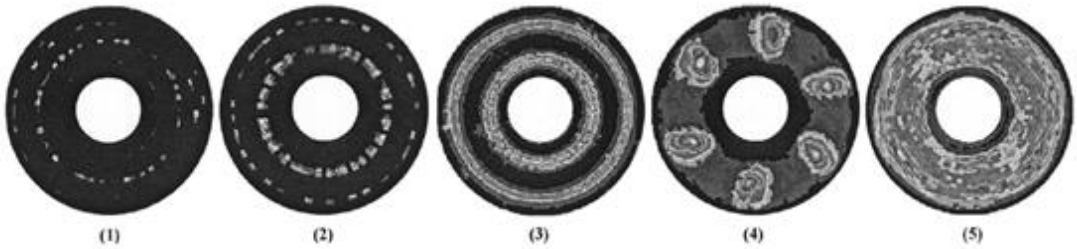

Figure 2.3 Thermo graphic of the gradient classification (Panier et al., 2006)

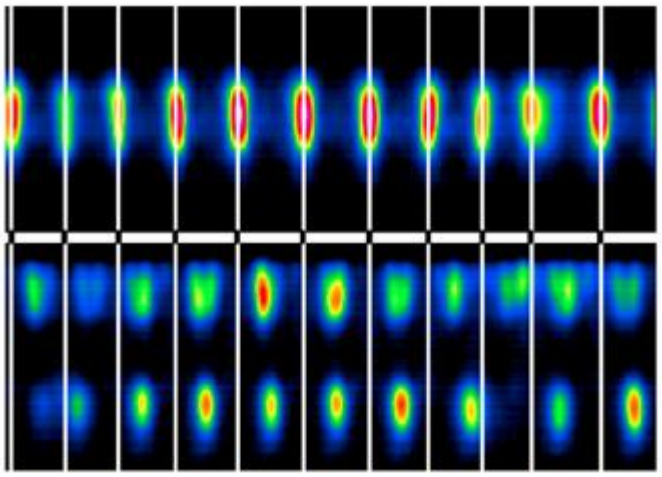

Figure 2.4 Alternating position of hot spots on both inboard and outboard disc surfaces (Panier et al., 2005)

Day, Tirovic and Newcomb (1991) indicated that the distribution of hot spot is periodical, uniform and regular. However, the random pattern of hot (blue) spots has been observed in an excessive hot spotting case (Bryant, Fieldhouse, and Talbot, 2011). It was augured that this can be caused by the overlaying of several symmetric patterns due to the pressure and speed dependence. Furthermore, through a set of experiments using an infrared camera, Sardá *et al.* (2008) found that the distribution pattern of hot spots on both sides of the disc were staggered i.e. the temperature maxima on one side was the minima on the other side, whilst both sides of the disc had an identical number of hotspots (see Figure 2.4). This means that the hot spots were anti-symmetrically distributed on the two sides of the disc rubbing surfaces which can lead or be caused by the disc waviness

distortions. In addition, regarding the radial hot spot/band distribution, Sardá *et al.* (2008) observed that the hot spots were concentrated at the mean rubbing radius of one side of the disc surface whereas two hot spots ring (or hot bands) were localised at outer and inner radii on the opposite side of the disc. It implied that the hot spots can be anti-symmetrically distributed in both circumferential and radial directions.

Regarding the number of hot spots, Panier *et al.* (2005) suggested that the number depends upon the contact length between the pad and disc which was also in agreement with the analytical predictions of Lee and Barber (1993). In 2011, Bryant, Fieldhouse, and Talbot provided investigated the relationship between the cooling channels (vents) with hot spotting and found that the number of hot spot was connected to the geometric irregularities of the ventilated disc in terms of uneven thermal capacity and cooling distribution (see Figure 1.2). Moreover, Bryant, Fieldhouse and Claffey (2013) further indicated that the number of hot spots was influenced by the energy input which corresponded with thermal buckling mode shapes of the disc under thermal load.

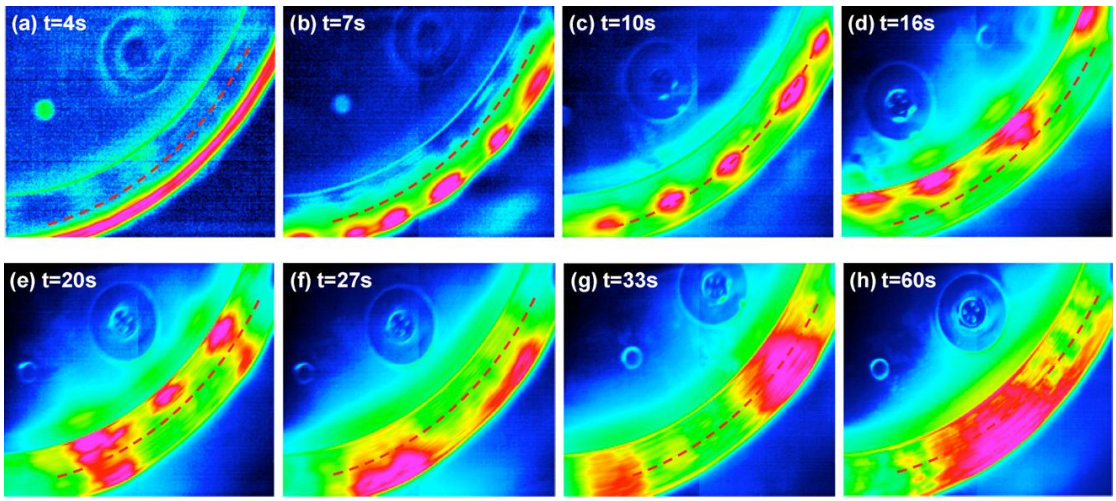

Figure 2.5 Thermal images of hot spots radial migration (Kasem et al., 2011)

In research by Kasem *et al.* (2011), the infrared (IR) camera images (Figure 2.5) of the disc rubbing surface clearly showed the radial migration of hot spotting. After the hot band formed, the hot spots initially appeared on the outer radius and then migrated to the inner radius. Thereafter, the hot spots returned back towards the outer radius and finally expanded in size. In 2013, Ostermeyer and Graf performed a systematic investigation of the phenomenon of migration of hot bands. It verified that the wear of pad is the trigger of hot band migration which is in agreement with the results by Dufrénoy (2004).

In terms of trigger condition, Yi *et al.* (1999) indicated that hot spots were triggered by unstable thermo-mechanical sliding when the sliding speed was sufficiently high. However, Kasem and Dufrénoy (2012) observed that input energy is the determinant of hot spot number. The generation of hot spots increased with high revolution speed and disc/pad friction ring thickness and diameter (Jacobsson, 2003). In fact, not only heavy brake applications can cause the hot-spotting phenomenon, but light duty brake applications also can lead hot spot due to the uneven contact pressure distribution under low actuation (Day, Tirovic and Newcomb, 1991). Anderson and Knapp (1990) summarized that the most critical brake application for hot spotting is high rubbing speed, low bulk temperatures, long frictional contacts, thick friction materials, and low material wear rates.

In summary, hot spots are thermal localisations which are most commonly evenly distributed on the disc surfaces. The inboard and outboard surface distributions are typically anti-symmetric which either results from or causes waviness deformation of the disc. The radial locations of hot spots or hot bands can migrate during and between braking events which is associated with wear of the brake pairs. High speed braking was the main trigger condition of hot spotting.

2.3 Hot spotting theories

2.3.1 *Overview of theories*

The hot spotting phenomenon was initially observed by Marshall (1948) and Hundy (1957) as martensite was observed on the disc surfaces after braking. Barber (1967, 1969) and Dow and Burton (1972) developed analytical models which considered the hot spotting problem as a thermo-mechanical contact problem which was known as the thermo-elastic instability (TEI). In addition, Panier *et al.* (2005) proposed an alternative model with a scenario of progressive waviness distortions (PWD) of the disc brake by considering the asymmetric thermal and mechanical loading of the automotive/railway brake system in the circumferential direction. Moreover, the disc thermal buckling theory developed by Ma (2004) was trying to explain the high order disc waviness distortions during hot spotting. It can be seen that various theories were proposed by the previous studies related to individual aspects. However, the mechanism of hot spotting in reality can be more complicated. As indicated by Brunel *et al.* (2014) the mechanism of hot spots is a complicated multiphasic process led by thermal surface imperfections due to heat transfer, material wear, dynamic behaviour, thermo-elastic and thermo-plastic behaviour (see Figure 2.6). It was summarized that the current theories of hot spotting, including TEI, PWD, buckling and thermo-mechanical coupling transient wear were mainly attributed to thermo-elastic, thermo-plastic, thermo-elastic-plastic and wear respectively. It implied that hot spots can be triggered by multiple mechanisms under different scenarios. Therefore, it was important to identify the effects of each hot spotting determinant to improve the understanding of the hot spotting mechanism.

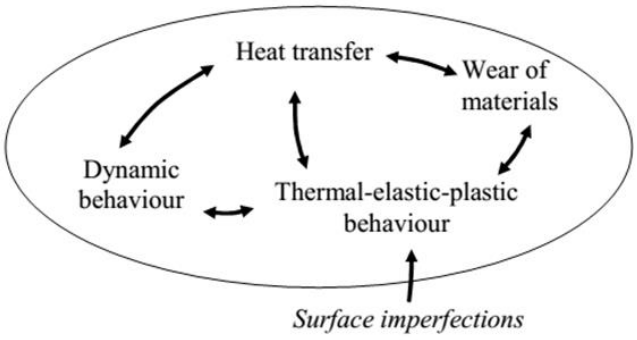

Figure 2.6 The multiphasic process of hot spotting (Brunel et al., 2014)

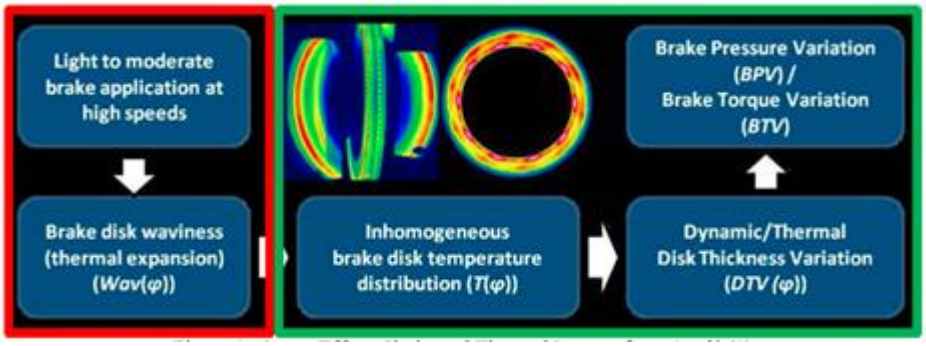

Figure 2.7 Cause-effect-chain of hot spotting and subsequent vibrations (Sardá et al., 2008)

Regarding the cause and effect chain of hot spotting, Sardá *et al.* (2008) investigated the chronological order of occurrence of waviness, hot spots, DTV and BTV/BPV through experiments and summarized the flow chart in Figure 2.7. As shown, high speed low deceleration braking events can generate axial thermal waviness deformation. Then the inhomogeneous temperature distribution in the circumferential direction can develop into hot spots which lead to local thermal expansions causing DTV. Furthermore, the DTV will develop into hot judder via BTV and BPV. This cause-effect chain explained the basic observations and theories during hot spotting and hot judder, but the effects of the hot spot determinants to the hot spotting characteristics such as number, magnitude, movement, and trigger conditions were not considered.

2.3.2 *Thermal Elastic Instability (TEI)*

Barber (1967 and 1969) proposed the basic TEI theory, which indicated that the hot spotting was caused by a perturbation of unstable structure, rotation speed, or contact pressure and the subsequent non-uniform thermo-mechanical deformation of the contact pairs. Through analytical modelling, Dow and Burton (1972) pointed out that when the relative sliding speed exceeded a ‘critical speed’, a small sinusoidal perturbation of contact pressure was observed implying the occurrence of TEI. The hot spotting was indicated as the results of the interactions between elastic contact and thermo-elastic deformation. The TEI models were then expanded by Barber, Dundurs and Comniou (1980), Barber and Zhang (1988) and Lee and Barber (1993) by representing the growth of contact pressure, heat generation, and temperature as exponential functions. The value of critical speed of hot spotting is therefore obtained by solving the analytical model which has system exponential growth rate equals to one. By using this analytical method, the non-linear relationship between the number of hot spot and the critical speed was found and validated by experiments (Lee and Barber, 1994). In addition, in order to consider more realistic geometry and boundary conditions, finite element TEI models were developed (Du et al., 1997, and Yi, Barber, and Zagrodzki, 2000) using an eigenvalue method to identify the relationship between different hot spotting mode shape and critical speed. The results of TEI theory was validated by Lee and Barber (1994), Yi, Barber, and Hartsock (2002) by comparison with the experiments in terms of critical speed against number of hot spot (see Figure 2.8). However, Cho and Cho (2008) argued that the critical speed was overestimated or underestimated by the TEI theory under different load conditions. This can be because of the simplifications of the TEI models and some hot spot determinants were not considered such as complex disc geometry and pad length.

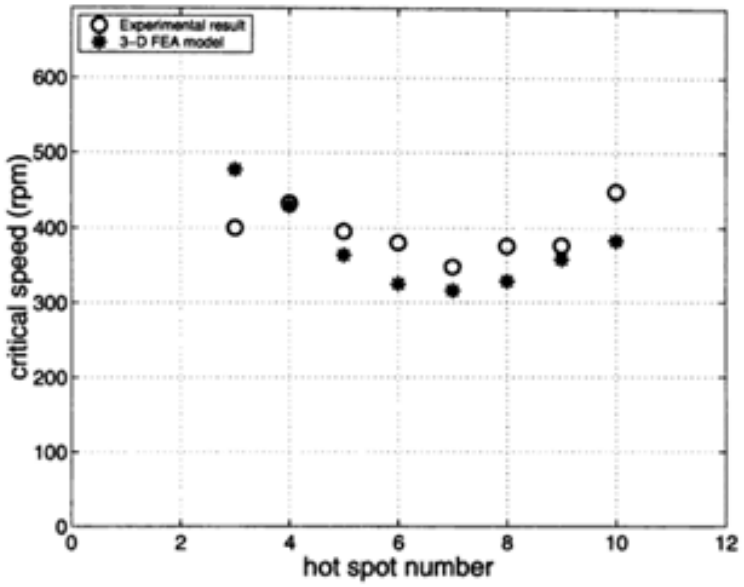

Figure 2.8 Comparison of experimental and finite element results of cirtical speed vs. number of hot spots (Yi, Barber, and Hartsock, 2002)

2.3.3 *Progressive waviness distortions (PWD)*

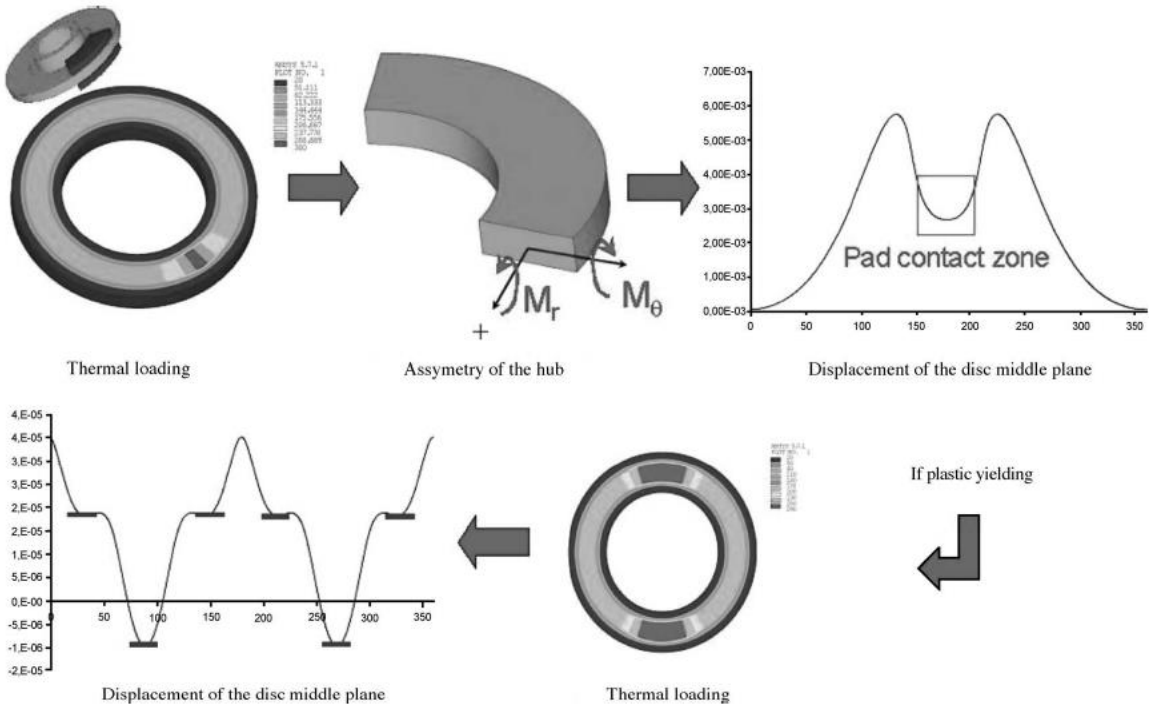

Figure 2.9 Theory of PWD (Panier, Dufrénoy, and Weichert, 2004)

Panier *et al.* (2005) proposed an alternative mechanism of hot spotting which is named PWD. As illustrated by Figure 2.9, due to the asymmetric thermal and mechanical loading since the pads have finite arc length, thermally induced bending moments can be introduced into the disc in both the radial and circumferential directions, resulting in 2nd order disc deformation. When the braking power or energy input level was high enough, plastic yielding was induced on the disc surface. As the thermo-elastic bending continuously affects the disc thermal deformation, higher order thermo-plastic waviness can be generated. Eventually, the hot spots will develop on the peaks of the disc waviness. This description of hot spotting considered the thermo-plastic deformation on the disc due to both thermal and mechanical loading from contact. It provided a different explanation compared with TEI (which only considered thermo-ealstic contact effects) in terms of the mechanisms of the relationship between the pad contact length with and waviness of the disc during hot spotting. The theory was validated by Panier, Dufrénoy, and Weichert (2004) and Kasem and Dufrénoy (2012), by comparing a FE PWD model with experiments. It was found that at the beginning of hot spotting (low energy levels), the hot spots were not equally distributed. However, after the energy increased, the successive braking applications finally generated circumferentially evenly distributed hot spots.

2.3.4 *Disc thermal buckling*

Since the disc showed waviness distortions during hot spotting based on the previous experimental observations (Lee and Barber, 1994, and Sardá *et al.,* 2008). Fan and Lippmann (1996), Ma (2004), Fieldhouse *et al*. (2008), and Bryant, Fieldhouse and Talbot (2011) indicated that the waviness deformation of the disc can be caused by the thermal buckling of the disc due to the thermal load.

Bryant, Fieldhouse and Talbot (2011) simplified the disc as a 3D beam and analytically calculated the critical buckling force due to uniform temperature increase of the disc and found that the lower order disc thermal buckling can occur. In addition, Fan and Lippmann (1996) investigated the thermo-elastic-plastic buckling of a solid disc brake, using the numerical eigenvalue method without considering the external mechanical force. As a result, the uniform thermal loading induced both conical buckling and circumferential folding of the disc in different shapes depending on the geometry of the solid disc and the number of waves. Ma (2004) extended the study in to a FE model and introduced non-uniform thermal loading in the circumferential direction. It implied that the thermal warping or buckling were both affected by the uneven thermal gradient in radial and circumferential directions. However, the critical buckling temperature predicted by Fan and Lippmann (1996) and Ma (2004) to trigger the higher order deformation was much greater than the realistic experiments. In 2015, Yang improved the FE model by introducing thermal gradients into the disc and non-uniform thermal loading. The results indicated that thermal buckling would struggle to trigger higher order disc waviness independently. But the residual stress caused by the thermal load provided a potential trend towards higher order thermal buckling. This meant that the thermal buckling could interact with other hot spotting mechanisms and promote the development of hot spots.

2.4 Hot spotting determinants

From the review of hot spotting theories, it was found that hot spotting can be driven by different mechanism and determinants. The main determinants studied in the published research are discussed in this section.

2.4.1 *Trigger conditions of hot spotting*

As indicated by Dow and Burton (1972), Lee and Barber (1993) and Zagrodzki (2009), the traction force and shear stress due to sliding have insignificant effects on hot spotting based on both experiment and TEI models. In addition, the brake pressure was irrelevant on the number of hot spot according to the analytical prediction (Dow and Burton), FE simulation (Altuzarra, Amezua, and Aviles, 2002) and experiment (Kim, Cho and Kim, 2007). But the amplitude of the temperature variation and BPV correlated with the actuation brake pressure as indicated by Kim, Cho and Kim (2007).

Panier *et al.* (2005) argued that another trigger condition of hot spot was the energetic level which leads to the plastic yielding and the PWD phenomenon. In addition, Kamen and Dufrénoy (2012) investigated the correlation between hot spot distribution with braking energy level. It was found that at different energy levels, the hot spotting distribution showed different mechanisms. At lower energy levels, the hot spots were not evenly distributed, whereas the distribution was symmetric at higher energy levels. Similarly, Bryant, Fieldhouse and Claffey, (2013) stated that the number of hot spots was influenced by the amount of energy input as it was observed that during the cooling phase after the brake test, the order of deformation decreased compared with the in-stop period. This indicated that the residual stress in the disc due to manufacturing was released and facilitated the thermal deformation when considerable heat was generated during braking.

2.4.2 *Disc and pad geometry*

Through both experiment and simulations, Zagrodzki and Truncone (2003), and Zagrodzki (2009) found that geometric imperfections (such as DTV) were the determinants of the excitation of the hot spotting, but the hot spotting can be

triggered without geometric imperfection as well. It implied that the hot spotting mechanisms for perfectly flat solid disc and ventilated disc were different. Bryant, Fieldhouse and Talbot (2011) found that the number of hot spot was correlated to the vent number (see Figure 1.2) for the ventilated disc in some instances. As the number of hot spot for solid disc was mainly determined by the speed according to the TEI theory, the findings of Bryant, Fieldhouse and Talbot (2011) implied that the hot spotting of ventilated and solid discs could be different.

In addition, both TEI predictions (Lee and Barber, 1993) and experiments (Steffen, 2006) indicated that a higher diameter-thickness ratio with constant energy input could lead to a higher maximum temperature and temperature variation.

Moreover, Eltoukhy and Asfour (2008) suggested reducing the pad arc length to prevent hot spotting which agreed with Panier, Dufrénoy and Weichert (2004*)* in their simulations and the TEI theory (Lee and Barber, 1993) that the decrease of the pad length generated more hot spots but the pad length should be longer than the minimal hot spot waviness to trigger hot spotting (Lee and Barber, 1993). However, Sardá *et al.* (2008) argued that the pad arc length was not the determinant of number of hot spot but the reduction of pad arc length could slightly decrease the peaks temperature and the temperature variations between peaks.

2.4.3 *Material selection*

In order to reduce the temperature magnitude and variation during hot spotting, material properties of disc and pads were investigated by previous researchers.

In order to achieve more uniform contact pressure distribution to reduce the thermal gradient, it was suggested that lowering the compressive stiffness or

Young's modulus of the pad would be successful (Jacobsson, 2001 and 2003, Thuresson, 2004, Shahzamanian *et al.*, 2010, and Cho *et al.* 2012). Regarding the disc Young's modulus, Kao and Richmond (1994) indicated that the influence was insignificant. Another strategy to provide uniform contact pressure was lowering the thermal expansion coefficient according to Jacobsson (2001 and 2003) and Kao and Richmond (1994). Moreover, Zagrodzki, and Truncone (2003) stated that the Poisson's ratio had little influence on the TEI solutions. Regarding the reduction of the radial hot band migration, Graf, and Ostermeyer (2014) indicated that the Young's modulus of the pad should be increased.

In addition, since lower the temperature at the contact interface can also reduce the thermal gradient. Thus increase specific heat capacity and conductivity of the pad were suggested by Jacobsson (2001 and 2003) and Eltoukhy, and Asfour (2008). However, Cho *et al.* (2012) argued that hot spotting was not sensitive to pad conductivity and Kao and Richmond (1994) and Graf, and Ostermeyer (2014) indicated that the conductivity should be reduced to prevent hot spotting.

Furthermore, as suggested by Barber (1969) and Kao and Richmond (1994), wear has cancelling effects to thermal localisation which implied that improving the wear rate of the friction material can promote a reduction in the hot spotting. Thuresson (2004) indicated that the lower heat generation could be achieved by reducing the coefficient of friction.

Even though the main effects of various material properties were studied, it can be found that the interactions between the materials properties have not been investigated. The effects of material properties on the radial hot band migration were not focused upon.

2.4.4 *Uneven wear*

Barber (1967) investigated the linkages between hot spotting and wear volume and found that thermal distortion resulting in temperature and contact pressure localisations was the main source of wear. Furthermore, Barber (1969) indicated that the stability of the thermo-elastic contact was determined by the relationship between thermal expansion and the wear rate which had positive and negative effects on contact pressure localisation respectively. To be specific, thermal localisations can be boosted by thermal expansion but reduced due to wear.

To investigate the distribution of wear and interface heat transfer, Day and Newcomb (1984) and Day, Tirovic, and Newcomb (1991) used finite element analysis to incorporate wear and thermal expansion effects. The results revealed good correlation between temperature, pressure and wear volume distribution in the radial direction as shown in Figure 2.10. Similarly, by implementing 3D scanning techniques, Fieldhouse and Beveridge (2010) found that the wear volume at the locations of hot spots was greater than surrounding areas resulting in concave regions after cooling.

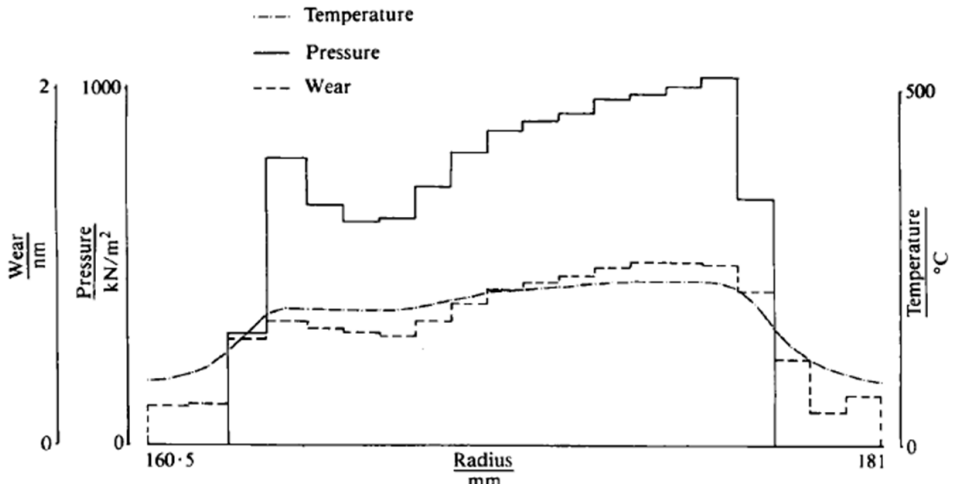

Figure 2.10 Temperature, pressure, and wear distribution on friction surface (Day and Newcomb, 1984)

Regarding hot band migration, Ostermeyer and Graf (2013) presumed that wear was the trigger of hot band migration and performed a two-rods-against-wall numerical model to verify. Wear, friction heating and thermal expansion effects were considered. It was found that wear significantly correlated with the periodicity of contact pressure within the two contact rods.

2.4.5 *Uneven cooling*

According to Jacobsson (2001), uneven cooling is another source of temperature variation. As convection accounts for ~40% to 80% of all heat dissipation from the brake disc (Tirovic, 2013), the cooling effect is significant in hot spotting research. In addition, Panier *et al.* (2005) indicated that some regional hot spots were areas with low thermal gradients on the whole surface of the disc due to inhomogeneous cooling. Similarly, Bryant, Fieldhouse and Talbot (2011) indicated that the proper design of the cooling channel of ventilated discs can significantly reduce the temperature variations.

Wu *et al.* (2008) investigated the nature of convective cooling due to the vibrational excitation for a metal plate. The results showed significant enhancement in cooling performance due to the high frequency vibration, but in the frequency range of hot judder (<1kHz) the improvement was insignificant.

Yi and Bendawi (2012) investigated the linkage between cooling effect and TEI using the 2D FE method. It was found that the convective cooling coefficient had no effect on the number of hot spot at the lowest critical speed, whilst it significantly affected the critical speed of higher order hot spotting. Therefore, the authors argued that the previous TEI researchers overestimated the critical speed due to inappropriate modelling of heat convection.

2.4.6 *Other determinants*

As indicated by Bryant, Fieldhouse and Talbot (2011), both thermo-elastic and thermo-plastic effects can affect hot spotting process. After the plastic yielding occurred, hot spots were more likely to be triggered at identical locations since the disc surface ripples from thermoplastic deformation cannot be removed after cooling. By using Scanning Electron Microscopy, Kasem *et al.* (2011) found that the hot (blue) spot locations on the disc surface were relatively irregular and rougher than the surrounding smoother locations. Therefore, it can be presumed that the disc circumferential roughness variation can affect the formation of hot spots by introducing a friction coefficient variation, contact pressure variation and subsequent heat flux variation.

2.5 Hot spotting simulations

In the aspects of hot spot modelling, various modelling techniques were implemented in the previous studies. A review of those simulations is provided in this section in order to identify the advantages and gaps of the conventional modelling approaches.

2.5.1 *2D numerical modelling approaches*

As indicated by Kao and Richmond (1994), the advantage of 2D hot spot modelling is the minimized computing time and file size, thus 2D simulations have been widely performed. Yi, Du and Barber (1999) indicated that the high computing efficiency of 2D modelling can permit parametric studies which can investigate the characteristics of hot spotting. The 2D hot spotting simulations can be classified into out-of-plane models which look at the radial and axial directions and in-plane models which investigate the circumferential and axial directions (Zagrodzki, 2009).

Regarding the 2D out-of-plane FE model, axisymmetric models have been widely used previous research. To solve the complicated thermal stress and thermal contact problem of a braking process, Day and Newcomb (1984) and Day, Tirovic, and Newcomb (1991) established an axisymmetric model as shown in Figure 2.11. A 0.5mm interface offset in terms of thickness was modelled to enable the simulation of thermal contact resistance between the contact pairs. Only the outboard disc and pad were modelled to reduce computing time. The results revealed that in the thermal localisation process, the temperature, wear rate, contact pressure distribution were consistent (i.e. high temperature zones also feature high wear rate and contact pressure).

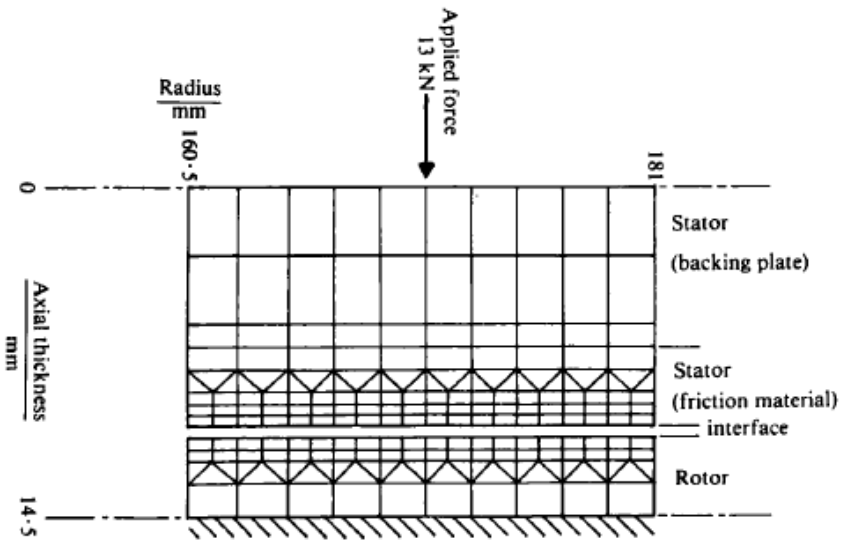

Figure 2.11 2D axisymmetric finite element model configurations (Day and Newcomb, 1984)

In addition, the out-of-plane model has the advantage that it can be used to investigate the radial migration of hot spots. Kao and Richmond (1994) considered the non-linear temperature dependent material properties and wear rate in an improved axisymmetric FE model. A TEI phenomenon was observed that initially localised at the outer radius due to the greater sliding velocity. Radial migration of thermal localisation due to wear was also observed.

Moreover, Choi and Lee (2004) initially investigated the TEI phenomenon under repetitive braking conditions and introduced the coupled thermo-mechanical element which enabled more accurate and effective prediction of both temperature and displacement field. The temperature distributions in Figure 2.12a demonstrate that at the first brake application, the high thermal gradients near the friction interfaces at both inboard and outboard disc faces were symmetric and localised at the outer radii due to the greater sliding speed. However, Figure 2.30b-d shows that, in the subsequent repetitive braking applications, due to the accumulated uneven contact pressure and temperature gradients, the inboard and outboard surfaces gradually became asymmetric. The work showed that in the TEI process, hot spots have the trend to show asymmetrical distribution in the radial direction.

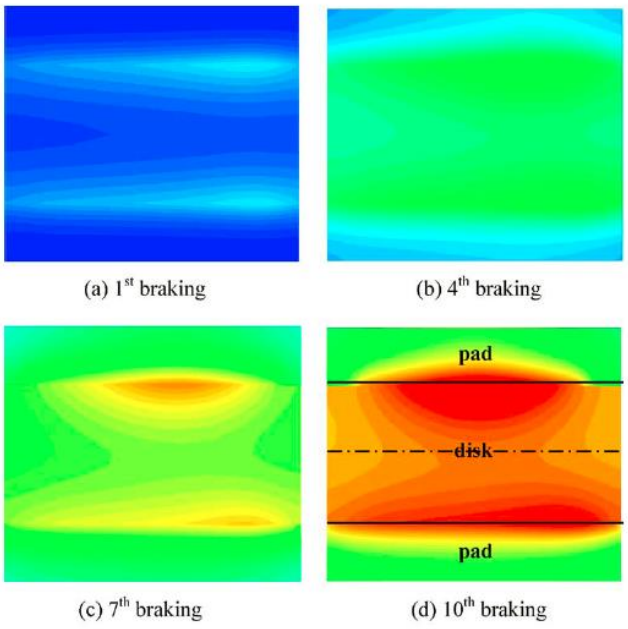

Figure 2.12 Temperature contour of different brake applications (Choi and Lee, 2004)

Another use of 2D modelling was for the investigation of the in-plane direction hot spotting which focused on their circumferential distribution characteristics. By comparing 2D and 3D FE models, Yi, Du and Barber (1999) suggested that the plain strain approximation was proper for 2D models.

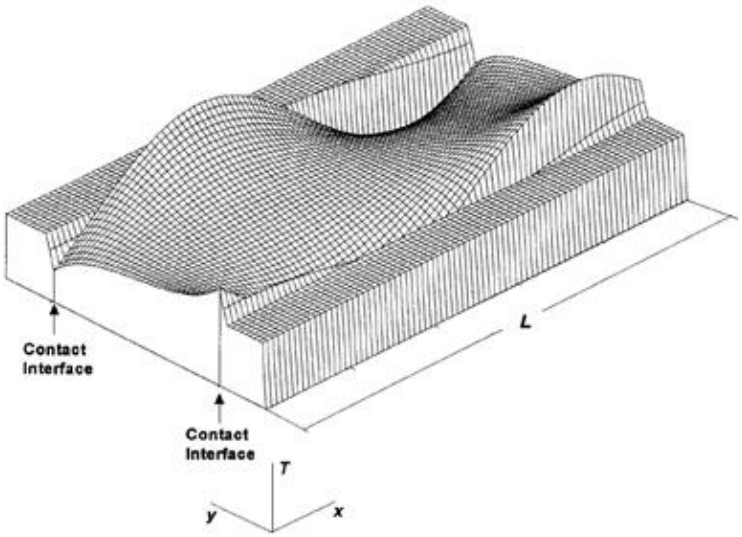

Figure 2.13 Temperature distribution of 2D in-plane model (Zagrodzki et al., 2001)

Zagrodzki *et al.* (2001) created a 2D in-plane model which simplified the pads as an axisymmetric 'homogenous friction layer' as shown in Figure 2.13. The length of the model L was identical to the actual pad arc length. The frictional shear stresses were neglected due to the effects being considered insignificant. The wavelength between hot spots can be obtained from this model and therefore the relationship between critical speed and number of hot spot can be predicted. However, this method was difficult to be implemented using a ventilated disc as the number of vents may not be divided evenly using the pad length. To overcome this limitation and to verify the PWD theory Panier *et al.* (2005) expanded the model using a full length disc model with axisymmetric pads covering 360° of the contact interfaces. The results showed two regions of plastic strain at the beginning and then multiple temperature localisations were observed. Eventually, hot spots formed due to TEI effects and were approximately uniformly distributed (Figure 2.14). The advantage of this method was its ability to identify the whole disc deformation characteristics under boundary conditions such as uneven initial disc surface ripples or even ventilated discs.

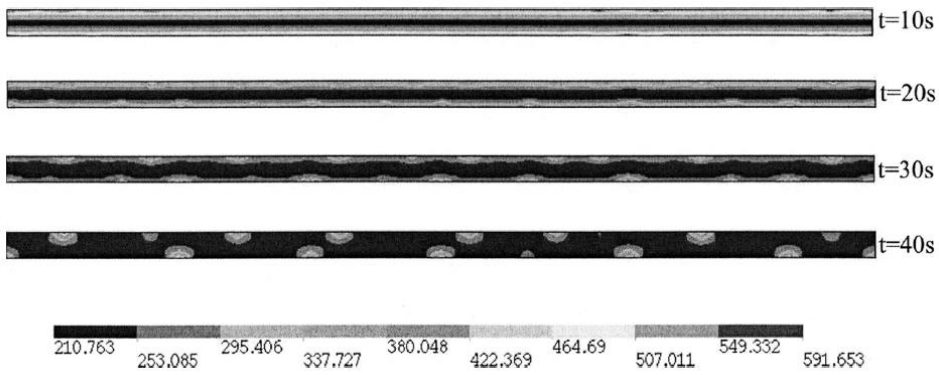

Figure 2.14 Temperature contour during braking in the PWD scenario (Panier et al., 2005)

In summary, it can be found that the 2D models were mainly focused on the simulation of the TEI phenomena of solid discs. Axisymmetric pad approximations were widely used in both in-plane and out-of-plane models. Since the direct increase of pad volume in the axisymmetric assumption can cause unrealistic contact conditions and pad thermal deformation, a friction material properties scaling method was indicated by Tirovic and Sarwar (2004) and ABAQUS example manual (2012) in order to provide equivalent pad hoop stress and thermal capacity. However, the detailed calculation of the scale factor has not been discussed in the previous literature covered in this section.

2.5.2 *3D thermo-mechanical modelling approaches*

Since the 3D model can provide information on the disc coning and radial migration of the hot bands, which also modelling the ventilated disc structure, it is significant for hot spot predictions and mechanism investigations.

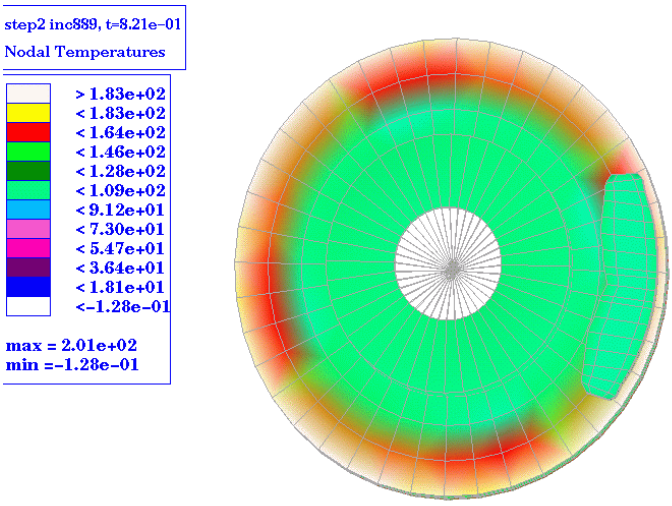

Figure 2.15 (Suryatama et al., 2001)

Suryatama *et al.* (2001) found that it was difficult to generate hot spots in 3D models due to complex mechanism. Thus four initial ripples were setup on the disc surface to create initial DTV and eventually generated hot spots (Figure 2.15). This work showed that by introducing geometry irregularity, hot spotting can be simulated. As indicated by Altuzarra, Amezua, and Aviles (2002), regarding the time step size for a 3D hot spot model with a rotating disc, it should be small enough to present the transient variation of contact pressure and boundary conditions. Therefore, to achieve accurate results for the rotating 3D disc model, the computing time or resources should be considerable.

In addition, the traditional FE model method of disc coning investigation that using uniform heat flux and load distribution on the contact surface may cause unrealistic temperature, pressure distribution and elastic distortions (Adamowicz, and Grzes, 2011). Therefore, the realistic modelling of the radial variation of thermal load based on contact pressure and velocity is important.

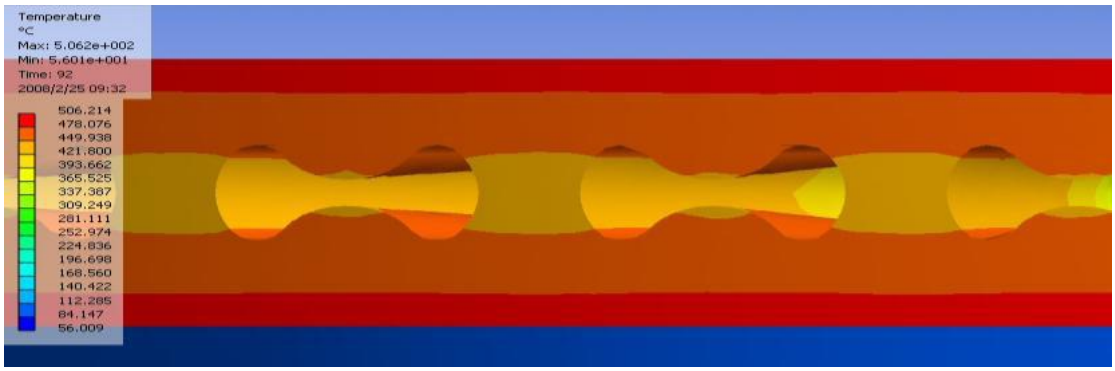

Figure 2.16 Temperature distribution of the modified vents (Bryant, Fieldhouse, and Talbot, 2011)

To provide more uniform heating, Bryant, Fieldhouse, and Talbot (2011) provided optimisation of the sculpting of the vent cross section. Both thermo-mechanical model and computational fluid dynamics (CFD) model were developed and considered in order to give more uniform surface temperature distribution. The thermal capacity and heat dissipation were well balanced across the disc blade. The simulation results (Figure 2.16) showed that the thermal gradients were reduced and the distribution of temperature was more even. In addition, Tang and Qi (2013) and Tang, Bryant and Qi (2014) provided a coupling method to achieve more accurate prediction of disc temperature by performing conjugate heat transfer through FE and CFD co-simulation. Similarly, Park *et al.* (2014) performed a 3D thermo-mechanical contact model sensitivity study to investigate the geometric significances of the ventilated disc regarding uneven thermal gradients. As shown in Figure 2.17, the increase of top-hat thickness (B), disc friction rings thickness (D and E) reduced the thermal gradients and therefore prevented hot spotting. Regarding the vent thickness (C), it was suggested that larger values would cause greater uneven temperature distribution.

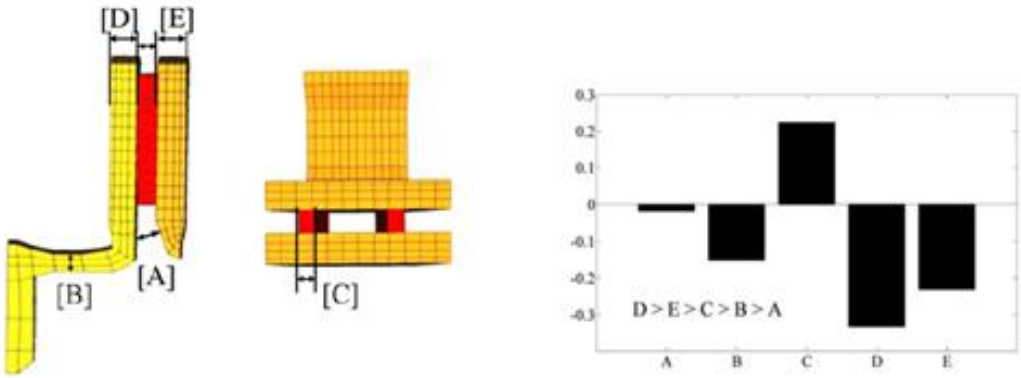

Figure 2.17 Sensitivity analysis parameters and results based on DOE (Park et al., 2014)

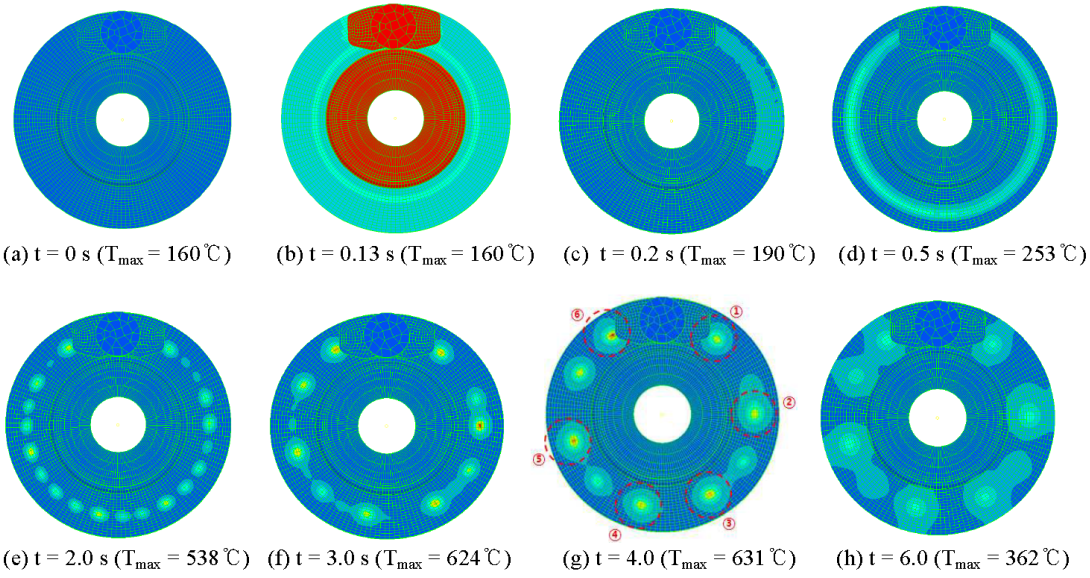

Figure 2.18 Hot spot development (Jung et al., 2014)

In 2014, Jung *et al.* modelled hot spotting using a 3D thermo-mechanical model that considered disc rotation without any initial DTV introduced. The results in Figure 2.18 showed that a hot band (radial temperature gradient) initially developed (t=0.5s) and then higher order hot spots developed (t=2.0s). The hot spots merged together and stabilised after t=3s. This implied that the number of hot spots was not constant depending on the working condition and time period. However, due to the actual modelling of the brake pads and high disc rotation speed, the computing time of this model is presumed to be considerable. The authors gave no further discussion and investigation on the hot spot mechanisms based on this model.

2.6 Main research gaps identified from the literature

From the above survey, the following references provide key guidance for this project:

1) Bryant et al. (2011) observed that the hot spotting was affected by the vane pattern of ventilated brake disc in experiment. This is the key motivation of this research.
2) Panier et al. (2005) performed the 2D in-plane hot spotting model with full length brake disc geometry. This work inspired the author using full ventilated disc geometry in 2D and 3D modelling.
3) Tirovic and Sarwar (2004) applied the axisymmetric pad assumption, scaling factor to material, and user-subroutine in heat flux and wear calculation in the 2D out-of-plane TEI model. This work provided modelling technique inspiration into the current project.

According to the above discussion of hot spotting theories, determinants and numerical modelling methods, the following research gaps have been identified and will be investigated in this research:

In the conventional analytical and 2D simulations of hot spotting, the discs were mainly considered as solid. The hot spotting characteristics of the more widely used ventilated disc have been less focused upon. However, as indicated by Sardá (2008), Bryant, Fieldhouse and Talbot (2011), the number of hot spots was affected by the vents of ventilated disc.

For conventional 3D modelling, the computational time is considerable due to complex thermo-mechanical contact effects. This causes difficulty in performing parametric studies for hot spotting mechanism investigations.

Regarding the determinants of hot spotting, the possible trigger conditions include speed and energy input. The relationship between these two factors has not been fully investigated yet. In addition, the geometric factors including pins, vents, rotor thickness, disc run-out have rarely been examined in the previous studies. Uneven cooling is another important factor that has to be considered in the modelling of ventilated disc hot spotting but has received less attention. Moreover, the anti-symmetric distribution of hot spots implied that the waviness distortion of the disc is another hot spotting determinant. The mechanism of the waviness development was still unclear since TEI, PWD and thermal buckling theories explained the problem in different aspects. Furthermore, the wear of the friction material was indicated as a main source of radial migration of hot spots, but the interactions between wear and thermal deformation were not fully discussed and simulated. Finally, the material selection had been widely investigated but the interactions between material properties on hot spots and the main effects of material properties to hot band migration have not been examined.

2.7 Summary

In this literature review, the relationship between hot spots and the main consequences–hot judder was initially discussed showing the position and importance of hot spotting research in automotive NVH investigations. Then, the characteristics of hot spots including classification, number, distribution, trigger conditions, radial migration were discussed. In addition, the main current hot spotting theories (TEI, PWD and thermal buckling) were introduced. It was found that the hot spotting could be triggered by different mechanisms or determinants. The discussion of the hot spotting determinants including trigger condition, geometry, material, wear, and cooling further confirmed that the complexity of hot spotting mechanism and the effects of some factors such as speed, energy and material properties are still controversial in the literature. Therefore, the main

research gaps were obtained from the literatures which are directly linked with the research objectives provided in Chapter 1.

Chapter 3 Methodology

3.1 Introduction

To address the research questions, the methodologies for this project will be discussed. Initially, an overview of methodologies will be given. Then, methodologies for achieving each research objectives identified from the literature review will be discussed. Furthermore, the basic theories of thermo-mechanical contact problem modelling in finite element environment will be introduced as well.

3.2 Methodology

3.2.1 *Overview of methodology*

In order to address the various research objectives listed in chapter 2, it was necessary to investigate hot spotting with various different methods. As shown in Table 3.1, the advantages and disadvantages of the common hot spotting research methods were listed. It can be seen that the analytical method was not ideal for solving complex geometry problems such as the ventilated disc hot spotting. Therefore, in this project, both experimental and 2D & 3D finite element methods were used to establish robust understanding and predictions of hot spotting through comparison and validation.

Table 3.1 Advantages and disadvantages of common hot spotting research methods

Methods	Advantages	Disadvantages
Analytical	Fast solving Parameter based Reveal the basic mechanisms	Not compatible for complex geometry, Governing equations are difficult to deduce, Many assumptions and simplification required
Experiment	Realistic	Expensive Difficult to measure Uncertainties due to effects of all determinants
2D simulation	Fast solving Economic More detailed geometry Reveal the basic mechanisms Easy to measure Fewer degree of freedom (DOF) Fewer uncertainties Flexible for parametric study	Simplifications on geometry and boundaries Not representative in some cases Limited representation for complex geometry
3D simulation	Improved geometry and boundaries More accurate representation Easy to measure Reveals more interactions	Complex to model High computing power required

As shown from the flowchart in Figure 3.1, it can be seen that there were four important parts in this project: experimental study, fundamental numerical study, 2D finite element simulations and 3D finite element simulations.

Initially, experimental studies based on a full scale brake hot judder test rig will be performed. The intention is to obtain realistic observations and measurements during hot spotting including the temperature distribution, disc deformation, vibration and pressure variation. The measurements will be set as the benchmark for further simulations regarding input parameters and results.

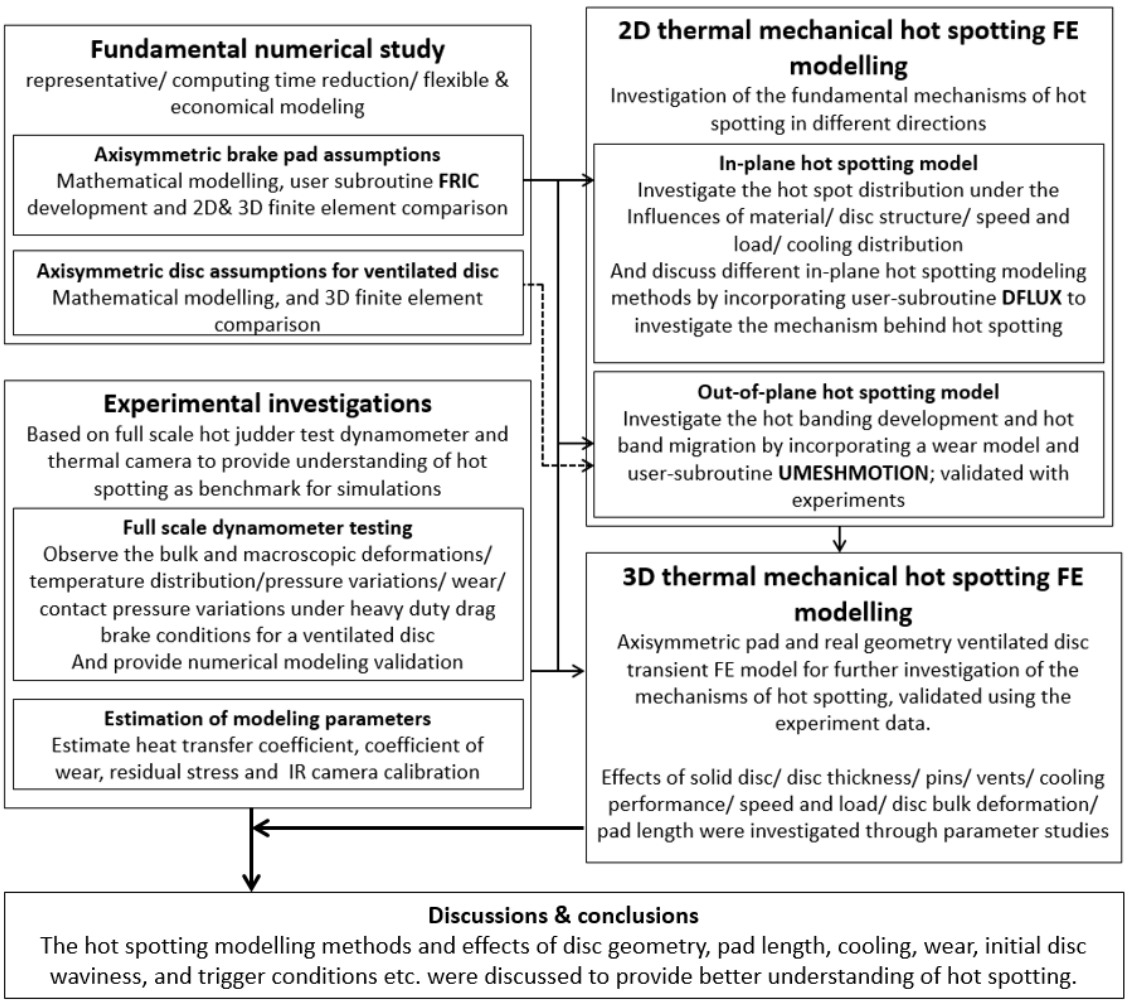

Figure 3.1 Flowchart of methodology

Then, a fundamental study will be performed to simplify the transient hot spotting problem into an axisymmetric quasi-static system. The main objective of the simplification is to improve computing efficiency by establishing a representative, economical and flexible modelling technique. By incorporating a material scaling factor method and FE package subroutine code, an axisymmetric brake pad modelling technique will be developed for the 3D and 2D in-plane models which maintain the complexity of ventilated disc geometry, whereas an axisymmetric brake disc assumption will be performed for the 2D out-out-plane models to investigate the radial migration of hot spots. Furthermore, feasibility study based on scaled brake FE models will be performed to verify the computing time and accuracy for such simplification methods.

In addition, the hot spot investigations in 2D will be undertaken in two distinct directions inspired by the studies of Zagrodzki (2009): in plane mode for investigation of circumferential hot spotting and out of plane for the radial hot spotting and hot band migration. Though the boundary conditions in the 2D simulations were limited, it is economical and flexible to investigate the basic mechanisms behind hot spotting. For the in-plane models, the main objective is to investigate the hot spotting characteristics for both ventilated and solid discs by performing parametric studies including disc and pad material properties, vent design, pins, brake speed and load, cooling and pad length. By incorporating wear effect using a subroutine, the 2D out-of-plane under axisymmetric disc and pad assumptions will be performed to investigate the effects of wear, disc coning, clamping force, material properties and pad length through parametric studies.

Moreover, the 3D simulations based on thermo-mechanical contact models with the axisymmetric pad simplification will be performed. The intention of establishing 3D models is to achieve more representative and accurate hot spotting predictions and validations. Due to the realistic disc geometry and boundary conditions, further parametric studies will be performed focusing on a comparison between ventilated and solid discs, effects of disc thickness, pad length, bulk deformation, speed and load, and cooling distribution.

3.2.2 *Research objectives and methodologies*

Since there are multiple research objectives and multiple methods used in this project. It is essential to introduce the relationship between the objectives and the corresponding methods.

Table 3.2 summarises the brief objectives, the main method used and chapter located in each case. As different methods have different advantages and disadvantages as listed in Table 3.1, the results obtained from each different method can be used to compare and validate, and therefore provide more insight into the hot spotting mechanisms and determinants. These are discussed in the following sections.

Table 3.2 Research objective brief list and corresponding research method

Objective ID	Main content	Main method used	Chapter
1	Identify the research gaps	Literature review	2
2	Improve computing efficiency	Fundamental study	5
3	Modelling disc waviness	2D	6
4	Trigger condition (speed, energy or load?)	2D, 3D, Experiment	467
5	Effects of geometry characteristics	2D, 3D, Experiment	467
6	Hot band migration	2D, Experiment	46
7	Effects of bulk disc deformation	3D, Experiment	46

- *To develop numerical hot spotting modelling techniques with effective computing efficiency*

As indicated by Altuzarra, Amezua, and Aviles (2002), realistic 3D rotating disc thermal contact finite element models are time consuming not only because of the considerable number of elements, but also due to the requirement of having a small step size to be representative. Thus, it is proposed that the most effective possible time reduction techniques are related to the effects that have little influence on hot spotting but consume significant computing resources. In this study, two assumptions which have been used by previous researchers were made and enhanced in order to satisfy the prediction accuracy of automotive ventilated disc brake hot spotting.

According to the literature review, axisymmetric pad assumptions have been widely used in the analytical and numerical investigations of hot spotting (Dow and Burton, 1972, Zagrodzki *et al.* 2001, 2009, and Panier *et al.* 2005). However, the methods have been mainly applied to clutch system hot spotting simulations which realistically feature axisymmetric friction material and solid disc. This method has had less focus on automotive brakes and the modelling method has not previously been fully described and discussed. Therefore, a proper modelling method under the axisymmetric pad assumption can be a significant time reduction method to the finite element modelling of hot spotting. In order to represent the brake pad (regard disc as stationary) using axisymmetric assumptions, the heat transfer functions, heat generation patterns and contact mechanisms have been investigated. As a result of the calculation, a scaling factor of the friction material properties was obtained. In addition, Dow and Burton (1972) and Zagrodzki *et al.* (2001) argued that the shear stress due to friction has negligible effects on hot spotting and validated these using experiments. Therefore, to further improve the computing efficiency, the relative rotation of the disc and pads will be regarded as stationary. To overcome the absence of frictional heat generation due to sliding, the friction behaviours especially the heat generation were defined using user-subroutine FRIC in ABAQUS. For verification, finite element models with and without incorporating axisymmetric brake pad assumptions were modelled and compared in both 2D and 3D in terms of temperature distribution and disc deformation.

- *To investigate the mechanism that can cause disc waviness, including thermal buckling, geometry characteristics, moving heat source and clamping forces.*

As discussed in the literature review, there are various possible mechanisms to generate disc waviness including TEI, PWD and thermal buckling. The relationship between the waviness and hot spotting is of interesting in this project. To investigate the mechanism of hot spotting, various 2D in-plane models were modelled as listed in Table 3.3. It illustrated the main simplifications and modelling techniques used which will be discussed in chapter 4 and 6 in details. Through comparing the models under different level of simplifications, it can reveal the significances of the possible mechanisms in disc waviness development.

Table 3.3 2D in-plane hot spotting models summary

Model descriptions	Main simplifications	Main modelling techniques
Uniform heat flux no pad	Regard the disc as a stationary 2D beam Heat flux uniformly applied on the disc No pad modelled	Cyclic boundary
Uniform heat flux with axisymmetric pad	Regard the disc as a stationary 2D beam Heat flux uniformly applied on the disc Axisymmetric pad modelled	Cyclic boundary
Moving heat source model	Regard the disc as a stationary 2D beam Gaussian distribution moving heat source and load source Axisymmetric pad	Subroutine DFLUX Subroutine DLOAD Cyclic boundary
Axisymmetric pad thermos-mechanical contact model	Regard the disc as a stationary 2D beam Axisymmetric pad and stationary contact pair assumptions	Subroutine FRIC Cyclic boundary
Axisymmetric pad thermos-mechanical contact model with moving heat source	Regard the disc as a stationary 2D beam Axisymmetric pad assumption and contact pressure dependent moving heat source	Subroutine FRIC Cyclic boundary

- *To explore the trigger conditions of hot spotting i.e. critical speed or critical energy.*

One of the most important outcomes of the TEI theory (Dow and Burton, 1972) was the critical speed that triggered the occurrence of hot spots. However, Sardá *et al.* (2008) argued with the support of experimental evidence that the energy level was more important than the speed in the development of hot spots. Therefore, experiments, and 2D & 3D simulations were undertaken in this project to investigate the relationship between speed, load, brake power, brake duration and energy level.

- *To evaluate the parameters of a ventilated disc that affect hot spotting e.g. pins, vents, thickness, cooling distribution and pad length.*

The traditional hot spotting prediction methods (Dow and Burton, 1972, Zagrodzki *et al.* 2001, 2009, and Panier *et al.* 2005) and models were mainly focused on solid rather than ventilated discs. The experimental works of Sardá *et al.* (2008), Fieldhouse and Beveridge (2001) and Bryant, Fieldhouse and Talbot (2011) revealed that the hot spot distribution was highly correlated to the periodic structural characteristics of ventilated discs such as vents and pins. Therefore, these characteristics were investigated in the present research by experiments as the initial benchmark. Then, both 2D and 3D simulations were performed and validated using the experiment results. The effects on pins to hot spotting were evaluated in the aspects of periodic constraints, and periodic heat conductor. Regarding the influence of vents, solid and ventilated discs were compared and different convective heat transfer coefficients on the vents were considered. For the solid disc, different thicknesses were investigated. Furthermore, the effects of pad length were investigated in both solid and ventilated disc models.

- *To evaluate the relationship between lower order deformation and hot spots i.e. the effects of bulk deformation to hot spotting.*

During heavy duty braking, the disc can exhibit various bulk deformation forms such as coning, and lower order waviness due to the thermal effect. The disc run-out and DTV are the main sources of lower order brake judder according to Jaccobson (2003). Thus it is important to understand if the bulk thermal deformation of the brake disc can affect the hot spotting.

In this study, the bulk thermal deformation will be modelled by simulating initial disc run-out. The development of lower order disc waviness and higher order waviness (hot spots) at different initial run-out magniudes will be evaluate in the 3D simulations.

- *To investigate the radial migration of hot spots/bands considering disc coning and wear.*

The periodic radial migration of hot spots or hot bands is an important characteristic of thermal localisation phenomena. As indicated by Ostermeyer and Graf (2013), wear was one of the most important determinants of hot band migration. However, the hot band migration phenomenon has received less attention in published numerical studies. Therefore, by applying the axisymmetric pad assumption, 2D out-of-plane simulations were performed to investigate the characteristics of hot band migration in repetitive braking applications. Wear models were implemented in the simulation by using subroutine UMESHMOTION, and the effective wear rate was measured by experiments. In addition, to represent the ventilated disc structure using a 2D axisymmetric model, a scaling factor was applied to material properties representing the vents. The factor was obtained through calculation and compared by finite element models. The disc

coning effect was also considered by modelling the top-hat and pins of the brake disc. The anticipated result was to establish a cause and effect chain of radial hot spot movement or hot band migration.

3.3 Theories of thermo-mechanical contact modelling

As discussed, the finite element modelling was the main research method performed in this project, thus it was essential to investigate the basic theories and algorithms of the finite element method. According to the literature review (Steffen, 2006), the hot spotting phenomenon involves transient heat transfer, thermal deformation, mechanical deformation, friction and thermal contact. Therefore, the related theories and algorithms based on the ABAQUS finite element package were introduced for solving this transient frictional thermo-mechanical contact problem.

3.3.1 *Heat transfer and thermal boundary condition*

The 3D transient heat conduction equation was established based on the 3D Fourier heat conduction law (Kolleck *et al.*, 2008):

$$\frac{\rho C_p}{k}\frac{\partial T}{\partial t} = \frac{\partial^2 T}{\partial x^2} + \frac{\partial^2 T}{\partial y^2} + \frac{\partial^2 T}{\partial z^2}$$

Equation 3.1

Where x, y, z are the spatial coordinates, *k* is the thermal conductivity (W/mK), *ρ* is the density (kg/m^3), C_p is the specific heat capacity (J/kgK), t is the time and *T* is the temperature. Then, in a cylindrical-coordinate system such as a disc brake system (see Figure 3.2), the 3D temperature field $T(r, \varphi, z, t)$ should satisfy the transient heat conduction equation which is rearranged from Equation 3.1:

$$\frac{\rho C_p}{k}\frac{\partial T}{\partial t} = \frac{\partial^2 T}{\partial r^2} + \frac{1}{r}\frac{\partial T}{\partial r} + \frac{1}{\varphi^2}\frac{\partial^2 T}{\partial \varphi^2} + \frac{\partial^2 T}{\partial z^2}$$

Equation 3.2

where r, φ, and z are radial, angular and axial coordinates respectively.

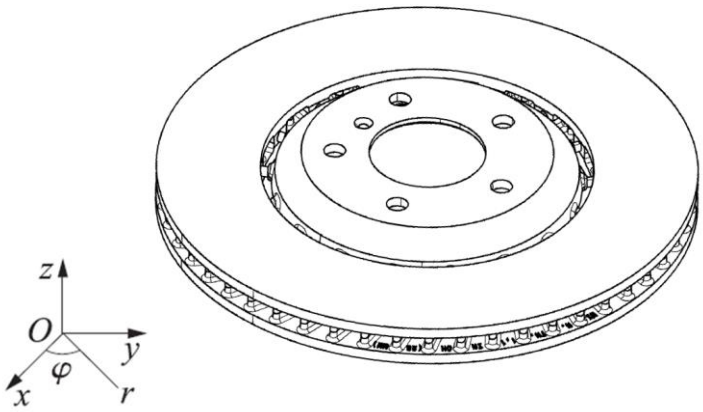

Figure 3.2 Cartesian and cylindrical coordinate systems of a brake disc

As the heat transfer problem of a brake system involves heat generation at the interface, heat conduction between contact pairs, heat convection and radiation with ambient air, the transient thermal boundary condition at the friction interface is

$$k\frac{\partial T}{\partial n} = q - \underbrace{h_c(T - T_0)}_{\text{Convection term}} - \varepsilon\sigma_{SB}\underbrace{A_{rad}(T^4 - T_0^4)}_{\text{Radiation term}}$$

Equation 3.3

At the surfaces exposed to ambient air:

$$k\frac{\partial T}{\partial n} = -h_c(T - T_0) - \varepsilon\sigma_{SB}A_{rad}(T^4 - T_0^4)$$

Equation 3.4

Where T_0 is the environment temperature and initial temperature of the system (°C), n is the unit vector in each normal direction, q is the heat flux density distributed into the brake system (W/m^{2}K), h_c is the convective heat transfer coefficient (W/m^{2}K), ε_e is the emissivity, σ_{SB} is the Stefan-Boltzmann constant

(W/m^{2}K^4), and A_{rad} is the area of radiation surface (m^2) (Tirovic, 2013). It can be seen that the radiation is very sensitive to the temperature difference between the brake disc surface to environment compared with convection. According to the study of Tirovic (2013), forced convective cooling makes up over ~39% (at 600°C) to 80% (at 100°C) of brake heat dissipation at 30km/h whereas radiation was ~43% (at 600°C) to ~5% (at 100°C). Since the convective cooling increases with the rotation speed (Limpert, 2011), and considering the high speed (~150km/h) brake application performed in this project, radiation was considered as less important heat dissipation type and neglected in the following FE simulations.

3.3.2 *Heat generation at the interface*

During a brake application, a vehicle's kinetic energy is converted into heat into the contact interface (Limpert, 2011 and Tirovic, 2013). In the following coupled temperature-displacement finite element models, the the heat flux density generated by the interface element due to frictional heat flux generation is given by

$$q = \tau \frac{\Delta s}{\Delta t}$$

Equation 3.5

where τ is the frictional stress, Δs is the incremental slip, and Δt is the incremental time. The frictional stress is determined by the normal contact pressure *p*, and the friction coefficient μ (ABAQUS theory manual, 2012). Therefore, the Equation 3.7 can be rearranged as

$$q = \mu p v$$

Equation 3.6

where v is the relative sliding velocity of the contact pairs.

3.3.3 *Thermal stress effects*

As earlier introduced, the brake process is not only a heat transfer problem, but also a thermo-mechanical problem incorporating elastic deformation due to mechanical load, thermo-elastic deformation which is temporary and even thermo-plastic effects which are permanent. Thermal stress can be generated due to the linear or non-linear thermal deformation and constrains that restrict these deformations.

The linear thermal strain can be formulated by:

$$\varepsilon_T = \alpha(T - T_0) = \alpha\Delta T$$

Equation 3.7

Where ε_T is the thermal strain, α is the thermal expansion coefficient, T is the current temperature, T_0 is the initial temperature and ΔT is the temperature variation. Then the thermal stress according to Hooke's law is

$$\sigma_T = E\varepsilon_T$$

Equation 3.8

Where σ_T is the thermal stress, and E is the modulus of the material.

Therefore, in numerical models, the stress matrix due to temperature variation is:

$$\boldsymbol{\sigma} = \boldsymbol{D}(\boldsymbol{\varepsilon_m} + \boldsymbol{\varepsilon_T})$$

Equation 3.9

Where **σ** is the stress matrix, **D** is elasticity matrix of the material, $\boldsymbol{\varepsilon_m}$ is the strain matrix under mechanical loading, and $\boldsymbol{\varepsilon_T}$ is the strain matrix due to temperature change.

3.3.4 *Heat transfer at the contact interface*

Two disc surface heat partition algorithms have been used in this research: Newcomb's theory of heat partitioning (Day and Newcomb, 1984) for the simulations only involved surface heat flux loading; and the thermal contact resistance method which enabled the rate (contact pressure and gap distance) dependent heat partition ratio between the contact pair in the thermo-mechanical contact simulations.

Regarding the thermal contact resistance method, since the contact interface involved relative motion, frictional force and normal contact pressure, different surface materials, surface roughness, and formation of transfer layer, the heat transfer of the interface has to be reproduced by a simplified mathematic algorithm in the numerical modelling. As shown by the Figure 3.3, it was assumed that there is a contact layer between the two contact bodies with temperature T1 and T2. The contact layer has thickness L and nominal contact area A. Thus the heat flux between the contact pair is

$$Q = \frac{kA}{L}(T_1 - T_2)$$

Equation 3.10

Where K is the thermal conductivity of the interface, $\frac{kA}{L}$ is the conductance and $\frac{L}{kA}$ is the thermal contact resistance. In reality, the real contact area cannot be identical to A, therefore the contact resistance is assumed to be a rate dependent variable to reproduce the variation of real contact area.

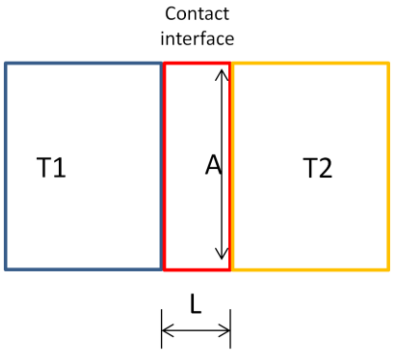

Figure 3.3 Modelling of the contact layer

A typical rate dependent thermal contact resistance definition is provided by Figure 3.4. It can be seen that there are two regimes in the determination of thermal contact resistance: separation and contact. The separation or contact is judged by the gap between two contact surfaces i.e. the clearance. When the local clearance is greater than interface thickness *L*, it will be considered separated with the thermal resistance increasing with the increase of separation. When the clearance is lower than *L*, it can be regarded as not fully contact. The resistance will be defined by the clearance as well. After the pair become fully in contact, the thermal contact resistance will be related to the contact pressure. The increasing of contact pressure causes the real contact area to be increased and the reduction of thermal contact resistance.

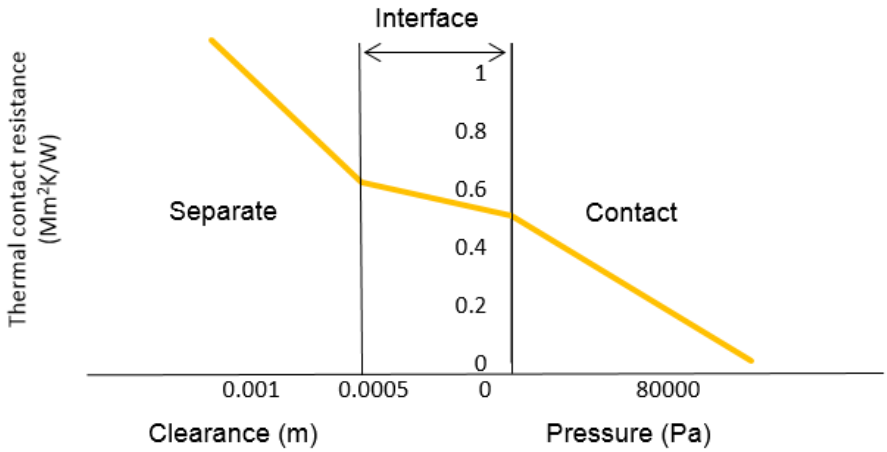

Figure 3.4 Thermal contact resistance against clearance and contact pressure

3.3.5 *Contact algorithm*

In the finite element method, the contact surfaces are discretised into nodes based on the mesh. Therefore, the algorithm to determine the contact points involved in a contact process is important. Regarding the contact surface discretisation and determination of contact points, there are two main methods available in ABAQUS: node to surface method and surface to surface method.

According to the ABAQUS manual (2012), the contact surfaces are defined as master and slave surfaces respectively based on the features of the two surfaces. In general, the master surface should have greater stiffness and coarser mesh, and only the master surface can penetrate the slave surface. Thus the ‘node’ in node to surface method was from the slave surface, whereas the ‘surface’ means the small segments or facets on the master surface as shown in Figure 3.5. When the contact occurs, the nodes will be enforced by constraints to prevent geometrical penetration between the contact surfaces or bodies which is generally unrealistic. In the small facets, the smallest distances between the nodes to the master surface are calculated and the nodal areas are assigned to the nodes for the further determination of contact pressure (Rajkumar, 2013). A problem of this method is that if a master node failed to be included in a facet (e.g. mismatch meshes between the two surfaces), this will cause the failure in pairing with slave nodes, then the master node will have free nodes that can freely penetrate the slave surfaces without any constraints. Subsequently with the undesired local penetration occurs resulting in the unsmooth contact surface.

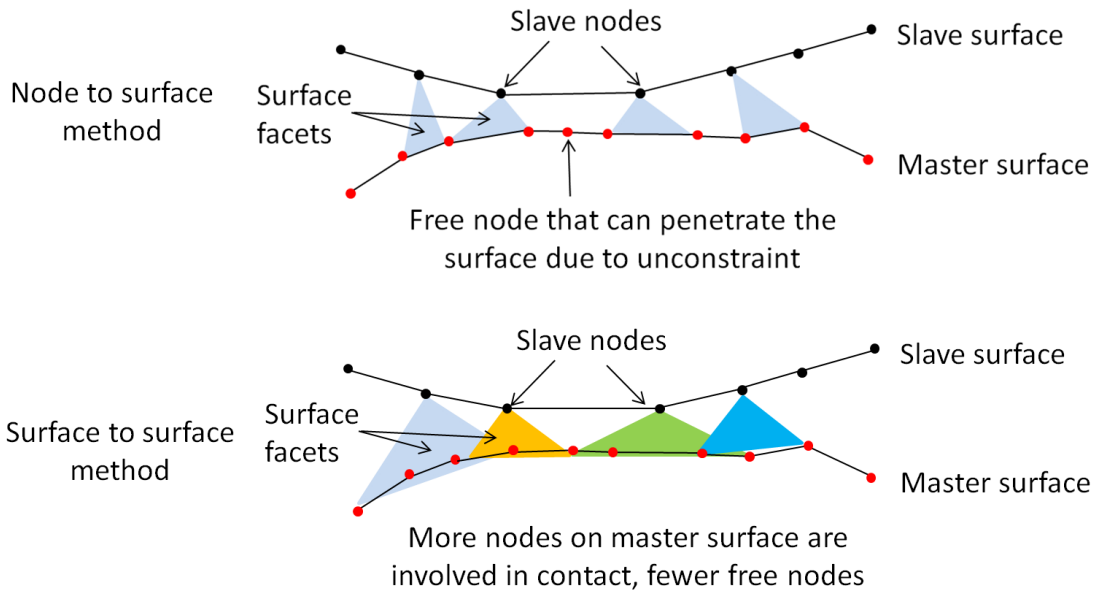

Figure 3.5 Node to surface and surface to surface contact discretisation methods (figure reproduced from Rajkumar, 2013)

An alternative contact discretisation method is called ‘surface to surface’ method. As illustrated by Figure 3.5, more facets on the master surface are involved in the contacts with each slave node. This enables an average approximation of the distance between the slave nodes to the master facets. Then the contact constraints will cover more nodes and the likelihood of penetration can be significantly reduced. Thus the mesh does not necessarily need to be matched for surface to surface contact (ABAQUS manual, 2012). Table 3.4 summarises some key comparisons between the surface to surface and node to surface methods according to Rajkumar (2013). In terms of contact stress predictions and robustness of the results, the surface to surface method is generally more accurate than the node to surface method due to fewer penetrations, less ‘snagging’, smoother surface, and lower sensitivity to mismatched meshes. Regarding the computing efficiency, since more nodes are involved in the surface to surface contact, its memory requirement is greater and the solving speed is lower.

In an automotive brake, the disc is commonly made of cast iron which is much harder than the bulk hardness of the friction material. Refinement of the global mesh of the disc will generate more elements than refining the pad mesh since the volume of the disc is much greater. Therefore, in the automotive brake case, the master surface should be the disc surface and the pad surface is the slave surface. As hot spotting is an excessive thermal localisation problem, the surface to surface method was selected in the following simulation to achieve more robust results.

Table 3.4 Comparisons between surface to surface and node to surface contact discretisation methods (Table reproduced from Rajkumar, 2013)

	Contact discretisation methods	
Features	Surface to surface	Node to surface
Contact stress	More accurate Fewer penetration points Smoother surface	Less accurate with mismatched meshes
Computing efficiency	Requires more memory and solution time	Faster due to less nodes involve
Robustness	More stable at edges and corners as considering average penetration	Free node penetration generates more 'snagging'

Regarding the judgment of contact occurrence and determining the contact pressure, the 'hard contact' method was applied in this research, which described the contact status by using the surface penetrations (i.e. over-closure) and contact pressure (ABAQUS manual, 2012). To be specific, when there was no

contact, the contact pressure was zero and the penetration was negative (i.e. a gap between disc and pad). While the contact pressure was greater than zero, contact occurred and the penetration equalled to zero. The relationship was defined in Equation 3.13 and Figure 3.6.

$$p = 0 \text{ when } h < 0 \text{ (separate)}$$
$$h = 0 \text{ when } p > 0 \text{ (contact)}$$

Equation 3.11

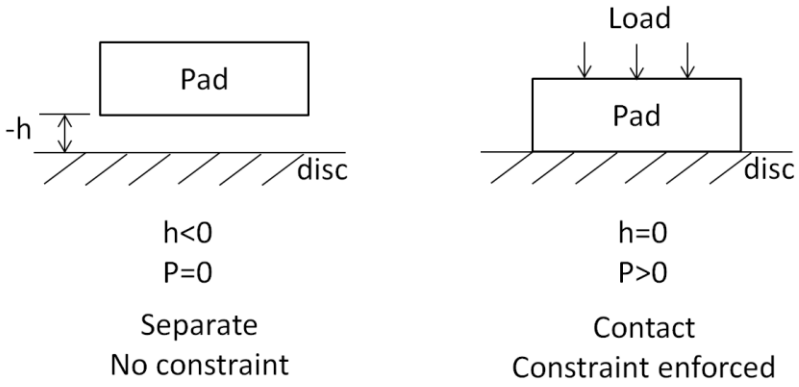

Figure 3.6 Contact and separation defined by pressure vs. penetration

When contact occurred, the 'penalty' method enforcement method was used to enforce the constraint (prevent and reduce penetrations) at the interface by introducing a penalty stiffness. As shown in Figure 3.7, the hard contact in theory strictly constrains the interface resulting in no penetration. Thus the contact pressure magnitude cannot be determined through the interface. When the penalty stiffness (the slope *k* shown in Figure 3.6) was applied to the surface, small penetration was allowed and then the contact pressure for a given node at the interface can be determined. The most significant advantages of the 'penalty method' were the fast convergence rates and solver performance since only one DOF (penalty stiffness) was applied to the model (ABAQUS manual, 2012). In addition, the linear penalty stiffness was used as shown in Figure 3.7, in order to provide further stability in convergence performance. The default penalty stiffness

of ABAQUS was determined by the underlying elements to achieve a balance between excessive penetrations and convergence rate (ABAQUS manual, 2012).

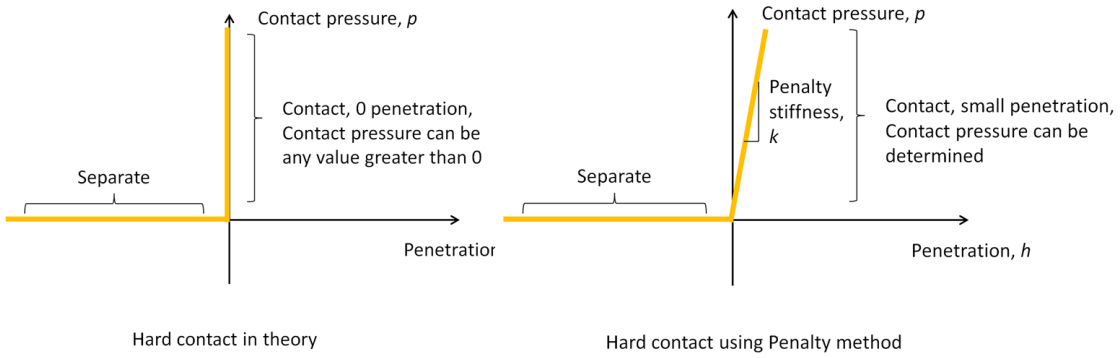

Figure 3.7 Hard contact approximation using Penalty method (figure reproduced from Rajkumar, 2013)

3.3.6 *Thermo-mechanical coupling*

The thermo-mechanical effects during braking comprises two main regimes (Meng et al., 2010): mechanical effects including the elastic or plastic deformation of the disc and pad under initial load and contact pressure which was determined by the contact algorithms (Equation 3.13) and thermostatic stress (Equation 3.11); and thermal effects including the frictional heat generation at the disc pad interface (Equation 3.8), the heat transfer inside the disc and pad (Equation 3.1, 3.2, 3.3) and the subsequent thermal deformations (Equation 3.9). The thermal-mechanical coupling interactions are illustrated in Figure 3.8.

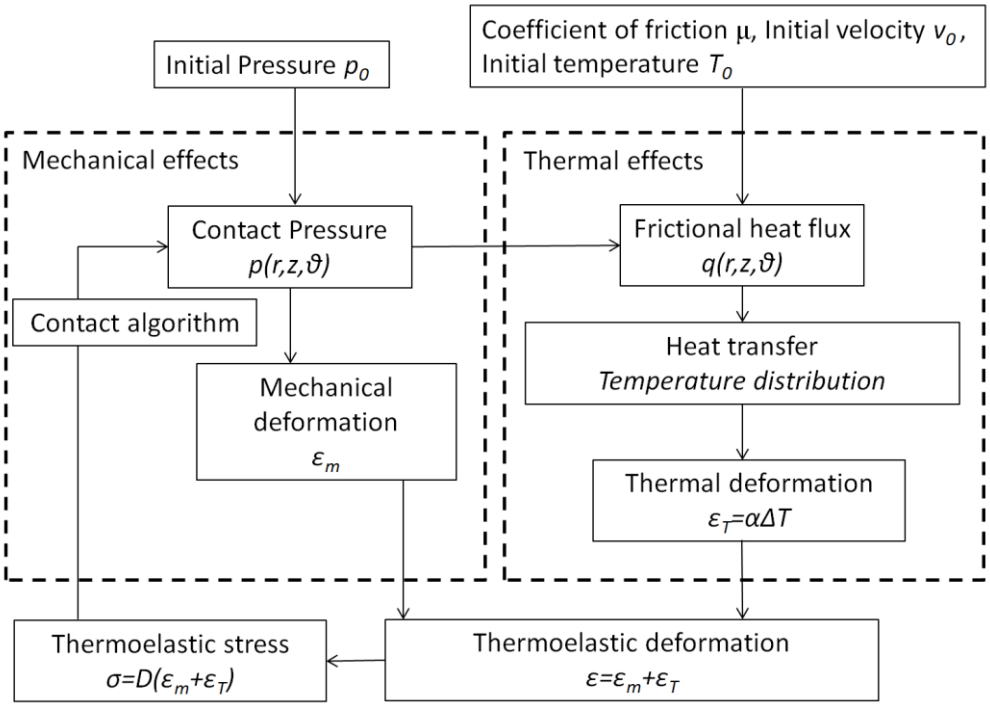

Figure 3.8 Thermo-mechanical coupling relationship (figure reproduced from Meng et al., 2010)

To enable the simulation of such a coupled thermo-mechanical problem, the finite element package ABAQUS provided two solving algorithms: implicit method (ABAQUS/standard solver) and explicit method (ABAQUS/explicit solver) (ABAQUS manual, 2012) which are common numerical solution schemes. In general, explicit method means that the solution can be directly calculated by using the known quantities, whilst the implicit method means that the solution should be calculated through matrices or sets of equations through iterations.

For the explicit method, the thermal and mechanical equations were solved simultaneously through an explicit coupling. This is due to the fact that both the thermal and mechanical equations were explicit. The thermal heat transfer in the explicit method was achieved by the explicit forward-difference time integration rule.

For the implicit method, the nonlinear coupled system between thermal and mechanical equations were solved by using a stiffness based solution technique and applying the Newton-Raphson iterations to correct each displacement increment until external and internal forces were in equilibrium.

Regarding the stability issues, the implicit method was unconditionally stable, but the explicit method was conditionally stable. Since the maximum time increment was decided by the time required for an elastic wave to cross the smallest element dimension in the model i.e. the stability limit was defined by the smallest element size (ABAQUS manual, 2012).

In this project, the implicit method (ABAQUS/standard) was used due to several reasons:

1) The implicit algorithm allowed simulations involving large time steps (large time step using the explicit method will cause inaccurate results) which saves computing time and storage. Meanwhile, because there was no rotation involved in the models, a large time step did not affect the accuracy of the results.

2) The implicit solver featured better support of the subroutines that were used for this project in terms of programming difficulty and functionalities. For instance, the wear simulation subroutine UMESHMOTION was only supported by the implicit solver.

3) According to the ABAQUS example models, the implicit and explicit model only showed differences when including rotation. Due to the fact that the majority of the models used in the thesis were quasi-static without rotation, implicit model was more suitable than the explicit model since the

centripetal loads were not considered in implicit algorithms.

4) Loizou (2011) investigated the thermal contact problem using both implicit and explicit models; the results suggested that the implicit models were more reliable in predicting the contact pressure distribution. Since the uneven contact pressure is very significant in a hot spotting simulation, the implicit algorithm was preferred in this project.

5) The accuracy of the explicit method was highly sensitive to the mesh quality (smallest element size) and the time step size, therefore, the overall computing time of the explicit method was greater than that of the implicit for fine meshing. The results of the implicit method were unconditionally stable and the accuracy at each time step was assured due to the Newton-Raphson iterations to correct each displacement increment until external and internal forces were in equilibrium.

It should be noted that the implicit algorithm also has some drawbacks that affected the simulations:

1) The implicit method solves large equations and matrices at each increment until equilibrium, this requires large computer memory. The PC used for this research had 16GB memory which could solve a minimum of 1.5mm approximate global element size for 2D models or 4.5mm for 3D models.

2) The implicit solver cannot utilise multiple cores of a CPU, so the computing efficiency was not 100%.

In summary, the hardware bottleneck of the implicit solver was the computer memory, whilst the bottleneck of the explicit solver was the CPU performance.

Comparing the advantages and drawbacks of the two methods, and considering the strong thermo-mechanical coupling during hot spotting, and quasi-static assumptions, the implicit model was used in this research.

Figure 3.9 shows the flowchart indicating the solving process for the coupled temperature displacement problem using ABAQUS/standard (Yu, 2010). For iteration, the temperature field and displacement field are calculated simultaneously. It moves to the next iteration until the solutions of both fields reaches the convergence criterion. As the two fields are highly dependent on the response of each other, the equilibriums have to satisfy various non-linear conditions. The more degrees of freedom each node has, the larger the governing matrix is which has to be solved. Therefore, the coupled thermo-mechanical simulation is generally time consuming.

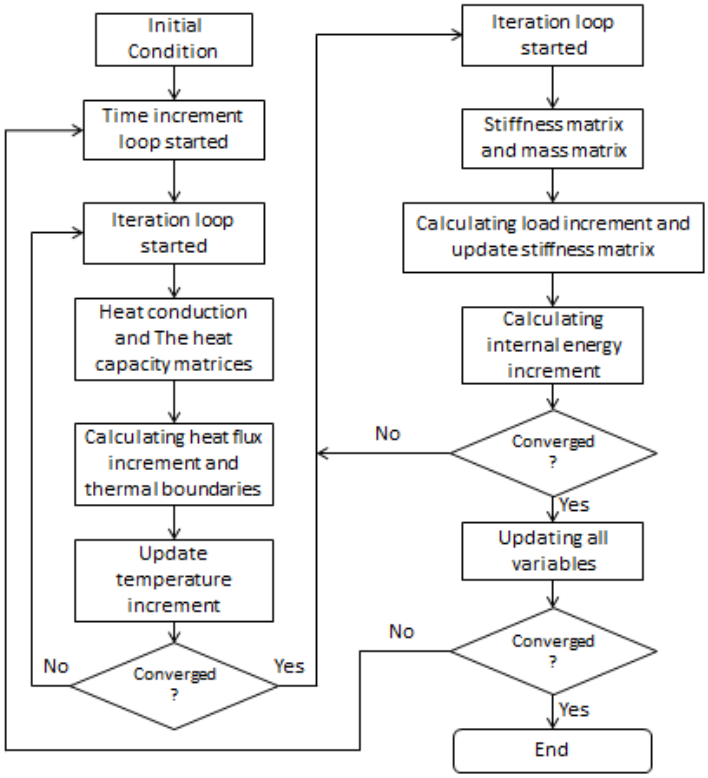

Figure 3.9 Computing flowchart of the thermo-mechanical finite element model in implicit method (figure reproduced from Yu, 2010)

3.3.7 *User-subroutines*

In ABAQUS, the subroutines are the programs that expand the functionality of the simulations. The language used for compiling is FORTRAN. Multiple subroutines can be attached to the models and run simultaneously. The solution dependent variables can be retrieved during each time step to enable the modelling for some complicated interactions such as thermal localisation and wear.

In the purpose of improving computing efficiency, by incorporating the subroutines, some model simplifications can be enabled without losing accuracy. Table 3.5 shows the subroutines used for this research. The detailed contents and explanations of the subroutines are provided in the Appendix 1 and 2.

Table 3.5 User subroutine used in this project

Type	Subroutines	Function in this project
Define heat generation	FRIC	Define nodal frictional heating
	DFLUX	Define moving heat source
Define mechanical load	DLOAD	Define moving load source
Define wear	UMESHMOTION	Define nodal wear as a function of contact pressure and speed

3.4 Summary

The numerical modelling is the main research method used in this project. The finite element models will be established on stages basis and starting from a fundamental study of the basic assumptions and simplifications of the model. Meanwhile, the experimental works will be carried out to provide basic benchmarking of the following simulation. Then, the 2D hot spot models will be established based on the verified assumptions raised in the fundamental study.

The 2D models will be distinguished into in-plane and out-of-plane. In order to address the research questions, parametric studies will be performed and the effects of the important hot spotting determinants will be investigated. Furthermore, 3D hot spotting model will be performed intending to provide more realistic simulations. Since there are six main research objectives in this project, the research objectives will be addressed by various method including the fundamental study, experiments, 2D and 3D numerical models. The detailed relationship between the objectives and the corresponding method were listed in Table 3.2.

Then, the basic theories of thermo-mechanical contact and numerical modelling were introduced. The basic equations such as heat transfer equation, frictional heat generation, and thermal contact resistance were implemented into the further fundamental study and numerical modelling including the compiling of user subroutines. The basic settings of the numerical models were also mentioned, including the contact surface definition, basic meshing strategies, thermal contact resistance, solver selections (implicit vs. explicit) and user-subroutines which are the foundations of the following FE models performed in this research. Regarding the FE solver, it is worth noting that there are novel approaches to time-stepping problems that combine the advantages of explicit and implicit methods, such as Hopscotch method (Gourlay, 1970).

Chapter 4 Experimental Investigations

4.1 Introduction

The intention for performing the hot spotting and hot judder experiments is to provide advanced understanding of the actual hot spotting and the related hot judder process, hence verify and facilitate the proper setup of the following numerical modelling. The experimental tests were carried out on a hot judder test dynamometer at the Braking Research Laboratory of the University of Bradford. The test consisted temperature, disc distortion, brake pressure variation measurements, and thermal imaging. The test rig setup, hot spotting related results and some numerical modelling inputs estimated through the tests will be discussed in this chapter.

4.2 Basic concepts and terminology

Before the formal investigations, some basic concepts and terminologies were introduced in order to clarify and unify the terminologies appeared in this research.

4.2.1 *Brake assembly*

Figure 4.1 illustrates the basic brake components on a laboratory dynamometer. The brake disc was a two piece pin-mounted ventilated disc. Comprising an aluminium top-hat and cast iron friction ring of rotor, the disc rotor was connected to the top-hat using steel pins. The side of the disc toward the centre of the vehicle is called ‘inboard’ direction whereas the direction toward the outside is called ‘outboard’ direction. The disc vents were periodically distributed between the two friction rings (layers) of the disc. The caliper was of single piston ‘sliding fist’ type as shown in the right hand side figure. During the braking applications, the brake line pressure was applied on the piston which therefore forces the inboard brake pad on the disc. Since the calliper type was ‘sliding fist’ type, there was no piston

on the outboard side, so the outboard pad was clamped to the disc by the reaction force.

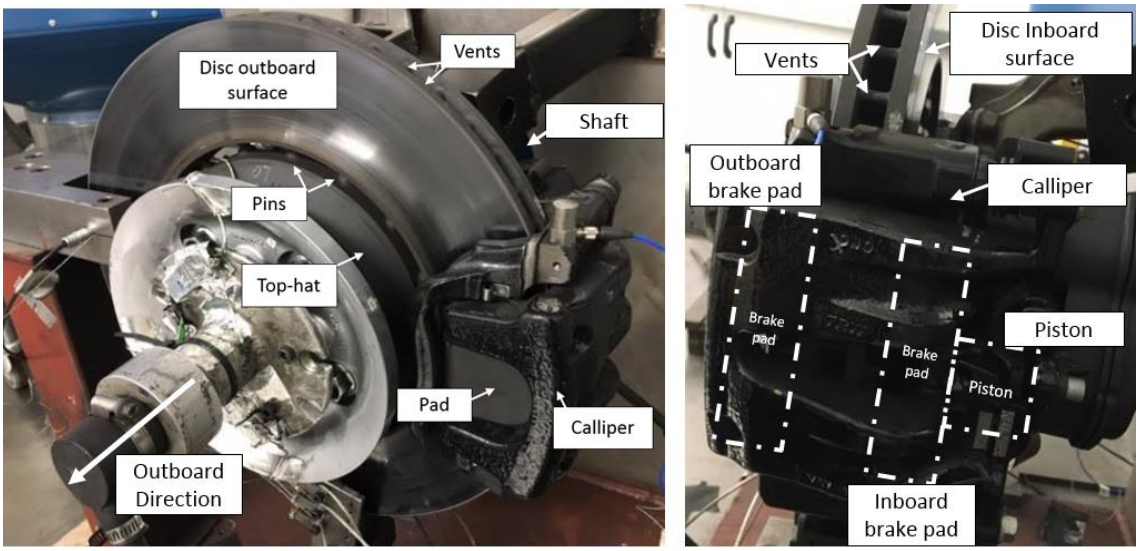

Figure 4.1 Basic disc brake system assembly on a dynamometer

4.2.2 *Terminologies of disc deformation*

During hot spotting and hot judder, the brake disc can thermally distorted into a wavelike shape. Figure 4.2 plots the general disc waviness deformation showing the disc deformation comprising three sine waves per revolution. Because the hot judder is a vibration caused by the disc thermal deformation, the vibration frequency is dependent on the disc rotation speed. To normalise the effects of speed to the vibration frequency, the term 'order' is widely used in the description of disc distortion or vibration. The order means the vibration frequency (or disc waviness) per disc revolution. Therefore, the disc waviness deformation shown in Figure 4.2 can be called '3rd order disc distortion'.

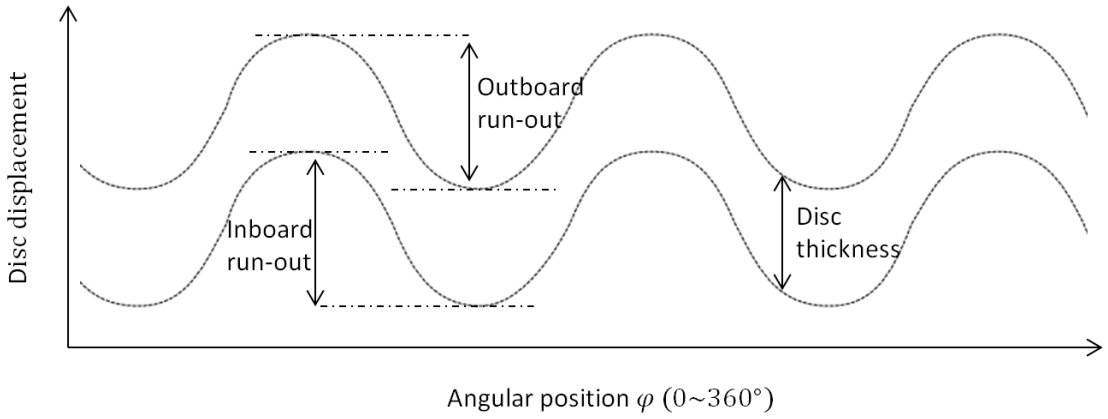

Figure 4.2 Basic terminologies of disc deformation

In addition, since there are both inboard and outboard rubbing surfaces on a disc, the disc distortion on one surface alone was called side surface run-out (SRO). The SRO can be defined as either a single value (max-min) or a set of time series data characterising the waviness. Likewise the DTV can be defined as a single value or time series defining the deviation from mean thickness. The SRO and DTV generate a brake pressure variation (BPV) which is characteristic of brake judder. The generalised and special concepts had the same principle with as SRO and DTV.

4.3 Dynamometer setup

Disc brake system hot judder is initiated by the thermal deformation of the brake disc, thus the judder test rig should be capable of providing sufficient brake energy input, rotational velocity and braking power. To obtain similar results to the real on-vehicle brake scenario, the uprights, hub, disc, pad and callipers were identical to the real vehicle. In this project, the main brake assembly tested on the dynamometer was based on a high performance vehicle rear right brake. In some of the tests, the thermal camera was implemented to provide thermal imaging of hot banding and hot spotting.

The schematic of the hot judder test set up is shown in Figure 4.3. The left hand

side room comprised the test rig and measuring/monitoring equipment. Whilst right hand side is the control room where the test activates can be controlled once the test rig was set up. A camera in the test room was connected to a PC in the control room in order to provide monitoring during the test.

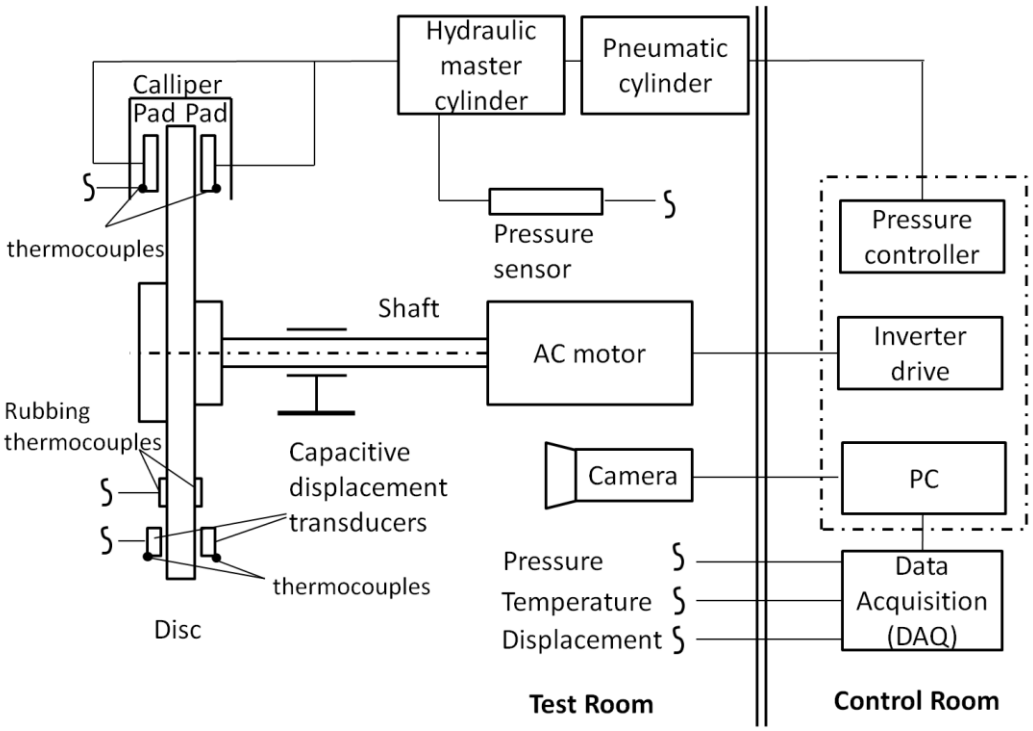

Figure 4.3 Schematic of the judder test rig

4.3.1 *Dynamometer*

The assembly of the dynamometer is illustrated in Figure 4.4. The drive of disc was provided by a 90kW AC motor, which can offer 579 Nm maximum brake torque and 1500rev/min maximum speed, via linkage with a vehicle drive shaft. In the tests performed, 500 Nm constant torque and 976rev/min constant speed were provided. The actuation pressure was provided by a pneumatic actuator attached to a hydraulic master cylinder.

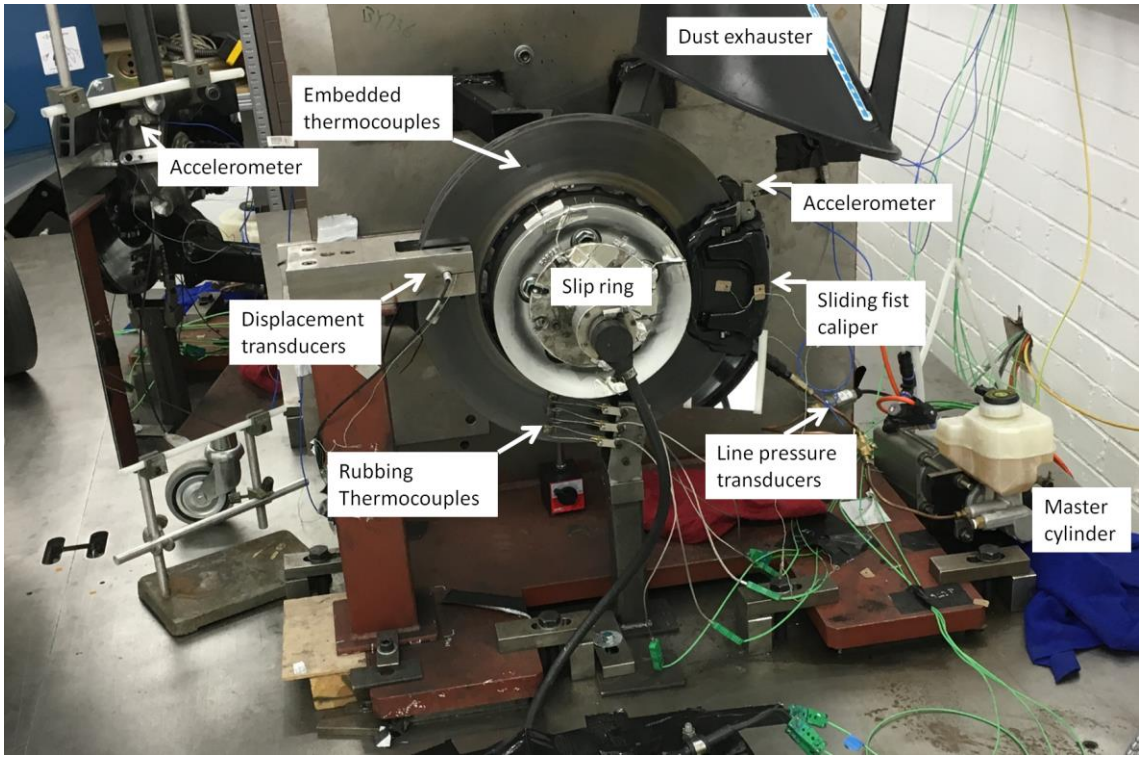

Figure 4.4 Dynamometer setup

4.3.2 *Sensors*

Multiple sensors were used in the test rig in order to provide a comprehensive understanding of the thermal and vibration effects during hot spotting and hot judder. To measure the BPV, a pressure transducer was connected directly to the brake line close to the brake calliper. There were two capacitive displacement transducers directed at the inboard and outboard sides of the disc at the same radius. 6 rubbing thermocouples were mounted on the disc surface on both sides in order to measure the temperature on inner mean and outer radii of the disc surface. Meanwhile, there were type K thermocouples on the pad back-plates to estimate the brake pad temperature and conductivity and on the displacement transducers ensuring that they did not exceed their calibrated range to prevent the failure of the transducers. Since the disc was rotating, a slip ring was mounted on the central hub of the brake in order to connect the embedded thermocouples to the data acquisition device. The embedded thermocouples were intended to

provide bulk temperature data at mean and outer radii of the disc. The specifications of the sensors are listed in Table 4.1. It can be seen that the sample rate of the thermocouples were relatively low due to their responsive time (85 Hz). Therefore, a thermal camera was used to observe hot spotting. This will be introduced in section 4.3.6.

Table 4.1 Specifications of sensors

Measurement	Sensor Type	Number	Sample rate (Hz)	Comments
Temperature	Embedded thermocouple	3	85	On outer and mean radius of outboard surface and mean inboard surface
	Rubbing thermocouple	6	85	On inner, mean and outer radius of both inboard and outboard surfaces
	Surface thermocouple	4	85	On inboard and outboard pad back-plates, and displacement transducers
Disc Displacement	Capacitive displacement transducers	2	50k	The displacement outputs of the two transducers were synchronized
Line Pressure	Pressure transducer	1	50k	
Vibration	Accelerometer	2	50k	On calliper (tangential) and knuckle (radial) respectively

4.3.3 *Brake components*

The brake components comprised of the rear foundation brake assembly from a high performance vehicle. The single piston sliding fist type brake calliper is mounted to the vehicle upright/hub assembly as shows in Figure 4.4. The ventilated brake disc structure to be investigated was shown in Figure 4.5, which is a two pieces pin-mounted ventilated featuring 17 pins and 51vents. The rotor, pins and top-hat were made of cast iron, steel and aluminium respectively. The brake disc and pad basic dimension are provided in Table 4.2.

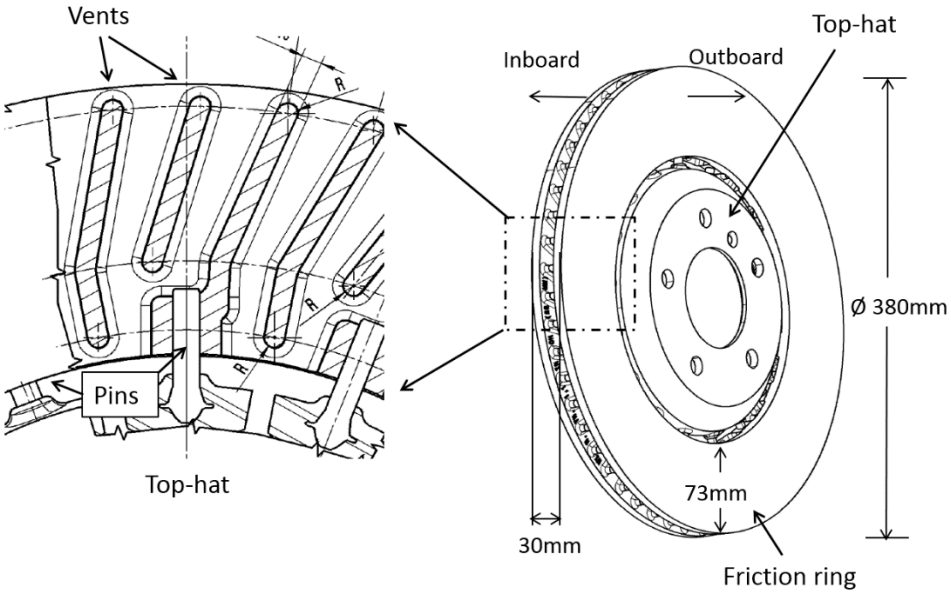

Figure 4.5 Ventilated disc structure and dimensions

Table 4.2 Brake dimensions

Braking parameters	
Brake disc outer radius, R_o (mm)	190
Brake disc inner radius, R_i (mm)	117
Brake disc thickness, T_h (mm)	30
Number of vents/vanes	51
Number of pins	17
Front or rear disc	rear
Brake pad arc length angle, θ(°)	30

4.3.4 *Test application*

To generate the hot judder phenomenon, the disc was initially heated to 60°C through 10bar drag brake applications at 370rev/min as the pre-heating phase. Once the disc temperature reached the required value, a 24 second drag brake application under 25.5bar actuation pressure at constant 976rev/min (~150km/h) was performed. The brake operation parameters are listed in Table 4.3. After cooling down to 60°C, two more identical applications were performed. All the cooling phase data were recorded in order to obtain DTV and SRO without the

in-braking thermo-elastic effects. As the dynamometer was limited to drag brake applications (constant speed), the brake applications were based upon dissipating an identical amount of energy as in the vehicle during a braking event from 240-70km/h. The motor speed was adjusted to give the desired energy, whilst the brake pressure and application time remained identical to that of the vehicle braking event (see Figure 4.6).

Table 4.3 Brake operation parameters

Braking parameters	
Rotational velocity, ω (rad/s)	102
Actuation pressure, P (bar)	25.5
Braking duration t (s)	24
Braking power P_w (kW)	51
Total energy input E_i (MJ)	1.2
Brake disc outer radius, Ro (mm)	190
Brake disc inner radius, Ri (mm)	117
Brake disc thickness, T_h (mm)	30
Brake pad arc length angle, θ(°)	30

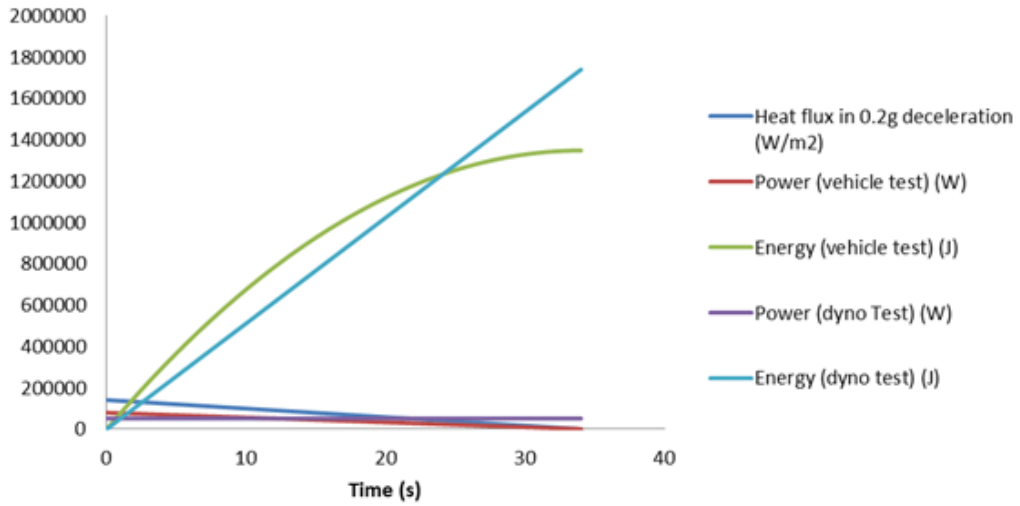

Figure 4.6 Comparisons of brake energy, power and heat generation between the vehicle test and dynamometer test

4.3.5 *Data acquisition and processing*

Pressure, temperature and displacement data from transducers were acquired using a DAQ device at sampling speed of 50kHz. This sampling rate enabled the high ‘resolution’ results of the disc deformation and pressure variation per disc revolution. A LABVIEW program was written for monitoring the results of sensors and writing into TDMS/TDM files. The signals from the two displacement transducers were synchronised using a data synchronisation box to prevent inaccuracy in the DTV calculation.

A MATLAB code was used to convert TDMS/TDM data into MAT format for further data processing. Nevertheless, in order to deal with large amount of test data and show insight of BPV and DTV in hot judder phenomenon, a Fast Fourier Transform (FFT) waterfall plot technique was performed which was developed by Bryant, Fieldhouse and Claffey (2013). In addition, various MATLAB codes were developed for data plotting and interpretations.

4.3.6 *Thermal imaging*

The intention of utilising thermal imaging in the research was to provide information on the temperature distribution variation over time to provide better understanding of hot banding and hot spotting, and verify the observations from the other sensors. The main advantage of thermal imaging is that it can directly provide the images of hot spot distribution and formation whereas the thermocouples can only provide temperature evolution for a given location (embedded thermocouple) or radius (rubbing thermocouple) of the disc surfaces at a much lower response rate.

There were two capture modes used in this study, named “full view” and “windowed mode”. For full view mode, the braking assembly was monitored as

shown in Figure 4.7. The objective of the full view mode is to investigate the hot spot characteristics such as number of hot spot, distribution, and temperature. A front surface mirror was mounted at 45° to the disc and camera, to reflect the temperature distribution of the back of brake disc (i.e. inboard surface). The resolution of the full view images were 650x512 and captured at 125Hz.

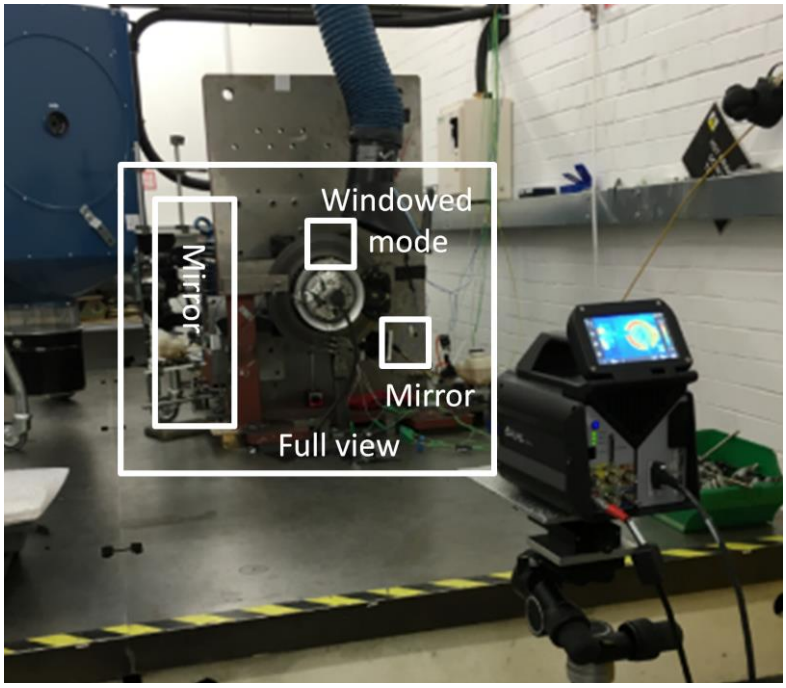

Figure 4.7 IR thermal camera and the monitoring zones setup

The windowed mode featured 160x128 resolutions at 1kHz to provide better thermal imaging of the hot spot localisation process. In the “windowed mode” mode, the shape, and relative location of pins, vents and hot spots could be examined in more detail. Due to the limitation of equipment, the traditional line “scan mode” which provides time-history development of hot spots cross a given angular position was not applied in this project.

The raw data obtained from the IR camera were voltage in mV rather than temperature. Thus it is important to calibrate the relationship between temperature and emissivity. In this calibration, the temperature time series data

were obtained from the three outboard surface rubbing thermocouples and the voltage time series data were retrieved from the pixels closed to the contact zones of the rubbing thermocouples as illustrated in Figure 4.8. After aligning the time series data at identical time period of the disc heating phase, the relationships between mV and temperature at inner, mean and outer radius can be obtained respectively (reflect the effects of different emissivity value at different locations) as shown in Figure 4.9.

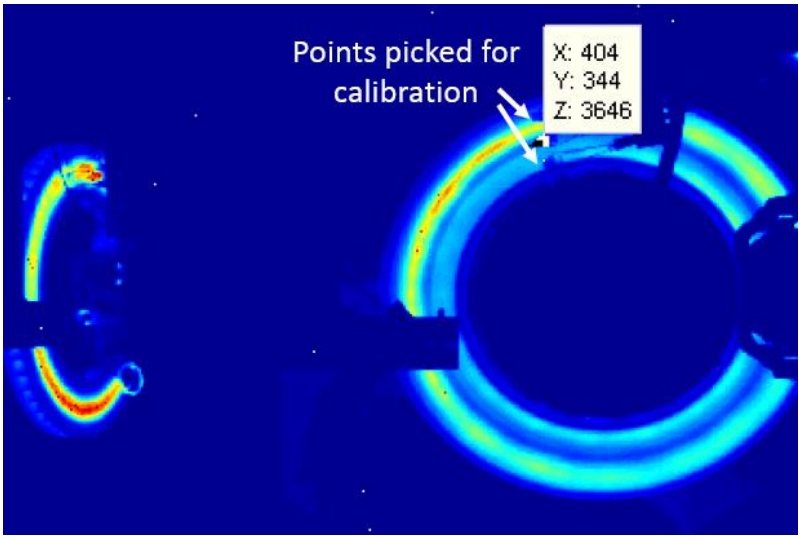

Figure 4.8 Picked location of the mean rubbing thermocouple in the raw mV data plot

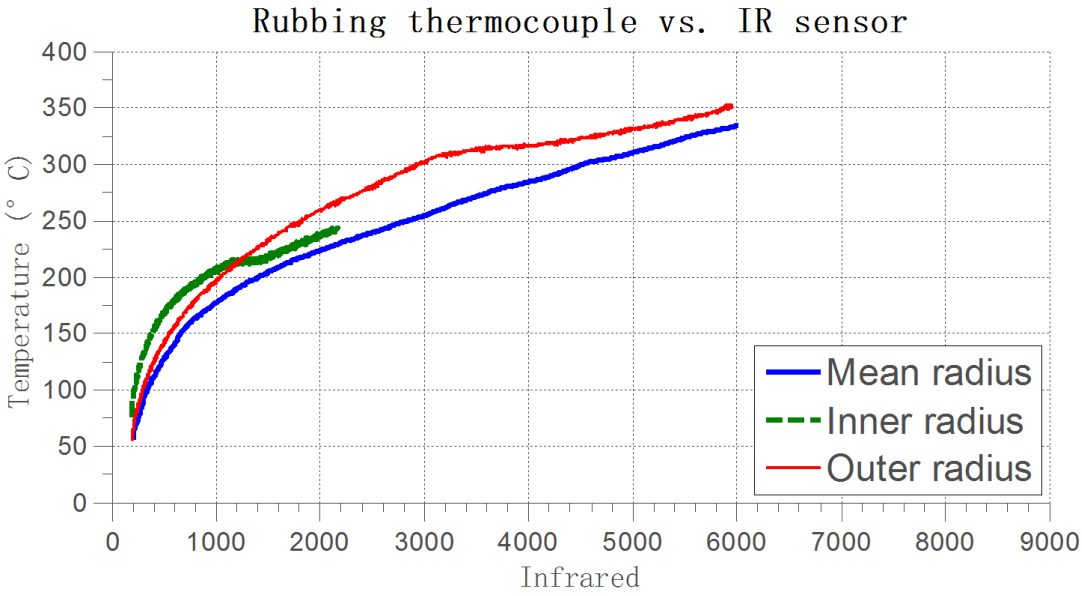

Figure 4.9 Relationship between temperature and output mV at different radii

4.4 Dynamometer test results

4.4.1 *Disc deformation and pressure variation*

Figure 4.10 presents plots of three revolutions at the end of a braking application (about 24s), including the disc inboard (IB) and outboard (OB) run-out, DTV, and line pressure variations. It shows predominantly 2nd order run-out and pressure variation, and 1st order DTV. The run-out of both inboard and outboard surfaces were approximately 70µm and the DTV was approximately 15µm. The 2nd order brake pressure variation was about 1.5bar. Meanwhile, the small ripples can be observed in all of the plots that implied the existence of hot spots and the corresponding pressure vibration (judder). It can be seen that the 17th order small surface ripples on the disc run-out are parallel between the inboard and outboard surfaces which is caused by the hot spotting. The maximum magnitude of the hot spots was between ~5µm to 10µm.

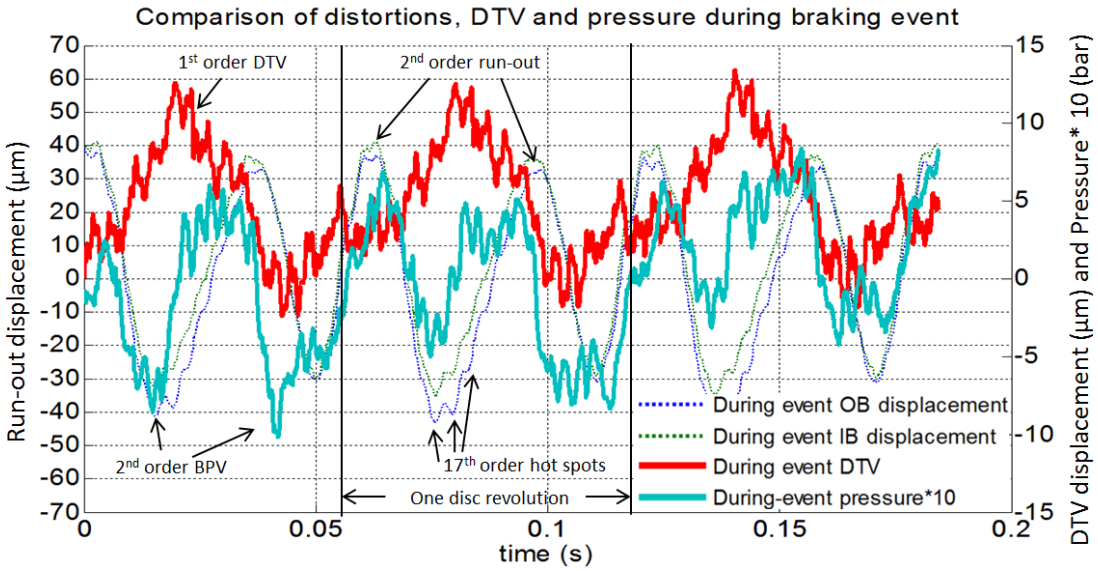

Figure 4.10 Comparison of disc distortions and pressure of three revolutions at the end of a brake application

The waviness plots in Figure 4.10 showed correlation between pressure, run-out and DTV. Therefore, a mathematical correlation coefficient matrix was presented in Table 4.4, in order to provide more details. It illustrated that the run-outs and DTV had similar correlation coefficients with the BPV which revealed that both run-out and DTV had similar contribution in brake judder in this case. In addition, the inboard and outboard run-out shows 99% correlation. This implied that the waviness distortion of the disc was a kind of bulk deformation rather than local surface behaviours. Moreover, the DTV showed negative correlation with run-outs, meaning that at the maximum differences between the IB and OB run-outs appeared at the peaks of the run-out waviness. It is believed that this phenomenon is caused by the non-uniform contact pressure resulting in wear at the peak run-out locations.

Table 4.4 Correlation coefficients between the run-out, DTV and BPV

Parameter	Pressure	OB run out	IB run out	DTV
Pressure	1.00	0.35	0.44	0.43
OB run out	0.35	1.00	0.99	-0.44
IB run out	0.44	0.99	1.00	-0.32
DTV	0.43	-0.44	-0.32	1.00

Figure 4.11 shows a water fall plot of the outboard disc run-out throughout 50s. Through FFT, the contribution of disc distortion at different frequency range can be easily distinguished and measured. The amplitude of the plot was the power spectral density (PSD) which was defined as

$$\mathrm{PSD} = 20 * \log(\mathrm{FFT(y)})$$

Equation 5.1

where y is the amplitude of the waviness distortion in m. The unit of PSD was in dB.

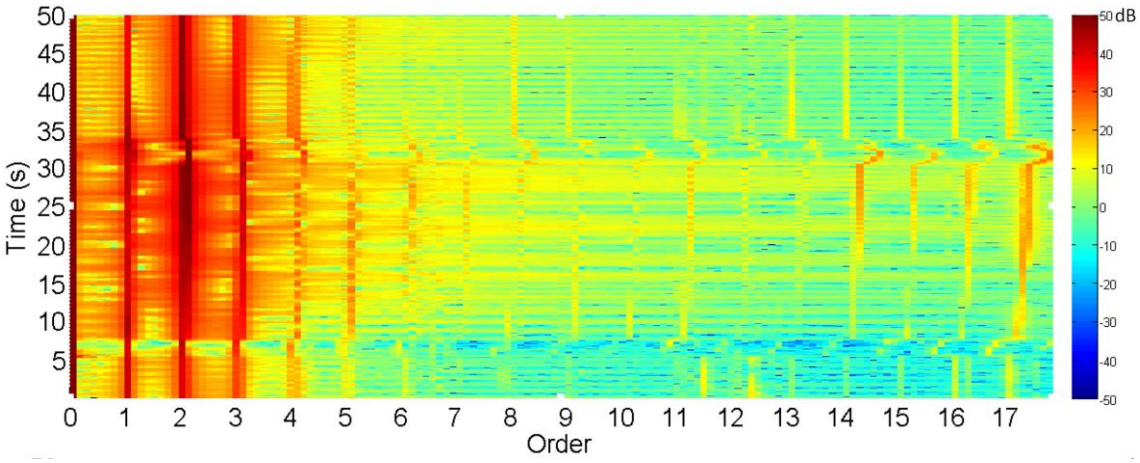

Figure 4.11 FFT waterfall plot of disc outboard run-out

The aim to implement the power spectrum was to facilitate the observations since the original amplitude of different order disc distortions might be significantly different and difficult to be observed in the same scale. The starting time point of the braking event was at about 6s and ended at about 30s. It can be seen that at all orders of revolution shown in Figure 4.11, the magnitude of distortion started to increase during the brake event due to the thermo-elastic deformation and gradually decreased after 30s due to release of the brake and the heat dissipation. It also shows that the disc distortions at various frequencies such as 1st to 6th, 16th and 17th orders were greater than zero before the braking application. The initial permanent disc waveform before any thermo-elastic distortion was predominantly 1st to 3rd order. In addition, the waterfall plot of distortions also illustrated the 2nd order run-out was the most significant distortion (~50dB) which matched well with the observation of the waviness plot in Figure 4.11. Moreover, in the higher frequency domain, 17th order showed greater magnitude (~10 to 30dB) than other orders. It implied that 17 hot spots was equally distributed on the OB disc surface; this correlated with the number of the pins of that pin-mounted two piece ventilated disc. It also illustrated that the 17th order hot spots was gradually developed rather than suddenly appeared. Moreover, it should be noted that the frequency of various orders shifted to right hand direction during

the brake application. It was caused by the slight reduction of the motor speed during the drag brake application since the motor was trying to maintain constant rotating speed.

Similarly, the pressure variation waterfall plot is presented in Figure 4.12. It provided similar observations to the distortion waterfall plot. To be specific, the pressure gradually increased at various orders and 2nd order was the most significant (40dB to 70dB). Meanwhile, 17th order pressure variation grew from zero to ~45dB during the 24s brake application. The figure illustrated that the 17th order vibration was gradually generated due to hot spotting, and 1st, 2nd and 3rd order brake judder was developed due to disc waviness bulk deformation.

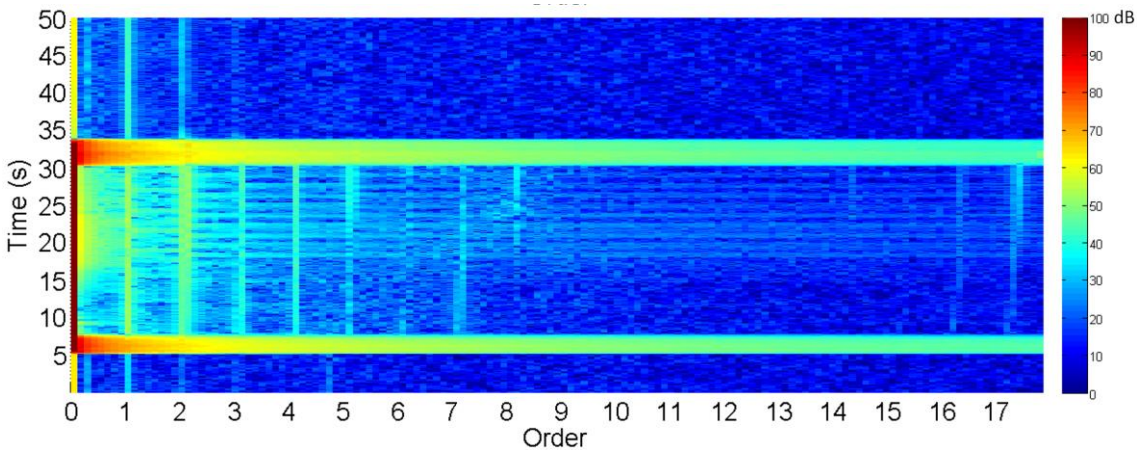

Figure 4.12 FFT waterfall plot of brake pressure

Regarding the contribution of different order distortions, Figure 4.13 and Figure 4.14 provided the predominant lower order and 17th order run-outs and DTV growth plots respectively. The 2nd order run-outs increased from 20μm to 65μm during the brake application due to thermo-elastic deformation and gradually decreased after 30s due to convective cooling and thermal conduction. It should be noted that there was a fluctuation of the 2nd order displacements right after releasing the brake (~30s to 35s). This could be due to the suddenly rotation speed increase when the load was removed from the motor as the brake was

released. The 1st order DTV showed a similar trend but the maximum magnitude was only ~10µm. As shown in Figure 4.14, 17th order disc run-outs grew from 1µm to ~5µm during the brake application, whereas the DTV grew from 0.5µm to 3µm. As the DTV was lower than the run-outs, it implied that the inboard and outboard hot spots were anti-symmetrically distributed since the symmetric distribution mode would develop, greater DTV than ant symmetric mode. In addition, significant fluctuation can be observed for the 17th order distortions which might be related to the radial periodic migration of hot spots during the brake application.

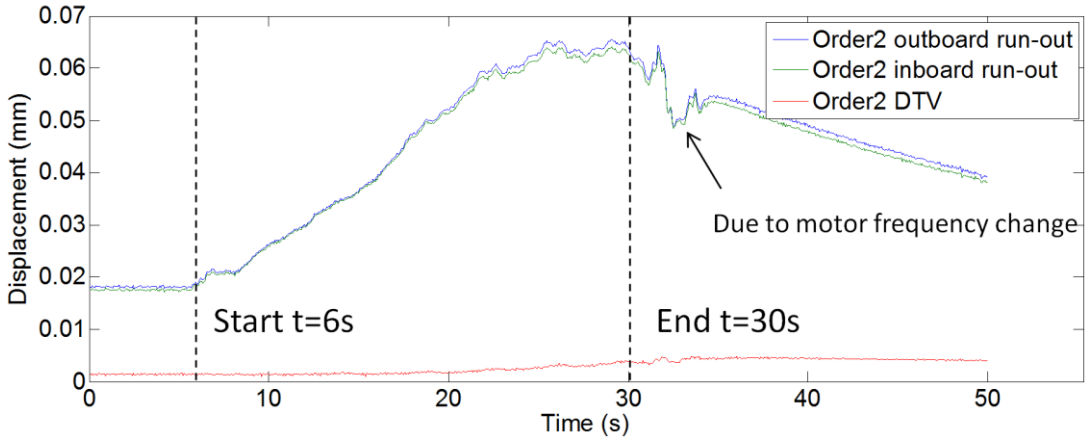

Figure 4.13 Predominant lower order disc distortions throughout one brake application

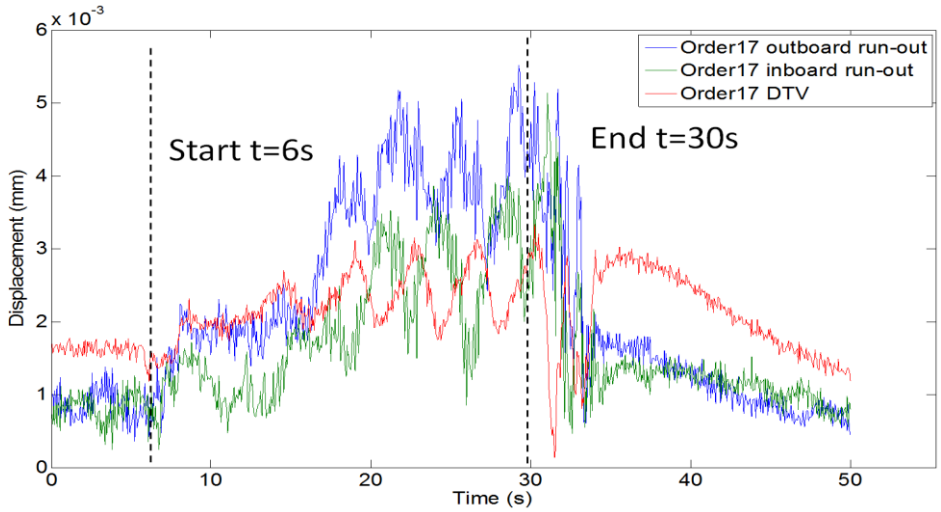

Figure 4.14 17th order disc run-out and DTV throughout one brake application

Besides waviness distortions of the disc, another important type of bulk thermal

deformation was the brake disc coning. Since one of the design purposes for pin-mounted two-piece discs was to reduce the coning of the disc, it was worthy to investigate whether there was disc coning phenomenon during the test. Figure 4.15 shows the adjusted locations of the displacement transducers for the coning analysis. The aim was to measure the displacement of the outer radii of the disc to prevent the potential position deviation between the hot band and displacement transducers. Thus the positions of the transducers were adjusted from the mean radius to outer edge of the disc surface.

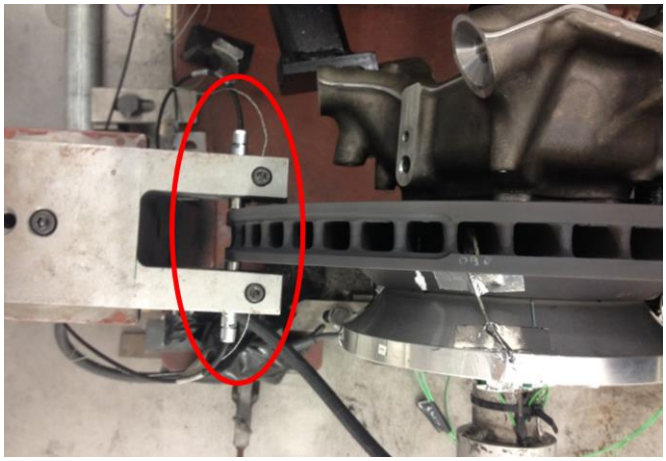

Figure 4.15 Location of the displacement transducers for coning analysis

The inboard and outboard displacement raw data is plotted in Figure 4.16. Due to the fast rotation of the disc, the raw data present as thick curves. The thickness of the curve was the run-out and the fitted curve shows the bulk axial movements of the disc surfaces i.e. coning. It illustrated that during the brake application, the disc run-outs significantly increased and gradually decreased after the brake application. Meanwhile, the outboard surface moved toward the outboard direction during the brake application whereas the inboard surface shows no significant axial movement. It was also clear that during braking, the disc thickness will grow due to thermal expansion of the disc. Therefore, the bulk inboard surface disc placement should have been affected by both inboard

direction expansion and unknown direction coning. The bulk outboard disc displacement will be decided by the outboard direction expansion and unknown direction coning. According to the observations shows in Figure 4.16, it revealed that the coning direction was toward the outboard side. Therefore, the coning effect resulted in a 150µm outboard direction disc outer edge deflection. Moreover, the temperature plot shows the temperature evolutions throughout the brake application. The temperature of both disc surface were similar implying the coning was due to the disc structural design rather than the bulk temperature differences between surfaces.

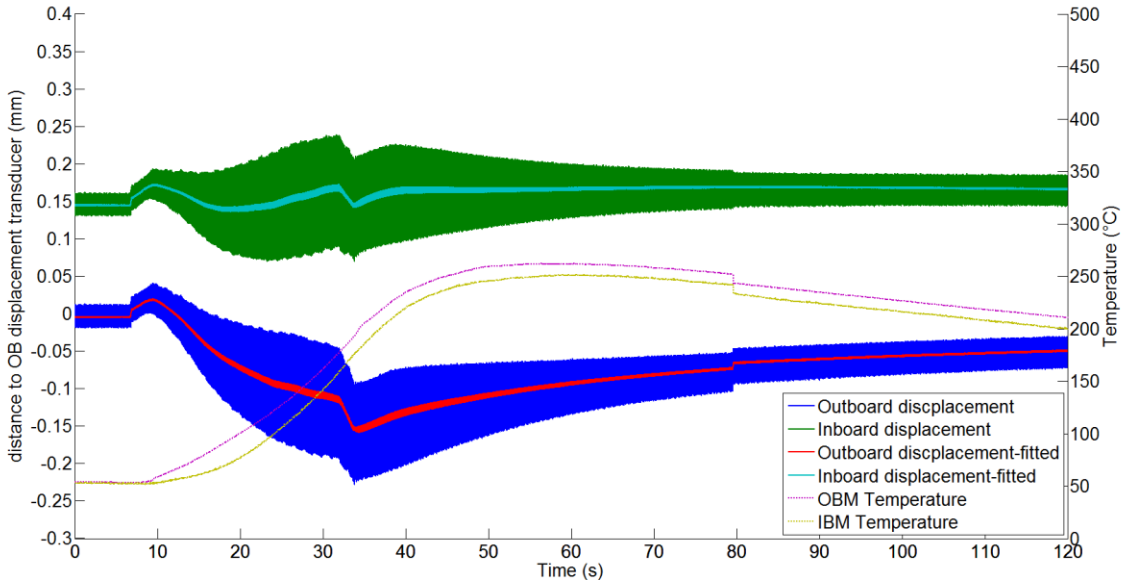

Figure 4.16 Disc temperature and run-out plots for coning analysis

4.4.2 *Hot spot distribution*

According to the previous investigation of disc run-out and DTV in section 4.4.1, 17th order ripples were observed. The thermal imaging of the outboard disc surface temperature distribution confirmed the ripples were the hot spots as shown in Figure 4.17. The maximum temperature of the hot spots were ~500°C or above and the circumferential temperature gradients were ~50°C and radially ~100°C greater than the surrounding areas. The hot spots were radially located on a hot band on the mean rubbing radius which covered ~1/3 of the disc depth

and was ~150°C hotter than the outer and inner radii. In the circumferential direction, the hot spots were located between two pins as shown in Figure 4.17. Thus 17 hot spots were found equally distributed. This implied that the periodic structure of the pin-mounted ventilated disc was the determinant of hot spotting.

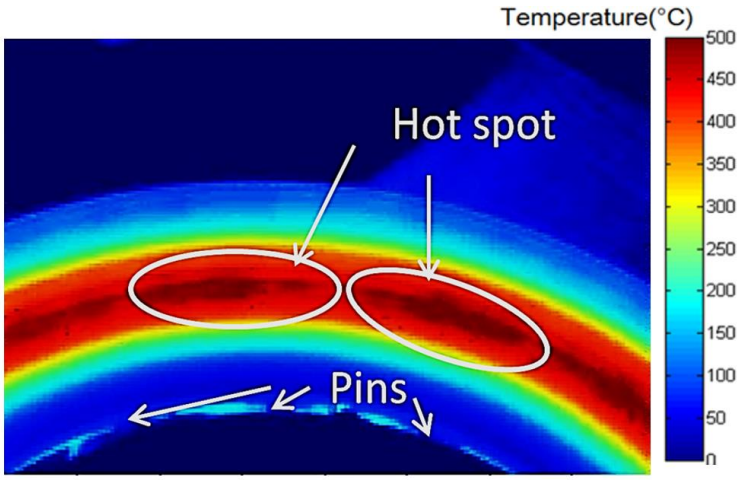

Figure 4.17 Thermal imaging of hot spots on the outboard disc surface

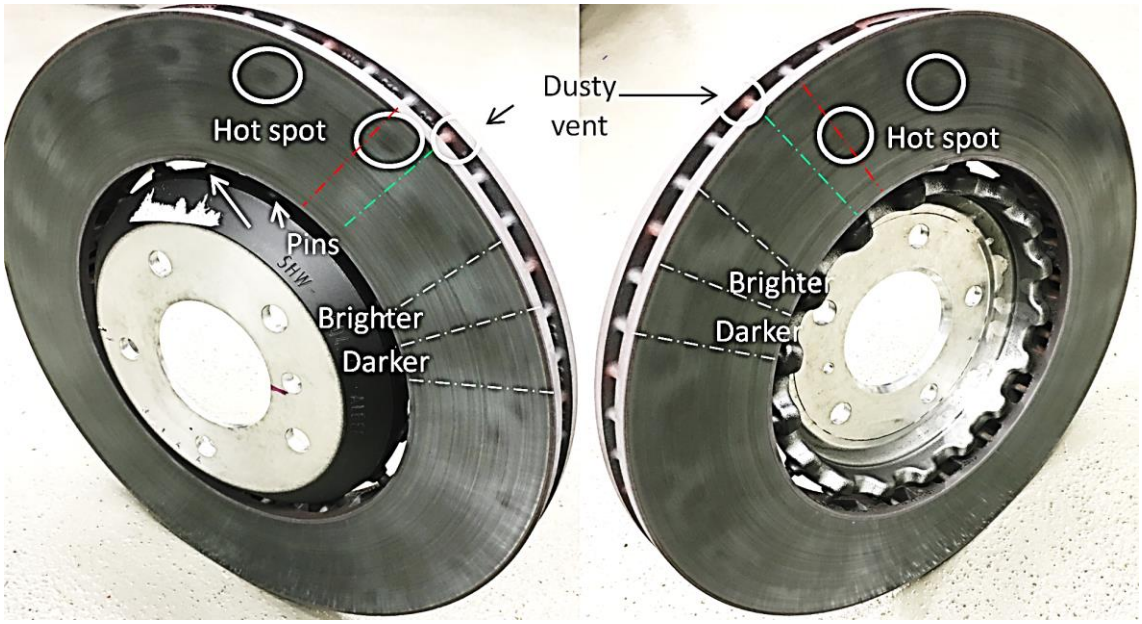

Figure 4.18 Permanent hot (blue) spots on the outboard and inboard disc surfaces after several tests

Furthermore, Figure 4.18 shows the permanent hot spots distribution of a used

brake disc after several hot spotting tests under the same test condition. It shows 17 ‘blue’ hot spots equally distributed on both outboard and inboard disc surfaces respectively. Initially, it can be found that the hot spots were distributed at the outer radius of the outboard surface whereas mean radius on the inboard surface. Then, the outboard hot spots were located between the circumferential positions of two consecutive pins, which matched the observation in Figure 4.17. Moreover, it can be found that there are 17 dusty vents equally distributed on the 51 vents of the disc that implied the periodic uneven convection of the vents due to the interference of pins to the design of the vents. In addition, by using the dusty vent and the vent next to it as the reference point, the angular position of the hot spots were shown to be anti-symmetric. Furthermore, the disc surface especially the outboard surface, clearly shows 17 circumferentially alternating ‘dark’ and ‘bright’ zones respectively. This indicates cast iron structure change or a 17^{th} order uneven wear (or uneven pad deposits) of the disc surface due to the disc waviness.

4.4.3 *Hot band migration*

According to the literature review, the periodic movement of radial hot spots or hot bands had been identified as an important characteristic of hot spotting (Kasem and Dufrénoy, 2012). The migration of effective rubbing radius can cause a brake torque variation (BTV) between brake applications and resultant vehicle vibrations. The movement of hot spots and hot bands can also affect the measurements of temperature and displacement due to the deviations between the hot zones and the sensors. Thus, to investigate the hot band migration, three thermocouples were attached on each side of the disc respectively as shown in Figure 4.19. The thermocouples were located at the inner, outer and mean rubbing surface at the same angular position.

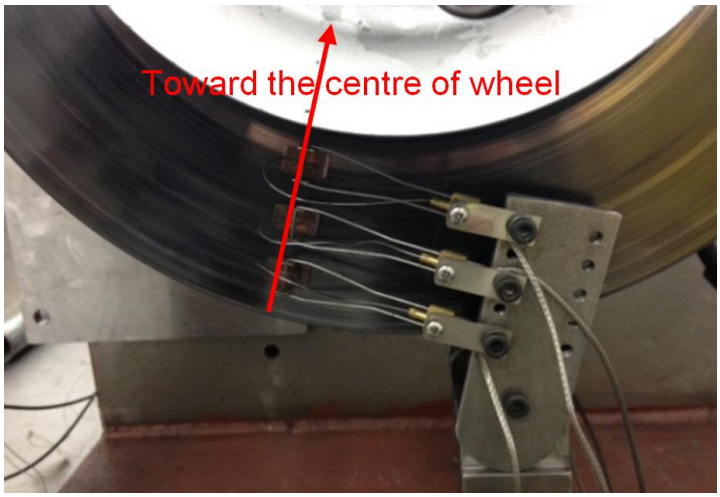

Figure 4.19 Rubbing thermocouples positions

Figure 4.20 shows the variation of peak temperature at different radii throughout three consecutive brake applications. It illustrated that the hot band or hot spot radial locations were not identical in each brake application with different thermocouples reading of the peak temperature. The maximum peak temperature decreased throughout the brake events and the similar temperature of the thermocouples at the third brake application implied that the hot bands were not located on either of the thermocouples at the third brake application.

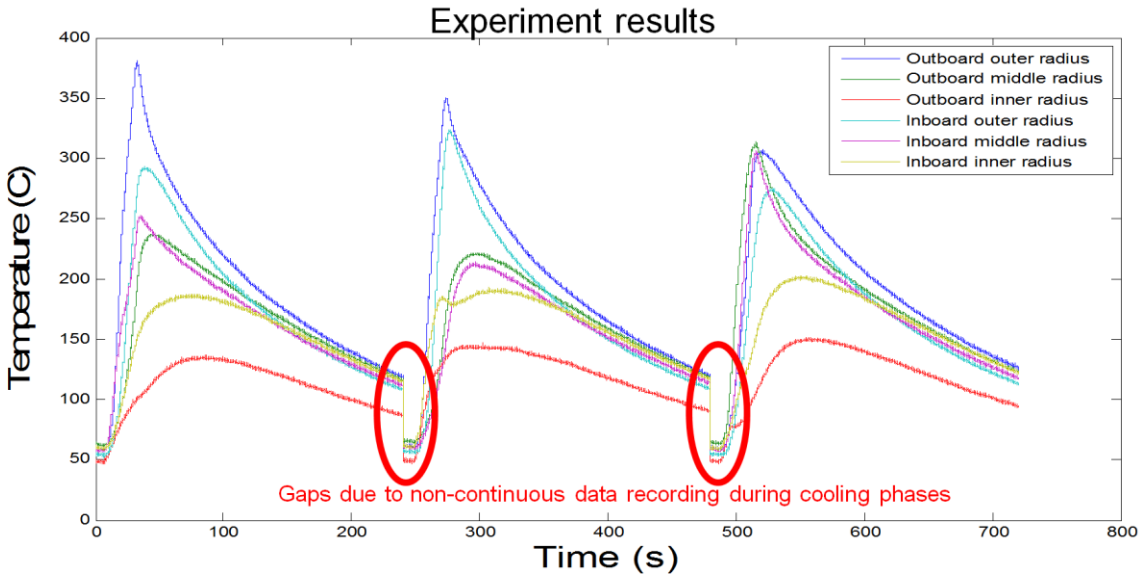

Figure 4.20 Temperature evolutions of the thermocouples throughout three braking applications

Figure 4.21 shows thermal images from a single braking event. Initially one hot band was localised on the inner radii of both inboard and outboard surfaces. Two hot bands then developed on the inboard side which eventually merged to form one central hot band after 24 seconds. Region 1 (Figure 4.21) shows that at the end of the brake application there was a hot region on the disc inboard surface circumferentially that achieved over 450°C. Region 3 shows the hot region of the outboard surface which reached 400°C. Comparing region 1 and region 3, it can be seen that the hot regions were located at different angular positions which implies a first order disc distortion. Two hot bands can be seen in region 2 (outboard), whereas only one hot band is present in region1 (inboard).

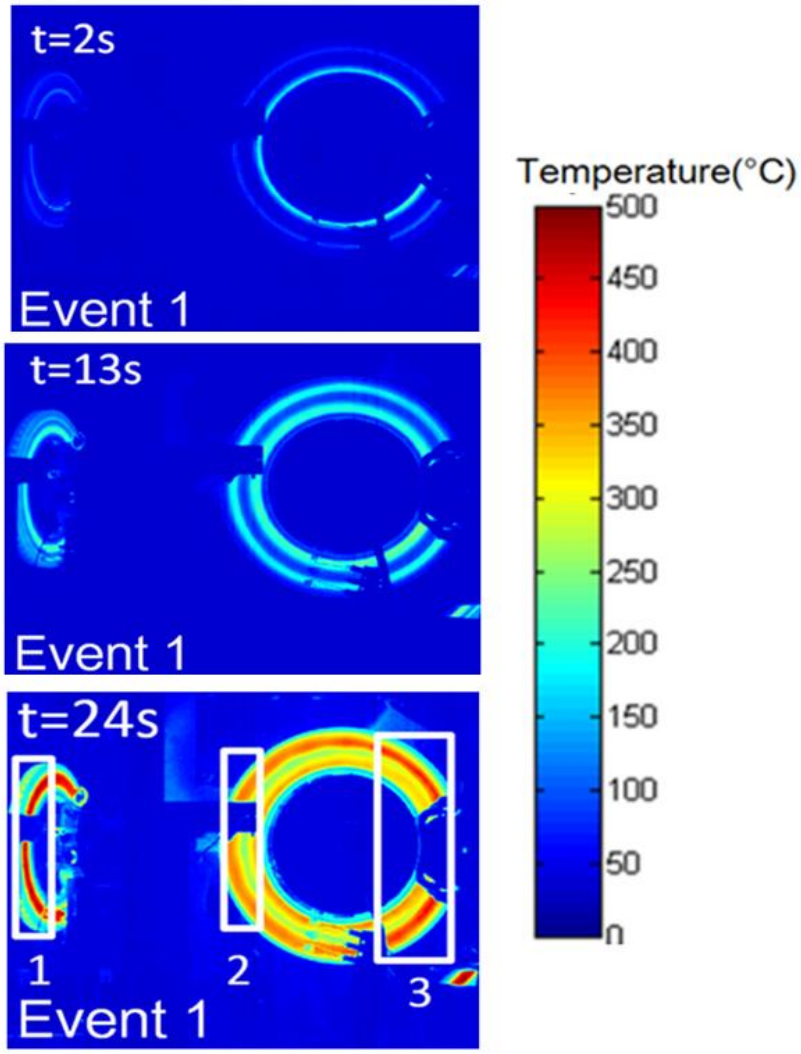

Figure 4.21 Thermal imaging of the development of hot bands

In the subsequent two braking events (Figure 4.22 left and middle), hot bands were concentrated on the mean and outer/inner radii respectively. This observation confirmed that the alternating of peak temperature between brake events was caused by the radial migrations of hot bands. In all of the four braking events (in Figure 4.21 and Figure 4.22), circumferential temperature gradients were developed on each hot band at ~15s, indicating hot spotting.

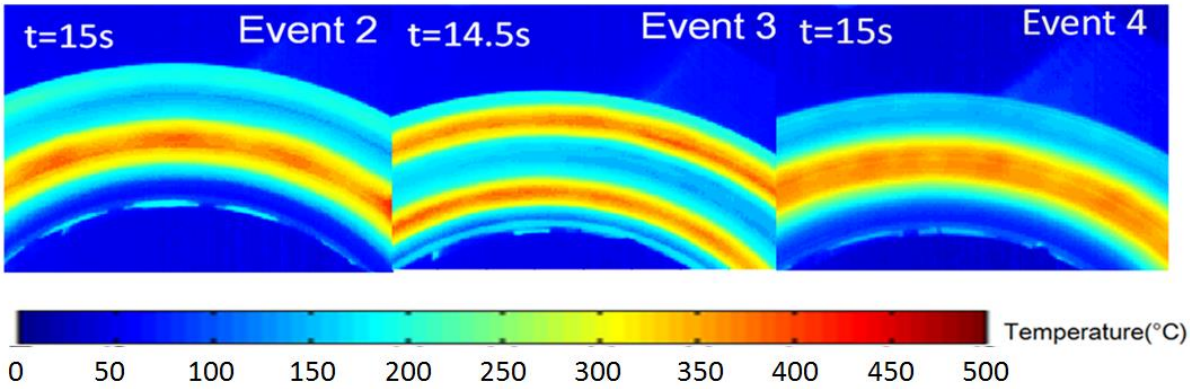

Figure 4.22 Hot band migration in three separate braking events (Thermal images)

In order to investigate the mechanism of the hot band migration, the static contact pressure distributions were measured between three brake tests (three repetitive brake applications in each test) as shown in Figure 4.23. The measurements were performed using Fujifilm Prescale film inserted at the disc pad contact interface at room temperature when the disc was static and applying 25.5bar brake pressure for 24s. Therefore, the contact pressure represented the status of the pads' wear. Since the 0.05 to 2.5MPa ('Super low' pressure range) cannot provide sensitive pressure distribution of the central of the pad, the measurement range was set to 0.05 to 0.6MPa ('Ultra super low' pressure range) in order to provide more sensitive contact pressure distribution results. It showed that the contact zones shifted radially and sometimes divided into two which matched the observations in Figure 4.22. It implied that the excessive wear of the pad might be the determinants of the radial movement of hot spots and hot bands.

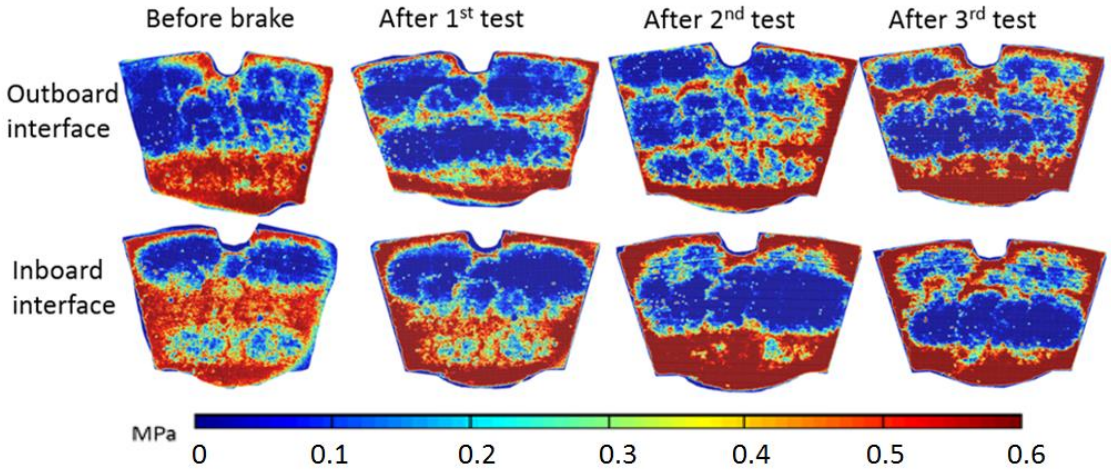

Figure 4.23 Variation of contact pressure before and after three brake tests

4.4.4 *Effects of different speed and pressure*

The debate of hot spotting trigger condition was mainly about whether there is a critical speed (Dow and Burton, 1972) or trigger energy (Sardá *et al.*, 2008). Therefore, to investigate the thermal deformation at different brake condition, five consecutive tests were performed at different rotation speed and brake pressure as shown in Table 4.5. Since the brake applications were drag brake, the brake power was constant. The durations were determined by the brake power to maintain same brake energy input at the end of brake application (the heat dissipation effects were ignored). As a result, the 2nd order (predominant lower order deformation mode) and 17th order (most possible hot spotting frequency due to disc structure) disc outboard surface displacement growth were plotted in Figure 4.24 and 4.25 respectively.

Table 4.5 Rotation speed, brake pressure and brake duration

Test ID	Rotation speed (% of 976rev/min)	Brake pressure (% of 25.5bar)	Brake power (%)	Duration (s)
1	100	100	100	24
2	100	80	80	30
3	100	50	50	48
4	80	100	80	30
5	50	100	50	48

Regarding the lower order deformation, the 2nd order run-out plot shows:

1) At the same speed but different brake pressure (Figure 4.24a), the growth rates of deformations were positively determined by the brake pressure.
2) At the same energy level and same speed, the magnitudes of 2nd order deformations were identical in the performed tests (~50μm).
3) At the same brake pressure but different speed (Figure 4.24b), the growth rates of deformations were determined by the speed significantly.
4) At the same energy level and same pressure, the magnitudes of 2nd order deformations were decreased with the reduction of speed (~50μm, 25μm and 5μm respectively).

The above observations implied that the rotation speed had more significant effects on the lower order thermal deformation than the brake pressure. At same energy level, the deformations were still affected by the speed and pressure.

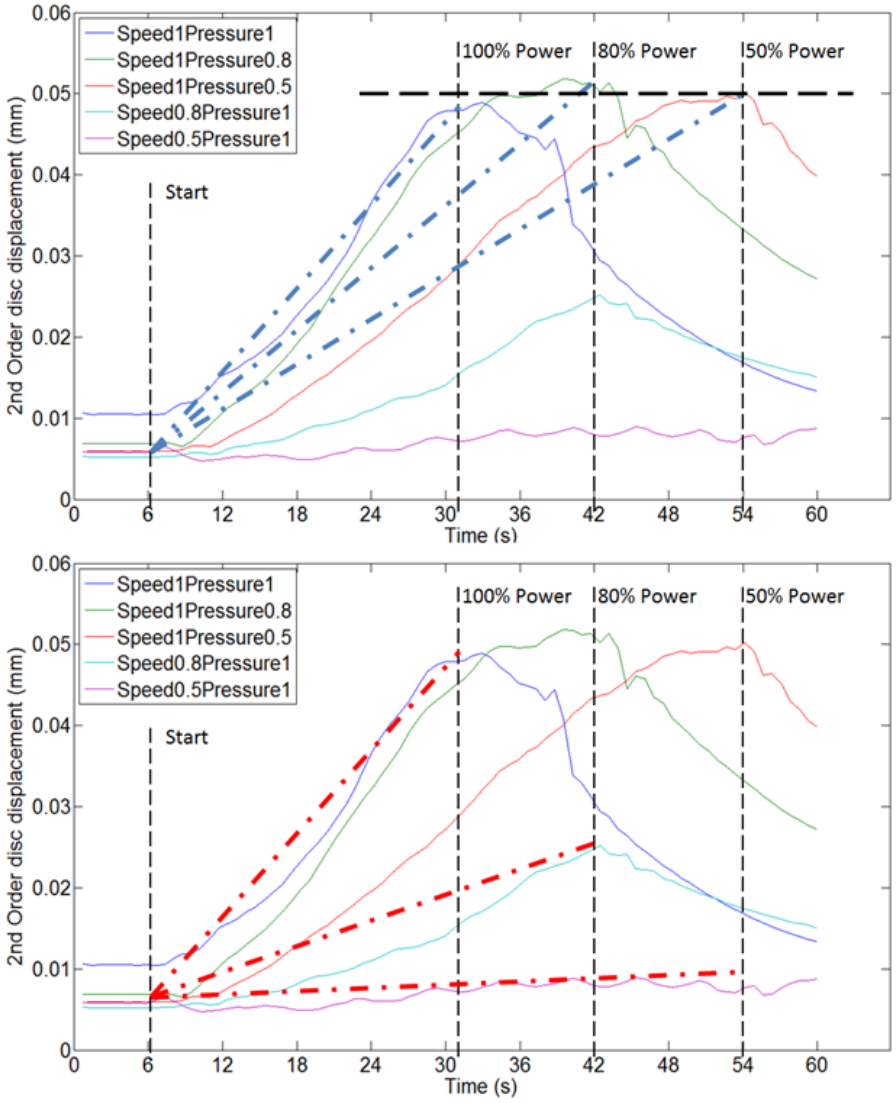

Figure 4.24 Growth of 2nd order disc run-out at various brake pressure (figure (a), blue dashes) and speed (figure (b), red dashes)

In terms of the 17th order of displacement, the following observations were found

1) At the same speed but different brake pressure (Figure 4.25a), the growth rates of deformations were slightly negatively determined by the brake pressure.
2) At the same energy level and same speed, the magnitudes of 17th order deformations were different (~3μm, 4 μm and 8.5μm respectively).
3) At the same brake pressure but different speed (Figure 4.25b), the growth rates of deformations were determined by the speed significantly.

4) At the same energy level and same pressure, the magnitudes of 17th order deformations were decreased with the reduction of speed (~3μm, 1.5μm and 1.2μm respectively).
5) As discussed in section 4.4.1, the 17th order disc displacement was noisier than the 2nd order. This might be due to the radial migration of hot spots which will be investigated in chapter 6.

Comparing the results of 2nd and 17th order deformation further implications can be found:

1) At the same speed but different brake pressure, the lower order deformation increased with the increase of brake pressure but the higher order deformation decreased. This might be related to the energy distribution between lower and higher order deformation during brake events.
2) At the same energy level, the brake speed only affected the hot spot magnitude rather than the lower order deformations.
3) At the same pressure but different speed, both 2nd and 17th order deformations were significantly determined by the rotation speed rather than brake pressure and energy level.

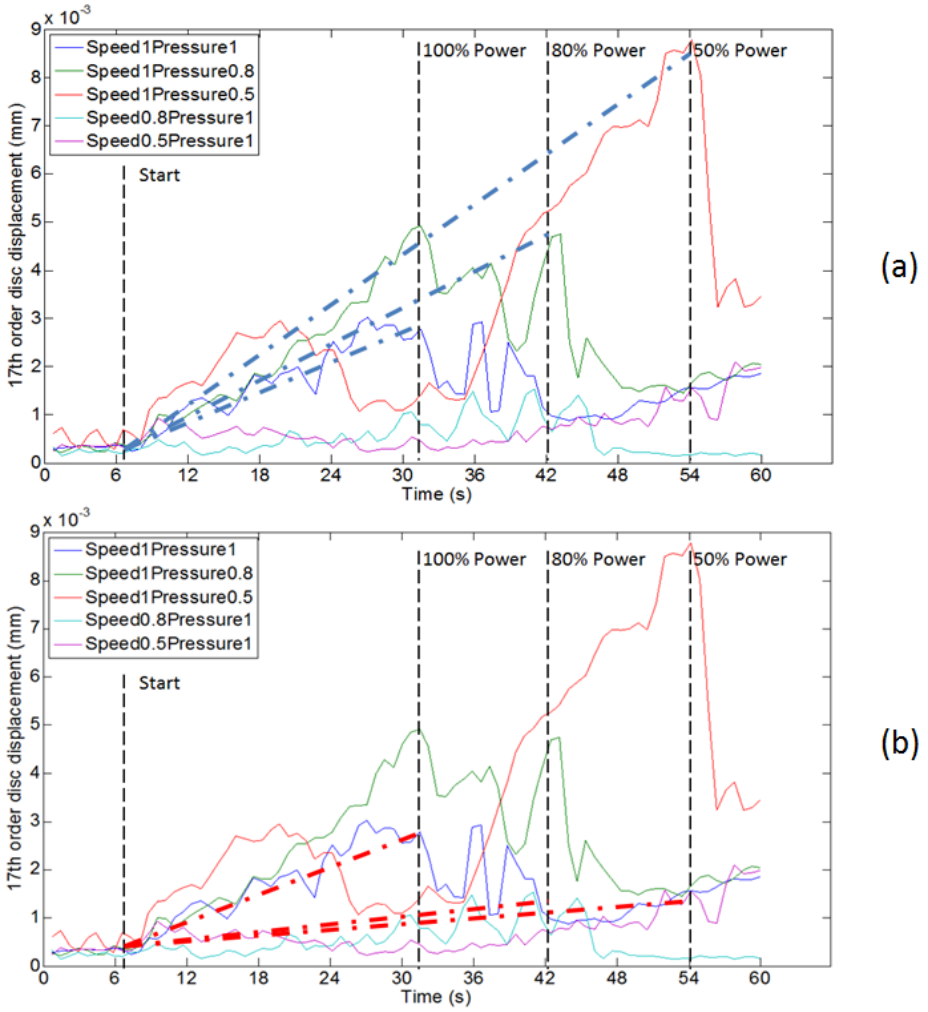

Figure 4.25 Growth of 17th order disc run-out at various brake pressure (figure (a), blue dashes) and speed (figure (b), red dashes)

In summary, the test revealed that under drag brake conditions, brake speed had a more significant role than brake pressure, brake power and energy level on the magnitude of both lower and higher order thermal deformation. However, in the realistic brake scenario, since the vehicle speed was not independent of the brake pressure (deceleration), their relationship and contribution to hot spots and hot judder could be more complicated.

4.5 Other measurements and estimations of modelling inputs

In addition to the hot judder/hot spotting tests, extra experimental works have been done to provide important modelling input parameter measurements or estimations.

4.5.1 *Heat transfer coefficient estimation*

Since the convective cooling is the most important heat dissipation type besides conduction and radiation, the proper estimation of the heat transfer coefficient is significant to the hot spotting modelling. According to section 4.4.4, the experiments had been performed at different rotation speed, thus the cooling curves can be obtained as shown in Figure 4.26. The curves present the average value of all the six rubbing thermocouples of both inboard and outboard disc surfaces. It can be seen that the peak disc temperature at lower speed were greater which was due to the longer heating duration and less cooling effects though the total energy input were identical.

Regarding the calculation of heat transfer coefficient, the Biot number was introduced to estimate the ratio between convective and conductive thermal resistance for a solid material in transient heat transfer. According to Incropera *et al.* (2007), the Biot number was defined as

$$\mathrm{B}_i = \frac{h_c L_{disc}}{k_{disc}}$$

Equation 5.2

Where h_c is the convective heat transfer coefficient, k_{disc}, is the thermal conductivity, and L_{disc} is the characteristic length of the disc defined by $L_{disc} = \frac{V_{disc}}{A_{disc}}$ where V_{disc} and A_{disc} are the volume and surface area of the disc respectively. When the Biot number was less than 0.1, then the convective cooling behaviour can be regarded as uniformly throughout the disc with less than 0.5% error. In this study, the Biot number is ~0.0007. Therefore, based on the cooling curves shows in Figure 4.26, the heat transfer coefficient can be estimated using the lumped heat capacity method (LHCM) as shown in the following equation (Incropera *et al.*, 2007):

$$h_{disc} = \frac{q_{disc}}{T_{disc} - T_{air}} = \frac{-2 * \rho_{disc} c_{disc} \delta_{disc} \frac{dT_{disc}}{dt}}{T_{disc} - T_{air}}$$

Equation 5.3

Where h_{disc} is the heat transfer coefficient, q_{disc} is the heat flux into the disc, T_{disc} is the disc temperature, T_{air} is the ambient air temperature, ρ_{disc}, c_{disc}, δ_{disc} and are the disc density, specific heat capacity and half thickness of the solid rotor respectively, $\frac{dT_{disc}}{dt}$ is the temperature change gradient with time.

An alternative method indicated by Tirovic (2014) and Galindo-Lopez and Tirovic (2008) was in similar principle:

$$h_{disc} = -\frac{1}{t} ln \frac{(T_{disc,t+1} - T_{air})}{(T_{disc,t} - T_{air})} \frac{m_{disc} c_{disc}}{A_{disc}}$$

Equation 5.4

where $T_{disc,t}$ is the temperature at a given time t, $T_{disc,t+1}$ is the temperature at next time step, t is the duration between the steps, and A_{disc} is the area of disc surfaces under convective cooling.

The results of the heat transfer coefficients of different rotation speed are shown in Figure 4.27. In the initial ~30 to 50s depending on brake duration, the negative heat transfer coefficient estimation was due to the heating and not reliable. After ~30 to 50s, the discs were entered the cooling phases and the heat transfer coefficient shows a rapid reduction and stabilised after ~80s. This was due to the fact that after the release of the brake the heat rapidly dissipated from the hotter zones (hot spots or hot bands) to the surrounding disc rotor and thickness. Therefore, the 2nd period was the predominant heat conduction phase. Then, the heat transfer coefficient stabilised after ~80s, they shows different average values at different speeds. At 100% speed (976rev/min), the average heat transfer

coefficient was ~130 W/m^{2}K, whereas ~115 and ~75W/m^{2}K for 80% and 50% speed respectively. It matched the empirical calculation that the brake disc heat transfer coefficient should be correlated with the rotation speed (Limpert, 1975).

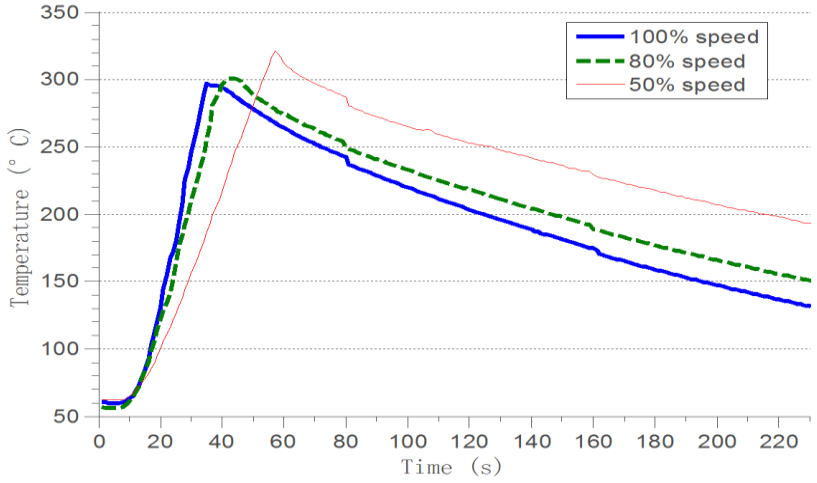

Figure 4.26 Temperature curves obtained from drag braking tests performed at different speed

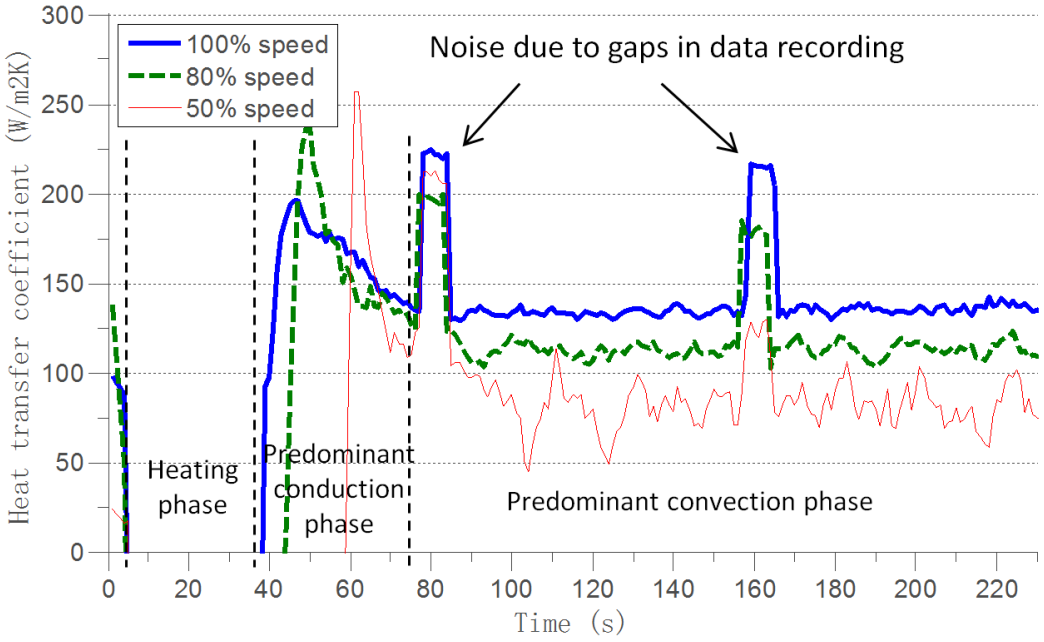

Figure 4.27 Heat transfer coefficient curves estimated from drag braking tests performed at different speed

4.5.2 *Wear rate measurement*

As stated in the literatures, wear can affect the hot spotting in terms of both magnitude of thermal localisation (Barber, 1969) and radial migration (Ostermeyer and Graf, 2013). Therefore, it is important to estimate the wear rate of the friction material for the following simulations in Chapter 6.

The wear model for the automotive brake system was obtained from Podra and Andersson (1999) and the effective wear coefficient was determined by the following equation:

$$K_{wear} = \frac{\Delta V}{\mu F_{piston} s} = \frac{\Delta V}{\mu P_{piston} A_{piston} v t}$$

Equation 5.5

Where K_{wear} was the effective wear coefficient, ΔV is the volume loss per brake application per pad, μ is the coefficient of friction F_{piston}, P_{piston} and A_{piston} are the brake force, brake line pressure and piston area, s, v and t are contact pair sliding distance, brake velocity and brake duration respectively. As shown in Table 4.6, it was clear that the brake force and sliding distance were already known. Therefore, to obtain the reduction of volume after each brake application, the measurement of friction material mass was performed for both inboard and outboard pads as shown in Table 4.7. 60 brake applications were undertaken and the measurements of pad mass were performed five times before and after every three brake applications in the first 9 braking applications and after the 60th. The results show that the mass loss was decreasing throughout the tests which were caused by the effects of bedding for the initial braking applications. As a result, the inboard and outboard pads average mass loss was ~0.11g per pad per brake application. The volume loss was ~8.56×10^{-7}m^3.

Table 4.6 Brake parameters for coefficient of wear estimation

Brake parameters	Value
Friction material density, ρ (kg/m^3)	1250
Piston area, A_{piston} (m^2)	0.0045
Actuation pressure, P_{piston} (MPa)	2.55
Rotational velocity, ω (rad/s)	102
Effective rubbing radius, *Rmean* (mm)	162
Brake duration, *t* (s)	24
Coefficient of friction, μ	0.38

Table 4.7 Mass measurement results for coefficient of wear estimation

Test ID	Total brake applications	Outboard pad mass (g)	Outboard pad mass loss (g)	Inboard pad mass (g)	Inboard pad mass loss (g)
Pre-test	0	458.12	-	458.11	-
1	3	457.26	0.86	457.11	1.00
2	6	456.82	0.44	456.56	0.55
3	9	456.61	0.21	456.33	0.23
…	…	…	…	…	…
20	60	451.42	5.21	450.56	5.77

Therefore, according to Table 4.6, the effective coefficient of wear was

$$K_{wear} = \frac{\Delta V}{P_{piston} A_{piston} vt} = \frac{8.56 \times 10^{-7}}{3790 \times 396.6 \times 0.38} = 1.68 \times 10^{-13}\ \mathrm{m^3/Nm}$$

Equation 5.6

According to the experimental measurements of Jang (2004), the typical effective wear coefficient was in range beteen 1.05x10^{-13} m^3/Nm and 1.78x10^{-13} m^3/Nm varying with the contact pair materials used. Thus the value obtained of wear coefficient was accepted and applied in the following simulations in Chapter 6 that considered wear.

4.5.3 *Disc deformation after stress relieving*

Based on the observations of section 4.4.1, it was clear that the disc showed a predominant 2nd order disc run-out. As indicated by Bryant, Fieldhouse and Talbot (2011), the residual stress during the brake disc manufacture process might be a

source of the lower order disc deformation. Therefore, a new brake disc (without brake bedding and testing) was stress relieved in order to investigate the effects of residual stress on disc deformation.

The 3D scanning plots measured using a coordinate measuring machine (CMM) before and after stress reliving are presented in Figure 4.28. Before stress reliving the disc showed insignificant 1st order run-out but a significant coning shape toward the outboard direction. The axial position of inner radius was ~20µm whereas the outer radius was ~50µm. After stress relieving, the 2nd order disc deformation was evident. The maximum axial displacement (~-30µm) occurred at the inner radius of the inboard surface and maximum axial displacement (~70µm) at the outer radius of the outboard surface.

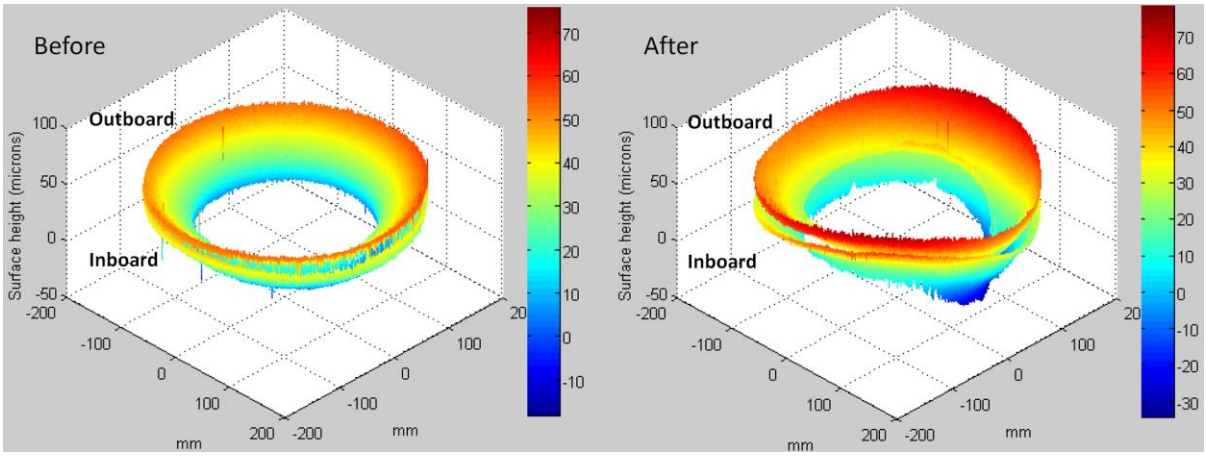

Figure 4.28 3D surface plots before (left) and after (right) stress relieving

In addition, Figure 4.29 provided a plot the mean radius disc displacement before and after stress relieving. It illustrated that the 2nd order run-out significantly grew after stress reliving from ~10µm to ~35µm. However, as expected, there was no apparent DTV change.

The investigation of stress relieving revealed that the thermo-elastic effect was not the only cause of disc deformation and the 2nd order disc run-out during hot

spotting tests might be initialised due to an ‘in stop’ partial stress reliving effect due to rapid heating and cooling. Therefore, it is important to investigate the influence of initial disc waviness on the disc thermo-elastic deformations, especially hot spotting.

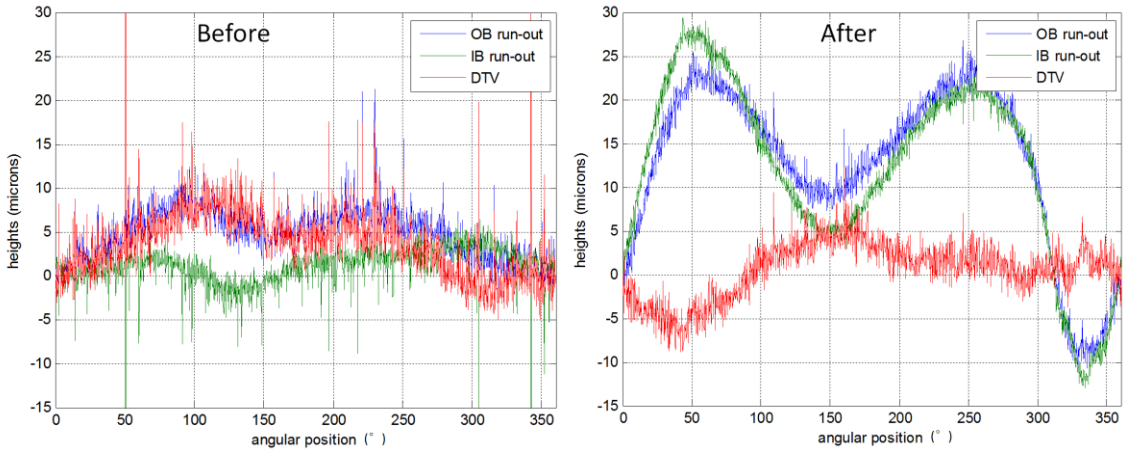

Figure 4.29 Disc distortions at mean rubbing radius plots before (left) and after (right) stress relieving

4.6 Summary

In order to provide benchmarking for the following 2D and 3D simulations (in chapter 6 and 7), the experiments based on a dynamometer and IR camera were carried out. The disc temperature, brake line pressure and disc displacement were measured simultaneously to provide a comprehensive understanding of the hot spotting process. Then, measurements and estimations for the experimental works were performed to provide data for the numerical modelling.

To be specific, the dynamometer provided constant high speed drag braking measurement of the hot spotting and hot judder. The results showed that the disc was predominantly deformed at 2nd order and 17th order (hot spots). The brake pressure was highly correlated with the disc run-out, DTV and hot spots which indicated the significant effects of disc thermal deformation on the brake judder. The development and distribution of hot spots were observed using a thermal

camera during the brake applications and visually after dismounting. It showed that the hot spots were distributed anti-symmetrically between the inboard and outboard surfaces, and the positions were related to the disc periodic structures such as vents and pins.

By using the thermal camera, the radial movements of hot spots were also investigated. It was found that the radial position of the hot spots/bands were periodically localised either on both outer and inner radii or mean radius and alternating between each brake event (applications). By measuring the static contact pressure of the disc/pad interfaces between tests, it was found that the wear of the pads also showed periodic radial migrations.

The effects of speed and load on the hot spotting were investigated to add weight to the main arguments between the conventional hot spotting theories and experiments in literature. The test results shows that the speed was more significant than the load in terms of both lower (run-out) and higher order (hot spot) disc deformations.

In addition, based on the temperature evolution measurements, the convective heat transfer coefficients were estimated. The wear rate was also estimated by measuring the mass loss between braking applications. In order to investigate the source of the 2^{nd} order disc distortions during the test, a disc was stress relived. The results suggested that the residual stress from manufacturing was a source of the disc run-out. It is proposed that the disc was partially stress relieved during brake events due to the high temperature, resulting in the initial run-out. In subsequent heat generation was non-uniform due to the run-out which resulted the significant growth of 2^{nd} order run-out.

Chapter 5 Fundamental FE Studies

5.1 Introduction

The numerical prediction of hot spotting is challenging with regards to the high demand on computing power, proper assumptions and simplifications, reasonable definition of material properties and boundary conditions. Therefore, this chapter details the fundamental numerical studies which were made in order to prepare for the hot spot modelling. The studies mainly comprised the introduction of the base concepts and terminologies of the hot spotting investigation, establishment and verification of the axisymmetric pad assumptions for both 2D and 3D modelling and the axisymmetric disc assumptions for the 2D out-of-plane models in order to facilitate good computing efficiency with acceptable error.

5.2 Axisymmetric pad assumptions

The most significant assumption made to the fundamental models of this project was that the brake pad was regarded as a 360° axisymmetric pad without circumferential sliding. In order to save computing time via the complexity of the model, the simplified axisymmetric pad model has been widely used in previous TEI research (Day and Newcomb, 1984, Day, Tirovic and Newcomb 1991, and Zagrodzki *et al.,* 2001). The TEI models can properly predict the hot spotting in a clutch system analytically (Lee and Barber, 1993). However, the disc brake system is not axisymmetric as it is composed of stationary pads with finite arc length and a rotating disc with more complex geometry than a clutch (e.g. vent, pins, and top-hat). As believed by Lee and Barber (1993), the axisymmetric pad assumption provided good approximation of the actual automotive brake system. But the converting algorithm between the finite arc length pad mode (or rotating model) and axisymmetric pad model were not clearly discussed in the previous

studies. Thus the conversion process will be discussed in this section including the mathematic formulations, and the numerical verification using FE method.

5.2.1 *Basic assumptions*

The following assumptions were made in this research in terms of the model simplification and computing time saving:

1. The pad was assumed to be asymmetrically ‘smeared’ and in contact with the brake disc surfaces over 360° in the circumferential direction. The aim was to provide a layer of equivalent homogenous friction material to represent the brake pad.

2. High rotation velocity: In the actual brake system, the heating process can be regarded as a fast moving heat source rotating in the circumferential direction of the disc surface. For a giving location on the disc surface, the heating procedure was composed by both heating and cooling phases in each disc revolution. Thus, the circumferential temperature difference on the disc surface was inevitable. However, the circumferential temperature difference will be negligible when the rotation speed is fast enough.

3. The pad was stationary and the traction behaviours due to friction were neglected. According to (Dow and Burton, 1972, Lee and Barber, 1993, and Zagrodzki *et al*., 2001), the traction force or shear stress does not significantly affect the prediction of hot spots.

4. The materials for disc and pad were assumed as homogenous isotropic materials and were not temperature dependent. The intention was to enable the investigation of the effects of material properties and their

interactions with hot spotting in the following hot spotting simulations.

5. According to Limpert (1975), the general proportion of radiation is typically less than 5% of the total braking heat dissipation (including convection, conduction and radiation). Thus to reduce the modelling complexity, the effects of radiation were not considered in the FE simulations in this research.

6. Plasticity is an important factor in disc thermal deformation as indicated by Bryant, Fieldhouse and Talbot (2011). However, in order to reduce the modelling complexity and obtain the trend of hot spotting under the effects of various determinants, disc plasticity was not considered in the following FE modelling verifications.

The aim of the axisymmetric pad assumption was to provide good approximation of the thermo-elastic deformation, heat transfer, and contact processes during hot spotting. Therefore, based on the assumptions made, the results of the simplified model should satisfy the following conditions:

1. Comparable disc temperature distribution. To reproduce the hot spotting generation in the axisymmetric pad model, the temperature distribution of the simplified model should be identical to the realistic scenario in order to achieve the same heat partition ratio and thermo-elastic deformation in axial direction.

2. Same total heat generation. In the previous heat transfer studies of disc brake systems, the total heat generation is one of the most frequently used assumptions. In order to achieve identical thermal deformation of the disc, the heat entering into the disc should be essentially identical.

3. Same total mechanical loading. This assumption is made to keep total clamping force and total strain energy identical.

4. Comparable heat flux distribution and contact pressure distribution. In order to achieve the same temperature field, the heat flux distribution should be identical in both models. As the heat flux is determined by contact pressure, comparable contact pressure distribution should be also satisfied.

5. Comparable strain energy on the disc. To achieve comparable contact pressure distribution, the total strain energy should be identical. The strain energy density distribution in both cases should also be the comparable.

To satisfy the above assumptions and conditions and to achieve the equivalent layer of friction material, the material properties of the pad had to be scaled. This scaling factor method was agreed by Tirovic and Sarwar (2004) and the ABAQUS example manual (2012). The calculation of the scale factor of the material properties will be discussed in the following section.

5.2.2 *Mathematic formulations*

Figure 4.1 shows the axisymmetric pad model and the real brake geometry with finite length pad (right) and axisymmetric pad (left).

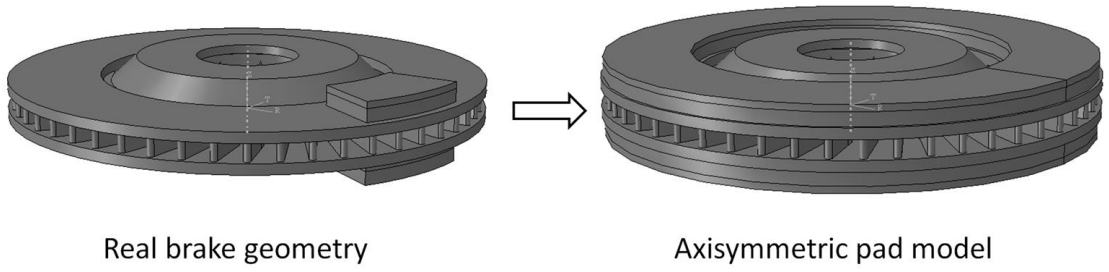

Figure 4.1 Real brake disc and friction material (lining) and back-plate model (left) and axisymmetric brake pad model with lining and back-plate (right)

5.2.2.1 Heat generation

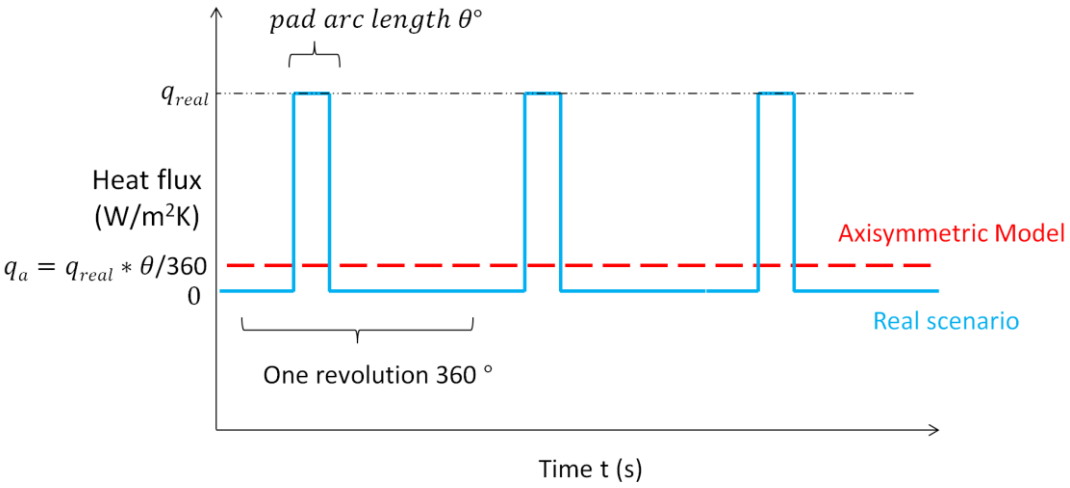

Figure 4.2 Representation of ideal heat generation time series at a fixed brake disc surface node for both periodic heating mode (real scenario) and continuous heating mode (axisymmetric approximation) with uniform constant contact pressure (Note: subscript 'a' indicates axisymmetric model and 'real' indicates the real model)

The heat flux generated in the real scenario:

$$q_{real} = \mu v p_{real}$$

Equation 5.1

Where the linear velocity $v = \omega R$, ω was the rotational velocity and R was the radius, μ was the coefficient of friction, and p_{real} was the contact pressure for the real scenario.

Similarly, the heat flux generated in the axisymmetric pad model was

$$q_a = \mu v p_a$$

Equation 5.2

where the subscript 'a' means the axisymmetric pad model, p_a is the contact pressure of the axisymmetric pad model.

The coefficient of friction μ and velocity *v* were identical for both scenarios. For a given point on the disc or spatial location in the track of the pad, the heat flux inputs of the two scenarios (axisymmetric) and (real) are illustrated in Figure 4.2. It showed that the total heat flux inputs were identical. But for a given location on the disc, the axisymmetric model was heated continuously and the realistic scenario was heated periodically. To keep the total heat generation the same, the total loading (contact pressure) was the same, which gave the axisymmetric model a mechanical loading of

$$p_a = p_{\text{real}} * \theta/360$$

Equation 5.3

where *θ* was the pad arc length angle.

5.2.2.2 Temperature field

In a cylindrical-coordinate system (r, z,*φ*) as shown in Figure 4.1, the heat transfer in the disc and pad in the axisymmetric model can be represented by

$$k_a\left(\frac{\partial^2 T}{\partial r^2}+\frac{1}{r}\frac{\partial T}{\partial r}+\frac{1}{r^2}\frac{\partial^2 T}{\partial \varphi^2}+\frac{\partial^2 T}{\partial z^2}\right)=\rho_a c_a\left(\frac{\partial T}{\partial t}+\omega_a\frac{\partial T}{\partial \varphi}\right)$$

Equation 5.4

Where $k_a, \rho_a,$ and c_a are conductivity, density and specific heat capacity for the axisymmetric model; r, φ and z are the radius, angular position and axial position in the cylindrical system; T is the temperature and t is time. The left hand side

of the equation represents the heat flux terms in three directions, whereas the right hand side is the total change in temperature with respect to time and angle of rotation. Assuming disc fixed coordinate system in the rotational direction, then ω_a will be the pad's rotation speed. The term $\omega_a \frac{\partial T}{\partial \varphi}$ represents the circumferential temperature variation due to rotation. When the rotation speed ω_a was high enough, the variation could be assumed to be $\omega_a \frac{\partial T}{\partial \varphi} = 0$, giving:

$$k_a \left(\frac{\partial^2 T}{\partial r^2} + \frac{1}{r}\frac{\partial T}{\partial r} + \frac{1}{r^2}\frac{\partial^2 T}{\partial \varphi^2} + \frac{\partial^2 T}{\partial z^2} \right) = \rho_a c_a \left(\frac{\partial T}{\partial t} \right)$$

Equation 5.5

This represented that for a given location on the disc, it was heated by the pad continuously rather than periodically heated and cooled due to pad rotation.

Similarly, the heat transfer equation of the real scenario was,

$$k_{real} \left(\frac{\partial^2 T}{\partial r^2} + \frac{1}{r}\frac{\partial T}{\partial r} + \frac{1}{r^2}\frac{\partial^2 T}{\partial \varphi^2} + \frac{\partial^2 T}{\partial z^2} \right) = \rho_{real} c_{real} \left(\frac{\partial T}{\partial t} + \omega_{real} \frac{\partial T}{\partial \varphi} \right)$$

$$\mathrm{T} = 0 \ \ (\theta < \varphi < 360)$$

Equation 5.6

Where θ was the pad contact arc length (°). The equation represented that for a given time point *t*, the temperature of a given point on the pad swept area was either non-zero when the pad was passing through $(\varphi < \theta)$, or zero when the pad had passed $(\theta < \varphi < 360)$.

The relationship between φ and time t was

$$\varphi = mod(\omega * \frac{180}{\pi} * t, 360)$$

Equation 5.7

In one revolution, time was represent by

$$t = \frac{\varphi}{\omega * \frac{180}{\pi}} = \frac{\varphi\pi}{180\omega}$$

Equation 5.8

Then the heat transfer can be rearranged into the function of angular position φ. Substituting the Equation 5.8 to Equation 5.5 and 4.6, gave

$$k_a\left(\frac{\partial^2 T}{\partial r^2} + \frac{1}{r}\frac{\partial T}{\partial r} + \frac{1}{r^2}\frac{\partial^2 T}{\partial \varphi^2} + \frac{\partial^2 T}{\partial z^2}\right) = \rho_a c_a\left(\frac{\partial T}{\partial \frac{\varphi\pi}{180\omega}}\right)$$

Equation 5.9

$$k_{real}\left(\frac{\partial^2 T}{\partial r^2} + \frac{1}{r}\frac{\partial T}{\partial r} + \frac{1}{r^2}\frac{\partial^2 T}{\partial \varphi^2} + \frac{\partial^2 T}{\partial z^2}\right) = \rho_{real} c_{real}\left(\frac{\partial T}{\partial \frac{\varphi\pi}{180\omega}} + \omega_{real}\frac{\partial T}{\partial \varphi}\right)$$

Equation 5.10

To achieve the same temperature distribution (average temperature of each revolution), the total heat flux in a given revolution was identical:

$$\int_{360}^{0} k_a\left(\frac{\partial^2 T}{\partial r^2} + \frac{1}{r}\frac{\partial T}{\partial r} + \frac{1}{r^2}\frac{\partial^2 T}{\partial \varphi^2} + \frac{\partial^2 T}{\partial z^2}\right) d\varphi = \int_{360}^{0} \rho_a c_a\left(\frac{\partial T}{\partial \frac{\varphi\pi}{180\omega}}\right) d\varphi$$

$$= \int_{\theta}^{0} k_{real}\left(\frac{\partial^2 T}{\partial r^2} + \frac{1}{r}\frac{\partial T}{\partial r} + \frac{1}{r^2}\frac{\partial^2 T}{\partial \varphi^2} + \frac{\partial^2 T}{\partial z^2}\right) d\varphi + \int_{360}^{\theta} 0\, d\varphi$$

$$= \int_{\theta}^{0} \rho_{real} c_{real}\left(\frac{\partial T}{\partial \frac{\varphi\pi}{180\omega}} + \omega_{real}\frac{\partial T}{\partial \varphi}\right) d\varphi + \int_{360}^{\theta} 0\, d\varphi$$

Equation 5.11

Neglecting the circumferential temperature difference due to the high rotation speed assumption gave

$$\omega_{real}\frac{\partial T}{\partial \varphi} = 0$$

Equation 5.12

Thus

$$\int_{360}^{0} k_a \left(\frac{\partial^2 T}{\partial r^2}+\frac{1}{r}\frac{\partial T}{\partial r}+\frac{1}{r^2}\frac{\partial^2 T}{\partial \varphi^2}+\frac{\partial^2 T}{\partial z^2}\right)d\varphi = \int_{360}^{0} \rho_a c_a \left(\frac{\partial T}{\partial \frac{\varphi\pi}{180\omega}}\right)d\varphi$$

$$= \int_{\theta}^{0} k_{real} \left(\frac{\partial^2 T}{\partial r^2}+\frac{1}{r}\frac{\partial T}{\partial r}+\frac{1}{r^2}\frac{\partial^2 T}{\partial \varphi^2}+\frac{\partial^2 T}{\partial z^2}\right)d\varphi = \int_{\theta}^{0} \rho_{real} c_{real} \left(\frac{\partial T}{\partial \frac{\varphi\pi}{180\omega}}\right)d\varphi$$

Equation 5.13

As the total heat flux (the expectation in statistical point of view) was identical in the two models and the temperature *T* were identical, so

$$\frac{\int_{360}^{0}\left(\frac{\partial^2 T}{\partial r^2}+\frac{1}{r}\frac{\partial T}{\partial r}+\frac{1}{r^2}\frac{\partial^2 T}{\partial \varphi^2}+\frac{\partial^2 T}{\partial z^2}\right)d\varphi}{\int_{\theta}^{0}\left(\frac{\partial^2 T}{\partial r^2}+\frac{1}{r}\frac{\partial T}{\partial r}+\frac{1}{r^2}\frac{\partial^2 T}{\partial \varphi^2}+\frac{\partial^2 T}{\partial z^2}\right)d\varphi} = \frac{K_a}{K_{real}}$$

Equation 5.14

$$\frac{\int_{360}^{0}\left(\frac{\partial T}{\partial \frac{\varphi\pi}{180\omega}}\right)d\varphi}{\int_{\theta}^{0}\left(\frac{\partial T}{\partial \frac{\varphi\pi}{180\omega}}\right)d\varphi} = \frac{\rho_a c_a}{\rho_{real} c_{real}}$$

Equation 5.15

Therefore,

$$k_a = k_{real} * \theta/360$$

Equation 5.16

$$\rho_a c_a = \rho_{real} c_{real} * \theta/360$$

Equation 5.17

Since the volume of the axisymmetric pad and real pad were different

$$V_a = V_{real} * 360/\theta$$

Equation 5.18

and

$$m = V\rho$$

Equation 5.19

In order to keep same total mass, $m_a = m_{real}$, it was assumed that the specific

heat capacity was identical in both cases but the density of the axisymmetric pad was scaled.

$$C_a = C_{real}$$

Equation 5.20

$$\rho_a = \rho_{real} * \theta/360$$

Equation 5.21

Alternatively, from a probability density point of view, the probability in the time domain was $P_t = \theta/360$ for a discreet point on the disc surface to access the temperature field of the pad. In order to achieve the same expectation for the temperature field, the integrations of the heat transfer equations (i.e. the total heat flux) should be identical which gave

$$\int k_a \left(\frac{\partial^2 T}{\partial r^2} + \frac{1}{r}\frac{\partial T}{\partial r} + \frac{1}{r^2}\frac{\partial^2 T}{\partial \varphi^2} + \frac{\partial^2 T}{\partial z^2}\right) d\varphi = \int P_t \cdot k_{real} \left(\frac{\partial^2 T}{\partial r^2} + \frac{1}{r}\frac{\partial T}{\partial r} + \frac{1}{r^2}\frac{\partial^2 T}{\partial \varphi^2} + \frac{\partial^2 T}{\partial z^2}\right) d\varphi$$

Equation 5.22

Therefore, similar relationships to those shown in Equation 5.16 and 4.21 were obtained.

5.2.2.3 Contact pressure and strain energy

As indicated by Stolarski (1999), the contact pressure is determined by strain energy. Strain energy density is a function of Young's modulus and strain,

$$U_0 = \frac{1}{2} E \varepsilon^2$$

Equation 5.23

Thus the total strain energy of the pad was

$$U = \int_V^0 U_0 \, dV U = \frac{1}{2} V E \varepsilon^2$$

Equation 5.24

As the total strain energy due to thermal expansion was to be the in both the

axisymmetric pad model and real scenario, so

$$U_a = \frac{1}{2} V_a E_a {\varepsilon_a}^2 = U_{real} = \frac{1}{2} V_{real} E_{real} {\varepsilon_{real}}^2$$

Equation 5.25

Since the volumes of the pads were different (see Equation 5.18), but the thermal strain in the axial direction was identical due to the same temperature T and Poisson's ratio ν (Barber, 2010)

$$\varepsilon_a = \varepsilon_{real} = \frac{\alpha(1+\nu)T}{1-\nu}$$

Equation 5.26

Therefore, substituting Equation 5.18 and 4.26 into 4.25, gave the scaled Young's modulus of the axisymmetric pad

$$E_a = E_{real} * \theta/360$$

Equation 5.27

In summary, the axisymmetric model increased the pad arc length, pad volume and contact area. In order to achieve equivalent approximate thermo-elastic deformation and contact pressure, the load, thermal conductivity, density and Young's modulus of the pad were scaled. The scaling factor was determined by the ratio between pad length and disc circumference. Regarding the output, the total heat generation was identical in both cases but the local heat generated per element was reduced due to the change in volume resulting in a higher element count in the axisymmetric model. The axial displacement due to thermal expansion of the pad was identical as well. In order to maintain identical average contact pressure at the interface, a scaling factor was applied to the pad elasticity whilst the total strain energy was identical and the strain energy density was scaled. A summary is resented in Table 5.1.

Table 5.1 Scaling factors in the axisymmetric pad model and real scenario

	Ratio	Total (of the Pad)		Localised (distributed in an element)	
	Model	Realistic	Axisymmetric	Realistic	Axisymmetric
Geometry	Pad arc length	1	$360/\theta$	-	-
	Pad volume	1	$360/\theta$	-	-
	Contact area	1	$360/\theta$	-	-
Input	Load	1	1	1	$\theta/360$
	Coefficient of friction	1	1	1	1
	Velocity	1	1	1	1
`Material properties	Thermal conductivity	1	$\theta/360$	1	$\theta/360$
	Density	1	$\theta/360$	1	$\theta/360$
	Specific heat	1	1	1	1
	Elasticity	1	$\theta/360$	1	$\theta/360$
	Thermal expansion	1	1	1	1
Output	Heat generation	1	1	1	$\theta/360$
	Temperature distribution	1	1	1	1
	Axial displacement	-	-	1	1
	Contact pressure (stress)	1	1	1	$\theta/360$
	Strain energy	1	1	-	-
	Strain energy density	-	-	1	$\theta/360$

5.2.3 *Feasibility modelling*

To verify the assumptions made in section 5.2.1, FE models based on a scaled brake system were performed. The scaled friction test rig was designed to measure friction force and coefficient of friction. In this case, due to the dimension of the brake disc and pad being much smaller than the actual automotive brake, the number of elements in the numerical model was lower, therefore, saving the computing time.

The geometry and the braking condition of the disc and pad were listed in Table 5.2 and the material properties are listed in Table 5.3. The disc was rotating at a constant speed of 30 rad/s, and the brake pad covered 30° of the disc in the circumferential direction.

Initially, a 3D finite element model with rotating finite arc length pad was modelled as the benchmark. Then, the axisymmetric assumption (scaling of material, loading, and non-rotating contact pressure dependent heat source) was applied in to both 3D and 2D models to verify the assumptions.

Table 5.2 Brake operation parameters for the scale disc models

Braking operation parameters	
Coefficient of friction, μ	0.38
Rotational velocity, ω (rad/s)	30
Actuation pressure, P (bar)	10
Brake duration, t (s)	5
Disc outer radius, R_o (mm)	50
Disc inner radius, R_i (mm)	10
Brake disc thickness, T_h (mm)	10
Pad arc length angle, θ (°)	30

Table 5.3 Material properties for the scale disc models

Material properties	Disc	Pad	Scaled pad
Thermal conductivity, k (W/mK)	48	0.5	0.042
Density, ρ (kg/m^3)	7200	1250	104.2
Elastic modulus, E (GPa)	100	0.7	0.7
Poisson's ratio, v	0.25	0.25	0.25
Thermal expansion, α (10^{-6}/K)	10	10	10
Specific heat, c (J/kgK)	480	1000	1000

Since the working condition was not heavy (10bar pressure and 30 rad/s), the total temperature change of the braking operation did not provide excessive disc deformation. Thus, for all models described in this section (5.2.3), the total heat

generation was scaled by 100. This ensured that any difference in the results was exaggerated and easily compared. There were no convective cooling boundaries applied to the models and the thermal contact resistances were as defined in section 3.3.4. The solver selected was ABAQUS/standard and the analysis type was fully coupled thermos-mechanical. Regarding the mesh, C3D8T: the 8-node hex thermally coupled displacement and temperature elements were selected for both disc and pad. In order to achieve minimum effects due to mesh sensitivity on the results, all the elements in this section were fixed at 2mm. According to Tirovic (2014) the Fourier number is defined as

$$F_o = d\Delta t/\Delta x^2$$

Equation 5.28

where d is the thermal diffusivity

$$d_i = \frac{k_i}{\rho_i c_i} \ (i = disc, pad)$$

Equation 5.29

where the Fourier number must satisfy

$$F_o \leq 1/6$$

Equation 5.30

Following this approximation would ensure that the accuracy of the results would be acceptable in terms of mesh sensitivity. The Fourier numbers calculated in Table 5.4 for the scale models were all much lower than 1/6. Therefore, it illustrated that for the approximate element size of 2mm, the analysis was sufficient to provide acceptable results.

Table 5.4 Fourier number calculation

Parts	Δx (m)	Δt (s)	F_o
pad	0.002	0.01	0.002
disc	0.002	0.01	0.035

5.2.3.1 3D real pad length with rotating disc model

The geometry and boundary conditions of the scale model are shown in the Figure 5.3. The disc is the rotor and the pad is the stator. The radial and tangential displacements of the pad were constrained but the axial displacement of the pad was free. A uniform pressure of 10bar was applied on the back of the pad constantly throughout the 5s simulation. The bottom plane of the disc was fixed in terms of its axial displacement, so that all deflections and stress in the disc were reflected in the contact surface. The heat flux was generated due to the friction between the disc and pad. It was assumed that the heat was generated at the interface on the pad side (Qi and Day, 2007), and then conducted to the disc based on the thermal contact resistance (pressure and gap dependent thermal contact conductance (30kW/m^{2}K)).

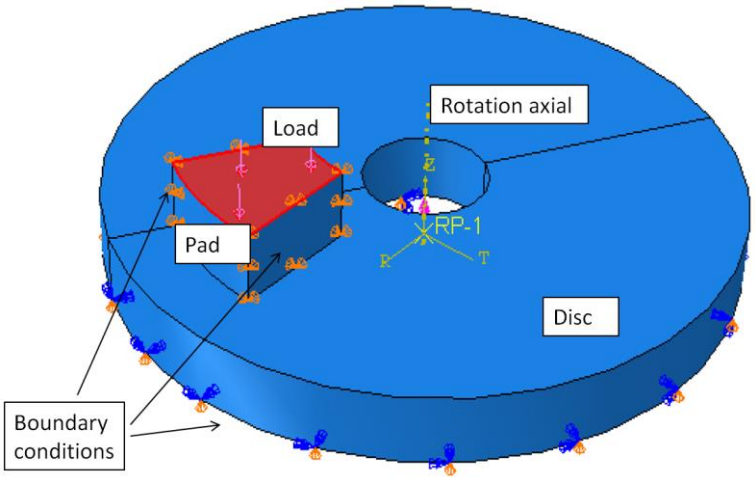

Figure 5.3 Realistic 3D pad model with rotating showing boundary conditions

5.2.3.2 3D axisymmetric pad models

To verify the assumptions of the axisymmetric pad and the simplification of neglecting disc rotation made in section 5.3.1, both 3D axisymmetric pad and rotating disc model and 3D axisymmetric pad and stationary disc model with user defined heat flux input were established as shown in Figure 5.4.

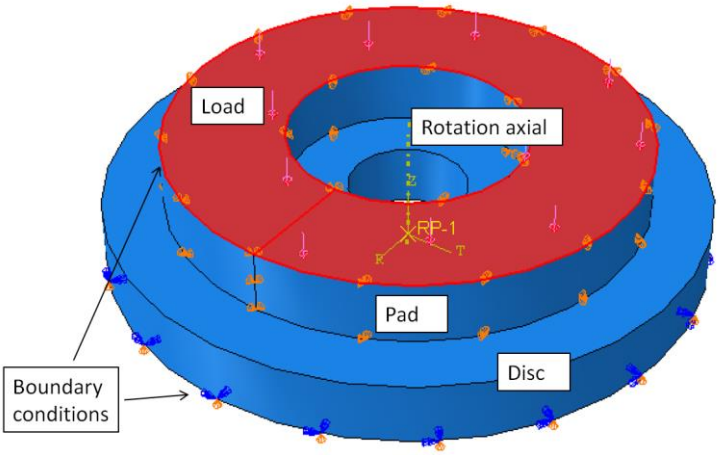

Figure 5.4 3D axisymmetric pad model assembly and boundary conditions

The mechanical load and material properties in both models were scaled using the factor $\theta/360$ mentioned in section 5.3.2 and Table 5.1. In this case, the scale factor is 30/360=1/12. For the rotating model, the heat was generated due to friction. Regarding the stationary pad model, there was no sliding between the disc and pad. The heat generation were defined using ABAQUS user subroutine FRIC, which is used to define the properties of friction e.g. the shear stress and the heat generation on the interface. In this model, the traction force was neglected. The frictional heating was defined as a function of contact pressure, coefficient of friction, and local sliding velocity (see Equation 5.2). The code of the subroutine was compiled using FORTRAN language and can be found in Appendix 1. The other settings of the models were identical to the previous 3D rotational model in section 5.2.3.1.

5.2.3.3 2D axisymmetric pad with periodic heating

The aim of the comparison between these two models was to confirm that the assumptions of continuous heating could give an acceptable representation of the temperature and displacement fields. In the 2D axisymmetric models as

shown in Figure 5.5, the scaling of the material properties and loads was identical to the 3D axisymmetric model. Two types of models were established: periodic heating and continuous heating model. Both of the models had identical scaled loading conditions. The only difference between periodic heating model and continuous heating model was the heating cycles. The heating cycles can be represented in Figure 4.2. In the periodic model, the heat generation only took place over a time duration equivalent to 1/12 of a revolution with a magnitude 12 times greater than the continuous heat model. This was enabled by modifying the user subroutine by adding if sentences. The total amounts of energy inputs were identical in the two models.

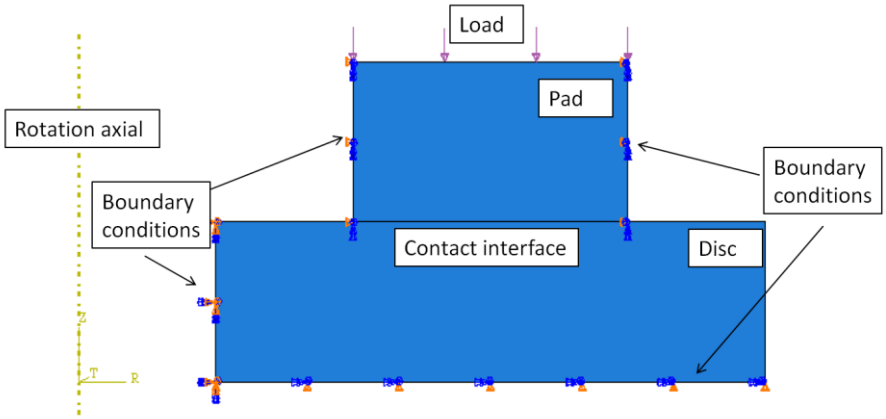

Figure 5.5 2D axisymmetric model assembly and boundary conditions

In terms of mesh, to simulate the transient thermo-elastic and thermal contact effects, CAX4T: A 4-node axisymmetric thermally coupled displacement and temperature element was selected in the 2D axisymmetric models with periodic or continuous heating. There were 600 elements in both of the 2D models.

5.2.4 *Results of the scaled models*

The most significant aim of the axisymmetric model was to improve the computing efficiency (shorter computing time) whilst still providing acceptable temperature and displacement results. The comparison of the DOF and computing time is

listed in Table 5.5. In terms of DOF, the 3D axisymmetric pad models (B and C) had 98207DOF which were greater than the 3D standard pad rotating disc model (A), this was due to the increased volume of the pad. However, the computing time was much shorter than the rotating model (A). This can be explained by the contribution of eliminating the computing of shear traction behaviours in the axisymmetric model. For the rotating and stationary 3D axisymmetric pad models (B and c), the implementation of user defined heat flux input model significantly reduced the computing time from 50 hours to 1 hour. Regarding the 2D models, both model had identical element size, number and DOF, but the 2D continuous heating model (E) completed in just 2min which is much faster than the periodic heating model (D). In general, the results suggested that in both 2D and 3D, axisymmetric pad models with continuous heating (C) & (E) defined by subroutine is the most time efficient method featured very close temperature, displacement and stress field predictions.

Table 5.5 Models performed and the computing efficiency comparisons

Models	Specifications	Total DOF	Computing time
A	3D standard pad rotating disc	50615	10hour 1min
B	3D axisymmetric pad rotating disc	98207	50 hour 33min
C	3D axisymmetric pad stationary disc	98207	1hour 16min
D	2D periodic heating	2166	28min
E	2D continuous heating	2166	2min

Figure 5.6 and Figure 5.7 respectively compare the temperature and axial displacement at the end of the simulations of the five models at the end of the simulations (5s). The upper and lower colour range of the plots were identical, e.g. the maximum temperature limit was 1548°C and the minimum limit was 60°C. The high temperature predicted is attributed by to exaggeration of thermal expansion coefficient, heat generation and deflections, in order to show the trends of temperature distribution between different assumptions. The

temperature contours show that high temperature was concentrated at the mean radius of the contact surfaces for all models and the temperature magnitude gradually decreased in inner and outer radii and through disc thickness. Similarly, the axial disc displacement contours show a maximum displacement concentrated at the centre of the disc rubbing surfaces in all models which is known as hot bands. The results suggested that the average temperature field and displacement distributions for all five scale models were similar. Though there were circumferential peak temperature and displacement variations (~ 400 °C or ~100µm) due to the periodic heating in the rotating brake disc model generating higher surface temperatures at the trailing side of the pad, the average temperatures (351°C, 369°C, 368°C, 369°C, 369°C) and displacement (199µm, 213µm, 212µm, 214µm, 213µm) of the rubbing surfaces were similar.

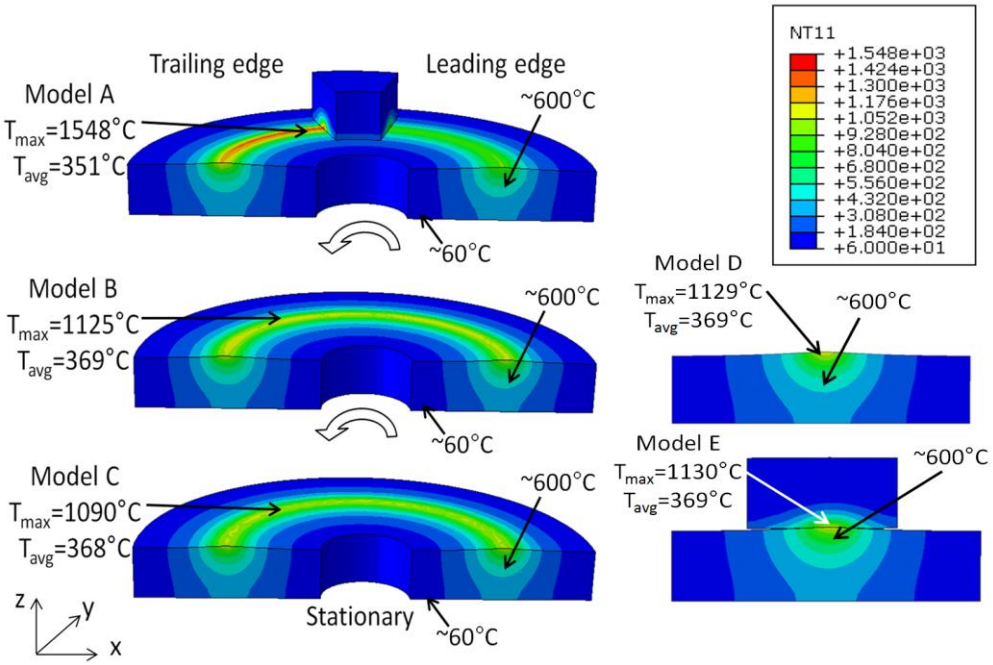

Figure 5.6 Temperature fields and maximum brake disc temperature (°C) for the scale models at 5s

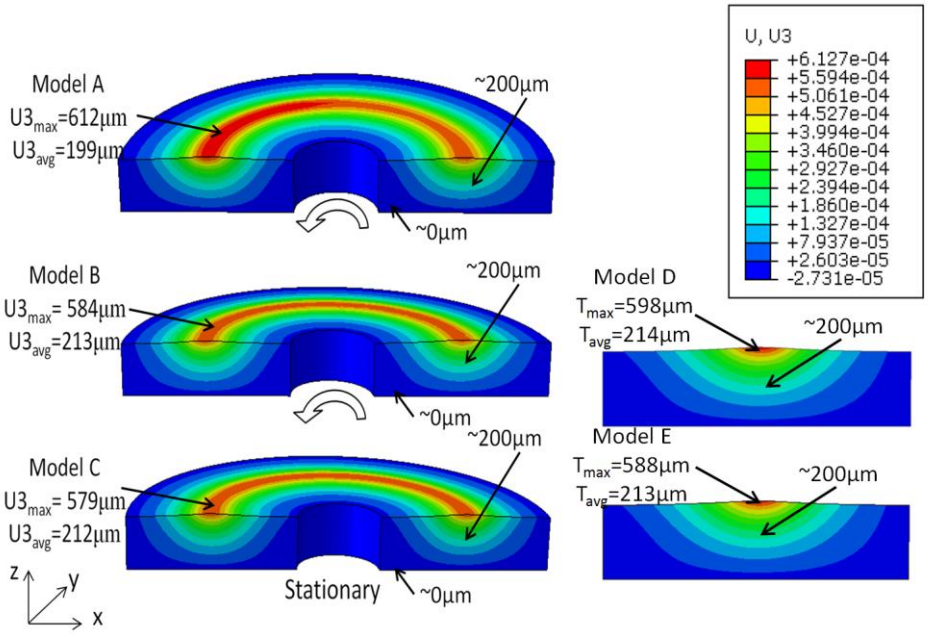

Figure 5.7 Displacement field with the colours indicating the maximum axial (z-direction) brake disc displacement (m) for the scale models at 5s

Figure 5.8 and Figure 5.9 provides the out-of-plane temperature and displacement distributions at the disc contact interfaces of the models. It can be seen that the 2D axisymmetric (E) and 3D axisymmetric pad (C) models achieved identical temperature fields and displacement fields.

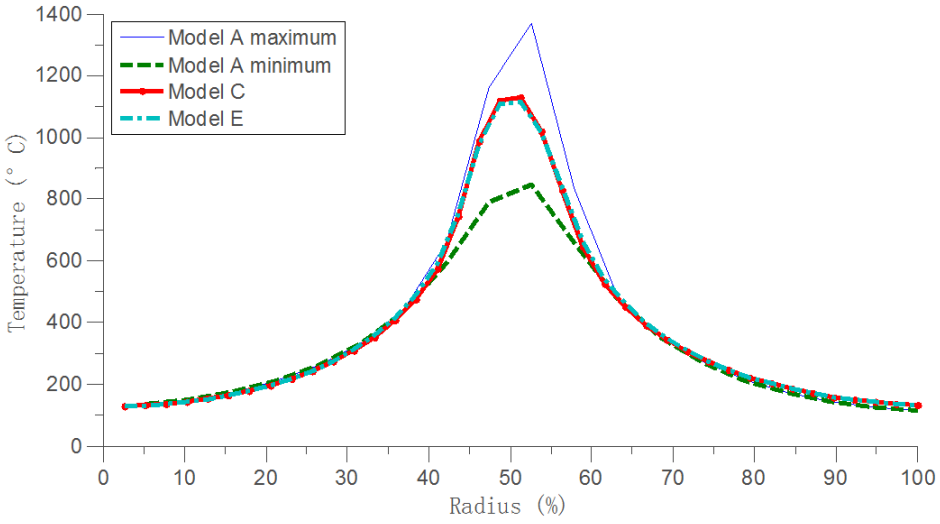

Figure 5.8 Disc surface temperature distribution comparison along the disc radii

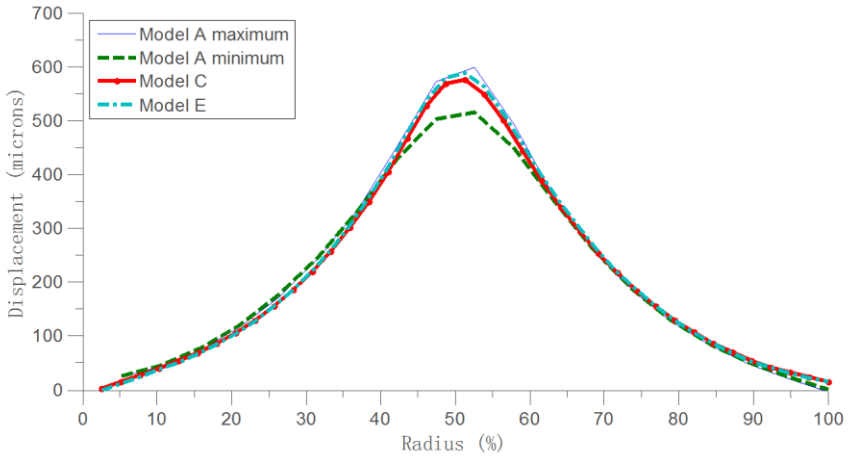

Figure 5.9 Disc surface axial displacement distribution comparison along the disc radii

Figure 5.10 shows the peak disc temperature time series comparison for each model. Significant fluctuations of the temperature curve of model A are evident which shows the cooling and heating phases due to rotation. It also illustrates that the temperature curve of the continuous heating model showed good correlation with the other models.

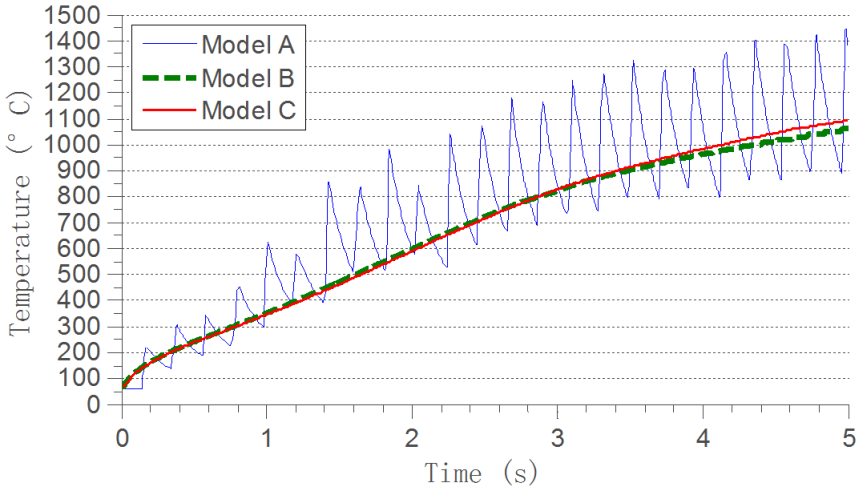

Figure 5.10 Brake disc temperature evolution of a single node on the mean rubbing surface; comparison between periodic heating (model A) and continuous heating in (axisymmetric models B and C)

Similarly, the maximum disc displacement time series comparison is shown in Figure 5.11. It shows that the 3D axisymmetric pad models (B and C) again provided good approximation of the 3D finite pad length model (A).

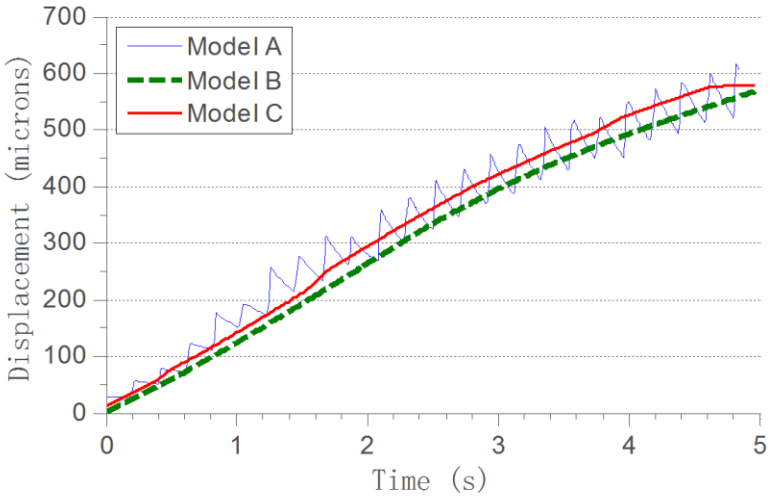

Figure 5.11 Evolution of brake disc displacement of a single node on the disc mean rubbing surface; comparison between periodic heating (model A) and continuous heating (axisymmetric models B and C)

In summary, to achieve a more time efficient FE method to predict hot spotting, several assumptions were made to enable the simplifications of a numerical brake disc model from the most complicated 3D rotating scenario into a 2D axisymmetric case. The material properties and loading conditions were modified based on a scaling factor approach. To verify the assumptions made, a finite element method based feasibility virtual test was performed. The results suggested that the axisymmetric pad, scaled pad material properties and stationary disc could provide good approximations of temperature and displacement fields. Meanwhile, the computing time was significantly reduced.

5.3 Axisymmetric ventilated disc and pins

The mounting pins and vent geometry of the actual brake had periodic symmetry equivalent to 17 ‘partitions’. Therefore, in order to the represent in the 2D axisymmetric model, a simplification of the vent area was performed by modelling the ventilated layer and pins as solid and applying material property scaling factors to reproduce an ‘equivalent homogenous material’ (Yi, Barber and Hartsock, 2002).

5.3.1 *Basic assumptions*

Similar to the axisymmetric assumption for the pad, the assumptions of the ventilated disc focused on achieving the same or similar disc temperature and deformation. Therefore, the circumferential variations of the disc temperature and displacement field were neglected. In addition, as the relative modulus of the disc was much greater (over 100 times) than the pad according to Table 5.3, the disc compression due to mechanical contact was ignored. Thus the identical strain energy assumption was not applied.

The main assumptions:

1) The circumferential vent deformation and ‘hoop’ stress were ignored.
2) The circumferential temperature and displacement variation were assumed to be zero.
3) A global convective heat transfer coefficient was used according to the experiment (see section 4.5.1).
4) The energy partition into the vent area was assumed to be identical in the axisymmetric disc model, compared with the real scenario.

5.3.2 *Mathematic formulations*

Figure 5.12 demonstrates the geometry changes according to the axisymmetric ventilated disc/pins simplifications and the equivalent layers. The total angle covered by the vents and pins covered angle was set to θ_{vent} and θ_{pin} out of 360° in this simplification. Thus the possibility of the vents passing through a given angular position in the ventilated layer is $P_{td} = \theta_{vent}/360$. Similarly, the possibility of the pins passing through a given location in the pins layer is $P_{tp} = \theta_{pins}/360$.

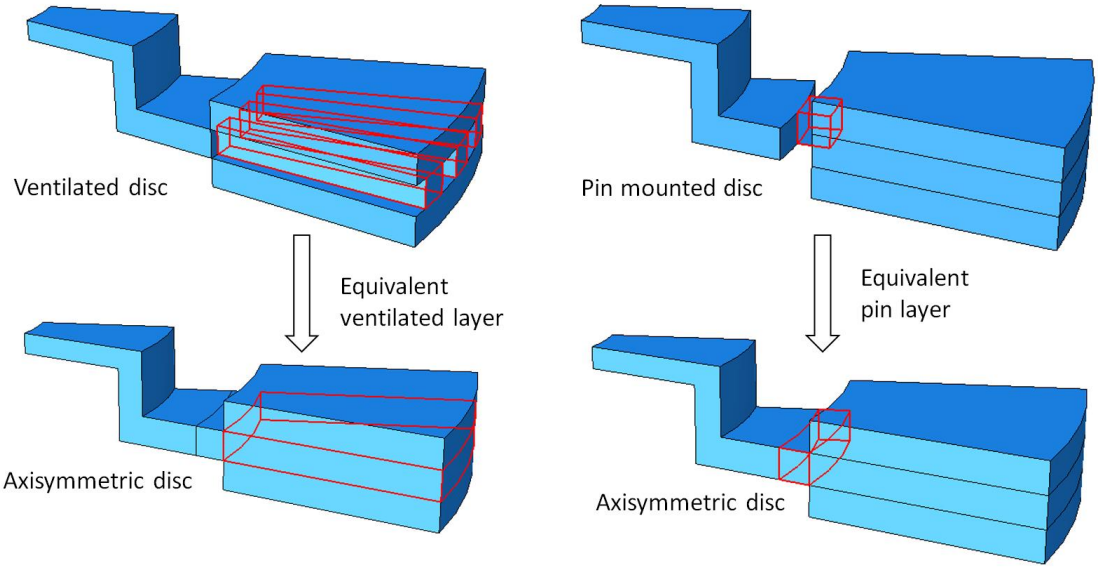

Figure 5.12 The axisymmetric equivalent vent/pin simplifications

For the ventilated disc, its equivalent ventilated area should satisfy similar temperature distribution compared to the real scenario. The heat transfer equations of the ventilated disc and axisymmetric solid disc with equivalent ventilated layer should be

$$k_{vent}\left(\frac{\partial^2 T}{\partial r^2}+\frac{1}{r}\frac{\partial T}{\partial r}+\frac{1}{r^2}\frac{\partial^2 T}{\partial \varphi^2}+\frac{\partial^2 T}{\partial z^2}\right)=\rho_{vent}c_{vent}\left(\frac{\partial T}{\partial t}+\omega_{vent}\frac{\partial T}{\partial \varphi}\right)$$

Equation 5.31

$$k_{solid}\left(\frac{\partial^2 T}{\partial r^2}+\frac{1}{r}\frac{\partial T}{\partial r}+\frac{1}{r^2}\frac{\partial^2 T}{\partial \varphi^2}+\frac{\partial^2 T}{\partial z^2}\right)=\rho_{solid}c_{solid}\left(\frac{\partial T}{\partial t}+\omega_{solid}\frac{\partial T}{\partial \varphi}\right)$$

Equation 5.32

Due to the high rotation speed (for instance, 976rev/min in the experiment) of the disc, the equation can be converted in to probability density functions. To achieve the same temperature distribution under the same total energy input in the disc ventilated layer, the integration of the heat transfer equations should be the same:

$$\begin{aligned}\int k_{vent}\left(\frac{\partial^2 T}{\partial r^2}+\frac{1}{r}\frac{\partial T}{\partial r}+\frac{1}{r^2}\frac{\partial^2 T}{\partial \varphi^2}+\frac{\partial^2 T}{\partial z^2}\right)d\varphi &= \int \rho_{vent}c_{vent}\left(\frac{\partial T}{\partial t}+\omega_{vent}\frac{\partial T}{\partial \varphi}\right)d\varphi \\ &= \int P_{td}\cdot k_{solid}\left(\frac{\partial^2 T}{\partial r^2}+\frac{1}{r}\frac{\partial T}{\partial r}+\frac{1}{r^2}\frac{\partial^2 T}{\partial \varphi^2}+\frac{\partial^2 T}{\partial z^2}\right)d\varphi \\ &= \int P_{td}\cdot \rho_{solid}c_{solid}\left(\frac{\partial T}{\partial t}+\omega_{solid}\frac{\partial T}{\partial \varphi}\right)d\varphi\end{aligned}$$

Equation 5.33

Therefore, the disc conductivity and density should be scaled thus

$$k_{solid}=k_{vent}*\theta_{vent}/360$$

Equation 5.34

$$\rho_{solid}=\rho_{vent}*\theta_{vent}/360$$

Equation 5.35

In addition, in order to achieve the same deformation of the ventilated layer under the mechanical loading from the pad clamping force, the disc Young's modulus had to be scaled due to the increase in volume, which gave

$$E_{solid}=E_{vent}*\theta_{vent}/360$$

Equation 5.36

Regarding the disc thermal deformation, the axial displacement field should also be identical, thus the axial thermal expansion of the ventilated layers should be identical. Integrating the axial strain probability density function, gives

$$\int \frac{d\varepsilon_{vent}}{d\varphi}d\varphi=\int \alpha_{vent}\frac{dT}{d\varphi}d\varphi=\int p_{td}\frac{d\varepsilon_{solid}}{d\varphi}d\varphi=\int p_{td}\cdot\alpha_{solid}\frac{dT}{d\varphi}d\varphi$$

Equation 5.37

Thus the coefficient of thermal expansion was scaled

$$\alpha_{solid} = \alpha_{vent} * \theta_{vent}/360$$

Equation 5.38

Similar to the ventilated area, the following material properly scaling factors were applied in the axisymmetric equivalent pin layer:

$$k_{solidpin} = k_{pin} * \theta_{pin}/360$$

Equation 5.39

$$\rho_{solidpin} = \rho_{pin} * \theta_{pin}/360$$

Equation 5.40

$$E_{solidpin} = E_{pin} * \theta_{pin}/360$$

Equation 5.41

$$\alpha_{solidpin} = \alpha_{pin} * \theta_{pin}/360$$

Equation 5.42

5.3.3 *Feasibility modelling*

In order to verify the axisymmetric ventilated disc and axisymmetric pin assumptions. Four models with different geometry and assumptions were performed as shown in Figure 5.12 and Table 5.6. The load and boundary conditions are shown in Figure 5.13. Symmetric boundaries were applied to the two cross-section surfaces in order to reproduce the axisymmetric disc. Identical surface heat fluxes were uniformly applied on the disc outboard and inboard rubbing surfaces. A uniform heat transfer coefficient of 130 W/m^{2}K was applied on the ventilated areas and disc rubbing surfaces to simulate the convective cooling.

Table 5.6 Models performed for axisymmetric ventilated disc and pins assumption comparison

Model ID	Convection	Pins	Vents
A	Yes	Axisymmetric	Axisymmetric
B	Yes	Axisymmetric	Real
C	No	Axisymmetric	Axisymmetric
D	No	Real	Axisymmetric

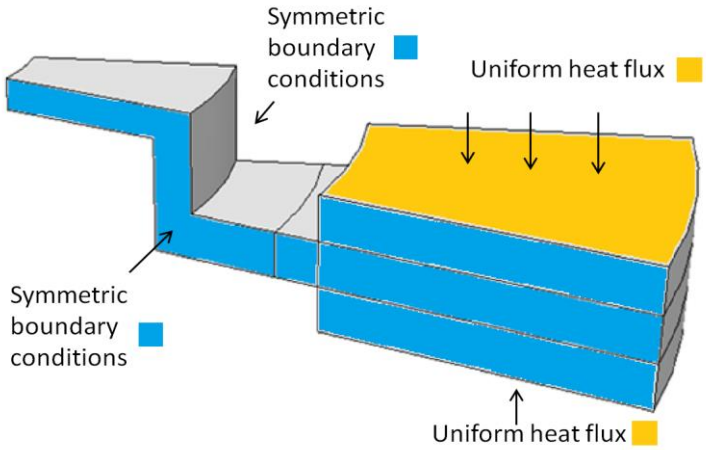

Figure 5.13 Boundary conditions for the axisymmetric vents and pins model

Figure 5.14 shows a comparison of the radial disc outboard surface temperature distribution (from inner to outer) for each model. It illustrates that the model A (axisymmetric vent layer assumption) and model B showed similar temperature distribution with a temperature difference of ~3°C. The temperature of model A was greater than the model B since there was less convective area in the axisymmetric vent model. In terms of the axisymmetric pin layer assumption (model C and D), the maximum temperature predicted and the temperature distribution at the mean and outer radii were well correlated. However, the temperature at the inner radii showed ~12°C difference. Therefore, the maximum error in temperature caused by the axisymmetric simplifications was ~6% (12°C/200°C).

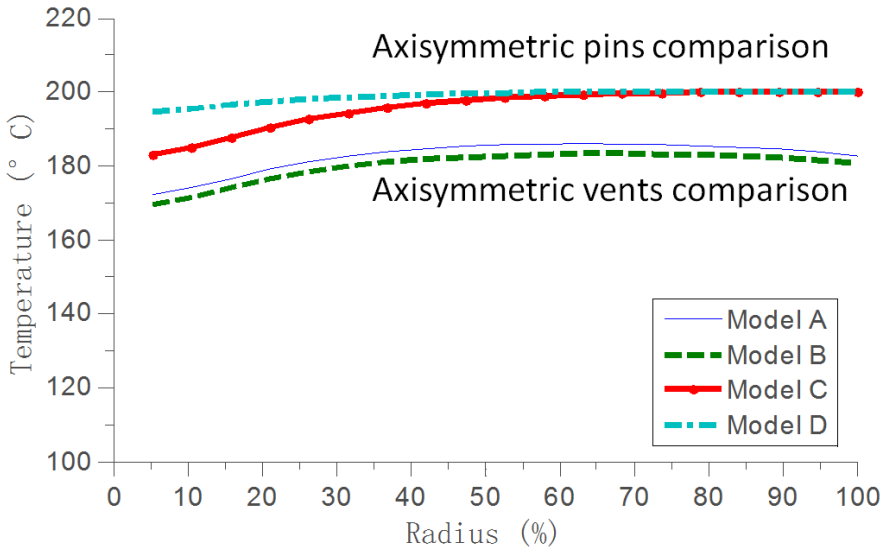

Figure 5.14 Comparison of disc outboard surface temperature distribution with and without axisymmetric pin and vent assumptions

Figure 5.15 shows the displacement distribution comparison of the disc outboard surfaces. Regarding the axisymmetric vents assumption, the displacement distributions of the axisymmetric disc (model A) and ventilated disc (model B) were matched well and the maximum difference was ~10μm. For the axisymmetric pins assumption, the comparison between the normal pin model (model D) and axisymmetric pin model (model C) showed similar displacement distribution and the maximum difference was ~15μm. Therefore, the maximum error in displacement caused by the axisymmetric simplifications was ~10% (15μm/150μm).

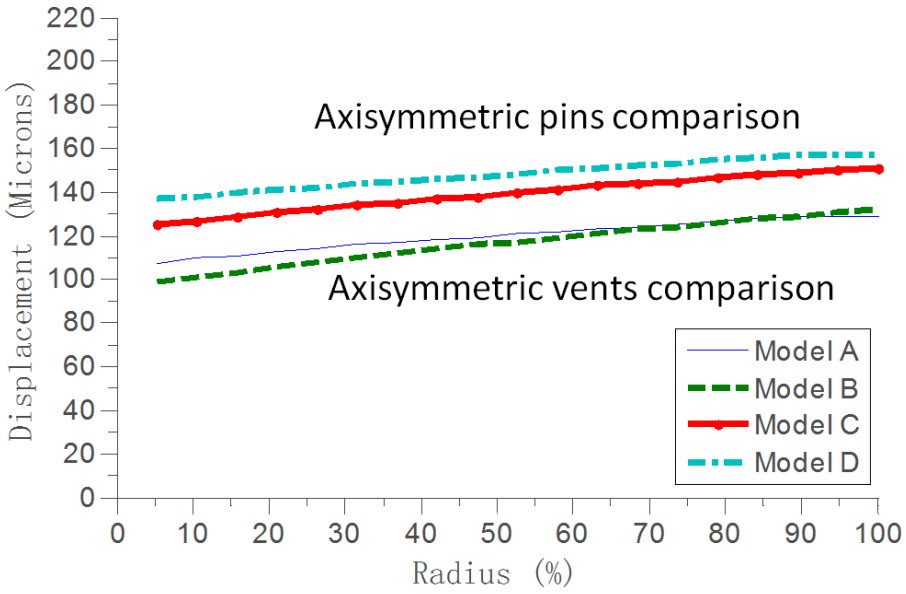

Figure 5.15 Comparison of disc outboard surface displacement distribution with and without axisymmetric pin and vent assumptions

In general, the temperature distribution and displacement distribution achieved good approximation based on the axisymmetric ventilated disc and axisymmetric pins assumption based on the results present in Figure 5.14 and Figure 5.15.

5.4 Summary

In this chapter, the fundamental studies were performed by calculating the material scaling factors for the axisymmetric pad, axisymmetric vents and axisymmetric pin assumptions and correlated using FE models. The intention was to improve the computing efficiency via the simplification of the geometry of the symmetric components of the friction pair. Such assumptions will be applied in the further FE modelling of hot spotting and will enable the parametric studies to be performed due to the improved computational efficiency.

In the axisymmetric pad assumption the brake pads was assumed to be 'smeared' in the circumferential direction. In order to achieve the same temperature, displacement and contact pressure distribution after the simplification, the

analytical calculation estimated a scaling factor which was related to the pad length. The conductivity, Young's modulus and density were modified by applying the scaling factor. FE modelling verifications were performed and five models with different levels of assumptions were established including: 3D finite length pad and rotating disc model; 3D axisymmetric pad rotating disc model; 3D axisymmetric pad stationary disc model; 2D periodic heating axisymmetric model and 2D continuous heating axisymmetric model. By comparing the results of the FE models, it was found that the temperature and displacement distribution of the models were well correlated. It revealed that 1) in the 3D model, the rotation of the disc did not affect the results when compared with the stationary disc model incorporating the contact pressure dependent heat generation using subroutine FRIC; 2) in the 2D models, the periodic heating (in order to reproduce the rotation of disc in 2D) can be replaced by the continuous heating; 3) The axisymmetric pad assumption did not affect the temperature and displacement field of the disc, even though the heat generation were exaggerated in this model.

Finally, the axisymmetric ventilated disc and axisymmetric pin assumptions were established in order to reproduce the pin-mounted ventilated disc in a 2D axisymmetric model. Similar to the axisymmetric pad simplification, the scaling factors were applied to the conductivity, Young's modulus, density and thermal expansion coefficients of the vents and pins. The results showed good correlation before and after applying the simplifications.

Chapter 6 2D FE Modelling of Hot Spotting

6.1 Introductions

The aim of 2D modelling was to investigate the basic mechanism and determinants of hot spotting and its radial migration. Both in-plane (circumferential) and out-of-plane (radial) models will be performed in this chapter. Initially, the 2D in-plane axisymmetric pad hot spotting model was developed and the determinants will be investigated by parametric studies. Then, in-plane models under different simplification levels will be established to evaluate the proper modelling technique and the basic mechanism of hot spotting. In addition, the 2D out-of-plane models will be presented incorporating with wear model aiming to investigate the mechanisms of radial hot spot/band migration.

6.2 2D In-plane axisymmetric pad hot spotting model

Based on the axisymmetric pad assumption, a transient thermo-mechanical contact model was performed using the ABAQUS finite element package to investigate the in-plane hot spotting. The brake system simulated was identical to the high performance vehicle ventilated disc tested on the dynamometer discussed in Chapter 4.

6.2.1 *FE models setup*

In the in-plane model, the disc and pads were regarded as long beams as present in Figure 6.1. The length of the disc and pads was 1.02m which identical to the circumference on the mean rubbing radius. In the axial direction, there were five layers: outboard back-plate (steel), outboard pad (friction material), ventilated disc with 51 vents, inboard pad (friction material) and inboard back-plate (steel). In the circumferential direction, the system was fixed in the x direction (x direction symmetric boundary conditions) and the middle plane points of the disc were

pinned at 17 locations in both x and y direction as shown in Figure 6.1 to present the pins.

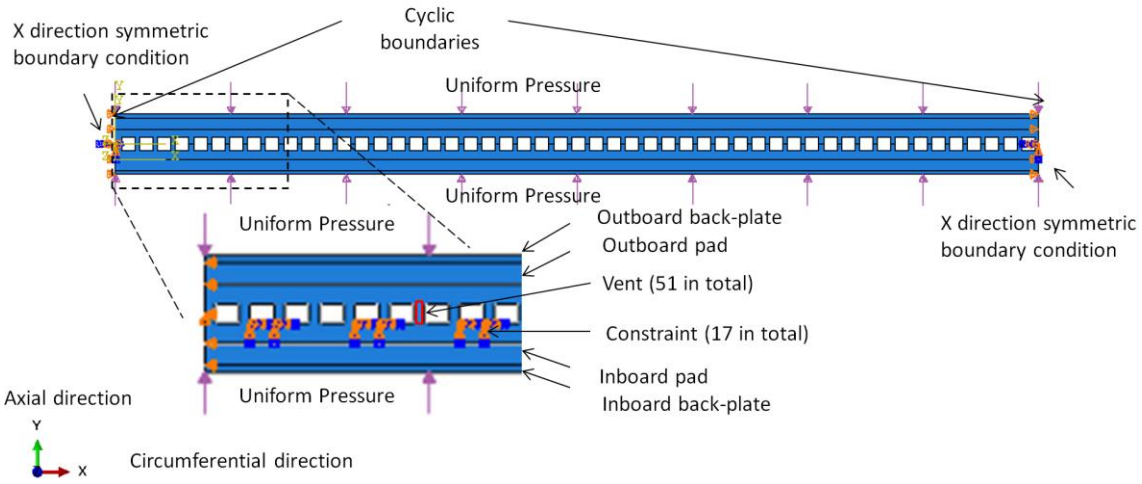

Figure 6.1 In-plane axisymmetric pad model assembly and boundary conditions

In order to represent the brake system as a continuous beam in circumference, cyclic boundary conditions were applied to the left and right edges of all five layers. The cyclic boundary mapped the displacement and temperature distribution of every single grid on the mesh of the two corresponding edges. A PYTHON code was developed to align the nodes using the "*equation" keyword constraint function as a processing batch by modifying the ABAQUS input file. To illustrate, the *equation constraint was defined as:

$$\mathrm{DOF11}_{Li} - \mathrm{DOF11}_{Ri} = 0$$

$$\mathrm{DOF2}_{Li} - \mathrm{DOF2}_{Ri} = 0$$

$$(\mathrm{i} = 1,2,3 \cdots 9 \cdots)$$

Equation 6.1

where DOF11 represented degree of freedom for temperature, and DOF2 was for y direction displacement, and the index Li and Ri were the node identities of left and right surfaces respectively as shown in Figure 6.2. Since the PYTHON code automatically aligned the nodes, the cyclic boundaries can be applied to refined meshes in an effective manner.

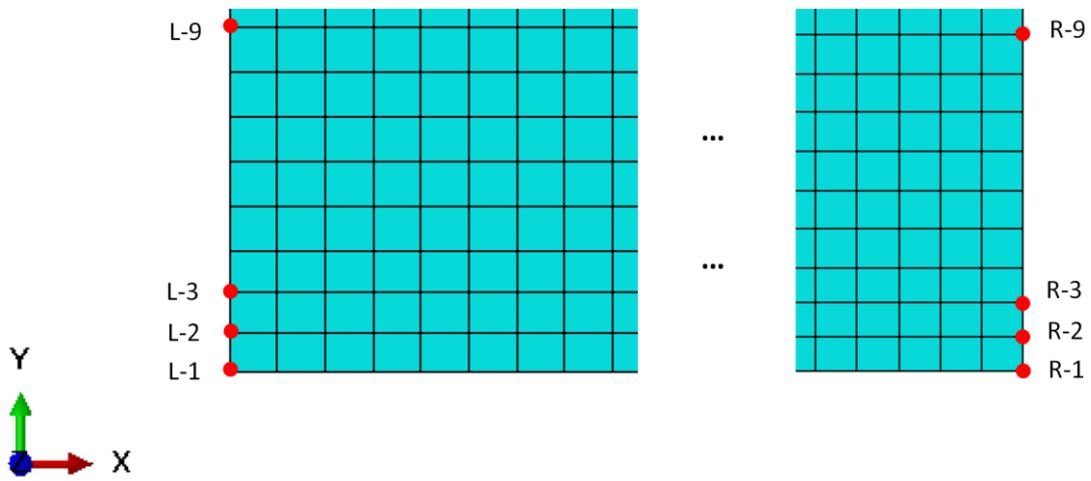

Figure 6.2 Illustration of the cyclic boundary conditions on the mesh

Figure 6.1 lists the material properties for the disc, pads and back-plate and the basic brake parameters. The braking condition was identical to the experiments in that a 24s constant 102rad/s (~976rev/min or ~150km/h) speed and 25.5bar brake pressure drag brake was carried out. Based on the axisymmetric pad assumptions in Chapter 5, the scaling factor applied to the uniform back-plate pressure thermal conductivity, elastic modulus and specific heat capacity in this scenario was $\frac{\theta}{360} = \frac{30}{360} = 1/12$. Considering the real pad surface area and the single piston area, the actual applied uniform pressure on the back-plate in the FE model was 80000Pa. The initial temperature was 60°C throughout the whole model which was identical to the experiment. The convective heat transfer coefficients obtained from the experiment (Chapter 4) were applied on the disc surface and vents.

Table 6.1 Material properties and braking operation data for out-of-plane model

Material properties	**Disc**	**Pad**	**Back-plate**	**Top-hat**	**Pins**
Thermal conductivity, k (W/mK)	48	0.5	50	113	17
Density, ρ (kg/m^3)	7250	1250	7800	2680	7800
Elastic modulus, E (GPa)	196	0.7	210	71	210
Poisson's ratio, v	0.25	0.25	0.3	0.33	0.34
Thermal expansion, α (10^{-6}/K)	10	10	11	21	11
Specific heat, c (J/kgK)	480	1000	500	880	500
Braking operation parameters					
Coefficient of friction, μ	0.38				
Rotational velocity, ω (rad/s)	102				
Actuation pressure, p (MPa)	2.55				
Piston radius, Rp (mm)	22.5				
Disc outer radius, Ro (mm)	190				
Disc inner radius, Ri (mm)	117				
Pad arc length angle, θ(°)	30				

Source of data: industry and literatures (Day and Newcomb, 1984, and Choi and Lee, 2004)

Regarding the mesh, CPE4T elements were used which stands for 4-node plane strain thermally coupled temperature displacement element (ABAQUS theory manual, 2012). In order to represent the thermo-elastic deformation in the modeled plane, the plane strain element was used (Yi, Du and Barber, 1999, and Al-Shabibi, 2011). The approximate element size was 2mm which was within the range of acceptable element size according to the Fourier number criteria discussed in section 5.2.3 and a further mesh sensitivity study was carried out in the following section 6.2.2 for verification. The mesh is shown in Figure 6.3 which illustrated that the mesh around the contact interface for both disc and pad were refined to obtain more precise (i.e. higher resolution) thermo-elastic contact results since the thermal gradients at the interface was high as suggested by (Day, Tirovic and Newcomb, 1991, and Tirovic, 2013).

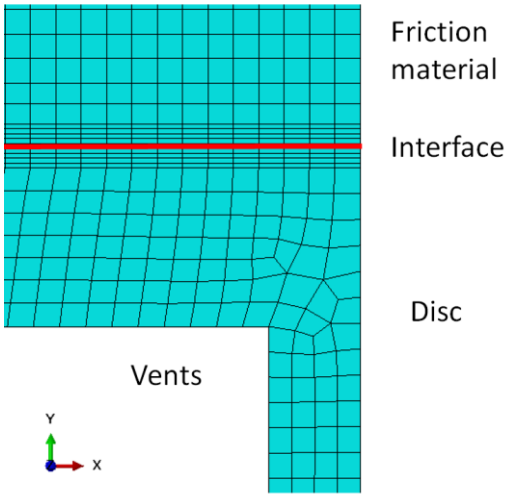

Figure 6.3 Illustration of the mesh

To prevent the penetration and excessive distortion, or local over interference due to unsmoothed mesh or deformation of the two surfaces on the interface, the master slave contact method was used. In this case, the disc was the master surface whereas pads were the slave surface due to their difference in modulus as discussed in section 3.3.3. The penalty contact method was used to calculate the contact pressure. The heat generation was defined by user-subroutine FRIC, which was compiled in a FORTRAN code (see Appendix 1). This subroutine initially retrieved the nodal contact pressure, coordinates and time increment size. Then, the nodal heat flux generated in a time increment was calculated by

$$\Delta q_{nodal} = \mu v_{nodal} p_{nodal} \Delta t$$

Equation 6.2

where μ is the coefficient of friction, v_{nodal} is the nodal linear velocity defined by the rotational velocity times nodal radius $v_{nodal} = \omega R_{nodal}$, p_{nodal} is the nodal contact pressure and Δt is the time increment. By implementing the subroutine, the heat can be generated without actual relative sliding in the model. Thermal contact resistance which determines the heat partition between disc and pad on the interface was defined using nominal thermal conductance of 30kW/m^{2}K which is as a function of contact pressure and clearance as shown in Figure 3.4.

6.2.2 *FE model results*

In order to check the robustness of the simulation, mesh sensitivity studies were performed as shown in Figure 6.4 and Figure 6.5 respectively. Various global approximate element sizes were compared regarding the maximum global temperature and number of hot spots. In terms of the maximum disc temperature, it can be seen that when the mesh was relatively coarse (element size ≥3.5mm), the temperature was greater than ~680°C. With the reduction of element size, the maximum temperature stabilised at ~520°C. Similarly, the number of hot spot was initially varied significantly when the mesh was coarse and then stabilised at 17 when the element size was smaller than 3mm. It revealed that the coarse mesh cannot effectively represent the hot spotting process. Therefore, a 2mm approximate global element size was used to provide sufficient 'resolution' of the results (e.g. 51st order temperature variation can be identified as shown in Figure 6.7) and efficient computing time (~20min).

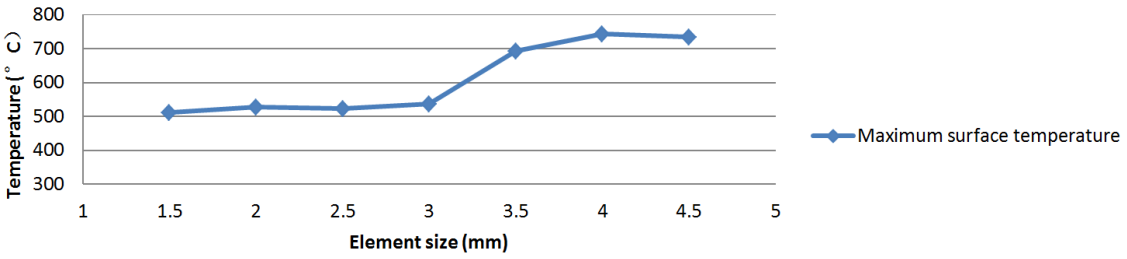

Figure 6.4 Mesh sensitivity study of the global maximum temperature for the 2D in-plane model

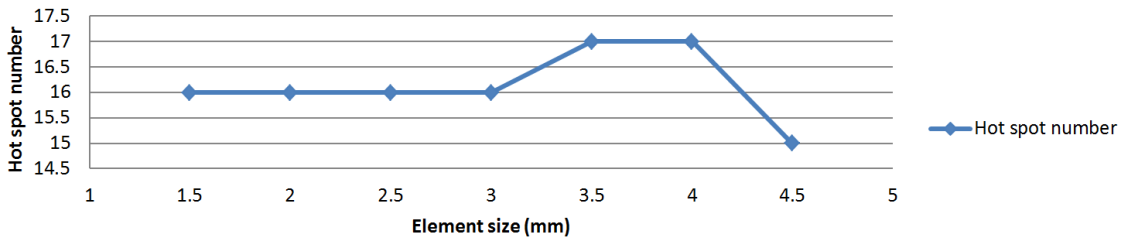

Figure 6.5 Mesh sensitivity study of the number of hot spot developed for the 2D in-plane model

Figure 6.6 shows the temperature distribution of the disc and pads at various time points. The hot spotting phenomenon was observed when high temperature areas were localised on the disc surface and the circumferential temperature distribution showed significantly non-uniform. The maximum temperature predicted was 534°C which was similar to the experimental measurement illustrated in Figure 4.17. Regarding the temperature distribution on the pads, the variations were not as great as the disc due to much lower thermal conductivity of the friction material which matched the numerical predictions of Zagrodzki *et al.* (2009).

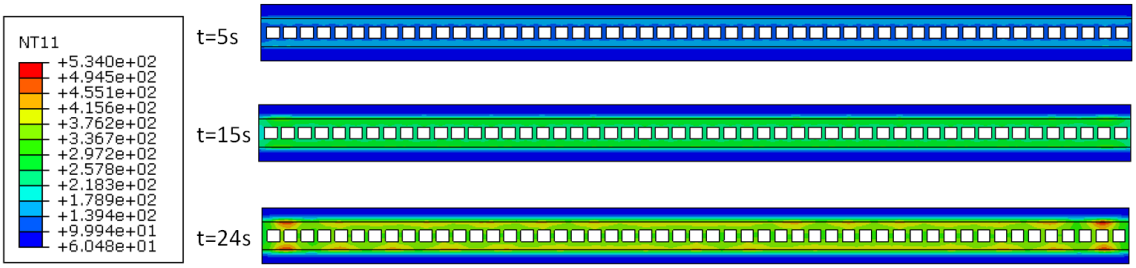

Figure 6.6 Temperature distribution contours varying with time for both disc and pads

The temperature distribution on the outboard disc surface at various time points is presented in Figure 6.7. Initially, the temperature distribution at 5s was relatively uniform but a 51st order small temperature variation (~10°C) was observed which was related to the number of the vents of the brake disc. This can be explained by the uneven thermal mass in the periodic structure of the ventilated layer. By 15s, 17 hot spots were developed and showed a ~50°C temperature circumferential variation where 17 was the number of the pins and also 1/3 of the 51 vents. At the end of simulation (24s), the maximum disc temperature reached ~500°C. 17 hot spots on each side of the disc had clearly developed in an anti-symmetric pattern which is the typical automotive hot spotting distribution mode according to the experimental investigation of Panier *et al.* (2005), Bryant, Fieldhouse and Talbot (2011) and analytical predictions of

Lee and Barber (1993). The maximum circumferential temperature variation was ~70 to 200°C. It should be noted that the maximum temperature variations were localised at the left and right sides of the model. This was caused by the nature of the beam simplification which did not allow the beam to expand circumferentially (cyclic boundaries only aligned the temperature and displacement on both sides, but no stress transfer). Therefore, the actual temperature variation of the hot spots was ~100°C on average except the extreme left and right hot spots. In addition, there was no circumferential migration of hot spots observed when comparing the hot spot positions at 15 and 24s due to the fact that shear stresses were not considered in this model; this was indicated as insignificant to the development of hot spots (Lee and Barber, 1993).

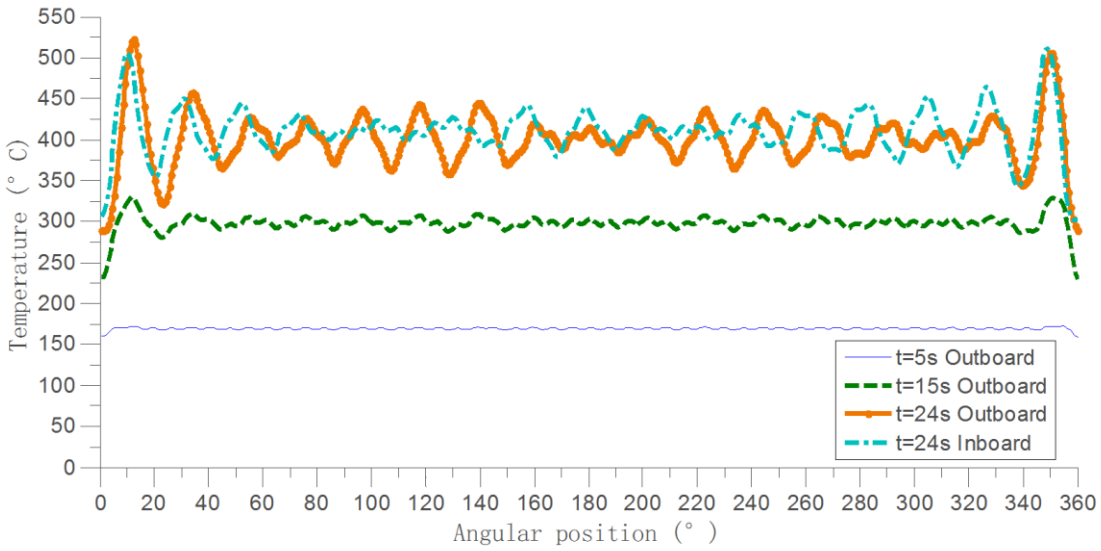

Figure 6.7 Temperature distribution of the outboard disc surface at different time increments

Figure 6.8 provides the temperature distribution across the disc, pad and back-plate thickness in the axial direction at 24s. Both the 'hot zone' on the hot spot and the 'cold zone' between hot spots were plotted. Regarding the 'hot zone', the disc temperature gradually decreased from the outboard surface (~450°C) to the centre of disc (~300°C) whereas the temperature rapidly decreased from the pad

contact surface (~460°C) to the back-plate (~80°C). The lower thermal gradient on the disc side compared to the pad side is because of the thermal conductivity of the disc was much greater than the pad. For the 'cold zone', both disc and pad sides showed lower thermal gradients. The temperature difference between the maximum temperature of the 'hot zone' and 'cold zone' was ~200°C. As a better conductor made of cast iron, the disc temperature was greater than the pad. In addition, it can be observed that the temperature at the disc and pad surface were not identical. This was caused by the thermal contact resistance which reduced the heat transfer and increased the temperature difference between the contact pairs.

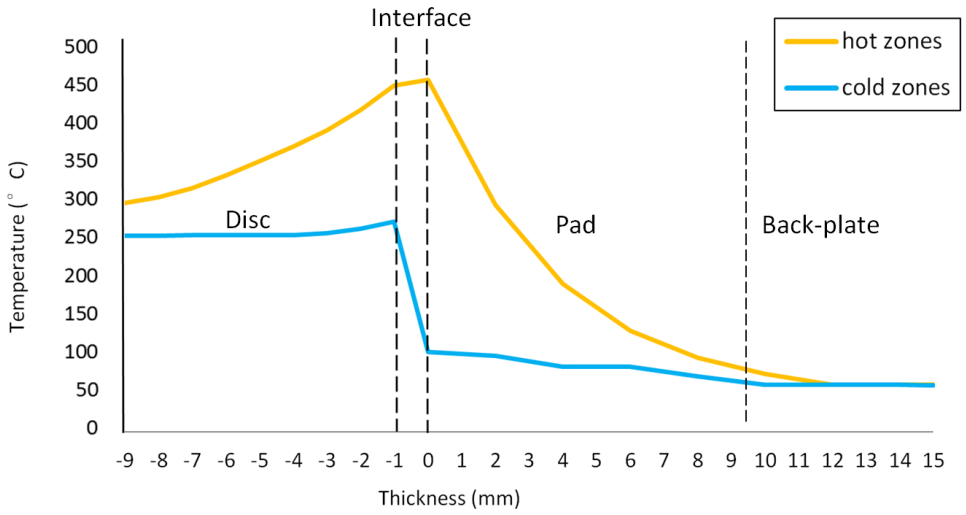

Figure 6.8 Temperature distribution across the disc and pad thickness at both 'hot zone' and 'cold zone' on and aside the hot spot at 24s

The interface thermal gradient (temperature difference between disc and pad) at the 'cold zone' was more considerable than the 'hot zone' as illustrated in Figure 6.8, which implied that the thermal contact resistance at the 'cold zone' was much greater than the 'hot zone'. Since the thermal contact resistance was defined as a function of clearance and pressure, it implied that the thermo-elastic deformation of the 'hot zone' reduced the clearance and increased the contact

pressure. In reality, it meant that the interface tribo-layer was compressed and the thermal contact resistance reduced for the ‘hot zone’. It implied that the uneven contact pressure cannot only cause uneven heating through frictional heat generation, but also through affecting the heat partition ratio between the disc and pad.

Moreover, the significant temperature variation on the pad between the hot and cold zones illustrated that the pad surface was more sensitive to the temperature variation due to its much lower thermal conductivity than brake disc.

Regarding the temperature growth, Figure 6.9 illustrates the nonlinear temperature evolutions of the maximum and minimum disc surface temperature as a function of time. It can be seen that the temperature at different locations showed uniform temperature in the initial 10s. Then, the temperature difference started to become significant (~50°C) at 15s and finally increased to ~200°C. It revealed that the results matched the TEI theory that the temperature field should grow exponentially during the hot spotting process (Barber, 1969).

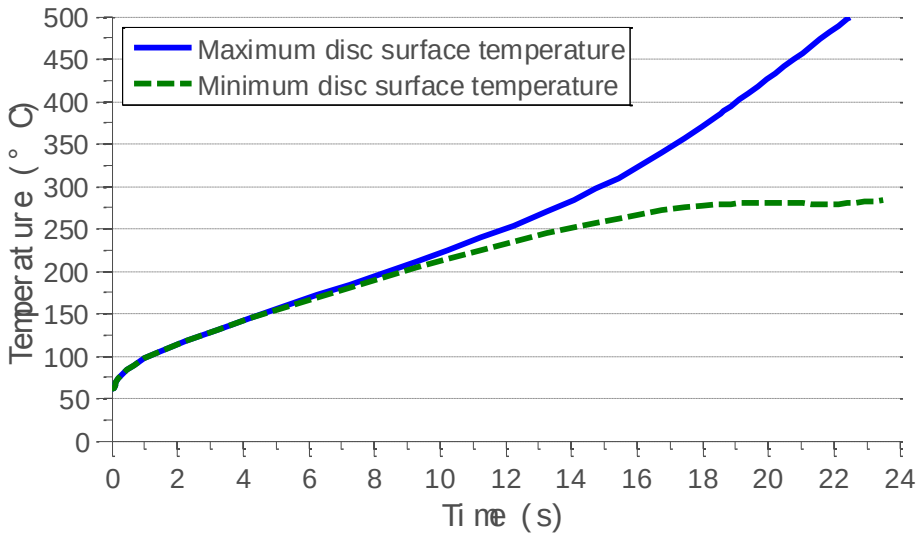

Figure 6.9 Temperature evolutions of the maximum and minimum disc surface temperature

Figure 6.10 provides a comparison of the disc outboard surface displacement at different time instances. At 24s, the 17th order distortions had developed significantly and the maximum height of the hot spots was within range between ~5 to 20μm which matched with the experimental results (see Figure 4.10).

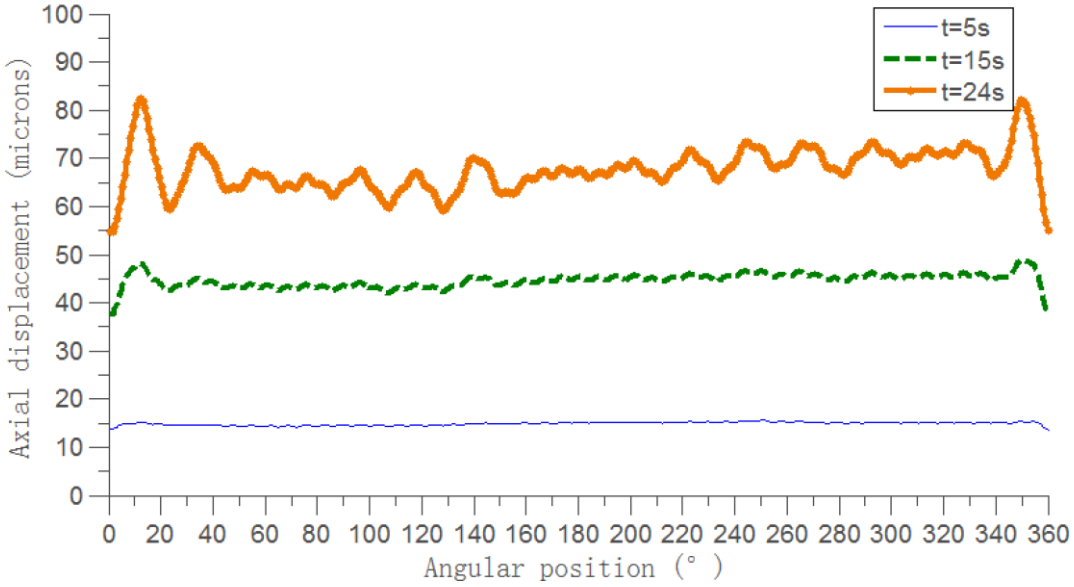

Figure 6.10 Disc outboard surface displacement distribution at specific time intervals

Furthermore, Figure 6.11 shows the disc stress fields at the end of braking event for both hot spotting model (top) and the same model with only mechanical loads and no heat generation (bottom). It illustrated that high stress zones were localised at the hot spot locations comparing with the temperature field (see Figure 6.6). The maximum magnitude of stress reached 487MPa which was much greater than the mechanical stress (8.79MPa). It revealed that the thermal stress dominated the stress field during the hot spotting process. Therefore, due to the excessive stress developed, the local surface thermal buckling may be triggered (see the discussions in section 6.2.4).

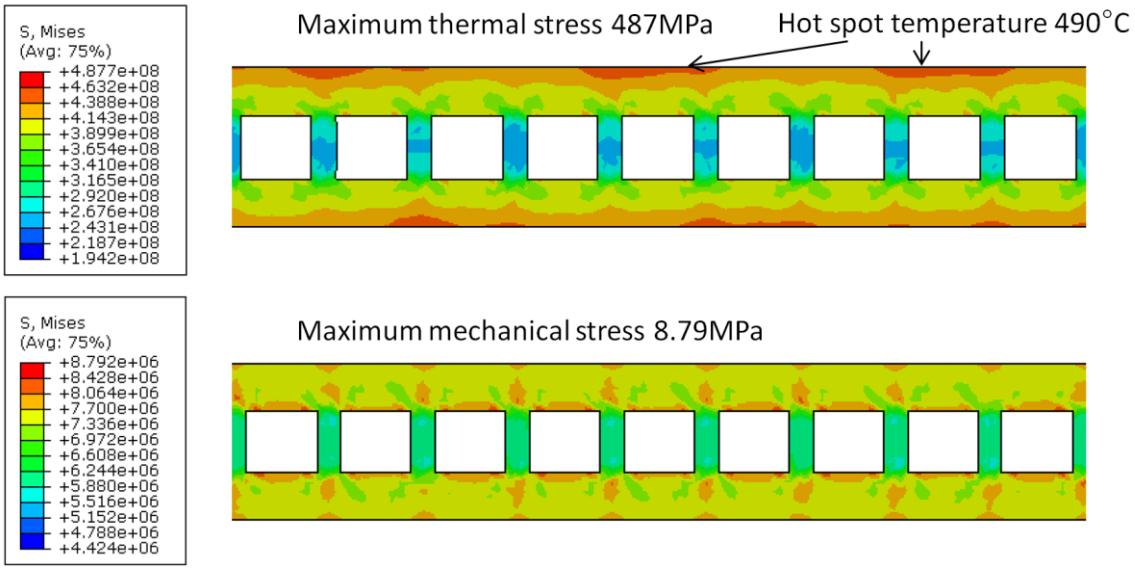

Figure 6.11 Thermal stress (top) and mechanical stress (bottom) at 24s for the in-plane axisymmetric disc

6.2.3 *Experimental validation*

Since the bulk disc deformation has not been considered in most of the previous published literature about hot spotting e.g. Lee and Barber (1993), Zagrodzki *et al.* (2009), and Jung *et al.* (2010), and the effects of bulk deformation on hot spotting have not been widely discussed, the validation of the numerical modelling has mainly focused on the aspects of disc temperature evolution, number of hot spot and height.

Regarding the temperature evolution, Figure 6.12 provides a comparison between the simulation and the experiment results of the maximum disc temperature. The experimental results were obtained by a rubbing thermocouple mounted at the mean rubbing radius, while the simulation results were picked form a node of the 'peak' of the hot spot. The results indicated good correlation between simulation and experiment.

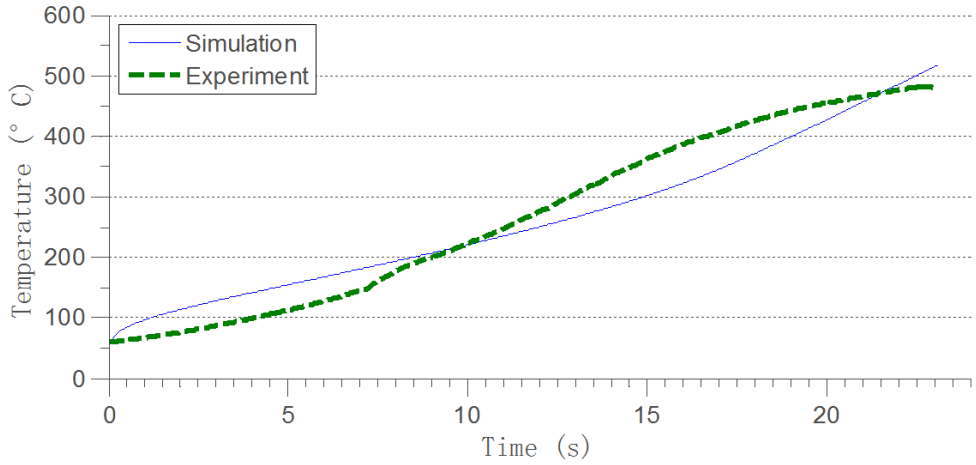

Figure 6.12 Maximum disc surface temperature comparison between simulation and experiment

Regarding the disc distortions, Figure 4.10 showed that the height of hot spots was ~10μm in the experimental test whereas the simulation results in Figure 6.10 predicted the heights within the range between ~5 to 25μm dependent on the bulk deformation of the disc. Therefore, it revealed that the in-plane model provided a good approximation of the hot spot heights. In addition, it was clear that both experiment and in-plane simulation developed 17 hot spots on each friction ring in an anti-symmetric pattern.

6.2.4 *Local thermal buckling*

Since considerable thermal stress was observed at the hot spotting zones according to Figure 6.11, it might be possible to trigger the thermal buckling in the small segments of the brake disc which results the initial wave-like disc deformation and the subsequent hot spots. Thus it was important to investigate if local surface buckling could occur, resulting in the 17th order disc waviness distortions.

The calculation method was mainly based the method of Bryant, Fieldhouse and

Talbot (2011) which regarded the disc as a 3D long beam (see Figure 6.13), and assumed the temperature rise of the disc was uniform and no radial expansion (i.e. purely circumferential expansion). Then the thermal buckling problem can be analysed by calculating the thermal stress within the beam due to the circumferential thermal expansion and the Euler's critical buckling force of a beam. Since the brake disc investigated was constrained by the 17 pins, the thermal buckling investigated was mainly focused on each periodical segment of the disc imposed by the mounting pins. Thus the 1st order thermal buckling of 1/17 length of the disc circumference was the main focus of this investigation.

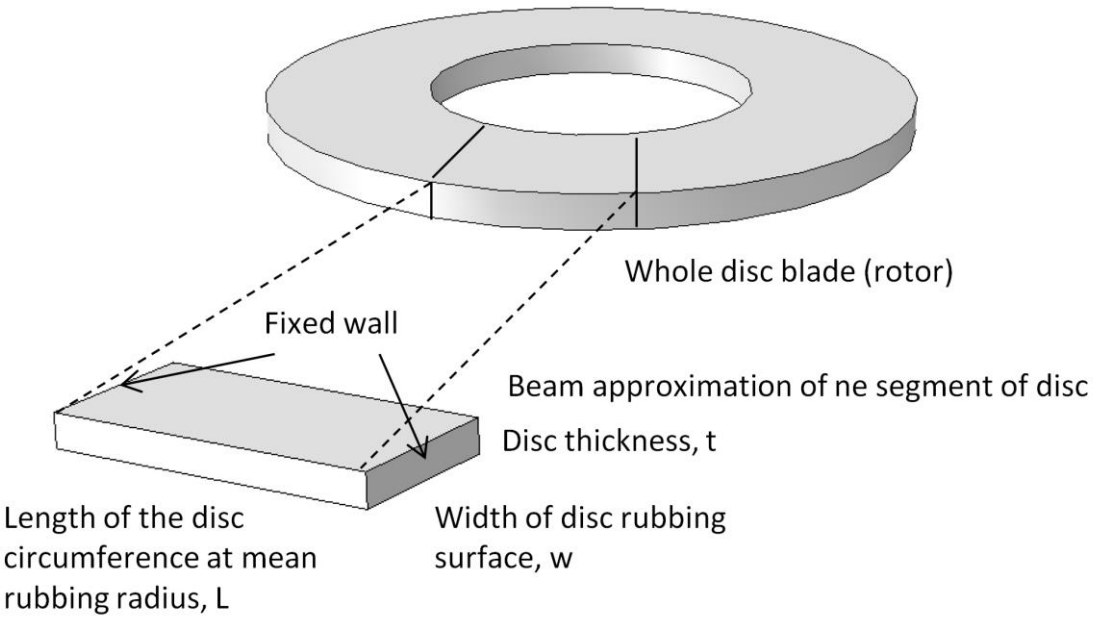

Figure 6.13 Disc blade segment represented as a beam constrained at its ends

$$Thermal\ Force = \alpha * \Delta T * E * w * t_h$$

Equation 6.3

$$Critical\ Buckling\ Force = \frac{\pi^2 E w t^3}{12 L_{disc}^2}$$

Equation 6.4

where α is the thermal expansion coefficient, ΔT is the increment of temperature, E is the elastic modulus, w, t_h, L_{disc}^2 are the width, thickness and

length respectively. The parameters for the thermal buckling calculations are provided in Table 6.2. Since the experimental and numerical results suggest that there were 17 hot spots developed at both disc surfaces. Therefore, to investigate if the disc could generate 17th order buckling, the length of the disc *L* was 1/17 of the circumference which gave 1.017/17=0.06m. In addition, since the disc was constructed by three layers comprising two solid friction rings and one ventilated layer, the disc was regarded as solid in the calculation. Though the heat transfer of the disc was highly transient and the temperature distribution was significantly nonlinear throughout the axial thickness, uniform temperature increase of the disc was assumed for the calculations at different temperature stages as shown in Table 6.2.

Table 6.2 Parameters for thermal buckling calculations

Disc data	Symbols	Value and Units
Temperature rise	*DT*	100 to 600°C
Disc length	*L*	1.017m
Width	*w*	0.073m
Thickness	*thick*	0.001 to 0.03m
Modulus	*E*	100GPa
Thermal expansion coefficient	α	10 10^{-6}/K
Specific heat capacity	*c*	480 J/kgK
Density	ρ	7200 kg/m^3

Figure 6.14 shows the ratio between thermal force and critical buckling force as a function of disc thickness and disc temperature for 1/17 length of the disc circumference. When the ratio of forces is greater than one, it means that the thermal force was greater than the critical buckling force and then the disc could show a 17th order waviness due to thermal buckling. On the contrary, when the ratio of the forces was lower than one, the thermal force was not sufficient to trigger buckling so the disc would be in the 'none thermal buckling zone' as shown in Figure 6.14. At a constant disc temperature, e.g. 200°C, the ratio of forces

increased with the reduction of disc thickness exponentially. The critical disc thickness to trigger the 17th order thermal buckling was ~5mm, which was much lower than the actual disc thickness (30mm). When the temperature increased to 600°C, the critical disc thickness was ~11mm, which was lower than the whole disc thickness but already greater than one solid layer of the brake disc (9mm). It implied that if the bulk disc temperature was greater than 500°C in average, the thermal force was sufficient to trigger the 17th order disc waviness for the solid layer of the disc if the effects of geometric constraints from the vents were ignored. It also illustrated that when the temperature increased, the maximum disc thickness to trigger the thermal buckling would increase.

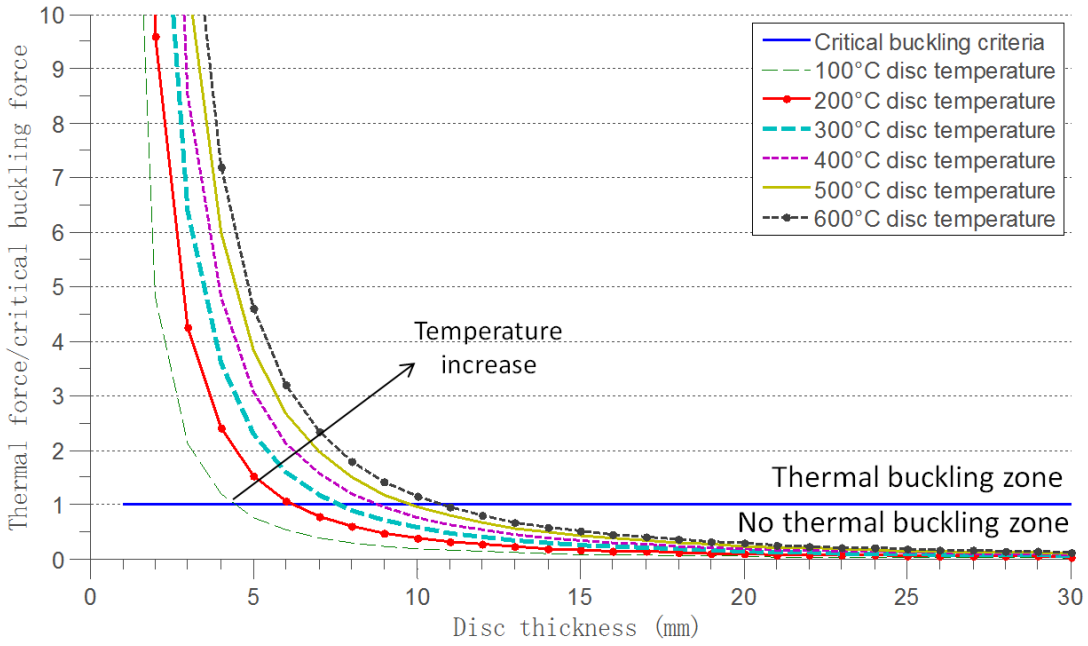

Figure 6.14 Critical thermal buckling criteria for various disc temperature and thickness for 1/17 disc circumference

It can be seen that when the disc thickness was thinner than 3mm at 200°C, the thermal force was ~9.5 times of the critical buckling force. Due to the fact that the ratio of the forces exponentially increased with the decrease in thickness and the axial temperature distribution was nonlinear, it can be presumed that a thin layer

of the local disc surface can be in an instable status due to the high circumferential local surface thermal force. According to the simulation results shows in Figure 6.8, high axial thermal gradients were developed and the maximum hot spots temperature reached ~500°C which implied that the high local surface thermal force was concentrated in a thin disc surface layer. In such a layer, the thermal force was much greater than the buckling force, and the surface may therefore be locally buckled. Then, the deflections due to such local surface buckling can facilitate the further thermal localisation due to uneven contact pressure and disc waviness.

It should be noted that since the disc surface was not actually a beam due to the fact that the surface was only free to be deflected in the out-of-plane direction of the disc, so the actual critical thermal buckling force in reality would be greater than the case of the solid beam. But as indicated by Yang (2015), even though the thermal buckling may not occur due to insufficient buckling force, the bending stiffness can be significantly reduced. Therefore, the thermal buckling can not only independently trigger disc waviness distortions, but can also couple with other mechanisms such as TEI and PWD to trigger higher order disc deformation and hot spotting.

6.3 2D In-plane clamp force and heating distribution models

In addition to the 2D in-plane hot spotting model using the axisymmetric pad assumption, several other in-plane models were established under different levels of simplifications. The intention was to investigate the mechanism of hot spotting by distinguishing and comparing the thermo-elastic deformation caused by sliding heating, thermal buckling and clamping force.

6.3.1 *Model setup*

Five models were performed in this section in order to investigate the effects of different levels of modelling simplifications on the hot spotting. Table 6.3 lists the models, main thermo-mechanical effects considered, heat generation method, and the subroutines used. Figure 6.15 shows the models assemblies and loading conditions.

Table 6.3 Models under different levels of simplification

ID	1		2		3		4		5	
Models	Uniform heat flux no pads		Uniform heat flux with asymmetric pads		Gauss distributed moving heat/load source with asymmetric pads		Pressure dependent heat source with asymmetric pads		Pressure dependent moving heat source with asymmetric pads	
Heat generation	-	-	-	-	-	-	Disc	Pad	Disc	Pad
Heat transfer	Disc	-	Disc	Pad	Disc	Pad	Disc	Pad	Disc	Pad
Thermal deformation	Disc	-	Disc	Pad	Disc	Pad	Disc	Pad	Disc	Pad
Contact pressure	-	-	Disc	Pad	Disc	Pad	Disc	Pad	Disc	Pad
Moving heat	NO		NO		YES		NO		YES	
Subroutines	-		-		DFLUX DLOAD		FRIC		FRIC	

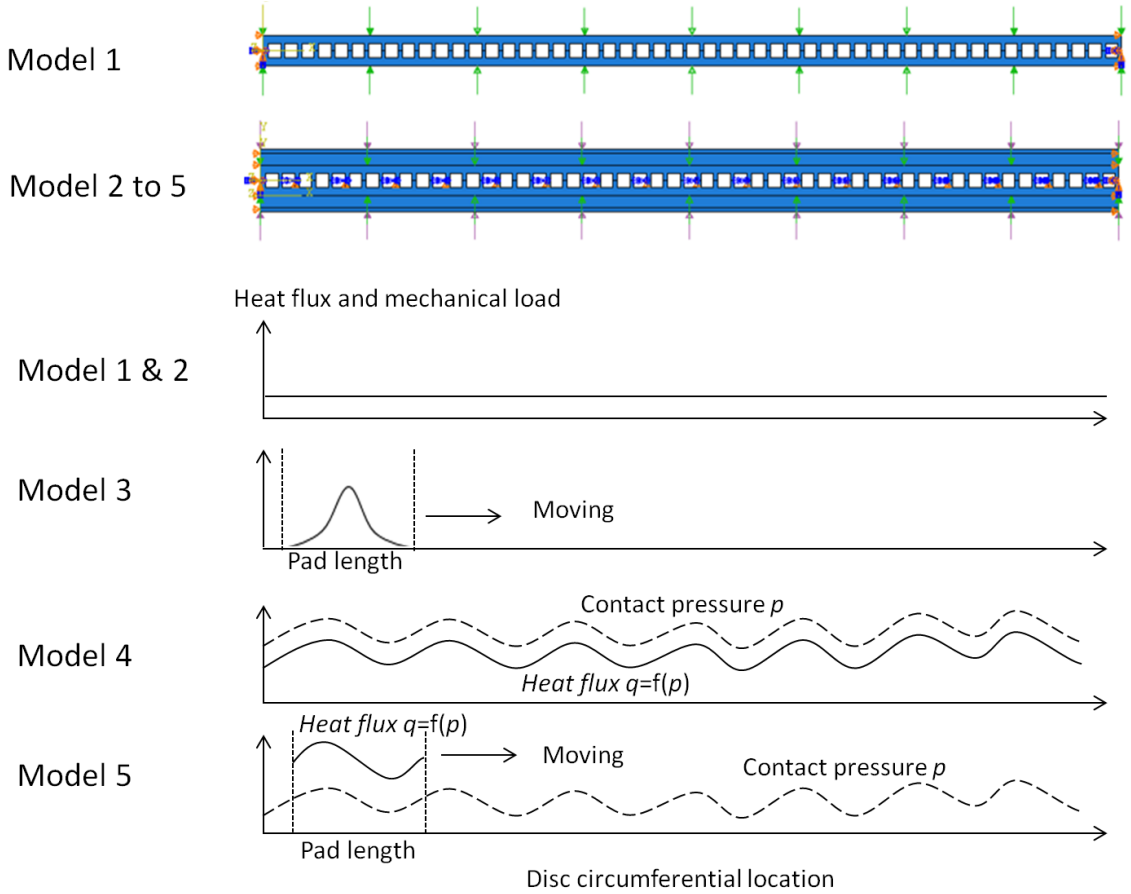

Figure 6.15 Assemblies and heat flux/load input distribution

In model 1, the brake disc was regarded as a 2D beam, but no pads were modelled (see Figure 6.15). The heat flux was directly applied into the disc outboard and inboard surfaces uniformly. The intention was to investigate if the hot spots can be generated with uniform heat flux input and without pad which was the common setup of brake disc heat transfer and deformation analysis in published literature. In addition, the heat partition ratio to the disc was set to 100% in order to compare with the models 2 to 5 in terms of the effects of thermal contact resistance.

In the model 2, the axisymmetric pads were modelled with (see Figure 6.15) uniform heat flux applied on the disc surface. The objective was to investigate if the existence of the pad can trigger the hot spotting due to the clamping force.

In the model 3, the heat flux was defined as a moving heat source (see Figure 6.15). The magnitude of the heat source was constant and the distribution was assumed to be obeyed the Gaussian distribution. The length of the heat source in the circumferential direction was identical to the pad length in order to simulate the effects of periodic moving heat source contact zones. The moving heat source and the heat flux distribution were defined using the user subroutine DFLUX. In addition, the moving load source was applied in same method using DLOAD. The objective was to investigate the effects of moving heat source and load on the development of hot spots.

Model 4 was identical to the model introduced in section 6.2 which modelled the axisymmetric pad and defined the heat generation as a contact pressure dependent function using the user subroutine FRIC. The heat source was generated on the disc surface simultaneously but not uniformly. Since the hot spotting was successfully observed in this model, the method was set to be a benchmark for comparison with the other models.

In the model 5, the magnitude of the moving heat source in model 3 was defined as a function of contact pressure which made the heat generation mode similar to the realistic case. The objective was to investigate the effects of the sliding heat source and load by comparing with model 4.

6.3.2 *Results*

Figure 6.16 shows a comparison of the models in terms of outboard disc surface temperature distributions. In general, the average temperature of the five models were mainly in the range between ~350 to 420°C. By comparing model 1 and model 2, the results of with and without pad illustrated that the overall temperature decreased due to the heat partition of the pad. In model 1, the heat was assumed

to be 100% into the disc but in model 2 the heat partition ratio was determined by the thermal contact resistance. It revealed that as a heat conductor, the modelling of pad can provide more realistic heat partition. In addition, in all models, especially model 1 to 3, the small disc temperature ripples (~51order) were observed which meant that the uneven temperature distribution due to disc geometry (ventilated disc) can be predicted by applying constant heat flux. However, hot spotting was observed in models 4 and 5 which implied that the contact pressure dependent heat flux was significant in the modelling of hot spotting. This meant that the uneven deformation (51^{st} order) could be caused by the uneven disc structure under uniform heat flux. However, the hot spots (17^{th} order) can only be developed (in this study) when considering the uneven heat flux caused by the uneven deformation and subsequent uneven contact pressure. Therefore, it illustrated that the hot spotting development was attributed to the thermo-elastic cause-effect chain suggested by Steffen, 2006, and the disconnection of this chain in the simulation will cause the failure in reproducing the hot spotting process. Furthermore, the results were similar between 2 and 3 (average temperature), and 4 and 5 (number of hot spot and thermal gradients), which revealed that the actual modelling of the moving heat source and load source was insignificant on the hot spotting simulation using the axisymmetric pad model. It also verified the observation in section 5.2.4 that the periodic heating can be replaced by continuous heating in order to save computing time.

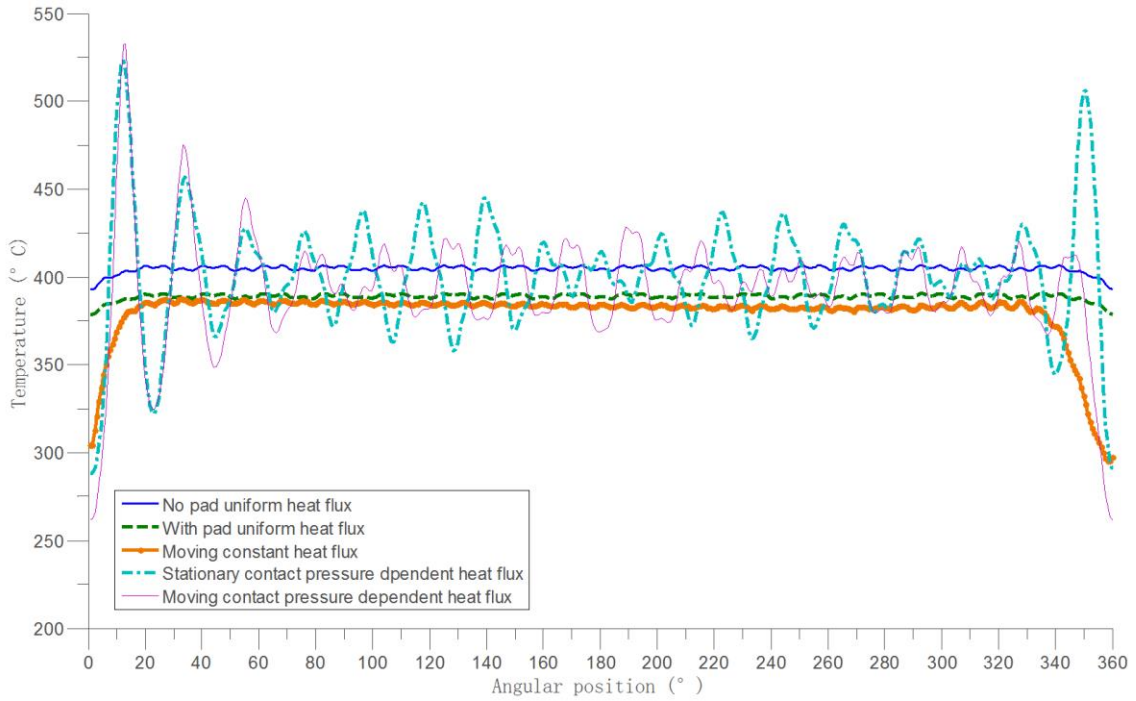

Figure 6.16 Temperature distribution comparison for the 2D in-plane models under different levels of simplifications

Table 6.4 provides a comparison of the DOF and computing time for the models. It can be seen that after considering the pad in the model, the computing time increased by ~5 times but the DOF was only increased to ~2.5 times in model 2. It illustrated that the computing efficiency decreased due to the extra elements on the pads and the computing of the contact interface. For models 2 to 4, the DOF were identical, but the computing time for the moving heat source models (3 and 5) was much longer than models 2 and 4. It implied that the moving heat source model was time consuming because of the much smaller time step size required in order to reproduce the effects of the moving source in each disc revolution. In addition, comparing models 2 with 4 and 3 with 5, it was found that the implementation of user subroutines increased the computing time by ~3 times.

Table 6.4 Computing time efficiency comparisons

Model ID	Moving heat source	DOF	Computing time
1	No	19158	1min 15s
2	No	47334	5min 58s
3	Yes	47334	12h 21min
4	No	47334	14min 54s
5	Yes	47334	36h 10min

Therefore, the results suggested that the implementation of contact pressure dependent heat generation was significant in the modelling of hot spotting. Since the hot spots were only developed in models 4 and 5, and considering the computing efficiency, model 4 was the most suitable model in this investigation.

6.4 2D In-plane axisymmetric pad model parametric studies

The intention of the parametric study was to investigate the effects of the important factors that affected hot spotting according to the literature review and research objectives. The investigated parameters included friction material properties, comparison between solid and ventilated disc, effects of brake condition (speed and load), cooling distribution, constraints from the pins, and influence of pad length.

6.4.1 *Effects of material properties*

The material properties of three important parts of brake system were investigated: back-plate, brake disc, and friction material. Initially, the thermal properties of the back-plates were not considered in this study, since the brake pad's thermal conductivity was relatively smaller than the disc as indicated by Barber (1969), Lee and Barber (1993), and Zagrodzki *et al.* (2009). Thus only the effect of Young's modulus was considered for the back-plate, which was presumed to influence the mechanical contact pressure distribution. Then the effect of thermal properties of disc and pad (friction material) on maximum hot spot temperature was studied.

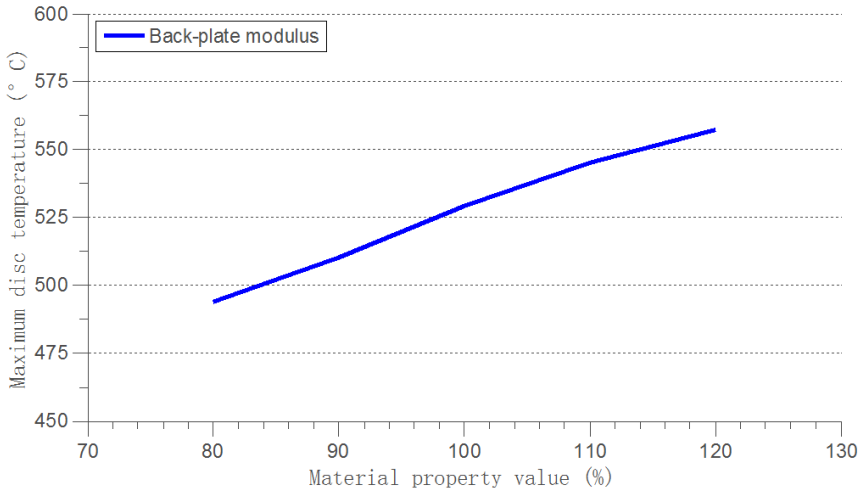

Figure 6.17 Effects of back-plate Young's modulus on maximum disc temperature

Figure 6.17 shows the effects of back-plate Young's modulus on the hot spot maximum temperature distribution. The material properties values ranged from 80% to 120% of the standard value provided by Table 6.1. The results illustrated that increasing the back-plate Young's modulus increased the maximum hot spot temperature. This effect can be explained by the fact that the stiffer back-plate restricts the thermal deformation of the friction material. This will therefore creatre higher thermal stress at the contact interface as the friction material is prevented from deforming with the disc; thus greater heat generation results at the hot spot locations,

Regarding the effects of brake disc material properties, the thermal conductivity (K), Young's modulus (E), thermal expansion coefficient (α), specific heat capacity (C) and the interactions between the properties were investigated using a full factorial design of experiment (DOE) method. Parametric studies of the four material properties were performed at 100% and ±20% levels of the standard material properties listed in Table 6.1, resulting 3^4=81 models. The results are presented in Figure 6.18, which shows the interactions between the material properties and the effect on the hot spot maximum temperature. All plots used same scale between 400 to 1000°C.

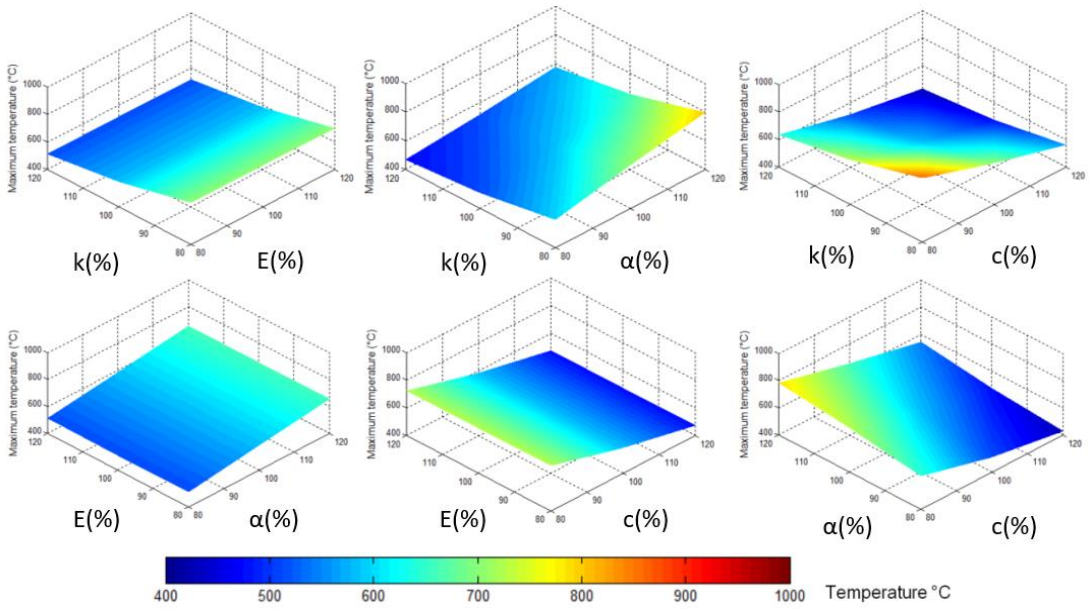

Figure 6.18 3D surface plots of the effects of disc material properties on maximum hot spot temperature

In terms of the main effects of the material properties, the plots show that the Young's modulus of the disc had insignificant influence on the temperature as there was no 'skew' in any of the surface plots. Both thermal conductivity and heat capacity had an inverse effect on temperature. The temperature was similarly sensitive to the variation of heat capacity and conductivity according to the top-right plot (K vs. C). In addition, the increase of the thermal expansion coefficient showed positive impact on the temperature. When increasing the coefficient of thermal expansion, the thermal deformations of the hot regions on the disc surface will be further enlarged and therefore increase the local heat generation accelerating the hot spotting process. The reduction of heat capacity will increase the bulk disc temperature. Therefore, when a thermal localisation occurrs, the local hot spot regions will be more sensitive to the change of frictional heat generated at the interface than the standard heat capacity disc. In addition, increasing the disc and back-plate modulii will both faciliate the thermal localisation process by increasing the contact pressure of the hot regions experiencing larger thermal deformation (thermal strain), but at the same time

increase the critial buckling force and therefore reduce the thermal localisations.

In the aspects of interactions between two factors, Figure 6.18 illustrates that changing the magnitude of the disc Young's modulus did not affect the results of the other material properties which means there was no interaction between disc modulus with other material properties tested. The thermal conductivity (K) and thermal expansion coefficient (α) plot shows that with the increasing of conductivity, the positive effects of the thermal expansion coefficient (α) on hot spot temperature decreased. Increasing the thermal expansion coefficient (α) increased the negative slope of thermal conductivity (K). In addition, the negative effects of thermal conductivity (K) on temperature can be reduced by increasing the heat capacity (C) and vice versa. Moreover, increasing thermal expansion coefficient (α) increased the negative slope of heat capacity (C) on temperautre. Therefore, it can be observed that the interactions between thermal conductivity (K) and thermal expansion coefficient (α), or Young's modulus (E) and heat capacity (C) had negative effects on the maximum hot spot temperature but the thermal conductivity (K) and heat capacity (C) interaction was positive. It revealed that in order to reduce the hot spot temperature, increase thermal conductivity (K) and reduce thermal expansion coefficient (α), decrease thermal expansion coefficient (α) and increase heat capacity (C) or both increase thermal conductivity (K) and heat capacity (C) are suggested. For realistic materials, Table 6.5 provides the data of three commonly used brake disc materials properties. According to the results of Figure 6.18, increasing heat capacity (by either increasing density or specific heat capacity), thermal conductivity, and/or decreasing thermal expansion coefficient of the brake disc was recommended. Therefore, the ratio of $\rho^* c^* k/\alpha$ shown in Table 6.5 was used as an indicator of the ability of disc materials to reduce the maximum hot spot temperature. It can be seen that the Carbon-Carbon composite has the greatest $\rho^* c^* k/\alpha$ value among the four materials which implied a better performance in minimizing the

hot spot temperature. However, the low temperature brake performance and the expensive cost of Carbon-Carbon composite was main limitations for its application in automotive Barton (2014).

Table 6.5 Disc material properties comparison for minimizing maximum hot spot temperature

Material properties	**High carbon cast iron**	**Generic 20% SiC-reinforced Al MMC**	**Carbon-reinforced SiC CMC**	**Carbon-Carbon composite**
Thermal conductivity, k (W/mK)	50	180	10	40-150
Density, ρ (kg/m^3)	7150	2800	2300	1750
Specific heat capacity, c (J/kgK)	438	800	1000	1000
Heat capacity, $\rho^* c$ (kJ/m^{3}K)	3132	180	2300	1750
Thermal expansion, α (10^{-6}/K)	10	17.5	4	0.7
Indicator $\rho^* c^* k/\alpha$	15660	23040	5750	100000-375000

Source of data: Barton (2014)

Similarly, Figure 6.19 demonstrates the main effects and interactions between the material properties of the brake pad on maximum hot spot temperature. Regarding the main effects, it can be seen that the hot spot temperature was positively affected by an increase of the pad thermal expansion coefficient, Young's modulus and thermal conductivity. The modulus was the most sensitive property, a 10% increase of the pad modulus can increase the hot spot maximum temperature by 50°C. As a common sense, increasing thermal conductivity can reduce the thermal gradients in the friction material and therefore reduce the hot spots temperature. However, as the thermal conductivity was low, this had a relatively samll effect on the hot spot temperature. Similar to the effects of disc

specific heat capacity, the decreasing of pad specific heat capacity also showed an increase in hot spot temperature. Futhermore, by comparing the effects of the disc (insignificant effect) and pad (significant effect) moduli on hot spot temperature, the different thermal localisation mechanisms of disc and pad can be revealed. For the brake disc, the increase of the elastic modulus results in a greater critical buckling stress (i.e. more difficult to be thermally buckled) (see Equation 6.4) and increase in the uneven contact pressure distribution (see Equation 5.23) which appeared cancel to each other out. However, the positive effect of pad modulus on temperature implied that the thermal localisation of the pad was mainly caused by the effects of uneven contact pressure rather than thermal buckling.

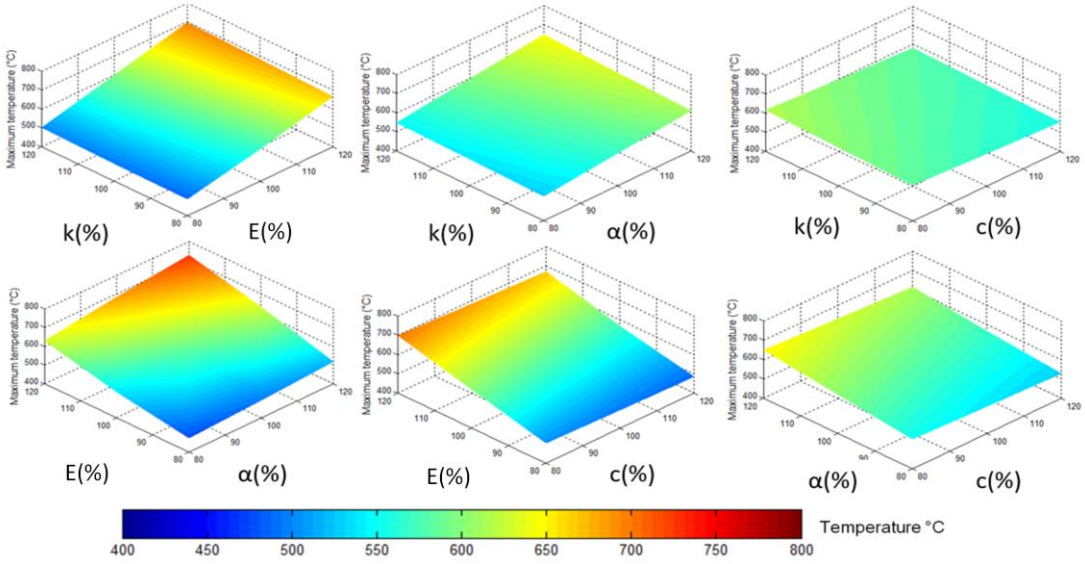

Figure 6.19 3D surface plots of the effects of pad material properties on maximum hot spot temperature

6.4.2 *Effects of periodic disc geometry: vents*

To investigate the effects of the disc vents on hot spotting and bulk deformation in ventilated disc, a comparison between a solid disc and a ventilated disc was performed. According to Limpert (1975), the equivalent thickness of a solid disc to achieve similar thermal effects should be about three times that of the individual

friction ring thickness (~9mm in this case), therefore, a 27mm thick solid disc was modelled under the same assumptions and setup as the ventilated disc model. The temperature results at the end of braking event (24s) are presented plotted in Figure 6.20. It was clear that both the solid and ventilated disc showed an anti-symmetric hot spot distribution, but there were 16 hot spots in the solid disc model compared to 17 in the ventilated disc model. It revealed that the periodic vent structure of the ventilated disc affected the distribution of hot spots. In addition, the 2nd order disc deformation (run-out) developed for the solid disc whereas the ventilated disc showed no bulk disc deformation (run-out). It implied that more circumferential thermal stress was generated in the solid disc resulting in a 2nd order disc thermal deformation.

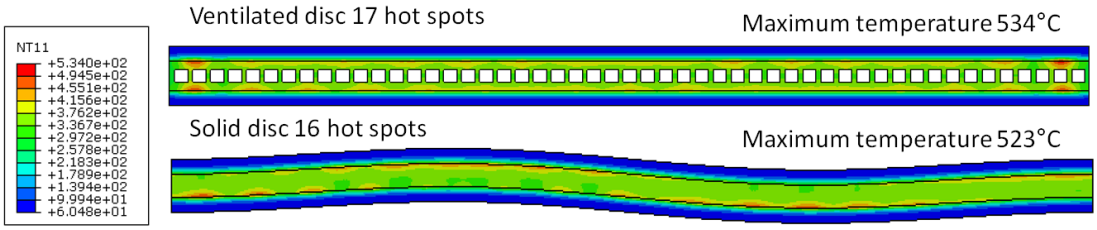

Figure 6.20 Comparison of the temperature distribution for ventilated and solid discs at 24s

Figure 6.21 shows the hot spot distribution and magnitude of temperature on the outboard disc surface for both ventilated and solid discs model. Again, it can be observed that 17 hot spots developed in the ventilated disc compared to 16 in the solid disc. The graph also shows that maximum and average temperature were similar for both models. Regarding the thermal gradients, both models showed similar temperature variations of approximately 100°C.

In addition, to investigate the effects of the design parameters of vent structure, a four parameter DOE with 3 levels were performed. The design parameters as shown in Figure 6.22 include friction ring thickness (*F*, 9mm by default), ventilated layer thickness or vent height (*V*, 12mm by default), ratio of vane (*a*) over vent (*b*) in terms of circumferential thickness (*R*=*a*/*b*, 0.25 by default), and the total number of vents.

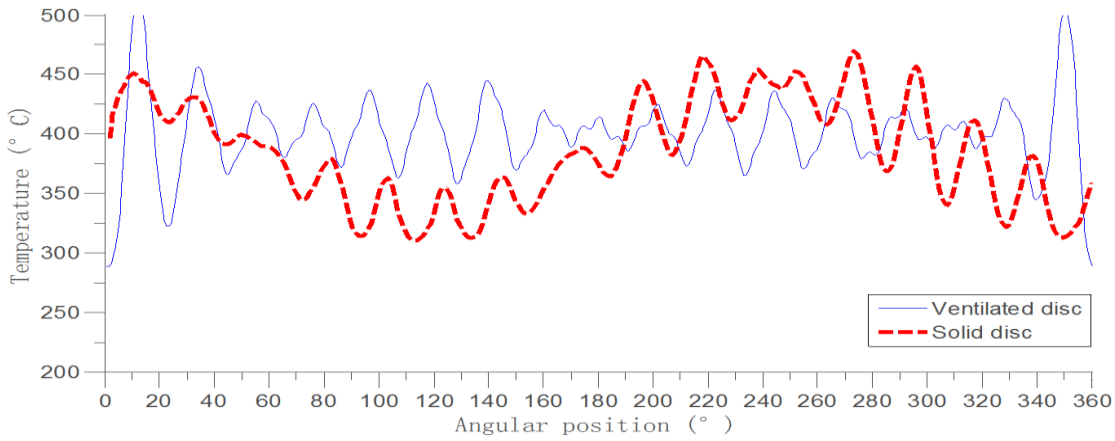

Figure 6.21 For comparison of outboard disc maximum surface temperature for ventilated and solid discs at 24s in simulation

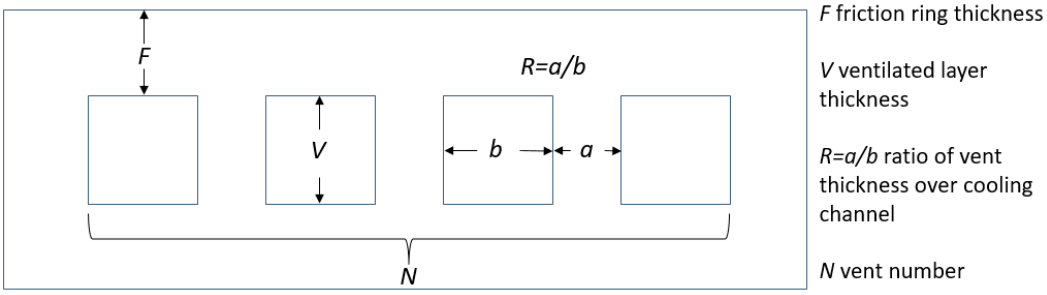

Figure 6.22 Design parameters of the vent structure

The results of the DOE study were present by Figure 6.23 and Figure 6.24 in aspects of maximum hot spots temperature and hot spots circumferential temperature variation (maximum thermal gradients). The former mainly illustrates that increasing the friction ring thickness (*F*), vane height (*V*) and number of vents (*N*) can reduce the maximum hot spot temperature. The effect of the ratio between vane and vent (*R*) was shown as insignificant in both terms of main effects and interactions with other parameters in this study. Thus, a thicker brake disc especially with thicker solid layers and more vents can lower the maximum disc temperature as suggested by the simulation results. In addition, Figure 6.24 indicated that to reduce the hot spot thermal gradient, increase the brake disc friction ring thickness (F) is the most effective design.

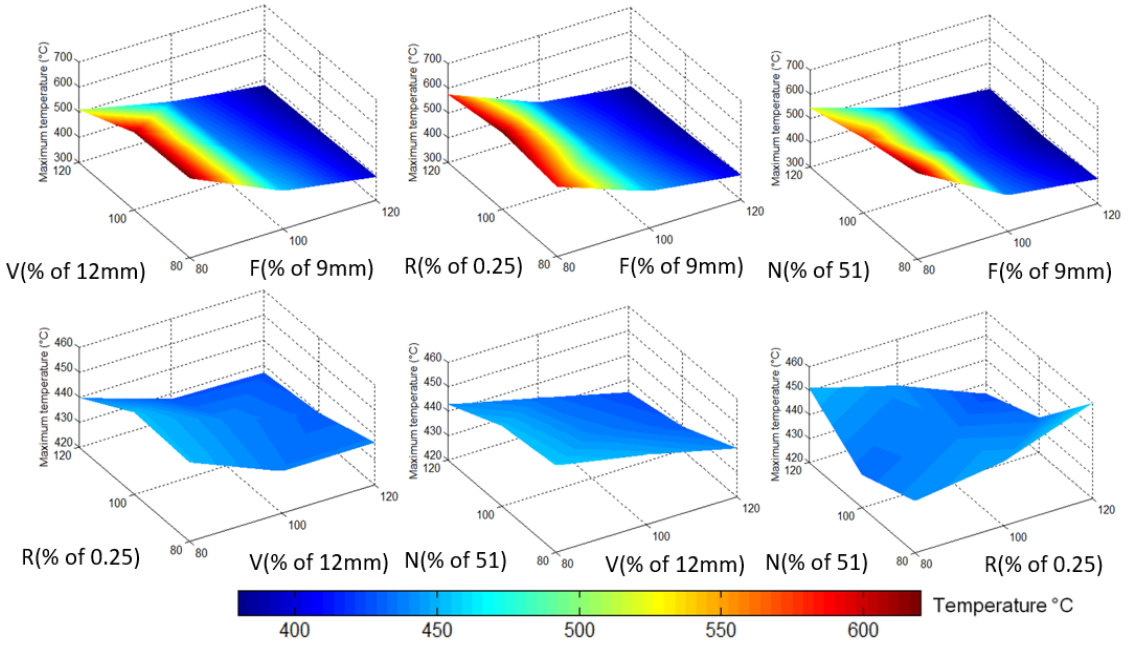

Figure 6.23 Effects of vent structure on maximum hot spot temperature

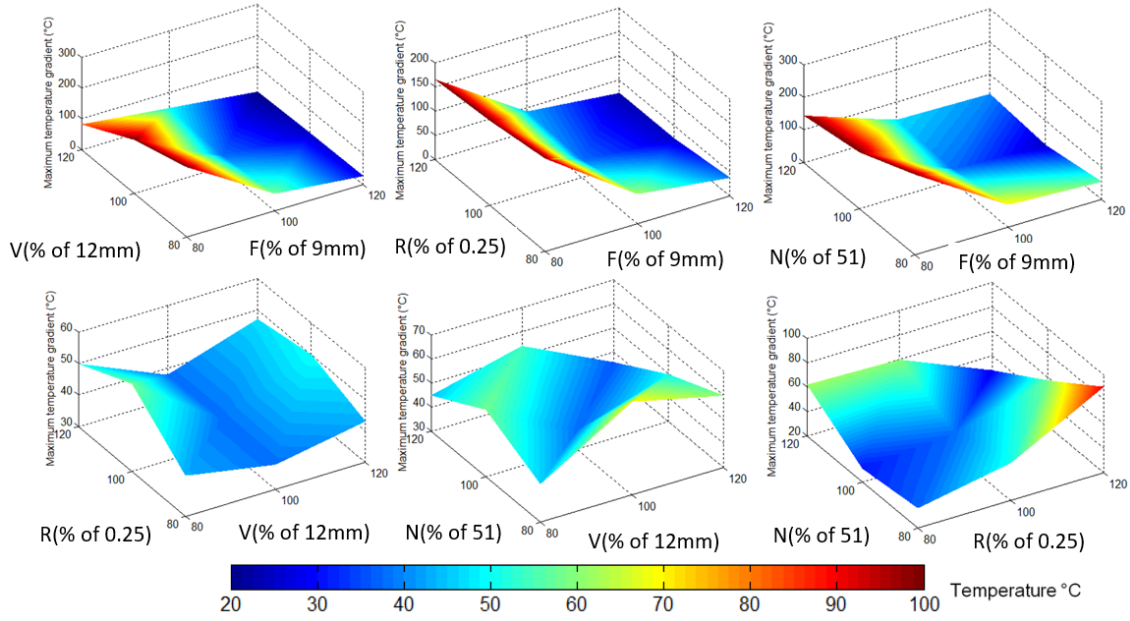

Figure 6.24 Effects of vent structure on hot spot temperature variation along disc circumference

6.4.3 *Effects of periodic disc geometry: pins*

As previously illustrated by Figure 4.5, the disc investigated was a two piece pin mounted disc. Since the experimental results suggest that the number of hot spots was correlated to the number of pins, the effects of pins on hot spotting was

investigated by using the 2D in-plane model. There are two possible mechanisms via which the pins could affect the hot spotting; one is providing extra thermal mass facilitating the uneven temperature distribution; the other is that the pins provided periodic constraints to the disc which influenced the uneven disc deformation. Due to the limitations of the 2D model, the former cannot be performed and will be investigated using the 3D model (see chapter7). The latter was performed by including 17 equispaced constraints as shown in Figure 6.1. It should be noted that the actual pins can provide more flexibility in reality, but due to the nature of 2D modelling, the constraints were rigid.

The brake system temperature distribution for both ventilated and solid discs is shown in Figure 6.25. It was clear that there was no significant variation of the temperature distribution for the ventilated disc with and without pins. However, the solid disc temperature decreased by ~50°C after the pin constraints were included and its 2nd order disc run-out was significantly reduced. This implied that due to the constraints of the pins, the 2nd order thermal deformation was removed thus removing the 2nd order temperature variation.

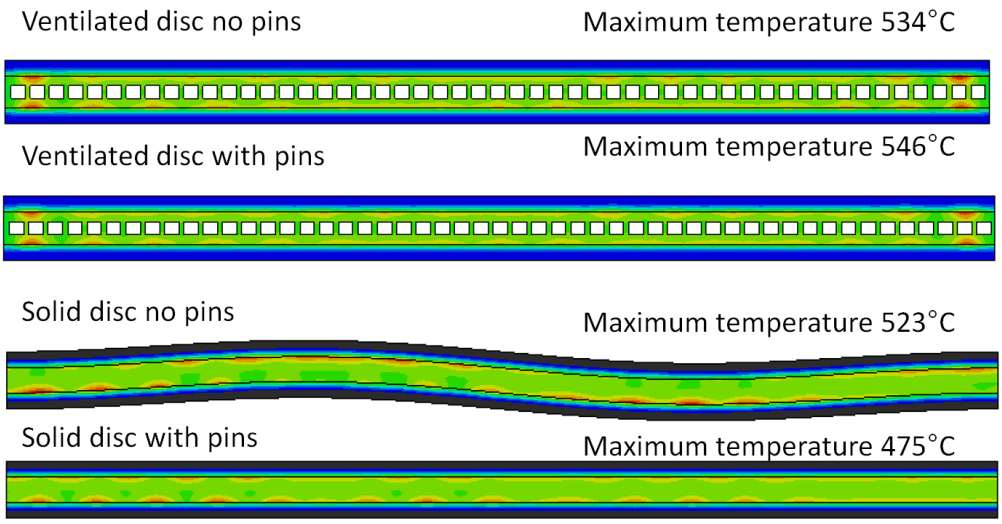

Figure 6.25 Temperature distribution of the brake system for both ventilated and solid discs with and without pins

Figure 6.26 provides a power spectral analysis of the disc temperature variation on its outboard surface at 24s. Lower order temperature variation was only evident for the solid disc without pins (2nd order). It indicated that the lower order deformation can affected the temperature distribution at same frequency. For the higher order temperature variations, the ventilated disc shows significant 17th order hot spots as observed form the experiments carried out in chapter 4. It can be seen that the hot spot temperature reduced at 17th order with the pins. Meanwhile, the solid discs generated 16th order hot spots with and without pins. It shows that even under constraints of 17 pins, the solid disc still developed 16 hot spots. Therefore, the effects of vents were more significant than the pins in terms of determining the number of hot spot developed for both solid and ventilated disc. It also revealed that the 2nd order run-out did not affect the magnitude of hot spot thermal gradient significantly.

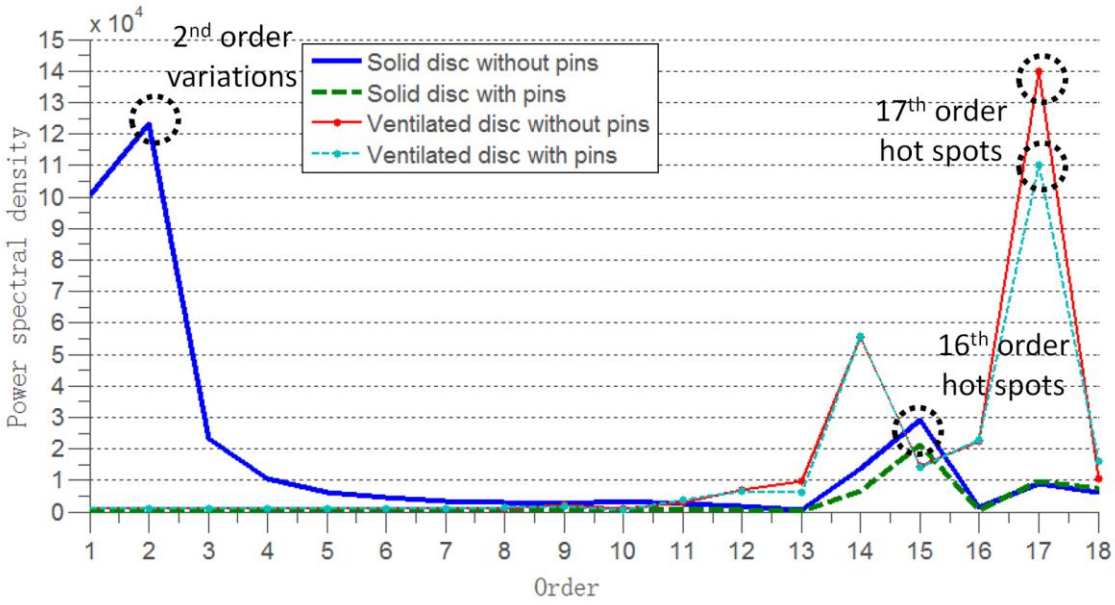

Figure 6.26 Power spectral density distribution of the disc temperature distribution on the outboard surface for both solid and ventilated disc with and without pins

Furthermore, Figure 6.27 provided the results of power spectral analysis of the disc deformation on the outboard surfaces. In terms of lower order deformation, both solid disc models show significant 2nd order run-out. The ventilated disc

model without pins developed a relatively insignificant 1st order run-out. It implied that both vents and pins can contribute the reduction of bulk deformation of discs. Regarding the higher order deformation, both ventilated discs shows similar 17th order hot spots. Both solid discs generated 16th order hot spots but the pins reduced its magnitude. It should be noted that the displacement of solid disc hot spots were greater than the ventilated disc hot spots, whilst the temperature were on the contrary. This difference between temperature and displacement field revealed that the deformation of the discs was not entirely a result of the thermal localisations; it was evident that the pin constraints also played an important role.

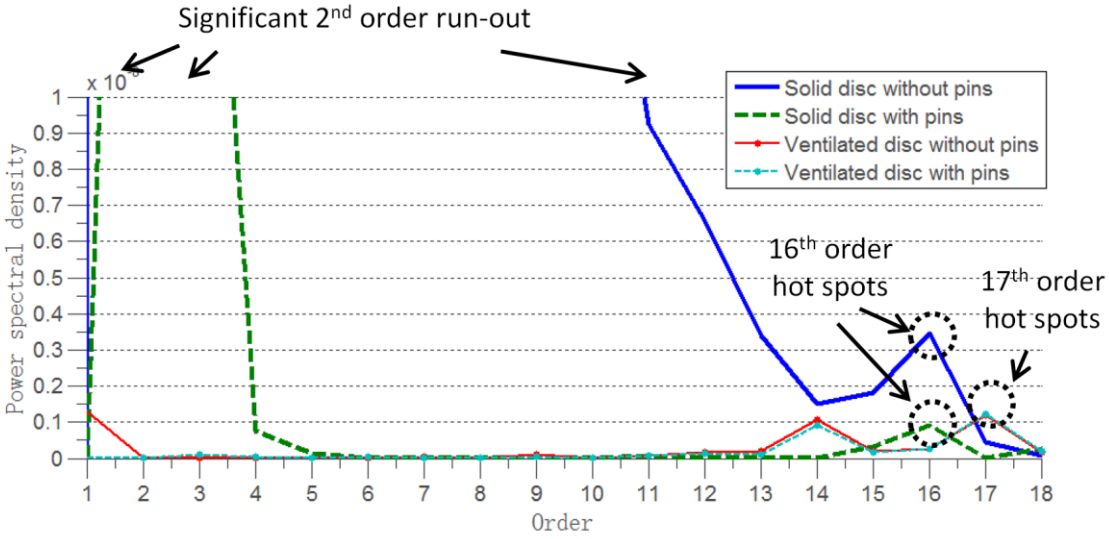

Figure 6.27 Power spectral density distribution of the disc deformation distribution on the outboard surface for both solid and ventilated disc with and without pins

6.4.4 *Effects of brake condition*

An important argument in the hot spotting research was about the trigger condition of hot spots: is hot spotting triggered by the critical speed or input energy? In order to provide better understanding of this research question, parametric studies of different speeds and loads were performed. 25 simulations were carried out and the speed and load (the uniform actuation pressure applied on back-plates) were varied from 50% to 150% of the standard model presented

in section 6.2. The braking duration of all simulations remained at 24s which allowed calculation and analysis of the effect of input energy.

Figure 6.28 provides a 3D plot of the maximum hot spot temperature as a function of speed and load for both solid and ventilated discs. It can be seen that the maximum temperature reached over ~1000°C at the 150% speed and 150% load in both case. In actual brake system, it was impossible to reach such a high temperature due to the effects of wear, plasticity and thermal fade which terminated the exponential thermos-elastic growth of hot spot. But the FE results based on thermos-elastic deformation still revealed the trend of temperature growth during hot spotting against speed and load. In both solid and ventilated cases, the temperature of both increased non-linearly with the increase of speed and load, which implied that the maximum hot spot temperature was highly dependent on the energy input level. From the 3D plot, it can also be observed that the effect of speed on temperature growth was greater than load due to the fact that there is an angle between the same energy level line (diagnose line) and the same temperature level line (distinguished by color) as illustrated in Figure 6.28. It shows that at same energy level, the temperature was not equally distributed. Since both speed and load contributed to the input energy, it revealed that the maximum temperature of the hot spots was more sensitive to speed, and decreasing the ratio between speed and load can facilitate the hot spot temperature reduction. Comparing between the solid and ventilated discs, similar temperature contour trends were found.

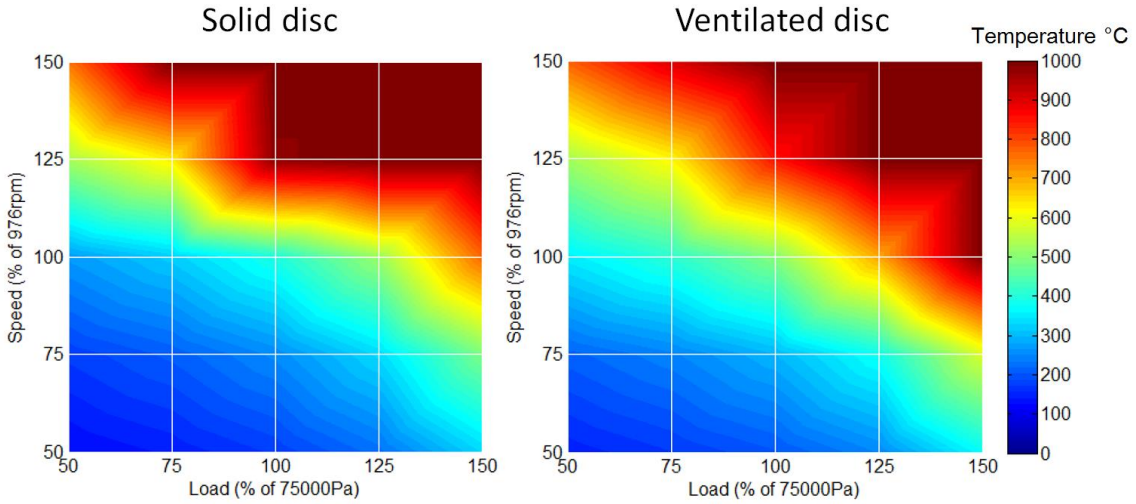

Figure 6.28 Maximum hot spot temperature of the solid and ventilated discs at various speed and load combinations

Regarding the ventilated disc number of hot spot, Figure 6.29 (right) shows that there are three possible hot spots distribution modes in the simulated ventilated disc: no hot spot developed, 17 hot spots developed at both sides of the disc and distributed anti-symmetrically, and 16 hot spots anti-symmetrically distributed at both sides of the disc. It clearly shows that the number of hot spots was significantly affected by the speed but the effects of load were insignificant except that only when the load reached over 130%, the number of hot spots changed both with speed and load (i.e. energy level). Moreover, Figure 6.29 (left) illustrates that the number of hot spots for the solid disc was also significantly affected by the speed. Since there was no interference from the vents, the results of the solid disc showed a more sensitive change in the number of hot spots. There were four distribution modes observed: no hot spots, 16, 15 and 11 anti-symmetrically distributed hot spots on both disc sides. The speed also affected the mode shape predominantly, but the anti-node distributed contour of number of hot spots shows a correlation with the increasing energy level. It implied that the energy level also affected the number of hot spots.

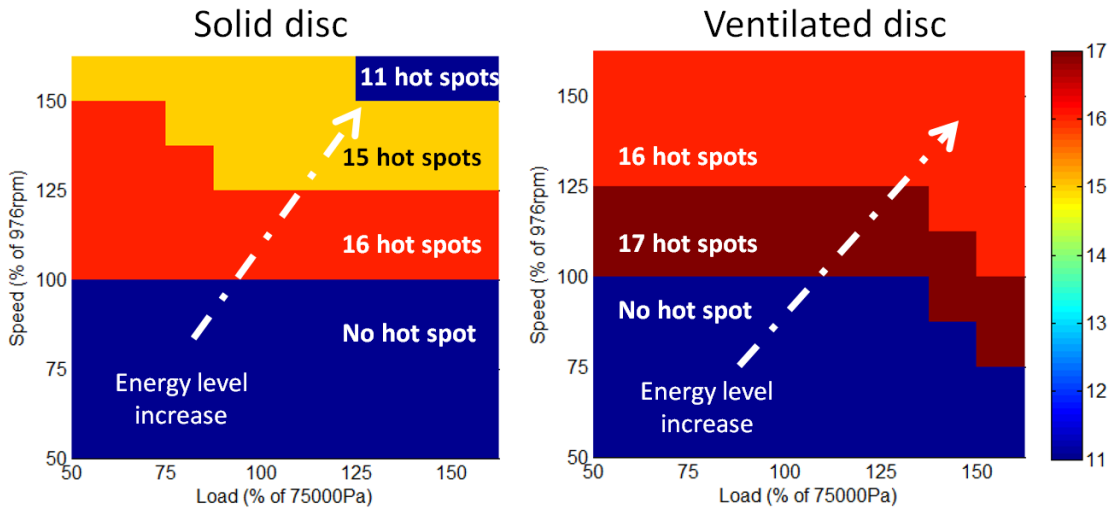

Figure 6.29 Number of hot spots of ventilated disc at various speed and load combinations

6.4.5 *Effects of cooling*

According to the research of Bryant, Fieldhouse and Talbot (2011), the variation of the circumferential temperature distribution was significantly affected by the vent design as shown in Figure 2.16, thus effects of cooling from the vents were investigated by modifying the heat transfer coefficient of the vents. Two investigations were performed: the effects of uneven cooling by blocking vents; and the effects of heat transfer coefficient on hot spotting.

Initially, 17 equispaced vents were blocked by setting the heat transfer coefficient to zero as illustrated by Figure 6.30 which represented the position of the pins in the real brake. The results of the temperature distribution before and after blocking are shown in Figure 6.31. It illustrated that the hot spots of the “blocked vents model” were symmetrically distributed between the inboard and outboard disc surface. This indicated that the uneven disc cooling can significantly affect the hot spot distribution. Meanwhile, due to 1/3 of the vents being blocked, the reduction of the overall cooling performance resulted in the increase of the maximum hot spots temperature by 60°C.

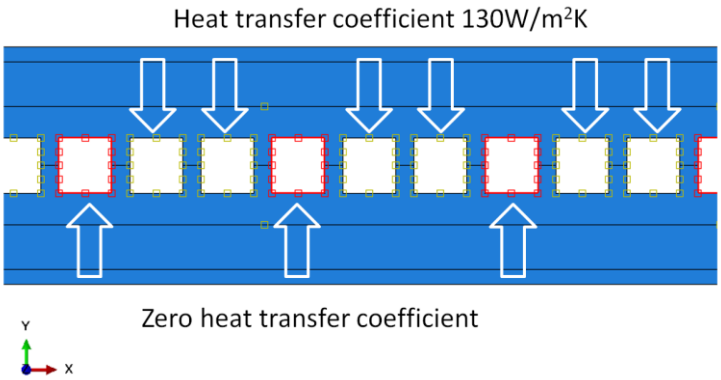

Figure 6.30 The 'blocked' vents with zero heat transfer coefficient

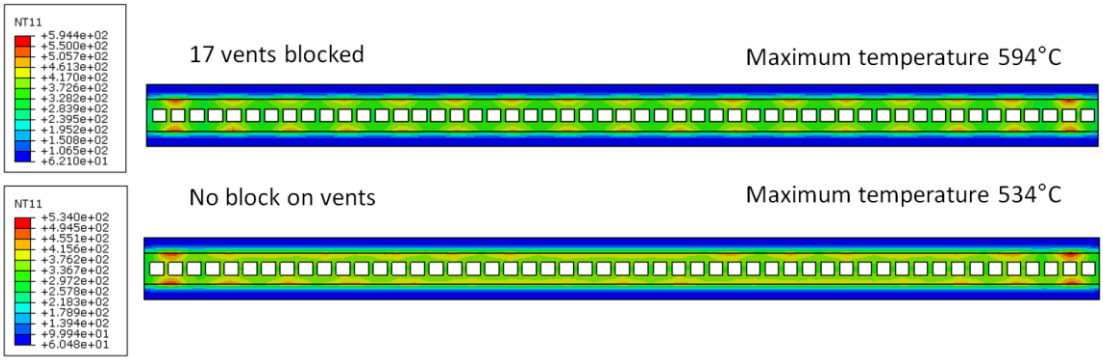

Figure 6.31 Temperature distribution of the 2D axisymmetric brake disc system with and without 17 vents blocked

Furthermore, the effects of overall cooling performance of the disc on hot spotting were investigated by varying the heat transfer coefficients of the 51 vents from 0 to 180W/m^{2}K. Figure 6.32 and Figure 6.33 shows the power spectral analysis of the disc temperature distribution and displacement distribution at 24s respectively. It can be seen that 17 hot spots were developed for all models. The temperature and displacement magnitudes of the hot spots were reduced with increasing heat transfer coefficient. It also revealed that the hot spot distribution was not affected when the cooling performance of all the vents changed uniformly. It should be noted that the significant lower order disc deformation did not affect the lower order temperature variation in these models.

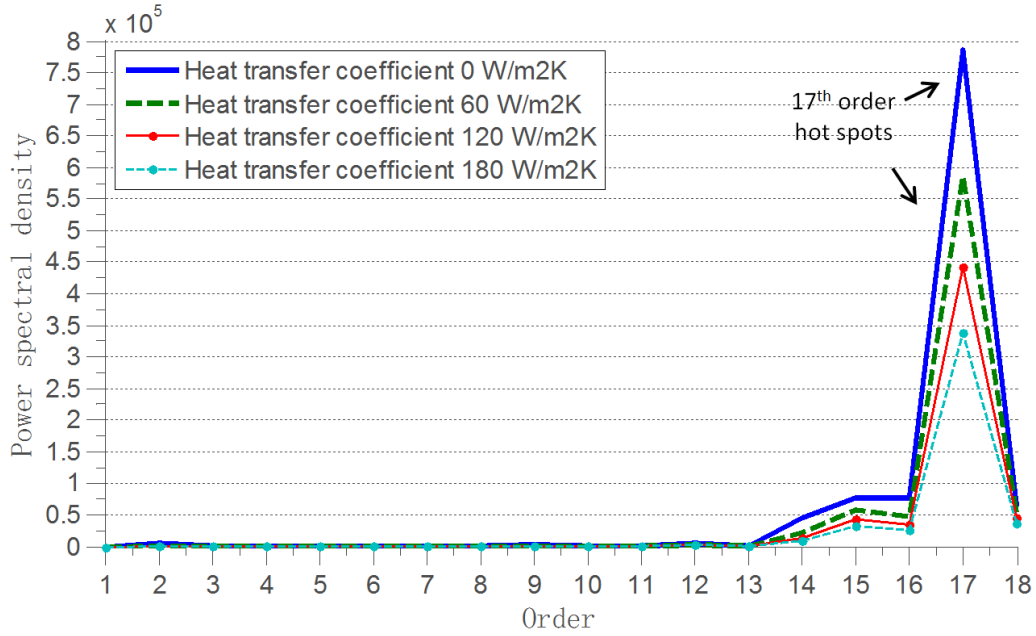

Figure 6.32 Power spectral density distribution of the disc temperature distribution on the outboard surface with various heat transfer coefficient

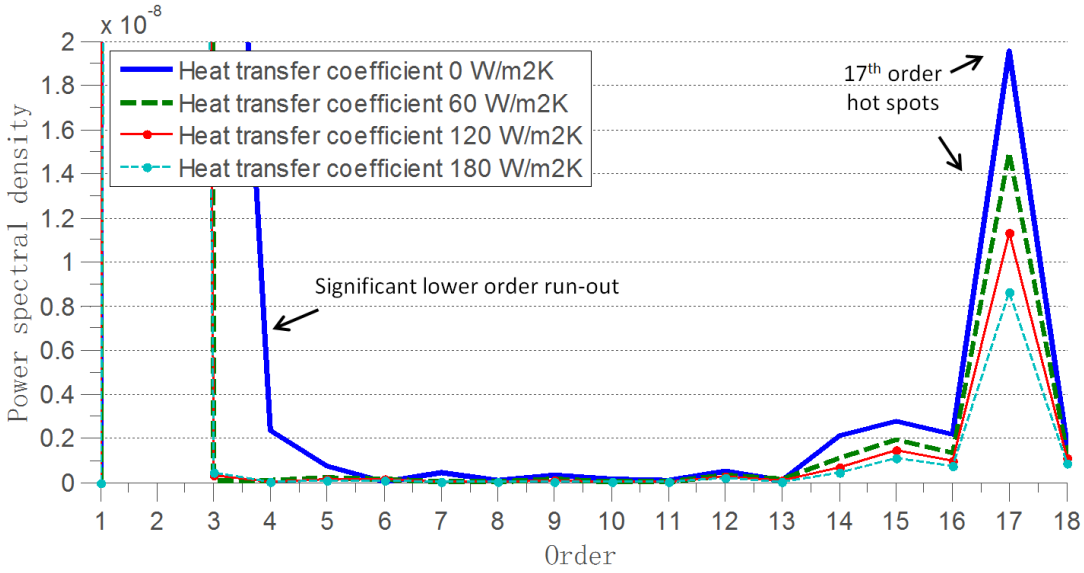

Figure 6.33 Power spectral density distribution of the disc displacement distribution on the outboard surface with various heat transfer coefficient

6.4.6 *Effects of pad length*

Pad length is another significant factor involved in of hot spotting according to the experiments performed by Sardá *et al.* (2008). Therefore, 2D in-plane models with various pad sector angles (i.e. pad length) within range 15° to 60° were performed. The modelling of pad length was achieved by modifying the scaling factors of the material properties of the pad and back-plate as discussed in section 5.2.

Figure 6.30 shows the results of maximum hot spot temperature of both solid and ventilated discs as a function of pad length. It can be observed that the maximum temperature increased with the increase of pad length for both solid and ventilated discs. The hot spot temperature of the solid disc was greater than the ventilated disc and the difference increased in a non-linear manner with the increase of pad length. It implied that the solid disc was more sensitive to the ventilated disc in terms of maximum temperature.

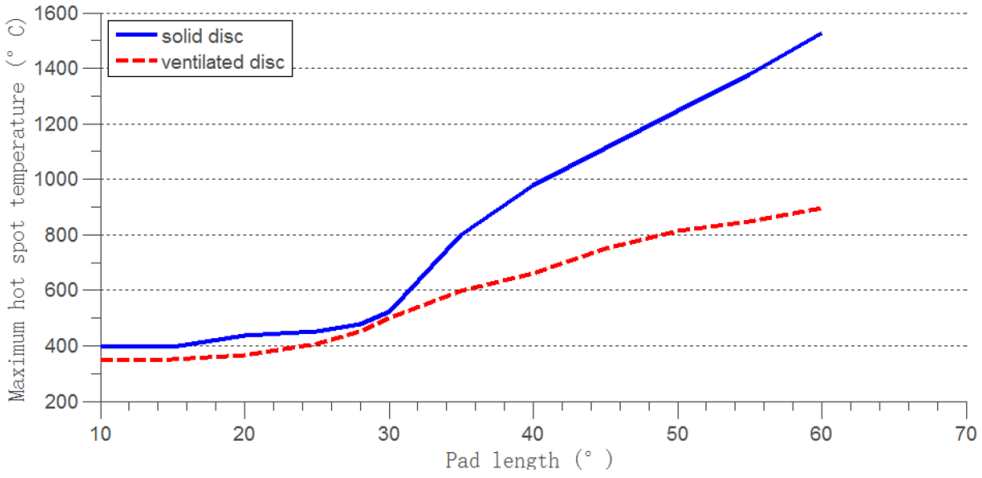

Figure 6.34 Maximum hot spot temperature of the solid and ventilated disc vs. pad lengths

In addition, Figure 6.35 shows that the number of hot spots at various pad lengths. When the pad length was shorter than 25°, no apparent hot spots developed. It

matched the TEI theory (Panier, 2006) that if the pad length was shorter than the minimum disc wavelength of possible hot spots, there would be no hot spots generated. After increasing the pad length to 25°, 17 hot spots developed on the ventilated disc surfaces and 16 on the solid disc surfaces. Then with the increasing of pad length, both the solid and ventilated discs showed a reduction of the number of hot spots. According to the observation of Figure 6.34, and Figure 6.35, it revealed that with the increasing of pad length, the thermal energy localised fewer hot spots and generated greater temperature on each hot spot. This is likely to be a result of loss of contact between the hot spots, creating higher contact pressure at the hot spot peaks.

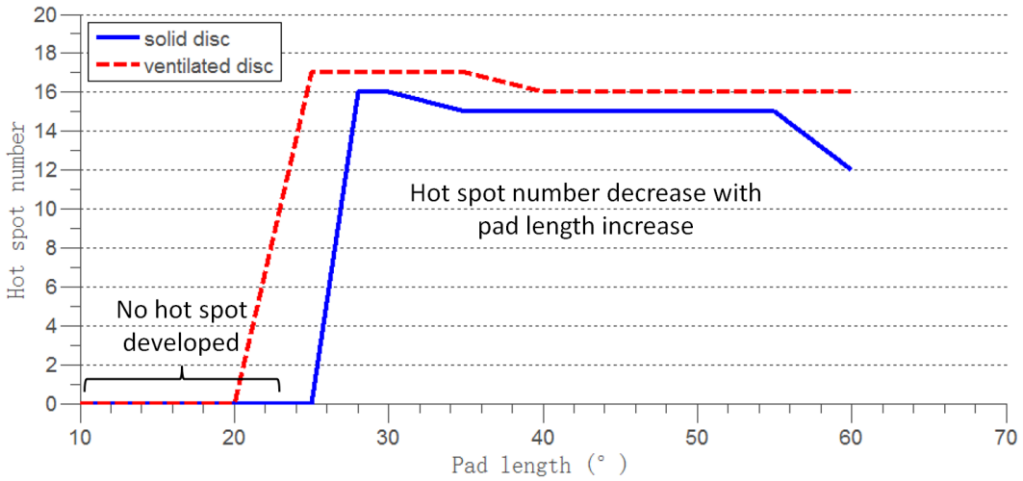

Figure 6.35 Number of hot spot of the solid and ventilated disc vs. pad lengths

6.5 2D Out-of-plane hot spotting: Radial migration

According to the experiments performed in chapter 4 and in published literature (Sardá *et al.*, 2008) the radial movement of hot spots or hot bands has been observed. Such a phenomenon not only significantly affected the brake torque variation (BTV) and subsequent vibrations due to the variation of the effective rubbing radius of the disc pad contact pairs between brake events, but also affected the accuracy of measurements in terms of displacement and temperature. Therefore, the 2D out-of-plane hot spotting model was used to

investigate the mechanism of radial hot spots/band migration throughout several brake applications. Due to the nature of the model, it cannot represent the circumferential variations of temperature and displacement. Therefore, the radial migration of the thermal localisation phenomena obtained in this study can be regarded as either hot bands or hot spots. Similar to the axisymmetric model performed by Day, Tirovic and Newcomb (1991), the out-of-plane model was an axisymmetric model that can be used to investigate the interactions between thermal localisations and wear. As wear was indicated as the primary determinant of hot spot/hot band migration by Ostermeyer, and Graf (2013), wear effects were considered in this model to evaluate its effects of the radial migration of the thermal localisations.

6.5.1 *FE model setup*

The assembly and boundary conditions are shown in Figure 6.36. As an axisymmetric model, the rotation direction was clockwise and out of the x y plane, where x is the radial direction and y is the rotation axis. The top-hat and pins were modelled in order to simulate the coning effects (i.e. bulk deformation in this case) of the disc. The back-plates and actual brake pads were considered as well to enable the proper modelling of contact pressure distribution at the disc pad interface due to the interactions between thermal stress and mechanical loading as discussed in section 3.3.6. In order to simulate the effects of a ventilated disc, the material property of the vent layer was scaled according to the axisymmetric ventilated disc assumption discussed in section 5.4. The actual calliper used in the experiments was a ‘sliding fist calliper’ which only featured one piston at the inboard sides and the clamping force at the outboard side was provided by the reaction force. Thus, the actuation pressure was uniformly applied on the outboard back-plate as shown in Figure 6.36, and at the centre of the inboard back-plate to simulate the piston. Regarding the boundary conditions; the top-hat

was constrained in the x and y directions to simulate the clamping effect of the wheel and hub. The pads and back-plates where constrained in the x direction. So that the pad could only move in the axial direction and the 'knock-back' effects of the pads can be achieved. This meant that when the brake was released, the pads could separate from the disc due to the removal of brake pressure and any axial direction force fraction such as the thermal stress at the interface.

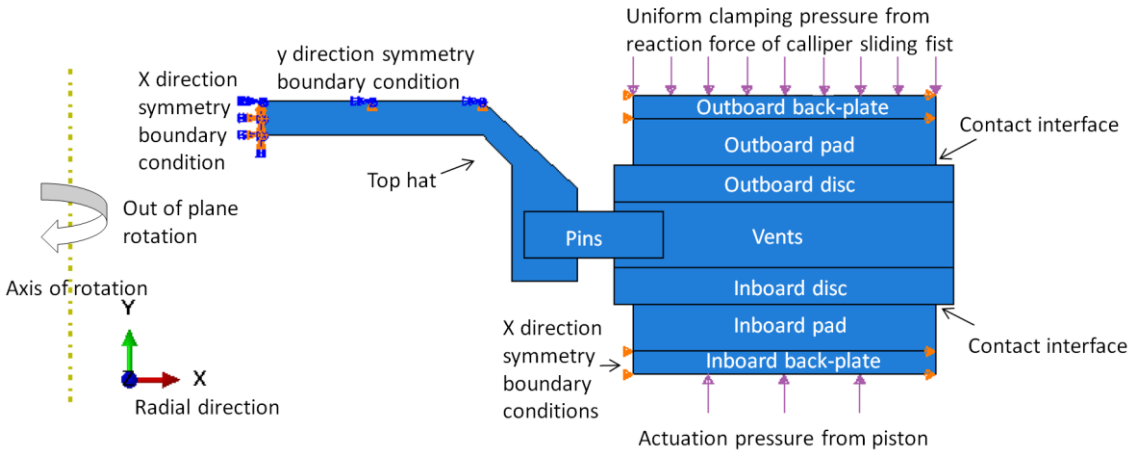

Figure 6.36 Assembly and boundary conditions of the axisymmetric out-of-plane model

The material properties and braking operation data were provided in Table 6.1. As discussed in section 5.2 and 5.3, the axisymmetric simplifications of pad and ventilated disc were implemented in the out-of-plane models by applying the scaling factor of $\frac{\theta}{360} = \frac{30}{360} = 1/12$ for the pressure applied on the back-plates, and the thermal conductivity, modulus, coefficient of thermal expansion and specific heat capacity of the brake pads. The brake applications were identical to the experiment which was a 24s drag brake at constant 976rev/min (~150km/h) speed and 25.5bar brake pressure. 9 brake applications were simulated in order to evaluate the repetitiveness of the hot spots/bands radial migration. Between two consecutive brake applications, 500s cooling phases were simulated in order to reset the system to the initial temperature and displacement conditions. The heat transfer coefficient obtained from the section 4.5.1 was uniformly applied on

the disc surfaces as illustrated in Figure 6.37 in red. In addition, considering the relatively low temperature differences between the wheel and top-hat and the relatively low heat dissipation of the stationary brake pads compared to the brake disc, a relatively low heat transfer coefficient of 30W/m^{2}K was applied on the pads and top-hat as shown in Figure 6.37 in orange and green respectively in order to simulate the heat conduction effects of the surrounding components such as calliper, axle, bolts and wheel. The estimation of this heat transfer coefficient value can be found in Appendix 3. Since the heating phases (24s) were significantly shorter than the cooling phases (500s), considerable thermal gradients can be generated throughout the brake disc and pad. The heat dissipation during the braking events was presumed to be insignificant effects on the temperature distribution in the short term. Therefore, a constant 30 W/m^{2}K heat transfer coefficient was applied to compromise the cooling objective and heating phase prediction accuracy. Moreover, the radiation effects were neglected due to this small proportion in disc brake heat dissipation as suggested by Limpert (1975).

The element type used was CAX4T which was a 4 node axisymmetric thermally coupled temperature displacement element (ABAQUS manual, 2012). The user-subroutine UMESHMOTION (see Appendix 2) was used to adjust the nodal position to simulate the effects of wear. Because of the high memory requirement of the implicit algorithm, the approximate global element size was set to 2.5mm to optimise the computing performance (Figure 6.37) with suitable accuracy. A mesh sensitivity study was carried out to investigate the robustness of the current element size selection. As the results in Figure 6.38 illustrated, when the element size was smaller than 3mm, the predicted hot band number on both disc surfaces was stabilised at 3 which matched the experimental results illustrated in Figure 5.16. Meanwhile, Figure 6.39 shows that the maximum temperature stabilised at

~360°C when the element size was set smaller than 3mm. Therefore, it can be seen that the 2.5mm global element size was acceptable.

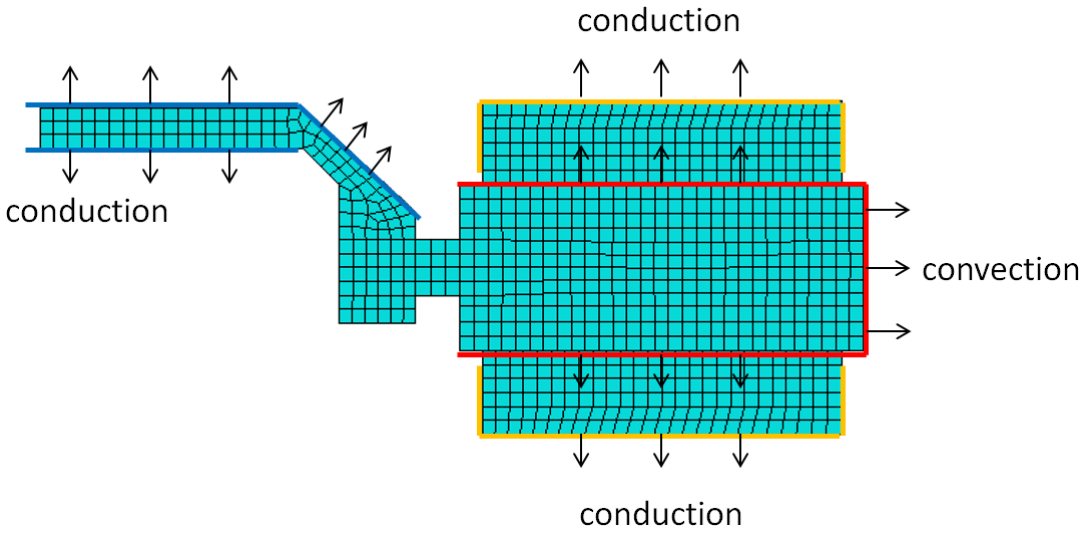

Figure 6.37 FE model showing the 2D out of plane axisymmetric mesh and boundary conditions

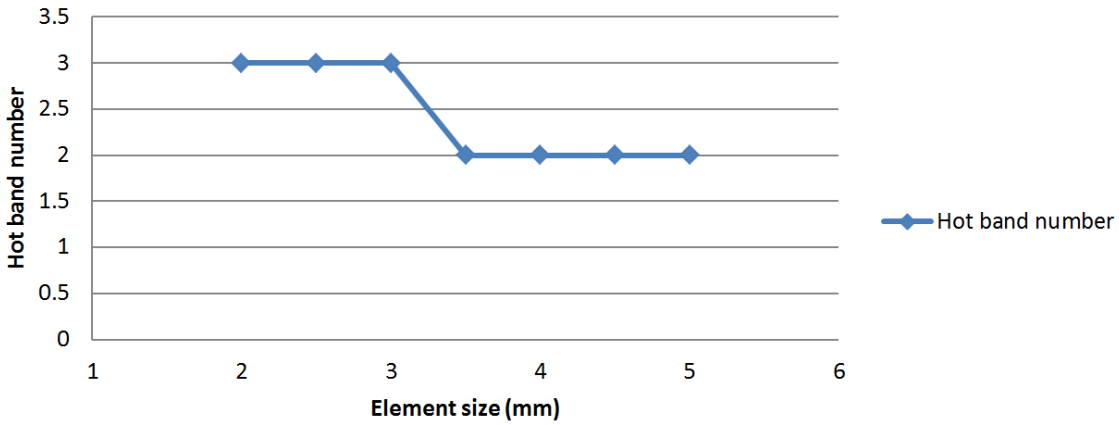

Figure 6.38 Mesh sensitivity study of hot band number vs. element size for the 2D out-of-plane model

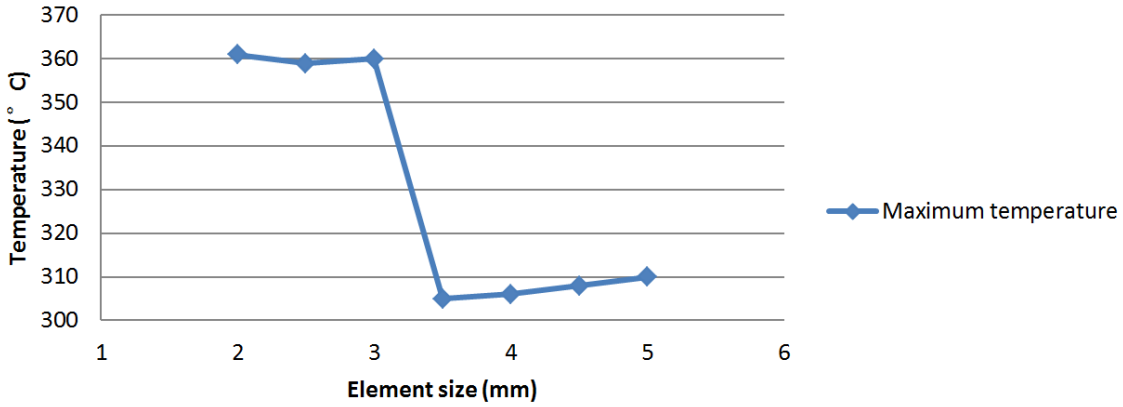

Figure 6.39 Mesh sensitivity study of maximum disc temperature vs. element size for the 2D out-of-plane model

The wear model and wear rate were discussed and measured in section 4.5.2, and 5.4.2 respectively. Since significant wear effects were observed on the brake pad side as shown in Figure 4.23, and Jang (2004) suggested that the wear of pad was more considerable, thus the adaptive mesh constraints were applied on the contact interfaces of the pads i.e. the wear occurred only at the pad in this simulation. Furthermore, the heat generation was defined using FRIC by using an identical method from the in-plane models. The difference was that the radius was not fixed in the out-of-plane model therefore the heat generation at the outer radius would be greater than the inner radius under the same pressure.

6.5.2 *Out of plane FE model results*

Figure 6.40 provides the temperature distribution contours of the 1st braking event (brake application). At the beginning (~0.1s), it shows that the outboard temperature was more uniformly distributed than the inboard across the contact surfaces. This is because the inboard brake pressure was concentrated at the middle of the inboard back-plate to simulate the piston effects. It revealed that, as expected, the heat generation in this model was a function of contact pressure by implementing the FRIC subroutine. At 5s, the thermal localisation phenomenon can be observed at both inboard and outboard surfaces. A 200°C

hot band was generated at the mean radius of the inboard interface whereas two hot bands with lower temperature were formed at the inner and outer radii of the outboard surface respectively. It should be noted that the outer radius hot band was hotter than the inner with a temperature difference of ~50°C. It implied that the heat generation was a function of the radius (i.e. linear sliding velocity due to identical rotational velocity) in this model. At the end of the braking event (24s), the maximum temperature reached 364°C and the two outboard hot bands radially migrated to the mean radius and merged together which is the 'in-stop' hot band migration phenomenon.

Regarding the disc deformation, Figure 6.40 also presents the axial deformation magnified by 100 times. It can be seen that the deformation of the disc was well correlated with its temperature distribution implying the thermal strain dominated the disc distortion during such heavy duty braking. Meanwhile, the temperature and displacement fields were not identical because the bulk modulus of the brake pad friction material was much lower than that of the disc. At 5s and 24s, it clearly shows that the disc was moving toward the positive axial direction comparing with the constrained top-hat, which is recognised as the coning effect of the brake disc due to the thermal deflections of the top-hat and pins.

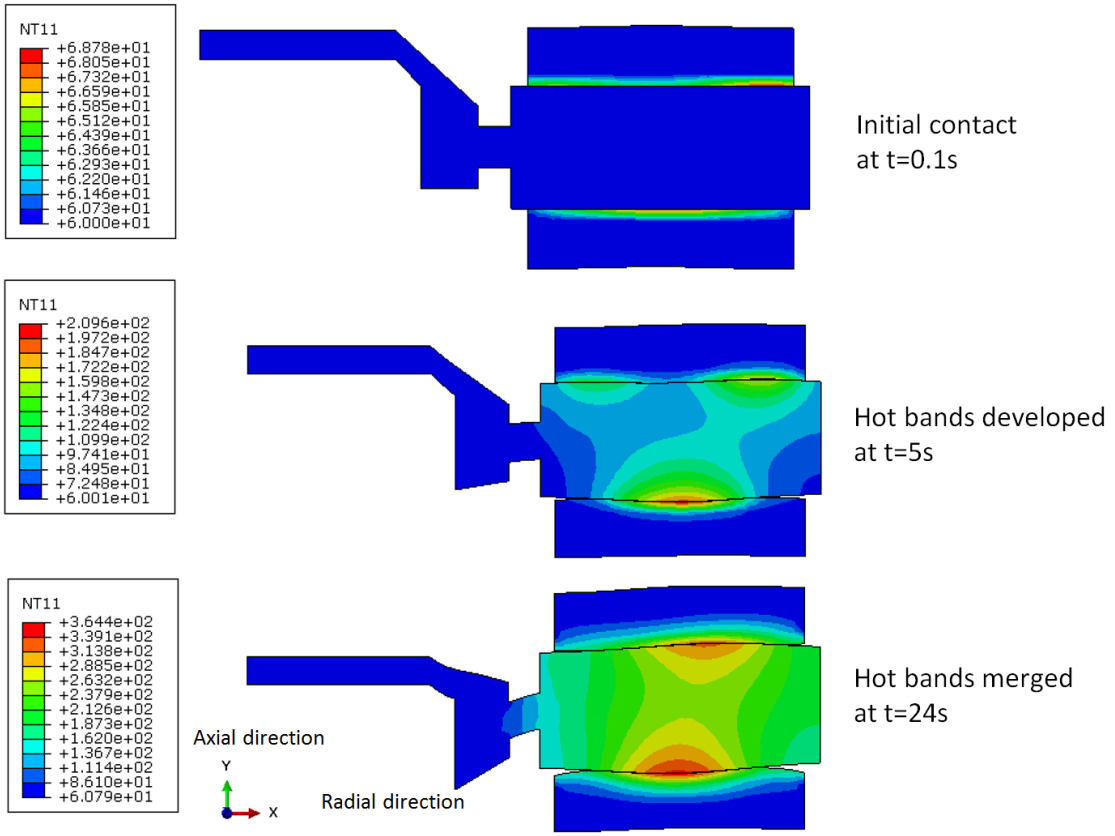

Figure 6.40 Temperature distribution and thermal localisations development of the 1st brake events (deformation scaled by 100 times in Y direction)

In addition, Figure 6.41 shows the thermal localisations of the initial four brake events. It illustrated that at same instance in time (15s) of each brake event; the hot bands occurred at different positions and alternated between events. To be specific, two hot bands developed in the first braking event on the outboard surface and one on the inboard surface. However, at the second braking event, two hot bands developed on the inboard surface whereas only one on the outboard surface. At the third event, the distribution of the hot bands was similar to the first event, and the fourth was similar to the second event. Therefore, it can be seen that the location of the hot bands migrated not only 'in-stop' but also 'between stops'.

Figure 6.42, Figure 6.43 and Figure 6.44 show the 3D plots of the outboard disc surface temperature, contact pressure, and wear rate across the pad radii throughout the 9 brake events. It can be seen that there is good correlation between temperature, contact pressure and wear rate with identical pattern of hot bands locations alternating between the braking events. This implied that the interactions between heat generation, contact pressure distribution and wear rate were successfully established by incorporating the FRIC and UMESHMOTION subroutines. The 3D plots also illustrated that the inboard maximum temperature, contact pressure and wear rate were greater than the outboard surface in general when one hot band developed on the surface. It revealed that the asymmetric mechanical loading distribution between the inboard and outboard pads affected the contact pressure distribution.

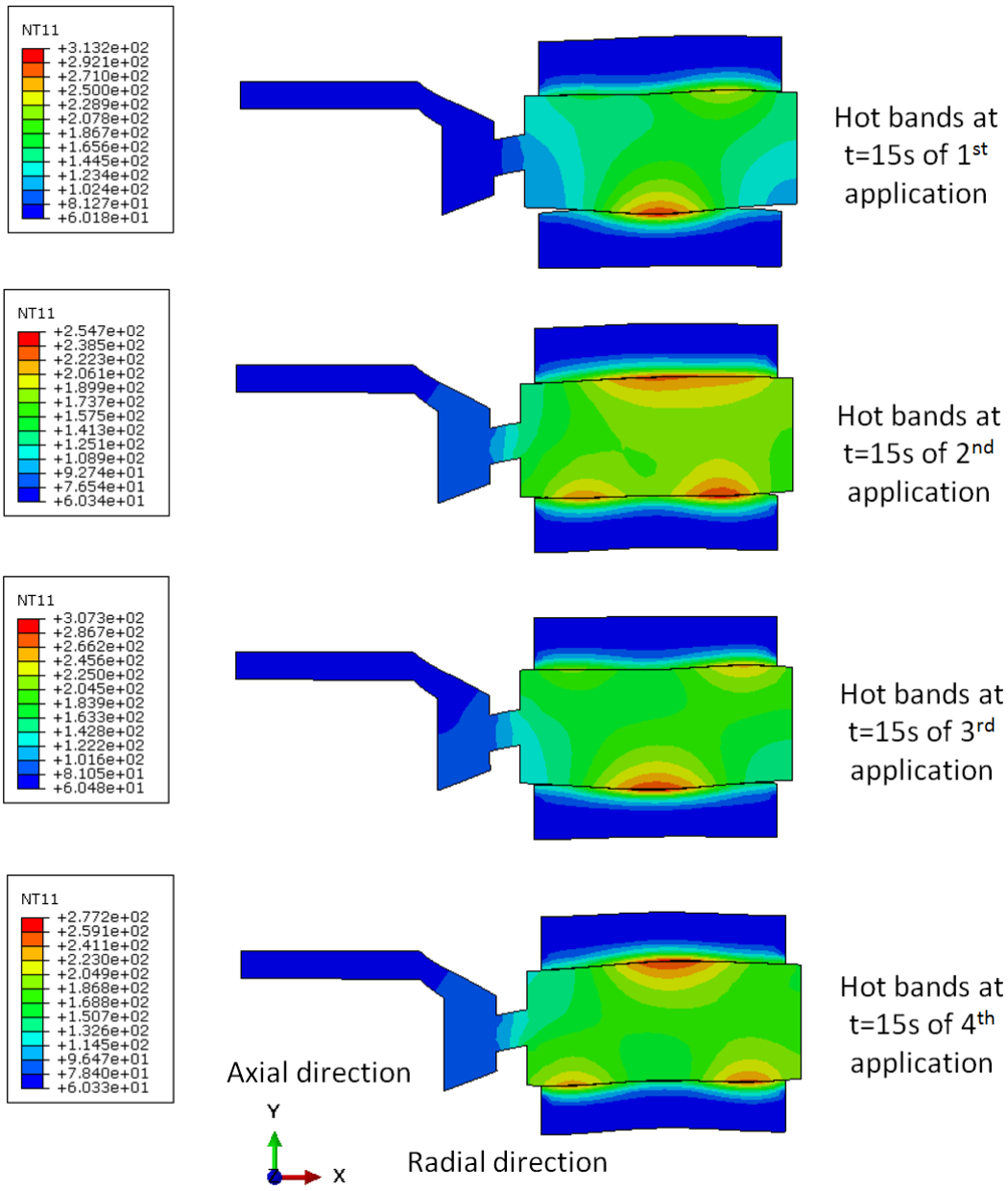

Figure 6.41 Temperature distribution contours of the first four brake events (deformation scaled by 100 times in y direction)

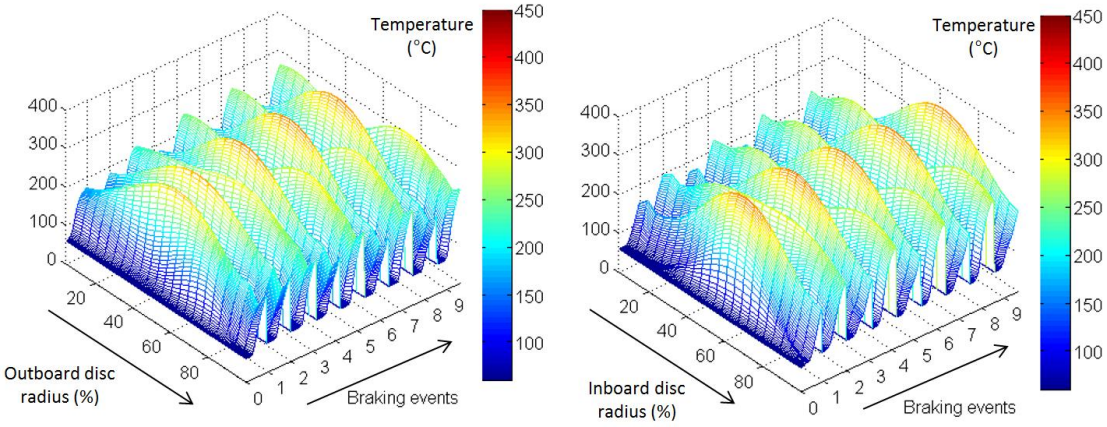

Figure 6.42 Simulated 3D temperature distribution across the pad outboard (left) and inboard (right) radii throughout 9 braking events

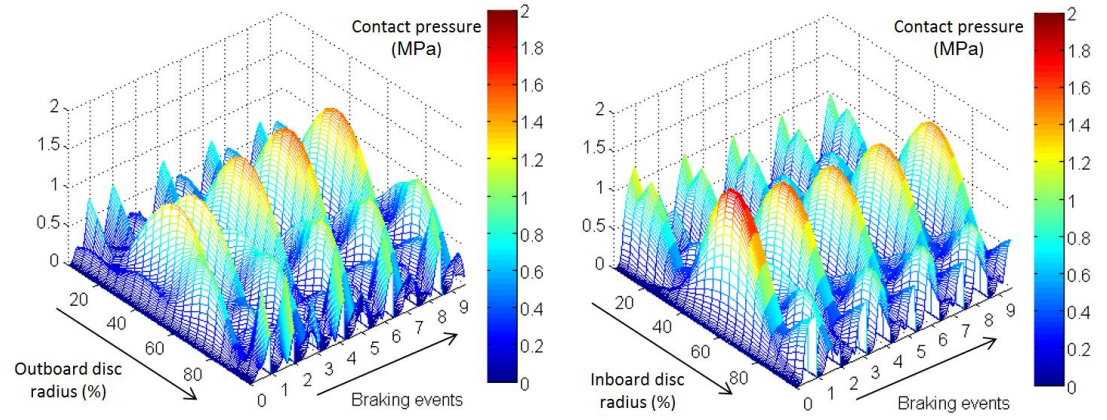

Figure 6.43 Simulated 3D contact pressure distribution across the pad outboard (left) and inboard (right) radii throughout 9 braking events

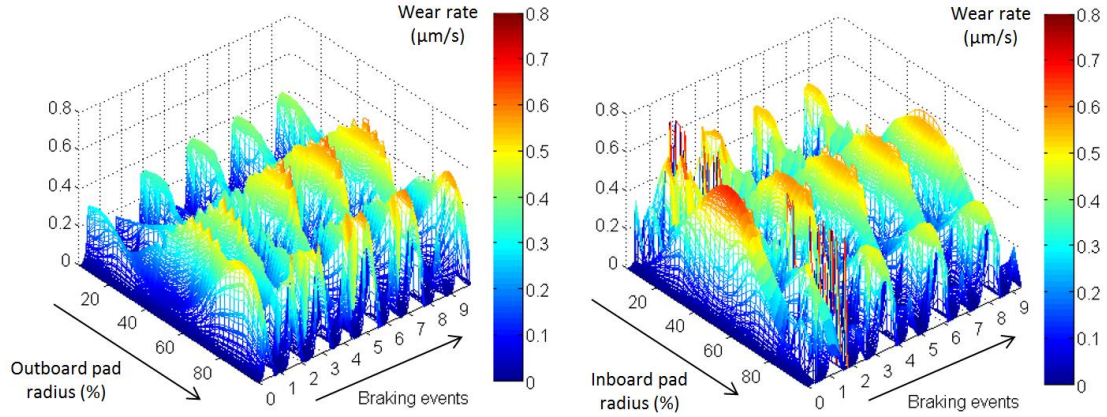

Figure 6.44 Simulated 3D wear rate distribution across the pad outboard (left) and inboard (right) radii throughout 9 braking events

It can be observed that the hot bands developed at the locations with relatively lower wear rate in the previous braking event. This was in agreement with by the theory of Ostermeyer and Graf (2013) that wear was the trigger of hot band migration. In order to confirm this hypothesis, Figure 6.45 was plotted which shows the temperature distributions at the end of the 3rd braking event, end of the 3rd cooling phase and during the 4th brake application. It illustrated that after the 3rd braking event, the wear of the pad was determined by the hot banding i.e. one concave location on the inboard pad and two on the outboard pad were observed after the 3rd braking event at locations that the hot bands developed during the 3rd event. Then, in the subsequent 4th braking event, hot bands developed at the radii with less wear. It illustrated that for the hot band migration process, the wear was determined by the thermal localisations, and in the following event thermal localisation was determined by the wear distribution.

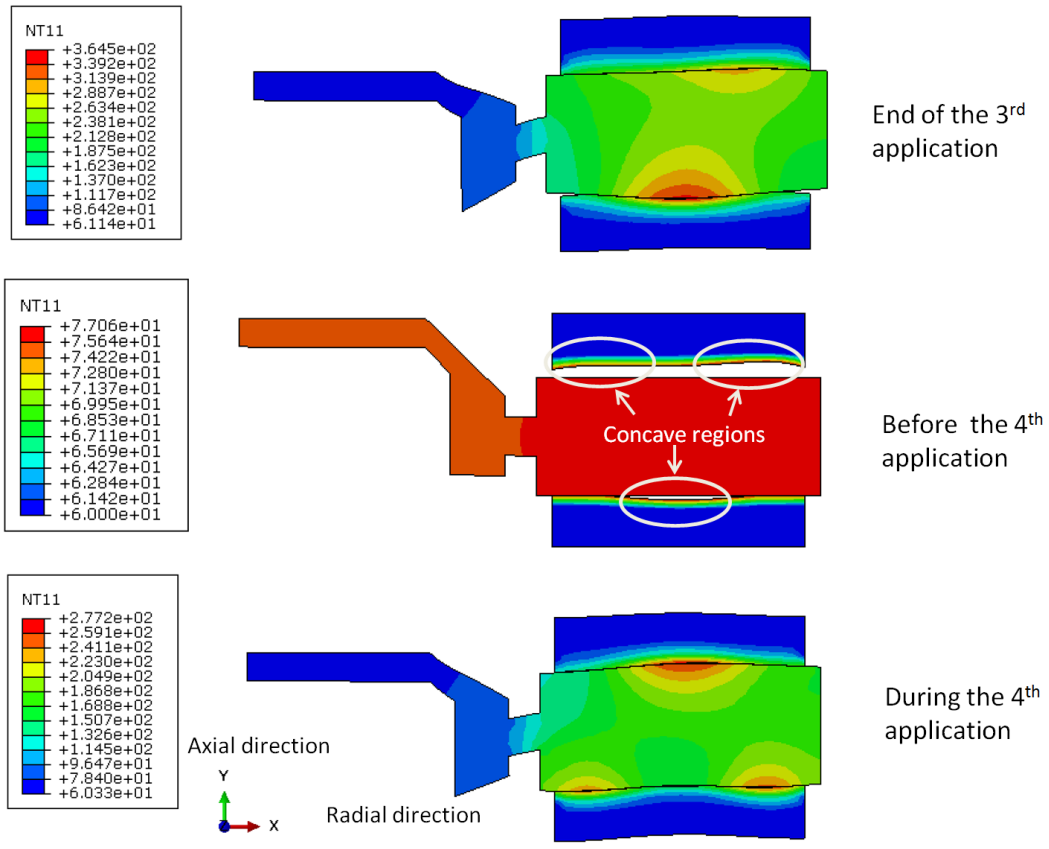

Figure 6.45 Thermal localisation and wear (deformation scaled by 100 times in y direction)

Furthermore, to provide better visualisations of the trend of hot band migration over time, Figure 6.46 presents the predicted brake disc radial peak temperature migration over time and the corresponding out-of-plane temperature contours. Both the 'in-stop' and the 'between stops' can be easily identified. It shows that the hot band migration in this simulation was highly repetitive throughout the 9 brake events. The out-of-plane plots display the hot band positions at the 1st, 4th and 9th brake event and their corresponding location in the peak temperature plot. It can be observed that when there were two hot bands on the same side of the disc, there was a trend that they would migrate toward the mean rubbing radii. Regarding the single hot bands developed at the inboard surface, the locations were more consistent than those at the outboard surface; this can be attributed to the asymmetric loading pattern of the brake pads.

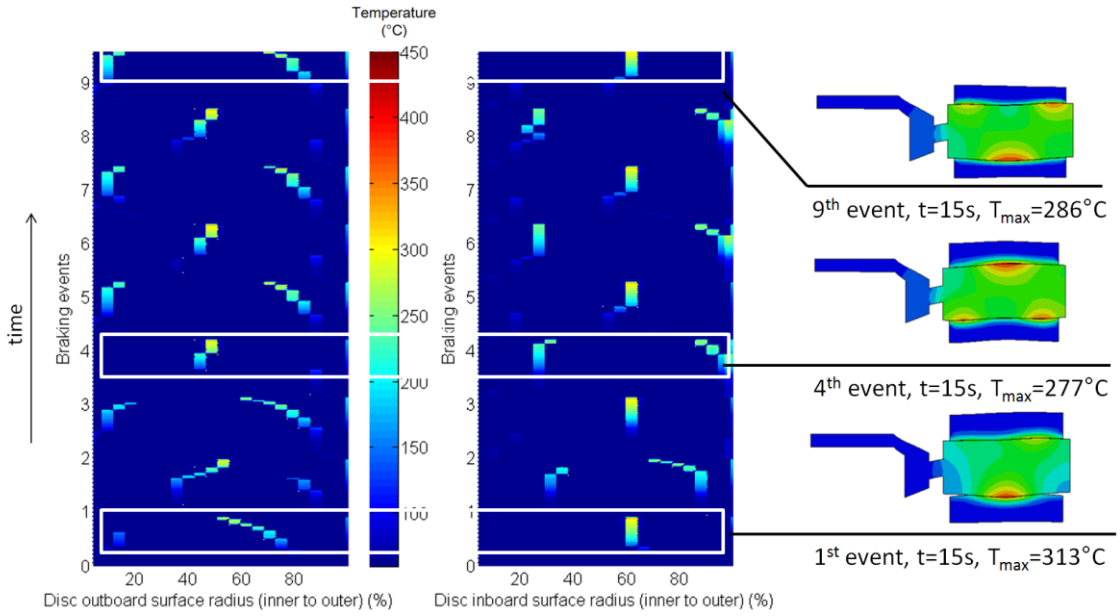

Figure 6.46 Predicted brake disc radial peak temperature migration over successive braking events (outboard surface, Left;, inboard surface, centre) and out of plane temperature distribution (right)

6.5.3 *Experimental validation*

The experimental validations were carried out using the dynamometer and IR camera discussed in chapter 5.

Figure 6.47 provides a comparison of the temperature distribution across the disc outboard radius for both the FE simulation and experimental data in the form of thermal images. Since the thermal camera used didn't featured line scan mode, the temperature distribution across the disc radius at a given angular position have been plotted in the 'line scan' mode by processing the 'frame by frame' raw images (measured at 1kHz) using MATLAB. Nine consecutive braking events were plotted for the simulation results and 3 consecutive braking events were measured using the thermal camera. The results in

Figure 6.47 illustrated that at same braking condition, the thermal images also show the radial alteration of the hot band locations between events. Regarding the magnitude of maximum temperature, the thermal image temperature results were greater than the simulation because the peak temperature of the hot spots were captured from the thermal images but the out-of-plane simulation only provided the average circumferential temperature.

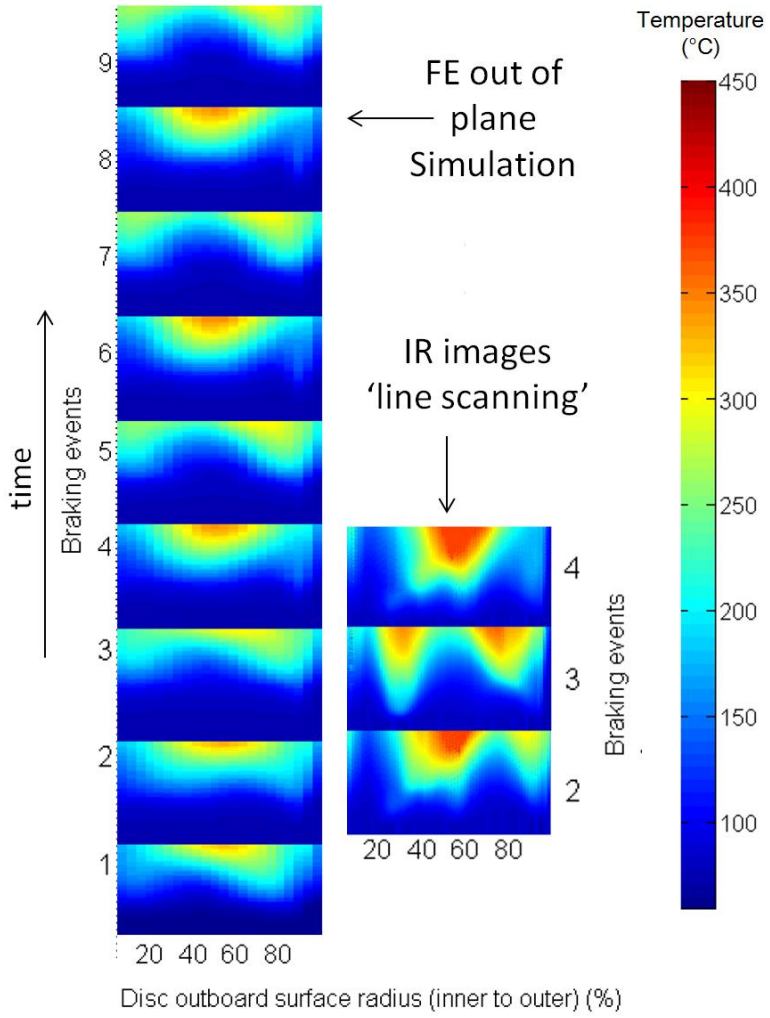

Figure 6.47 Outboard disc temperature distribution (heating phase only) across the disc radius throughout 9 braking events; simulation (left) and IR camera (right)

In terms of the disc coning, Figure 6.48 shows that the maximum disc axial displacement on the outer radius 'edge' (see Figure 4.15) reached ~150μm at 24s whereas the simulated value was ~160μm which demonstrated good correlation with the experiment. Regarding the temperature evolutions, both experiment (picked from the outer radius rubbing thermocouple) and simulation results at the same radius showed similar trends and similar temperature (~220°C) at the end of the heating phase (~24s).

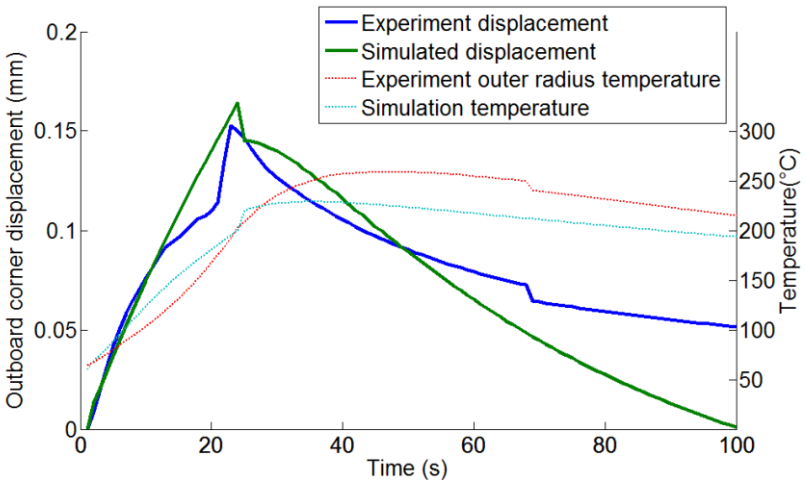

Figure 6.48 Displacement of the outboard disc outer radius and temperature during a single braking event; comparison of measured and predicted results

It should be noted that the cooling curves showed similar gradient but the axial displacement during the cooling phase showed considerable deviation between the experiment and simulation. This can be attributed by the difference between the heat transfer coefficients estimated at the top-hat in the simulation and the realistic heat conduction between brake system components. Since at the end of the simulation, the disc will be cooled back to the initial temperature and therefore displacement will be reset to the initial condition as it is a thermo-elastic model. This was deemed to be an acceptable limitation of the model given the accuracy of the predictions presented since the heating phase was more of interest than the cooling phase.

6.6 2D Hot band migration parametric studies

In order to further investigate the mechanism and determinants of the hot band migration. A parametric study was performed on the friction material properties, disc coning, loading types, wear rate and pad length. The details of the parametric studies are provided in Table 6.6. The aim of the study was to provide more insights into the design of friction pairs for the reduction in the radial migration of hot spots/bands.

Table 6.6 Out-of-plane hot spotting model: List of parametric studies and parameter values

Parameters	Unit	Values
Back-plate modulus	GPa	180
		200 (default)
		220
Pad modulus	GPa	0.6
		0.7 (default)
		0.8
		0.9
Pad conductivity	W/mK	0.45
		0.5 (default)
		0.55
Pad thermal expansion coefficient	10^{-6}/K	12
		15 (default)
		18
Pad specific heat capacity	J/kgK	450
		500 (default)
		550
Disc coning		With top-hat
		No top-hat
Loading types		Pistons on both sides
		Uniform on both sides
		Inboard piston (default)
		Outboard piston
Wear rate	10^{-13} m^3/Nm	0
		0.5
		1
		1.7 (default)
		2
		2.5
Pad length (sector angle)	°	24°
		30° (default)
		36°

6.6.1 *Effects of pad material properties*

The effects of increasing the magnitude of brake pad material properties on hot band migration are summarised in Table 6.7 (whilst the detailed results can be found in Appendix 4). The first factor investigated was the modulus of the back-plate. Since the friction material had relatively much lower thermal conductivity than the disc, the temperature rise at the back-plate can be considered insignificant according to Zagrodzki *et al.* (2009). Therefore, the effects of the thermal properties were not considered in these parametric studies. The effects of back-plate modulus on the peak temperature migration throughout 9 braking events was minor as indicated by the results. Regarding the effects of various pad moduli on the pattern of hot band migration; the results indicated that the influence of the asymmetric loading between inboard and outboard pads on the 'in-stop' hot banding reduced due to the increase of pad moduli, and thus more uniform contact pressure. In addition, Table 6.7 revealed that increasing the thermal conductivity of the friction material would reduce the hot band migration. On the contrary, lower conductivity would mean more heat would be concentrated at the contact interface which can facilitate the thermal localisation process and the resultant wear and cause more significant migrations. Moreover, the results revealed that greater hot band migrations resulted when the coefficient of thermal expansion increased. Since the expansion coefficient can magnify the thermal localisation, according to Lee and Barber (1993), the subsequent wear rate can be considerable with high expansion coefficient. Therefore, the results implied that the increase of thermal expansion coefficient boosted the cycle of thermal localisation-wear-contact pressure distribution. In terms of the influences of increasing the pad specific heat capacity, Table 6.7 illustrated that the hot band migration was more serious. It indicated that when the heat capacity was relatively high, the bulk temperature would be low and the heat would be more concentrated at the contact interface according to the basic heat transfer equation

(Equation 3.1) through the thickness. Thus the thermal localisations and migrations would be magnified.

Table 6.7 Simulation results of the effect of increasing the magnitude of pad material properties on hot band migration

Component	Material property	Radial migration
Back-plate	Young's modulus	Minor
Friction material	Thermal conductivity	Reduced
	Young's modulus	Reduced
	Thermal expansion coefficient	Increased
	Specific heat capacity	Increased
	Pad wear rate	Increased

6.6.2 *Effects of disc coning*

Another potential determinant investigated was the effects of disc coning. It can be presumed that axial disc coning might cause uneven contact pressure distribution. The radial proportion of the disc coning can change the relative radial position of the disc to the pads (the effective radius) and also the hot band locations.

Figure 6.49 presents the out-of-plane 2D FE models with and without the disc top-hat, and the corresponding results. Where the disc was modelled without the top-hat, the inner radius of the friction rings were constrained in the x direction and the central point of this surface was pinned (zero displacement but rotation permitted) to allow disc coning.

The results illustrate that the hot bands alternated between single and double bands on each rubbing surface for both of the models. When two hot bands developed, the distances of the migration (or separation) were similar in both models. Comparing zone 1 and 3 for the outboard surfaces in Figure 6.49, the

model without the top-hat shows a relatively more stable hot band in terms of migration. However, by comparing zone 2 and 4 (inboard surface), it can be observed that the hot bands at the inboard disc inner radius migrated toward the outer radius when there was no top-hat.

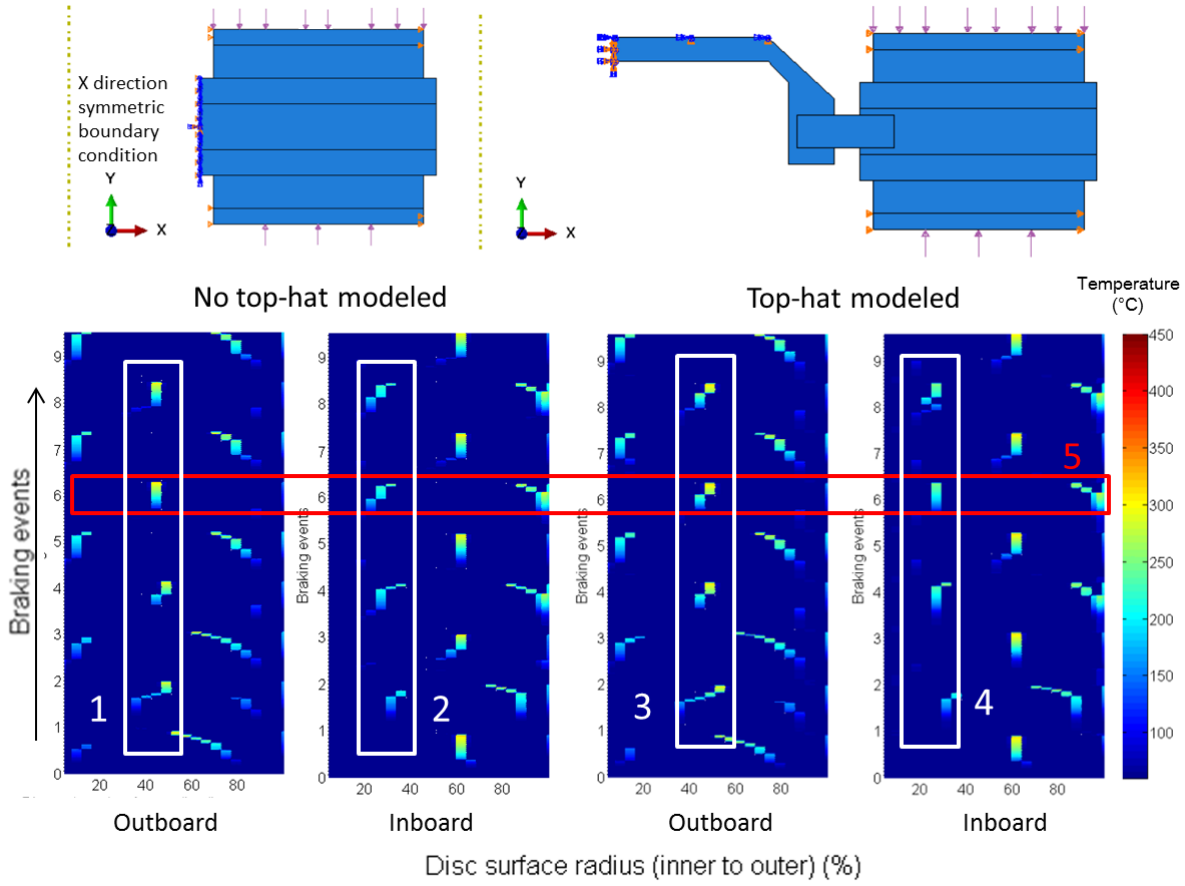

Figure 6.49 2D in-plane FE models (top) with (right), and without (left) top-hat; resulting hot band migration for the outboard and inboard disc surfaces (bottom)

In order to investigate the relationship between disc coning with the phenomena observed, Figure 6.50 was plotted which compared the disc deformation and thermal localisation for both models. The disc deformation in both the axial and radial directions was scaled by 100 times. The selected braking event was the 6th which is highlighted in Figure 6.49 at zone 5. Regarding the model with the top-hat, it illustrated that the disc deflected both in axial and radial directions due to the coning effect. Comparing the results at 5s and 24s, it can be found that due

to the considerable pad wear, and the anti-clockwise tilting of the disc, the outboard disc contact zones shifted toward the outer radius from the mean radius. On the contrary, the disc without top-hat shows no significant disc deflections. Therefore, the disc coning can be identified as a source of hot band migration.

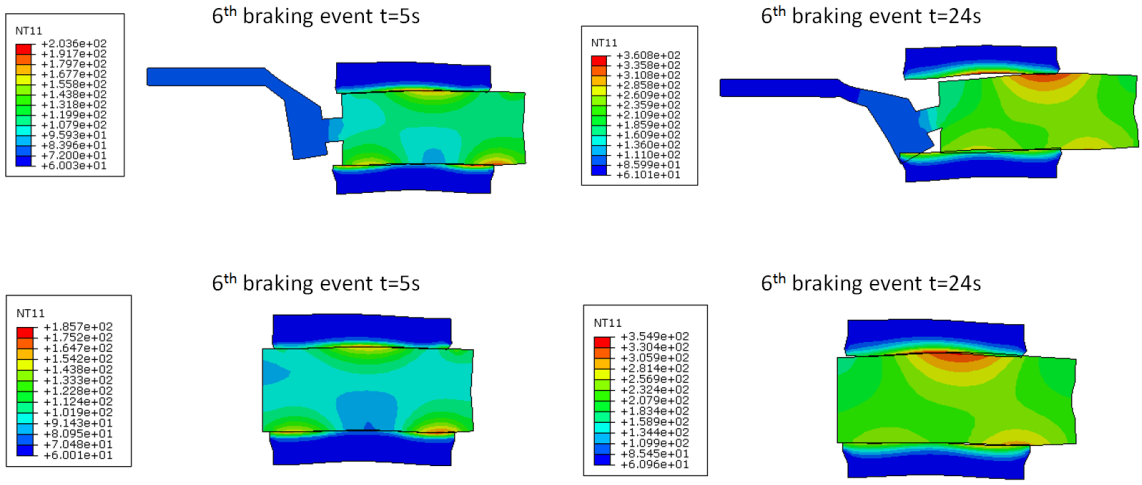

Figure 6.50 Comparison of the temperature fields and distortions for the discs with (top) and without (bottom) top-hat (deformation scaled by 100 times in x and y directions)

6.6.3 *Effects of loading distributions*

It was discussed in section 6.5.2 that the mechanical loading applied on the back-plates significantly affected the initial contact pressure distribution and the subsequent hot band development in the first braking event. Figure 6.51 provides a comparison among different combinations of loads applied on the inboard and outboard back-plate as listed in Table 6.6. Comparing load case 1 and 2, it can be found that a piston on each pad (case 1) was more stable than both pads with uniform loading in terms of hot band migration. For the uniform pressure loading cases, the uniform elastic deformation due to compression had no effects to stabilise the thermal localisation-wear-migration cause effect chain.

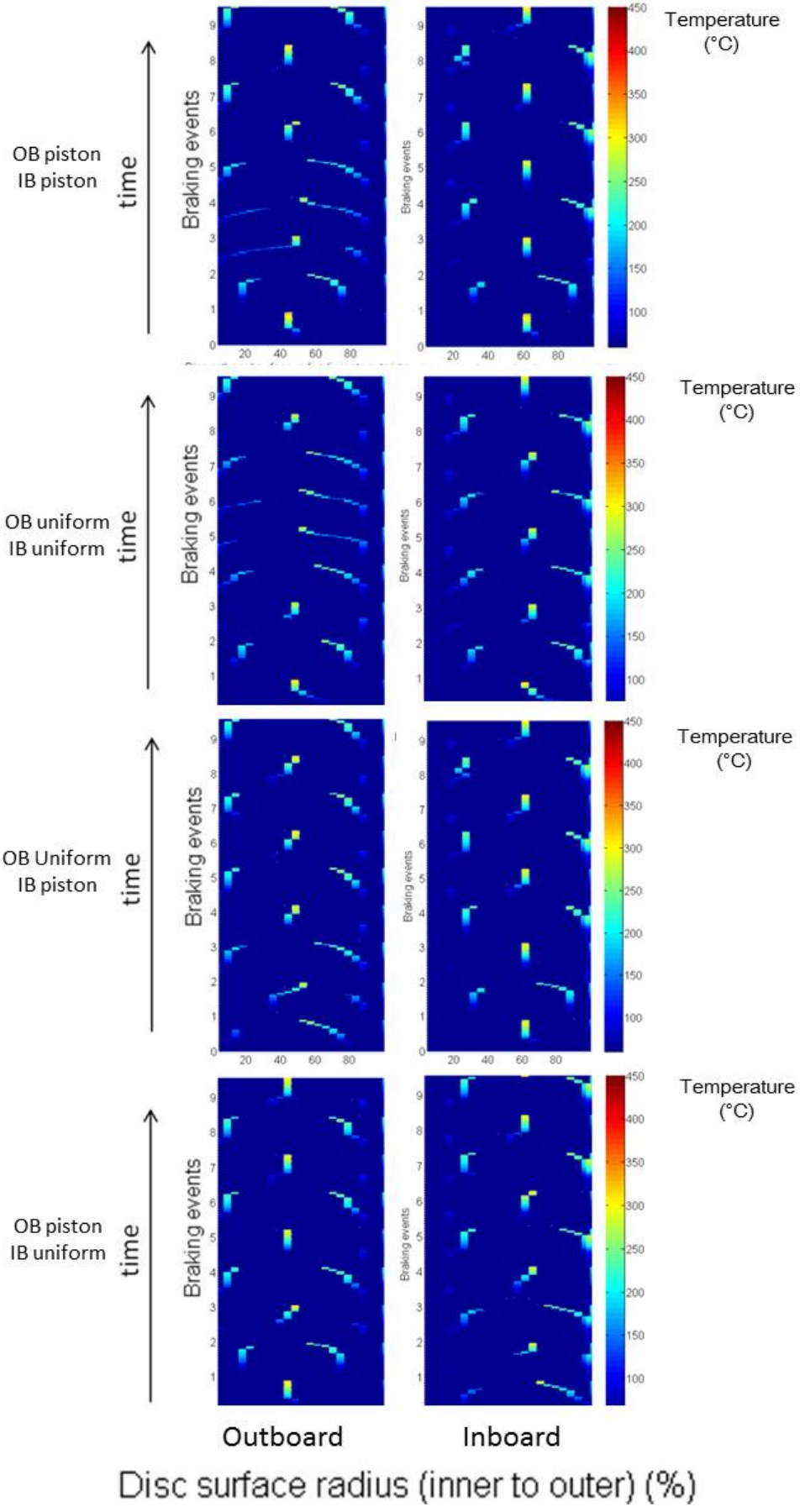

Figure 6.51 Effects of pad loading condition on peak temperature migration

In addition. the results also revealed that for the models representing a single piston on one pad and uniform loading on the other (Load case 3 and 4 in Figure 6.51), the initial hot band locations was affected by the mechanical load distribution on the back-plate. The inboard hot band migration of load case 3 was similar to the outboard in load case 4 and vice versa. This implied that the effect of initial loading distribution was more significant than the effects of disc coning in terms of inboard and outboard hot banding.

6.6.4 *Effects of wear rate*

According to Barber (1969), from the view of 1D (through disc and pad thickness) the effects of wear during the TEI phenomenon was cancelling or reducing the thermal localisation magnitude i.e. the thermal expansion were reduced by the wear. Figure 6.52 provides the hot band migration plots under different wear rates. It shows that, at relatively lower (0.5×10^{-13} m^3/Nm) and higher wear rates (2.5×10^{-13} m^3/Nm), the hot band migration was significant in terms of radial migration distance compared to the medium wear rate ($1\text{-}2\times10^{-13}$ m^3/Nm).

For the lower wear rate (0.5×10^{-13} m^3/Nm) model, two hot bands developed on both sides of the disc. Initially, the contact occurred at the inner and outer radii and rapidly migrated toward the mean radii. Due to the rapid and long distance migration, the wear of the pad was relatively uniform and didn't significantly change the pad contact surface shape. Therefore, a repetitive hot band migration pattern was observed throughout the 9 braking events.

For the medium wear rate (1×10^{-13} m^3/Nm) model, the higher wear rate triggered the changing of pad contact zones which caused the alternation of the contact zones and hot band migrations between braking events.

Regarding the results of the greater wear rate (2-2.5×10^{-13} m^3/Nm) models; due to the relatively high wear-thermal localisation ratio which cancelled the effects of wear, the hot bands were more difficult to become localised at a given radii. Thus the greater wear rate facilitated the radial migrations of the hot bands in the performed simulations.

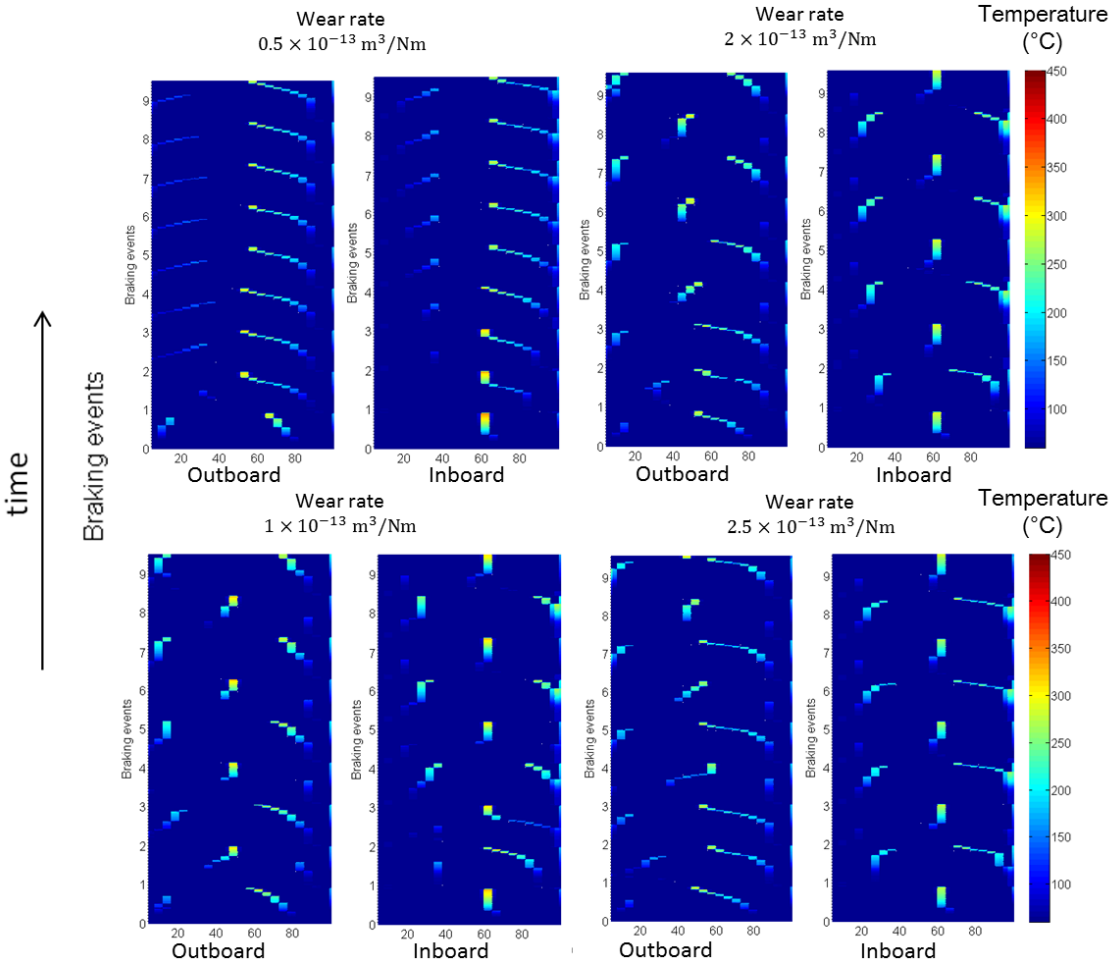

Figure 6.52 Effects of wear rate on peak temperature migration

In addition, Figure 6.53 illustrates the hot band migration results when the wear rate was zero. It was found that two hot bands developed at identical locations on the outboard disc surface in each of the braking events and exhibited minor radial migrations. A single hot band developed at the mean rubbing surface of the inboard disc surface and no migration was observed. No alternating of the hot

bands or significant migration were found in this model revealing that wear was the most significant determinant of both in-stop and between-stops hot band/spot migration in the present study.

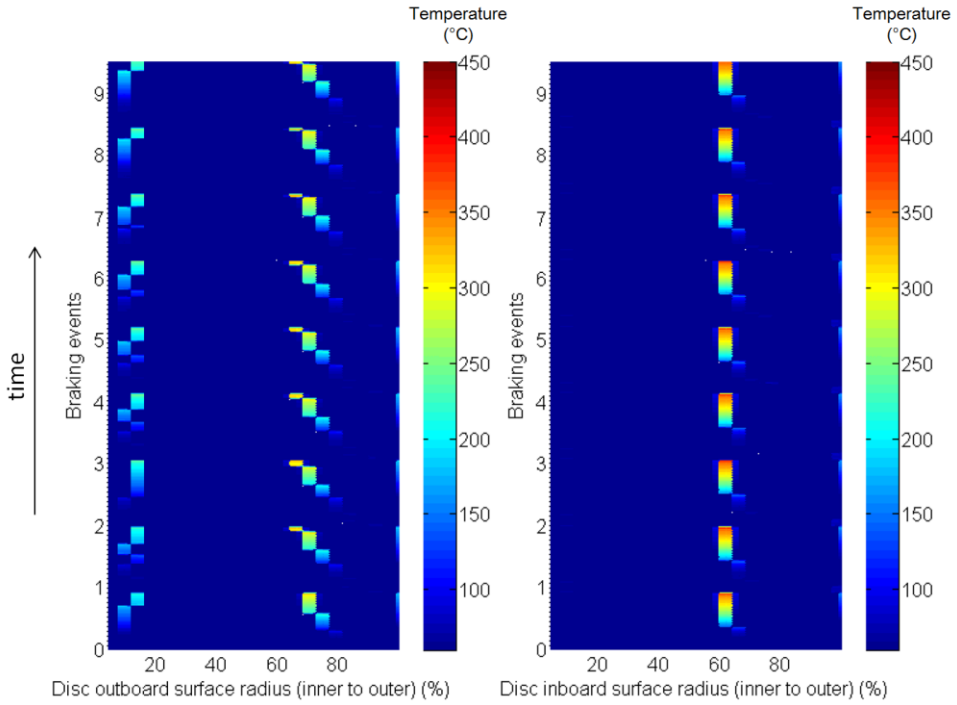

Figure 6.53 Simulated results of hot band migration with zero wear rate applied to the model.

6.6.5 *Effects of pad length*

The modelling results from section 6.4.6 showed that pad length was one of the determinants of hot spotting number and magnitude. Regarding the effects of pad length on the radial migration of hot band/hot spots; Figure 6.54 illustrates that significant migrations developed in the shorter pad (24°) model and two hot bands were developed on each side of the disc throughout most of the 9 braking events.

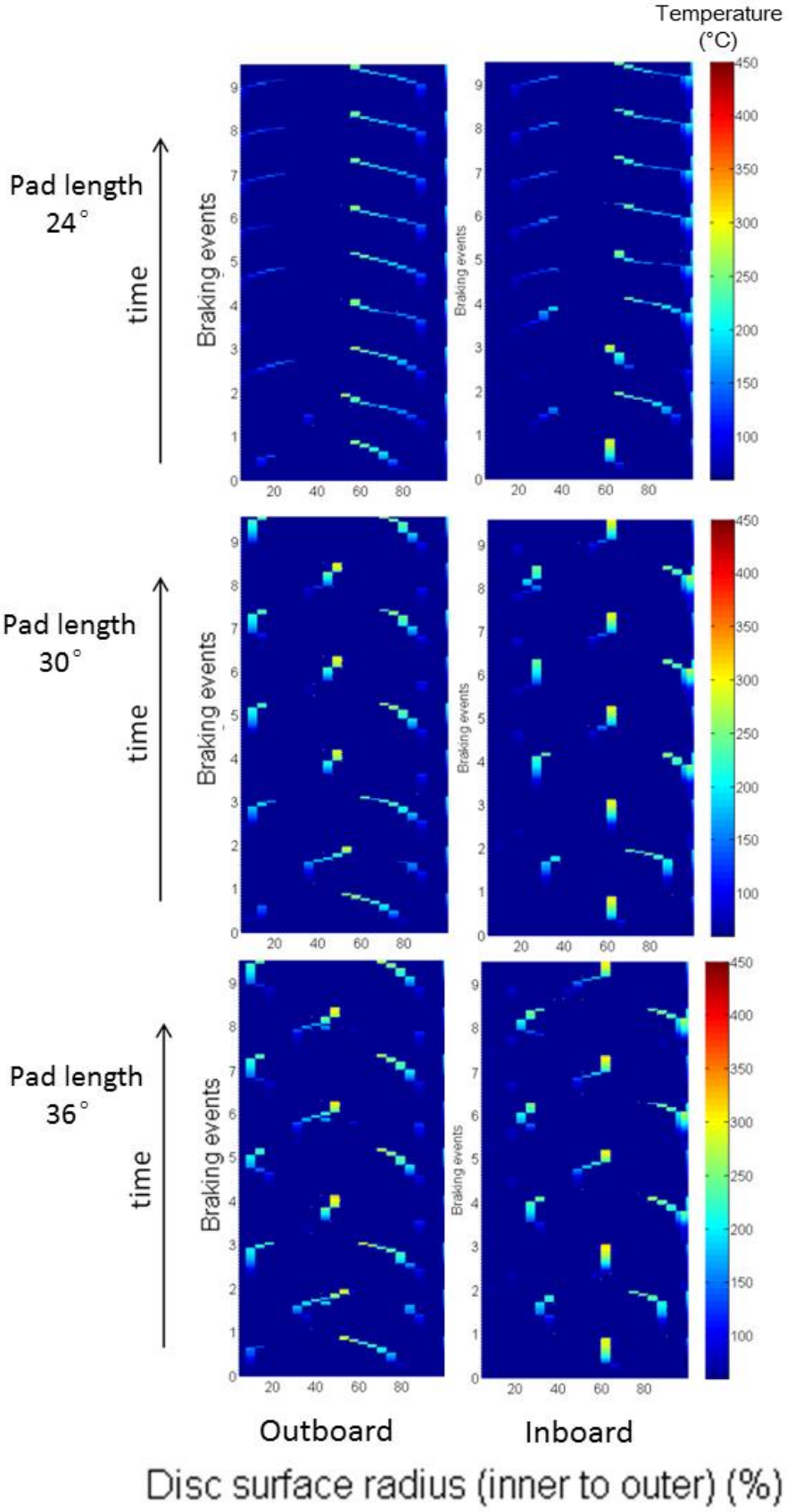

Figure 6.54 Effects of pad length on peak temperature migration

6.7 Summary

In this chapter, the 2D hot spotting models were established in both in-plane and out-of-plane modes. By implementing the axisymmetric pad assumption and user-subroutine FRIC, 17 anti-symmetrically distributed hot spots were developed in the 2D in-plane model which matched the experimental results in Chapter 5. Through the parametric studies, the influences of material properties, vents, pins, speed and loads, cooling effects, and pad length were investigated. The results suggested that

1) Increasing back-plate Young's modulus, disc Young's modulus, disc thermal expansion coefficient, pad thermal conductivity, pad Young's modulus, pad thermal expansion coefficient and decreasing disc and pad heat capacity can boost hot spotting both in aspects of maximum temperature and growth rate.
2) The comparison between solid and ventilated disc geometries revealed that the existence and the design parameters (disc thickness, vane height, vent thickness and vent number) of vents affected the number of hot spots and displacement magnitude due to the periodic structural interference. Meanwhile, the magnitude of hot spot temperature and displacement were affected by the disc bulk deformation.
3) Regarding the effects of speed and load on hot spotting, the results indicated that disc speed was more significant in determining the number of hot spots. The hot spot temperature was mainly affected by the total energy input level.
4) The model with partially blocked vents demonstrated that uneven cooling can boost the uneven temperature distribution and hot spotting. However, if the cooling performance of all the vents increased or decreased uniformly, only the hot spot magnitude (temperature and displacement)

was affected rather than the distribution.

5) The disc mounting pins provided periodical constraints to the in-plane models which did not affected the number of hot spots in this case but significantly affect the magnitude of both lower order run-out and higher order hot spots i.e. the thermal energy was redistributed between bulk and macro effects due to the pins.
6) The investigations of pad length showed that for both solid and ventilated discs, increasing the pad length will increase the maximum temperature. When the pad length was longer than the shortest possible hot spot wavelength (distance between hot spots, 360°/17 in this model due to geometry factors), no hot spots were generated. But when the pad length was greater than the shortest wavelength, the number of hot spots decreased with the increasing pad length.

To investigate the mechanism of hot spotting several in-plane models under different level of simplifications were performed (see Table 6.3). The results revealed that the incorporating of the contact pressure dependent heat generation through a user subroutine was significant to the modelling of hot spotting. It was also demonstrated that the hot spot cannot be triggered only by the clamping of the pad and the thermo-mechanical deformation due to uneven disc structure. In addition, the moving heat source models showed similar results to the continuous heating models which implied that the sliding effects without traction force were insignificant to hot spotting as suggested by Dow and Burton (1972), Lee and Barber (1993) and Zagrodzki *et al*. (2001). Moreover, the comparison of the computing efficiency suggested that the axisymmetric pad model with contact pressure dependent, and stationary heat source, was the most effective model in this research.

Moreover, the out-of-plane hot spot models were performed to investigate the generation of hot spots and their radial migration. By implementing the wear model using a user-subroutine, the interactions between thermal localisation and wear were predicted. The hot spot/band radial migration results were validated using a thermal camera. Through the parametric studies in terms of effects of pad material properties, disc coning, loading distribution, wear rate and pad length; a cause effect chain of the radial hot spot/band migration was obtained.

The results suggest that the initial contact area of the contact interface for each braking event was determined by the mechanical loads and the wear history; then, hot spots/bands generated due to thermal localisation effects at the initial real load bearing areas; during the braking events, the coning of the disc affected the radial movement of the load bearing area and caused the ‘in-stop’ hot band migrations; the periodical ‘between stops’ migration was mainly attributed to the thermal deformation of the disc and the wear depth distribution of the pad.

Therefore, to reduce the hot band migration and reduce the resulting brake torque variation; reducing the thermal expansion coefficient, heat capacity and wear rate of the friction materials; increasing the pad Young’s modulus, thermal conductivity and pad length; and improving the design of disc in terms of coning are suggested.

Chapter 7 3D FE Modelling of Hot Spotting

7.1 Introductions

The intention of the 3D modelling was to provide better understanding of hot spotting mechanism especially in the aspects that the 2D models were limited such as more realistic geometry and boundary conditions. Meanwhile, the 3D geometry of the disc can provide a more like-for-like comparison with the actual experiment due to fewer geometric simplifications. In this section, the 3D FE prediction of hot spotting will be performed for a ventilated brake disc. To further investigate the determinants of the hot spots, parametric studies will be performed including the effects of vents, pins, initial run-out, speed, load, cooling and pad length. By comparing the results of both 2D and 3D models, more insight regarding the mechanism of hot spotting will be revealed.

7.2 3D Axisymmetric pad hot spotting models

7.2.1 *FE Model setup*

The brake system and braking conditions of the 3D finite element hot spotting model was identical to the actual braking measurements performed on the dynamometer discussed in chapter 5 and the 2D models performed in chapter 6. The real disc geometry and the axisymmetric pad assembly (friction material with back-plates) and boundary conditions are shown in Figure 7.1 (right half). The brake disc was a two piece ventilated brake disc using 17 pins to connect the friction ring and the top-hat as illustrated in Figure 4.5. The material properties and braking conditions are provided in Table 6.1. The simulation was performed under 25.5bar line pressure at a constant disc speed of 976rev/min (drag braking) which was equivalent to ~150km/h for 24s. The brake pressure was uniformly applied on the back-plate surfaces. The axisymmetric pad and stationary disc

assumptions were implemented in this model and the material properties and load were scaled based on the scaling factor method discussed in chapter 5. Regarding the boundary conditions, the back-plates were constrained only in the radial direction so that the brake pads were free to move in the axial direction, and the friction material could thermally expand in the radial, axial and circumferential directions. The initial temperature was set to 60°C throughout the model to match the experimental results. Convective heat transfer coefficient on the disc surface was set to 100W/m^{2}K and the vents were 130W/m^{2}K based on experimental estimation. Radiative heat dissipation was considered small (Limpert, 1975 and Tirovic, 2013) and neglected in this model.

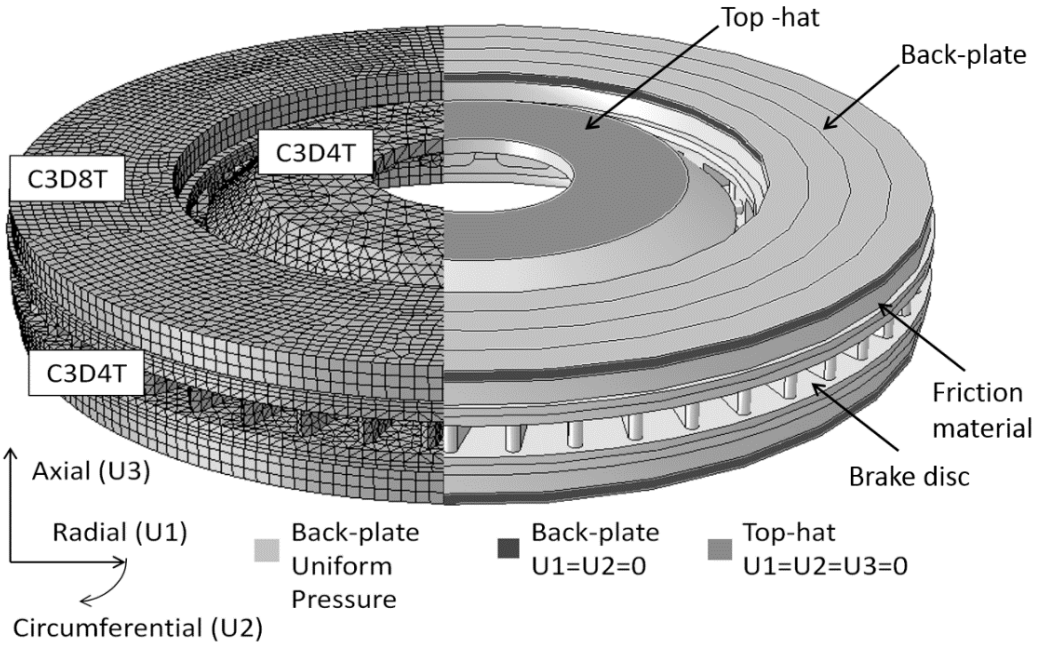

Figure 7.1 Mesh (left half) and boundary conditions (right half) of the pin-mounted ventilated brake disc brake FE model

The mesh of the disc and pads close to the contact surfaces were refined in order to achieve accurate prediction of hot spotting, since the deflections of the thermal localisation were generally much smaller than the disk thickness. Due to the complicity of the 3D disc geometry both C3D8T: 8-node hexahedron and C3D4T 4-node tetrahedron thermally coupled temperature-displacement elements were used in this model as shown in Figure 7.1 (left half). For the top-hat and the

ventilated layer, tetrahedron elements were used, whilst for the contact surfaces of disc and pad, hexahedron elements were used to provide a balance between accuracy and efficiency of the prediction.

Due to the absence of rotation, the heat generation was defined by a user subroutine; FRIC. In order to define the radial dependent linear velocity, the radial positions of the nodes on the disc surface were considered in the compiling of the subroutine. Since there was no rotation considered in this model and there was only one brake application simulated, effects of wear were not included in this model. The computing time for this 3D model was ~10 hours using a standard PC (computer specifications listed in Appendix 5).

7.2.2 *Mesh sensitivity study*

A mesh sensitivity study was performed in order to identify the proper approximate global element size for the 3D model. As discussed in section 3.3.6, a limitation of the implicit solver is that the required memory was greater than the explicit method. The minimum element size that could be meshed was 4.5 mm due to limitations with the computer hardware and since the implicit solver has higher memory utilisation. Figure 7.2 shows the maximum temperature predicted by the 3D model with different element sizes. It shows that when the element size was smaller than 6.5, the maximum predicted temperature stabilised at ~650°C. In addition, Figure 7.3 shows that when the element size was greater than 6, the predicted number of hot spots decreased due to the reduction of ‘mesh resolution’. The number of hot spots became consistent at 17 when the element size was smaller than 6mm. Therefore, considering both the accuracy and the hardware capability, an element size of 4.5mm was used for the 3D model.

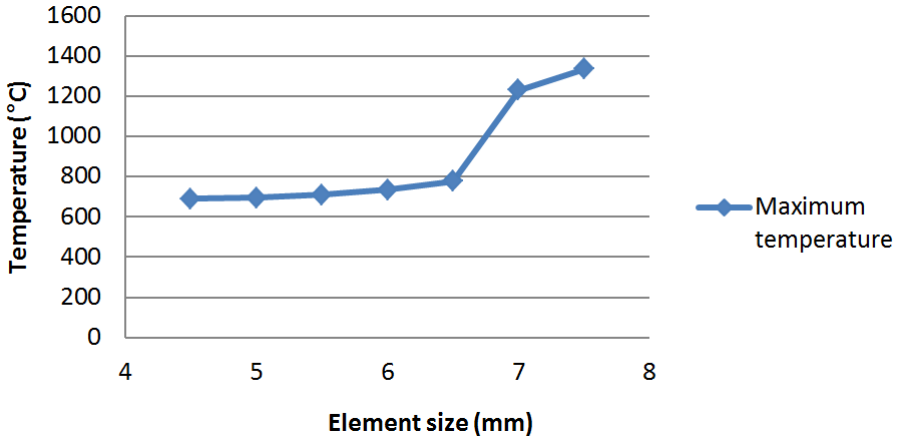

Figure 7.2 Mesh sensitivity test of maximum temperature vs. element size for the 3D axisymmetric model

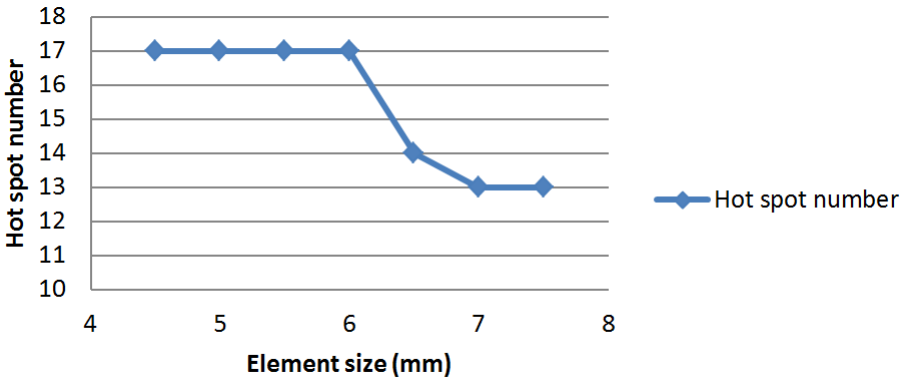

Figure 7.3 Mesh sensitivity test of number of hot spots vs. element size for the 3D axisymmetric model

7.2.3 *Simulation results*

The development of the outboard friction ring temperature distribution is shown in Figure 7.4. It can be seen that a hot band was initiated towards the outer radius of the disc surface at 6s. A circumferential temperature difference, indicating the onset of hot spotting, was observed at 15s. At the end of the braking event (t=24s), 17 hot spots had clearly developed. This was equal to the number of pins and one third of the number of vents, indicating relationship to the disc geometry and friction ring boundary conditions. The maximum predicted temperature was 565°C, and the radial temperature difference between the hot spots and

surrounding disc surface was greater than 150°C.

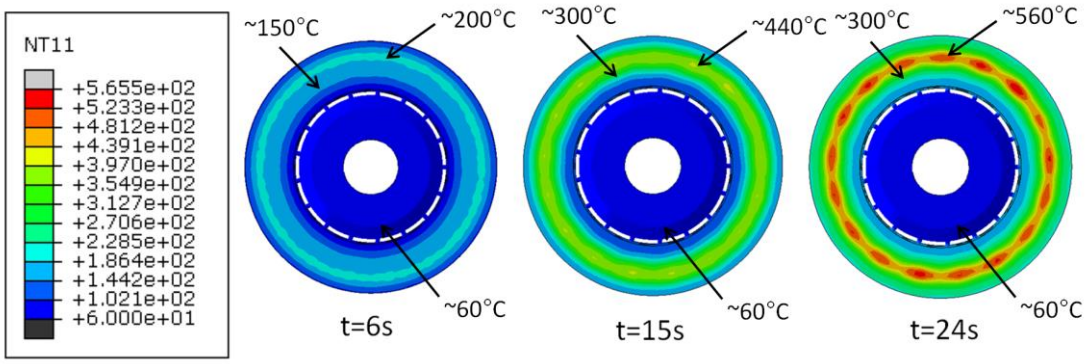

Figure 7.4 FE results showing the surface temperature distribution (°C) and hot spot development at the outboard disc surface

Regarding the temperature distribution between the inboard and outboard disc surface an anti-symmetric mode was observed in Figure 7.5, which is the general automotive hot spot distribution mode (Lee and Barber, 1993, Sardá *el al.* 2008, Bryant, Fieldhouse and Talbot, 2011). It also illustrated that the maximum predicted circumferential temperature variation reached ~100°C. The 3D plot of the temperature growth along the disc angular position at the mean radius was provided by Figure 7.6. It can be seen that there was no circumferential migration of the hot spots and the circumferential temperature gradients increased with time.

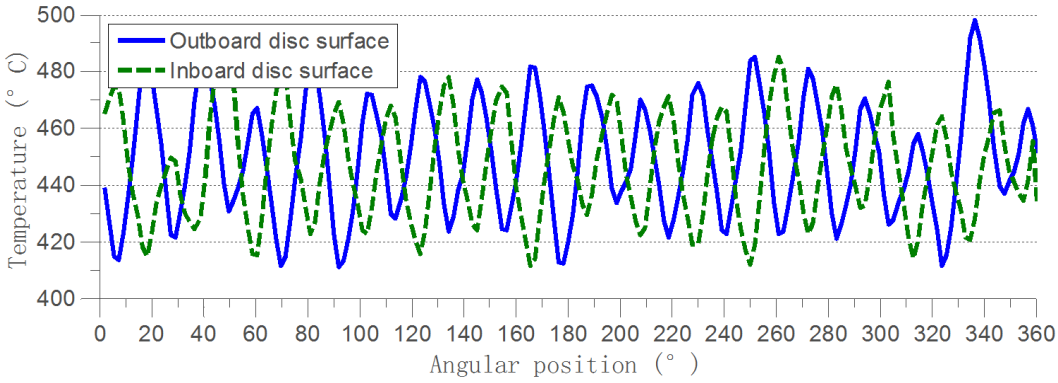

Figure 7.5 Predicted temperature distribution at the end of brake event when measured at the inboard and outboard mean rubbing radius

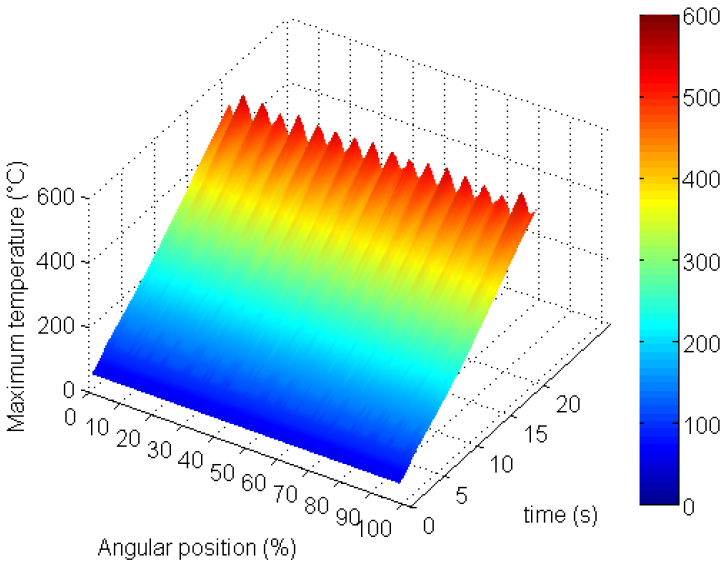

Figure 7.6 3D plot of predicted temperature distribution and growth of the disc mean radius over time

Figure 7.7 provides the axial disc deformation, stress and contact pressure distribution on the outboard disc surface in SI units at 24s. The displacement and contact pressure matched with the temperature distribution as both 17 disc surface ripples (or surface deflections) and 17 high pressure contact zones were observed. Such correlation revealed the significant contribution to hot spotting in terms of the interactions of uneven contact pressure, uneven temperature and uneven deformation. It should be noted that a 2nd order disc distortion was also observed in the displacement field results. It implied the disc run-out due to thermal buckling or TEI could be predicted in both the 2D and 3D hot spot models. In addition, the stress field in Figure 7.7 illustrated the high stress concentration on the mean rubbing radius of the disc surface during hot spotting. Meanwhile, the pins between the rubbing surface and the top-hat showed high stress as a result of the reaction to the deformed disc and the thermal stress due to inward radial thermal expansion.

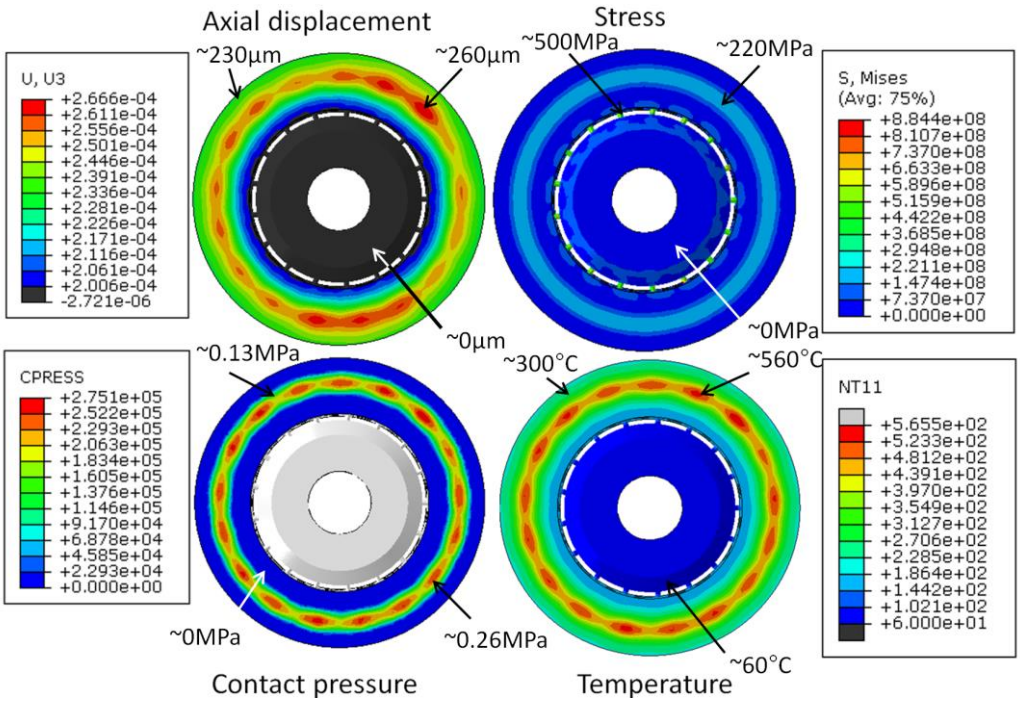

Figure 7.7 FE results showing axial displacement (m), stress (Pa), contact pressure (Pa) and temperature (°C) distributions of the outboard disc surface at 24s

Furthermore, if the drag brake continued and the duration were extended to 48s, the hot spot distribution is illustrated in Figure 7.8 which implied that with the continuous heat flux input and the total increase of thermal energy, the hot spots merged together into macroscopic hot spots with greater temperature (2386°C at 48s). This is clearly an over prediction of the temperature as a result of the inability of the model to predict thermal fade or plastic deformation.

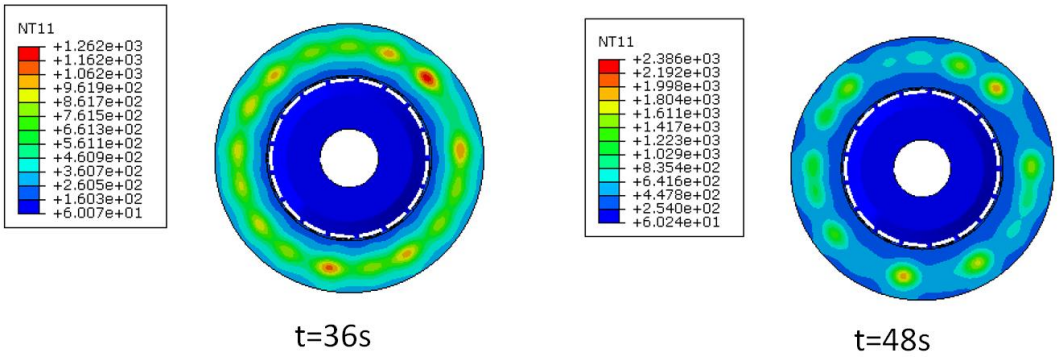

Figure 7.8 Temperature distribution of the ventilated disc if the simulation was extended to 48s

7.2.4 *Comparing 3D with 2D FE results*

A comparison of the circumferential temperature distribution at the mean rubbing radii for both the 2D in-plane model and the 3D model is presented in Figure 7.9. It shows that both 2D and 3D models generated 17 hot spots. The maximum temperature variations (thermal gradients) were both ~100°C. However, the average temperature of the 2D model was ~100°C lower than the 3D. It revealed the limitation of 2D hot spotting models whereby the radial thermal localisation/variation cannot be obtained so the radial temperature in the 2D in-plane model was only the radial average value.

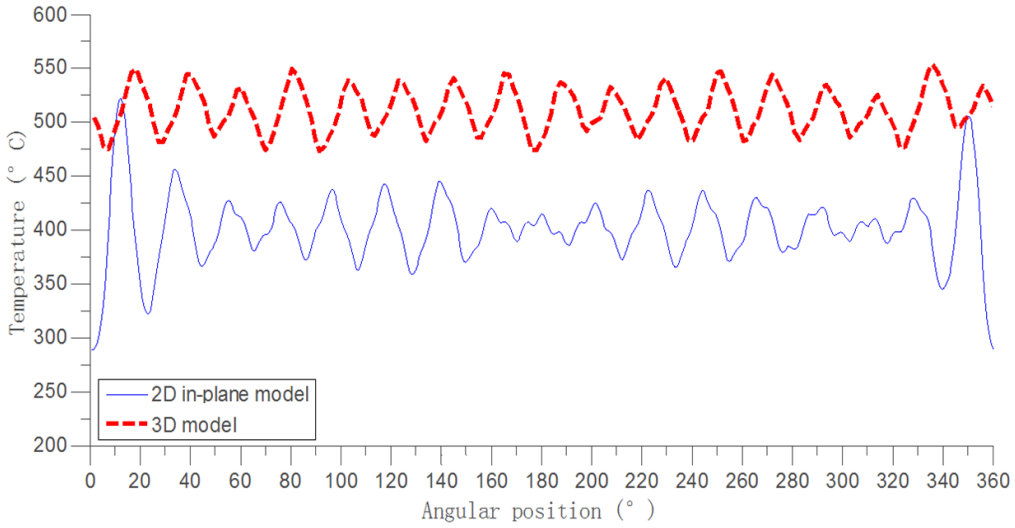

Figure 7.9 Circumferential temperature distributions at the mean rubbing radii of both the 2D in-plane model and the 3D model

Moreover, when the applied brake pressure on the inboard and outboard back-plates changed from uniform to asymmetric to simulate the sliding fist caliper (like the 2D out-of-plane model of Figure 6.36), the temperature distribution through the cross section of the 3D model is plotted in Figure 7.10. It can be seen that two hot bands developed on the outboard surface at the inner and outer radii respectively and one hot band developed at the mean radius of the inboard surface. The results matched well with the observations shows in section 6.5 and 6.6.

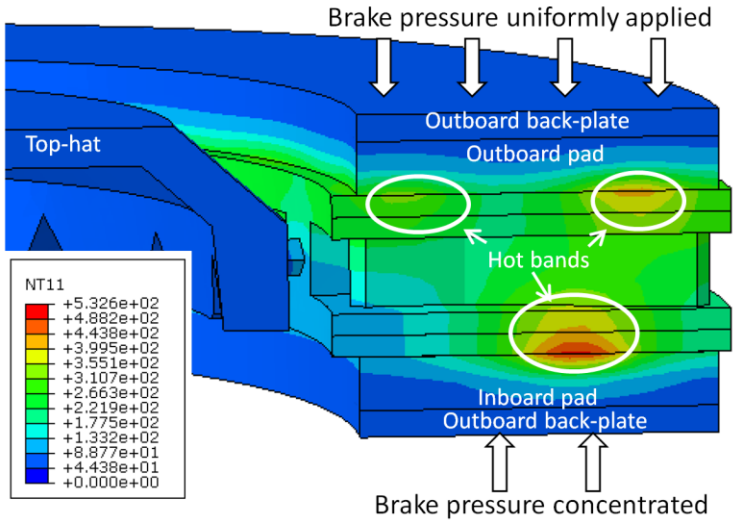

Figure 7.10 Temperature distribution through the cross-section of the disc and pads at 24s

The comparison between the 2D and 3D results illustrated that both the 2D in-plane and out-of-plane models underestimated the hot spot temperature due to the fact that the radial and circumferential thermal localisations cannot be reproduced respectively.

7.2.5 *Experimental validations*

The arrangement of the dynamometer transducers was previously shown in Figure 4.4. Multiple transducers were used including capacitive displacement transducers, pressure transducers and thermocouples. The physical tests and numerical simulations were performed under the same test conditions to provide a like-for-like comparison. The comparison of surface temperature evolution over time for both the experiment (rubbing thermocouple mounted at the mean rubbing radius) and the simulation results (a single node at the mean rubbing radius) is provided in Figure 7.11. The results illustrated that the numerical maximum temperature overestimation (510°C vs. 460°C) was only 6% which is acceptable considering the likely difference between the radial positions of the hot band when compared to that of the rubbing thermocouples.

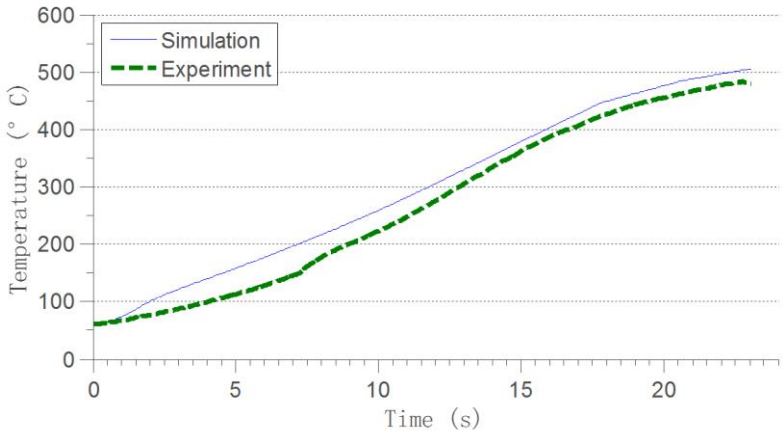

Figure 7.11 Temperature comparison between simulation and experiment at the mean rubbing radius of the outboard disc surface

The global temperature distribution was also obtained by infrared thermal imaging in the experimental studies. The comparison between thermal image and simulation is shown in Figure 7.12, which indicates that in terms of radial and circumferential distribution and the magnitude of the temperature gradients the simulation match well with the experiments. In addition, the hot spots were located between the pins in both simulation and experiment in terms of angular position.

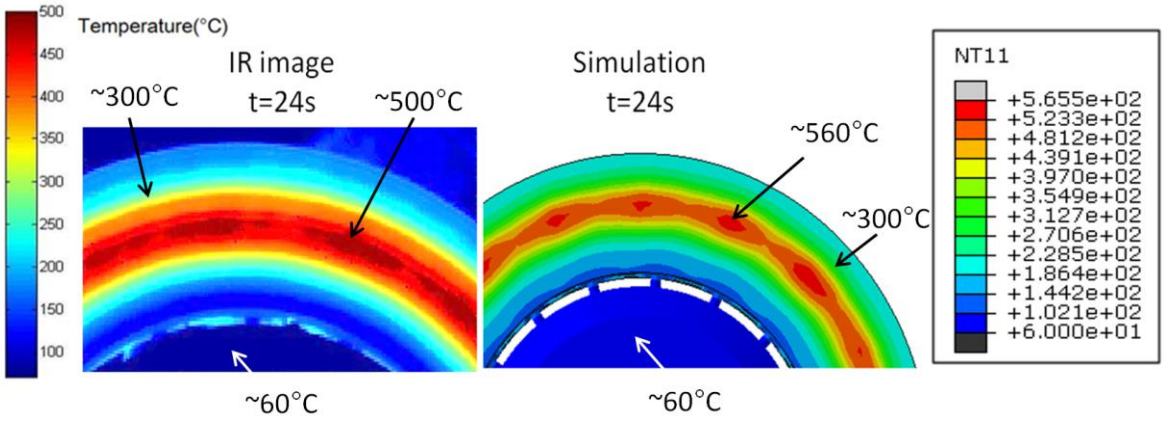

Figure 7.12 Thermal imaging (IR camera) of the brake disc outboard surface (left) and simulation results (right; °C) 24 seconds into the braking event

In the experiment, the outboard and inboard disc distortion were measured using displacement traducers with high sample rate (50kHz) that enabled the measurement of the disc surface ripples due to hot spotting. According to Figure 7.7, the height of hot spots predicted in the axisymmetric model was ~5 to 15 μm which matched well with the experimental measurements (~5 to 15 μm) as shown in Figure 4.10. Both the experimental results and the 3D FE models predicted an anti-symmetric distribution of the hot spots on the inboard and outboard friction rings.

7.3 3D Hot spotting parametric study

The theoretical debates identified in the literature mainly concentrated on the trigger condition of hot spots (critical speed vs. energy input), effects of disc structural characteristics (vents, pins, solid or ventilated), initial disc run-out and pad length. Therefore, to investigate the effects of these determinants on hot spotting and to complement and extend the 2D parametric studies from section 6.4, parametric studies were performed using the 3D hot spotting model established in section 7.2.

7.3.1 *Influence of periodic disc geometry: vents*

As discussed in section 2.6, the modelling of hot spotting of ventilated brake discs has had less focus than with solid discs in the previous published literature. Therefore, solid disc models were generated using the same axisymmetric pad method in order to investigate the effects of vents on hot spotting. According to Limpert (1975), to achieve a like-for-like comparison in terms of thermal mass (i.e. equivalent temperature rise), the effective solid rotor thickness for a ventilated disc should be three times of the one rotor plate. As shown by Figure 7.13, the rotor plate thickness was 9mm, therefore the effective solid rotor thickness was 27mm. Moreover, a double-thickness rotor plate solid disc model was also generated to investigate the effects of rotor thickness on hot spotting.

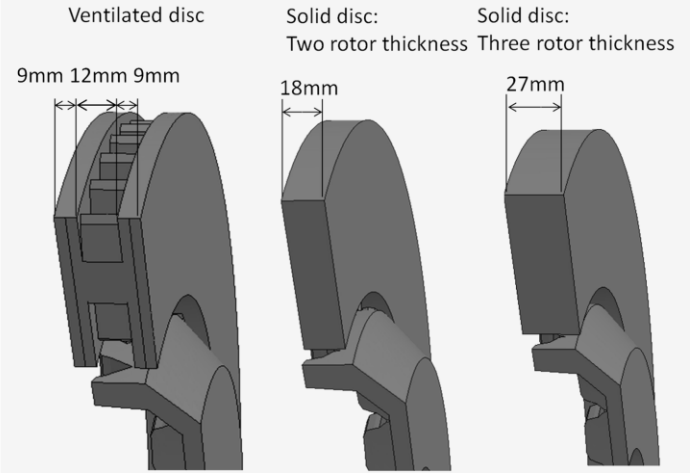

Figure 7.13 Thickness of the ventilated brake disc and solid brake discs for the parametric FE study

The surface temperature distributions of the ventilated and solid models are shown in Figure 7.14. The 3D plots of the temperature distribution and growth of the ventilated and solid discs are shown in Figure 7.6 and Figure 7.15 respectively. The results illustrated that there were 17, 13 and 16 hot spots appeared and the maximum temperature were 589°C, 689°C and 635°C respectively for the ventilated, 18mm rotor thickness and 27mm rotor thickness solid disc models. The number of hot spot did not change along the brake application. It implied that fewer hot spots were generated in the solid discs and the thicker disc generated more hot spots but lower temperature. In addition, Figure 7.15 shows that the thinner solid disc had greater circumferential thermal gradients than the thicker disc. Therefore, it is clear that the periodic vent and pin structure of the ventilated disc redistributed the braking energy into 17 sections and resulting 17 minor hot spots comparing with the solid disc. Moreover, it should be also noted that the distribution of hot spots were in anti-symmetric mode in the two solid models. It seems that the increase of the total thermal mass can reduce the bulk disc temperature and the hot spot temperature.

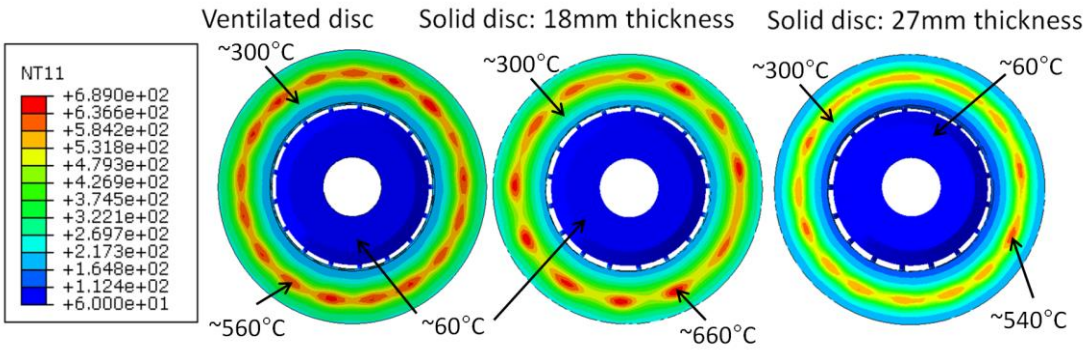

Figure 7.14 FE results showing the outboard brake disc surface temperature distributions (°C) of different brake disc structures (ventilated vs. solid) at 24s

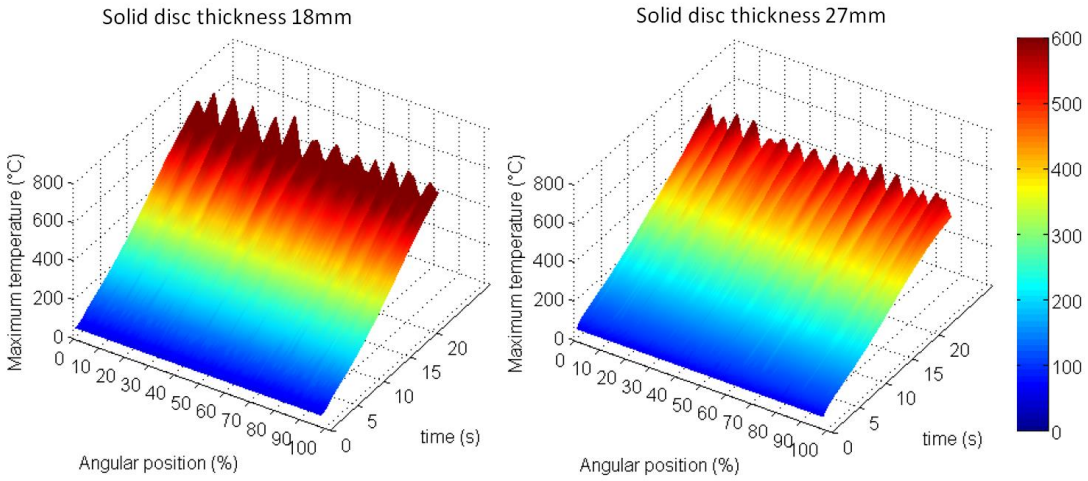

Figure 7.15 3D plot of temperature distribution and growth of the disc mean radius for 18mm and 27mm thickness discs

7.3.2 *Influence of periodic disc geometry: pins*

As identified in section 6.4.3, two potential ways in which the disc-hat mounting pins can affect hot spotting are: mechanical constraints or periodic extra thermal mass (or conduction). To further complement the 2D model, the structural perturbation effects were studied by modifying the elasticity modulus and specific heat capacity of the pins. A comparison of the temperature distribution results is shown in Figure 7.16. It illustrated that when the elastic modulus of the pin was reduced by 10 times, the overall temperature was ~100°C lower than the standard model, and the circumferential temperature variation was smaller as

well. When the elastic modulus of the pin was increased by 10 times, the overall temperature was still 50°C lower than standard, and the temperature variation was smaller as well. This meant that the temperature distribution in the radial direction was more even than the standard model since the total thermal energy into the disc was identical. The results revealed that the “soft pins” provided more even temperature distribution since there were fewer constraints, or more flexibility, for the disc to expand. For the “stiffer” pins, these constrained the circumferential expansion of the disc and caused a more even radial temperature distribution than the standard model.

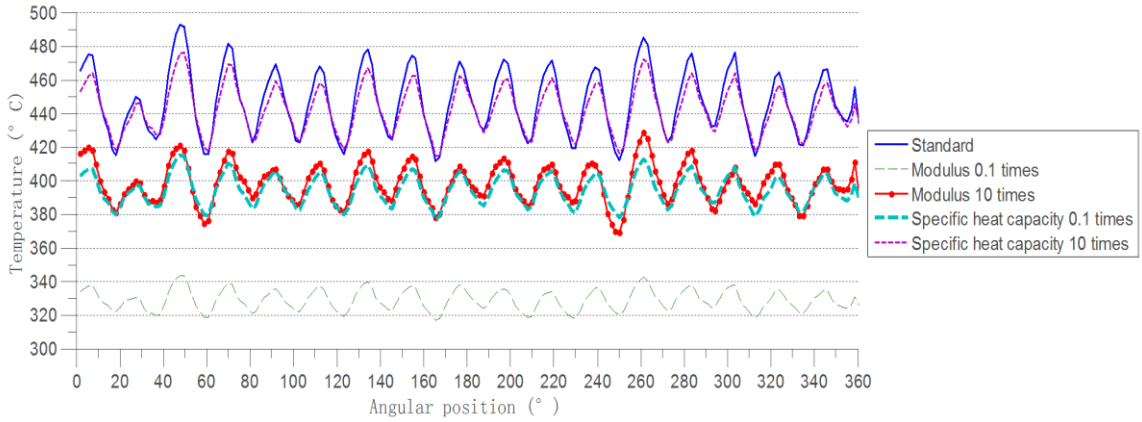

Figure 7.16 Comparison of temperature distribution for various pin material properties

Regarding the heat capacity of the pins, the results suggested that a reduction of the specific heat capacity reduced the overall temperature and thermal gradients. From Figure 4.17 and Figure 4.18, it shows that the hot spots and pins were anti-symmetrically distributed, which means that the reduction of the heat capacity will increase the temperature of areas near the pins hence reduce the thermal gradient. However, there was no apparent difference in temperature when increasing the specific heat capacity of the pins when compared to the standard model.

In addition, it was clear that the relationship between hot spots and each thermal material property was nonlinear, which means there may be some interaction terms between the factors. Therefore, a two parameter three level full factorial DOE was performed to identify the interactions between the Young's modulus and heat capacity of the pins with regards to hot spotting. Figure 7.17 (left) was plotted to show the maximum hot spot temperature under various combinations of the parameters. Again it illustrated that the main effects of both Young's modulus and heat capacity on hot spot temperature were nonlinear. The 'wrapped' shape of the surface plot demonstrated the significant interactions between the two properties. It shows that with increasing heat capacity, the positive correlation between Young's modulus of the disc pins and hot spot temperature becomes more clearly defined. In addition, Figure 7.17 (right) presents the average brake disc surface temperature under the influence of the same parameter combinations. This result illustrated an almost inverse trend compared to the maximum hot spot temperature whereby an increase in the specific heat capacity would tend to reduce the hot spot temperature. However since the temperature variation of the average surface temperature was within 2°C, the influence of the pins was insignificant. It should be noted that all models generated 17 hot spots. Therefore, the results presented by Figure 7.17 suggested that the effects of pins on hot spotting was complicated and highly dependent on the specific disc design and braking conditions. The effects and interactions of the mechanical and thermal properties of the pin should be both considered in the design process.

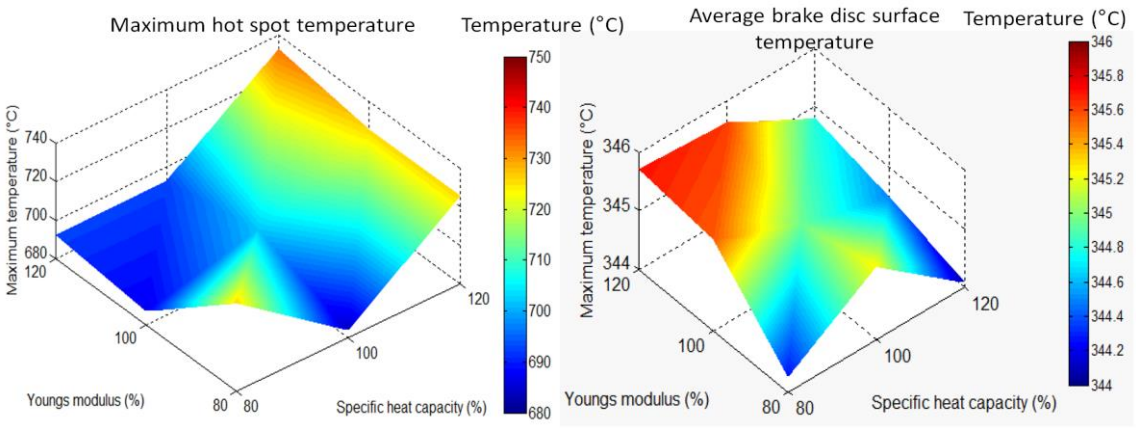

Figure 7.17 Interaction plot showing the variation of maximum hot spot temperature (left) and average outboard brake disc surface temperature (right) from the FE model with differing Young's modulus and specific heat capacity of the pins (100% = 210GPa and 500J/kg K)

In contrast to the two piece pin mounted disc; with a single piece disc the top-hat directly connects to the disc. Therefore, a solid single-piece disc was modelled to remove the effects of both vents and pins and compared to a solid 2-piece disc. Figure 7.18 shows the hot spot distribution comparison for single and two-piece discs with the same temperature scale. It illustrates that the number of hot spots was identical for both models, but the location, shape and temperature were different. The hot spots were localised at the outer radius in the one piece disc model which implied that the coning effects of the disc toward outboard direction had an influence causing the subsequent shift of outboard contact zone toward the outer radius. Meanwhile, the results of the pin mounted disc showed that the hot spots were localised at the mean rubbing surface which showed that the reduced coning had a direct effect on the hot-spot locations. In addition, for the one piece disc, the maximum temperature was 799°C and the hot spots were circular, whereas ellipse hot spots with a temperature of 689°C were developed on the pin mounted disc. The different shape and temperature of hot spots reveals the importance to consider the top-hat and its connection with disc in hot spot simulations. It is believed that the lower coning angle of the two piece disc

resulted in a more uniformly distributed contact pressure and thus lower hot spot temperature.

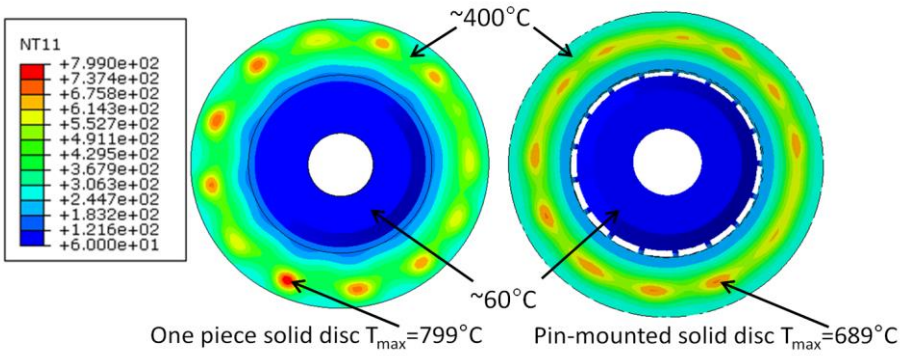

Figure 7.18 FE results of the outboard surface temperature distribution (°C) of a single piece solid brake disc and pin mounted solid brake disc at 24s

7.3.3 *Influence of initial disc waviness*

A 2nd order initial disc run-out was introduced to investigate its influence on hot spotting. The introduced run-out was much greater than the common values (less than 50 µm) in order to provide more apparent comparisons. Figure 7.19 shows the disc inboard mean radius (IBM) and outboard mean radius (OBM) run-out data with and without the initial disc waviness both before and after the single simulated braking event. It illustrated that without initial waviness, the disc thickness expanded by 100µm, whilst 200µm of coning toward the outboard direction was observed at the mean radius. Regarding the simulation with initial waviness; ± 200µm 2nd order run-out was introduced with no initial coning. After the braking event, both inboard and outboard run-outs significantly increased to ~800µm. Meanwhile, the disc thickness growth was less than 100µm and the coning toward the outboard direction was ~200µm.

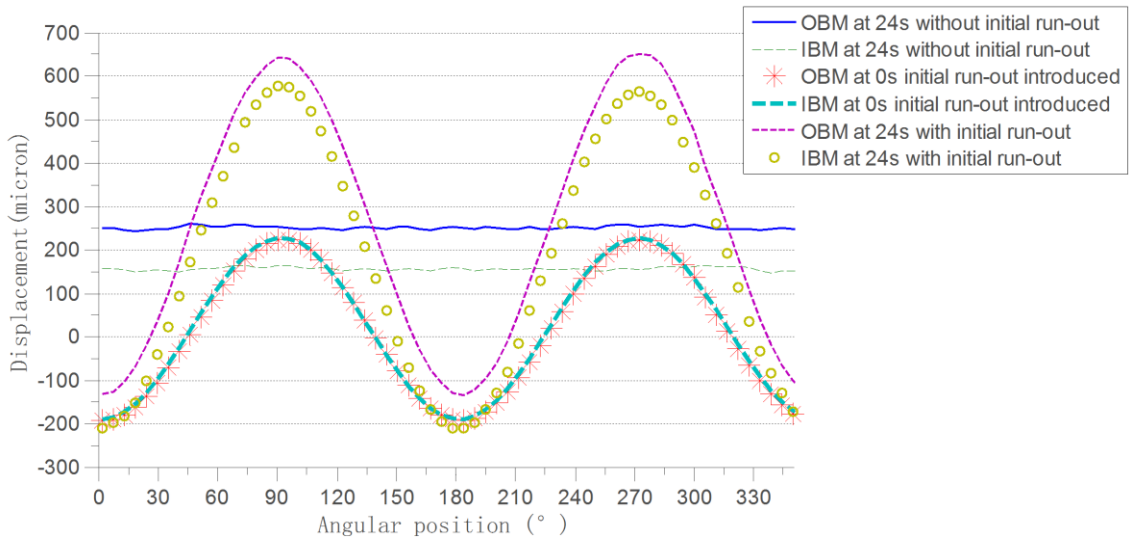

Figure 7.19 Relative displacement of brake disc inboard and outboard surfaces with and without initial 2nd order brake disc run-out before (0s) and after (24s) braking application

Figure 7.20 shows the hot spots overlaid on the 2nd order disc run-out with significant thermal gradients (~200°C). Whilst the standard model without introduced initial run-out developed more uniform 17th order thermal gradients. Thus it can be seen that the run-out redistributed the thermal energy in the circumferential direction and caused more severe hot spotting at the peaks of the 2nd order run-out. Regarding the average disc distortions in terms of their 'order', a power spectral analysis was plotted in Figure 7.21. The results shows after introducing the initial disc waviness, the 2nd order run-out significantly increased whereas the 17th order hot spots decreased in terms of amplitude. It implied that the lower order deformation and thermal localisations were triggered by the initial disc run-out, and that due to the excessive growth of lower order distortions and temperature variation, the magnitude of the hot spots were slightly decreased after introducing the initial run-out.

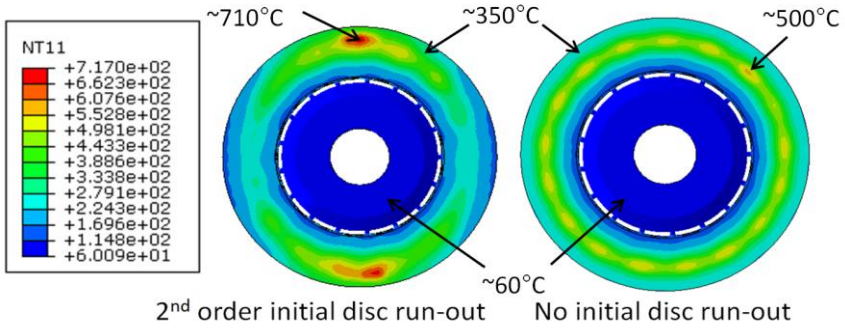

Figure 7.20 FE results showing the outboard brake disc surface temperature distribution (°C) with (left) and without (right) initial run-out

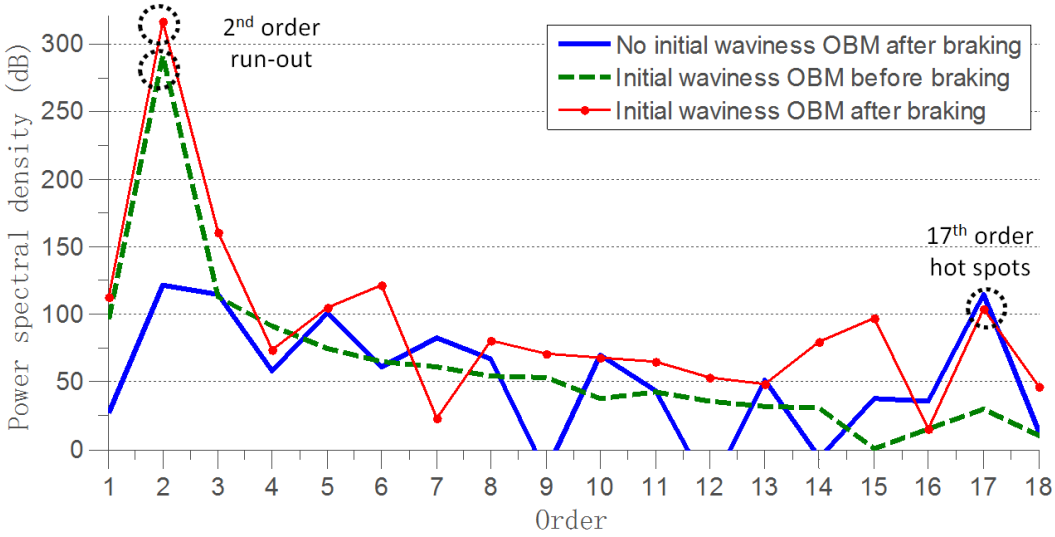

Figure 7.21 Power spectral analysis of the disc displacement with and without introducing initial 2nd order run-out

7.3.4 *Influence of braking operation: constant speed*

Since the debate about the trigger condition of hot spotting was focused on velocity and energy input, drag braking models under different speed and load were generated to investigate their effects. The details of the models are listed in Table 7.1. It can be seen that three velocities and three brake line pressure were given and provided nine combinations. The speed and pressure varied between 2/3, 1 and 3/2 times of the standard condition performed in section 7.2. Therefore, various braking power and energy input under the same speed or pressure were

able to be compared. In order to compare the hot spotting phenomena at the same braking time or same energy input condition, the brake duration was set to be as a function of brake power and all greater than 24s. Solid discs were selected in this study in order to remove the effects of periodic disc structure of the ventilated disc.

Table 7.1 Loading conditions of the nine models for hot spotting trigger condition investigation

Model ID	Disc speed (rev/min)	Vehicle speed (km/h)	Pressure (bar)	Power (kW)	Brake duration (s)	Energy at 24s (MJ)	Time that same energy input achieved (s)
1	654	100	17.1	22.9	54	0.6	54
2	654	100	25.5	34.2	36	0.8	36
3	654	100	38.3	51.3	24	1.2	24
4	976	150	17.1	34.2	36	0.8	36
5	976	150	25.5	51.0	24	1.2	24
6	976	150	38.3	76.6	24	1.8	16
7	1460	225	17.1	51.2	24	1.2	24
8	1460	225	25.5	76.3	24	1.8	16
9	1460	225	38.3	114.6	24	2.8	11

Figure 7.22 shows the outboard brake disc temperature distribution of the models at the same braking time (24s). The maximum temperature and time are given for each plot. The figure illustrated that at the same speed, the maximum temperature increased with increasing pressure but the hot spot distributions were similar. At the lowest speed (654rev/min) in the study, only hot bands appeared. At 976rev/min 12 hot spots were equally distributed on the mean brake disc rubbing radius. Since no wear and temperature dependent material property effects were considered in the models, the results of model 7 to 9 at 1460rev/min were discarded as the maximum hot spot temperature predicted was unrealistically high. In addition, when both speed and pressure were increased, the maximum temperature increased with the total energy input. But for identical brake power (Model 4 vs. 2 and 5 vs. 3); the high speed low pressure models

provided apparent hot spotting compared with the low speed high pressure models. Therefore, the comparison at the same braking time (24s) illustrated that the brake disc speed is more important than braking power and pressure in determining the hot spot distribution.

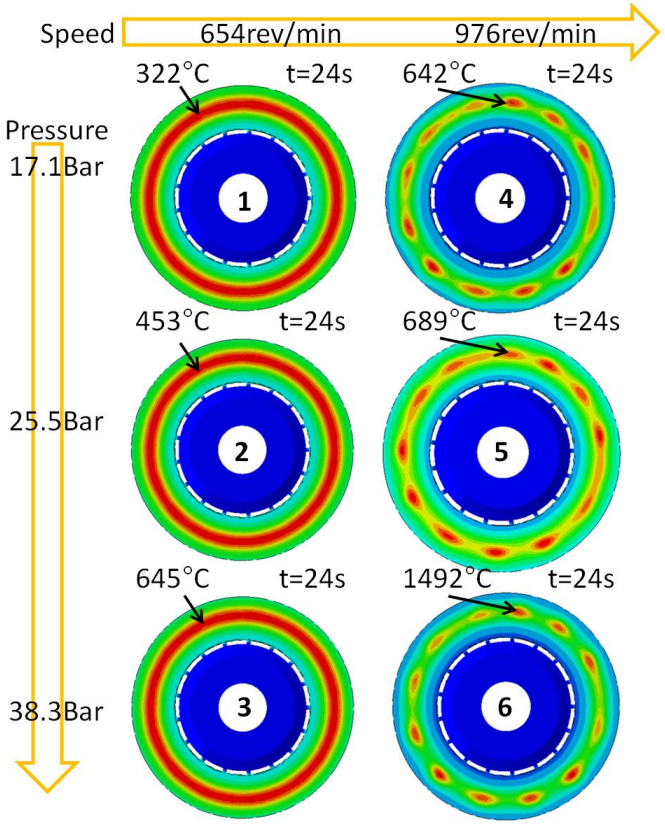

Figure 7.22 Outboard brake disc surface hot spot distribution and maximum brake disc temperature (indicated on figure) of the FE model at 24s at different speeds and loads

Figure 7.23 provides a comparison for different speed and pressure at identical total energy input into the brake disc (by varying the brake duration). It is clear that at the same energy level, the hot spot distributions were affected by speed and pressure. At the lowest speed in this study (654rev/min), there was no hot spotting, but the maximum temperature was increased with the pressure. At 976rev/min, the hot spots were more distinguished and with decreasing pressure, more heat was concentrated into each hot spot giving greater temperature.

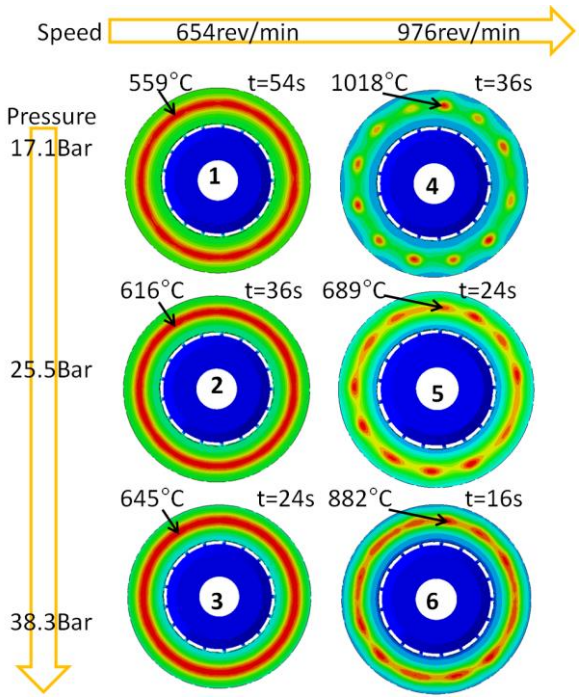

Figure 7.23 Outboard brake disc surface hot spot distribution and maximum brake disc temperature (indicated on figure) of the FE models with the same energy at different speeds and loads

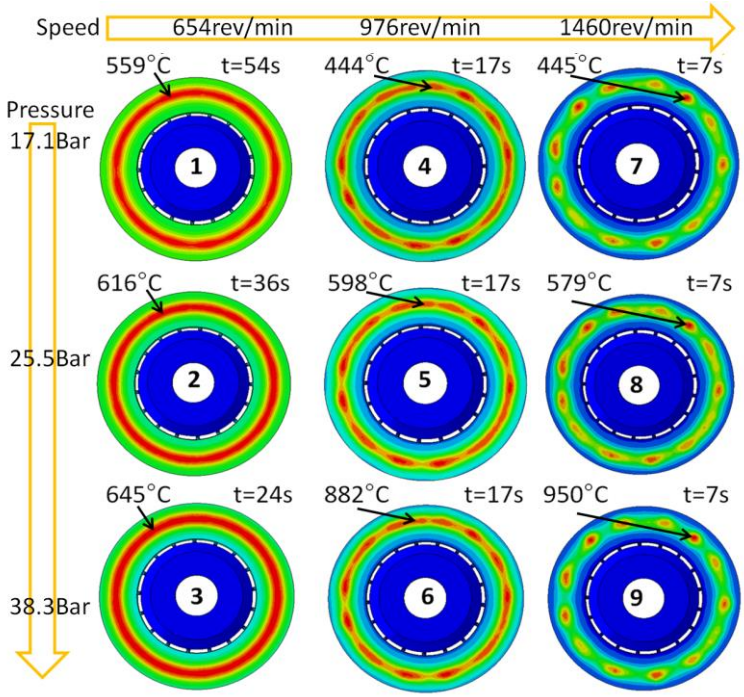

Figure 7.24 Brake disc outboard surfaces temperature distribution and maximum temperature (indicated on figure) of the FE models at the moment that hot spots appeared at different speeds and loads

Regarding the occurrence time of hot spots, Figure 7.24 provides the temperature distribution and the time at which the hot spots became apparent. It can be seen that with differing pressure, there was no change in the hot spot or hot band distribution or the time at which the hot spots appeared. The only difference is that the maximum temperature increased with increasing pressure. In addition, 12 hot spots appeared at 17s at 976rev/min, whilst 12 more distinguished hot spots can be observed at 7s at 1460rev/min. Therefore, it is clear that the hot spot distribution and trigger time were affected by the brake disc speed; greater the speed, shorter the trigger time with clearer hot spots.

7.3.5 *Influence of braking operation: deceleration*

Table 7.2 Loading conditions of the four hot spotting models for deceleration effects investigation

Model ID	Initial speed to end speed (km/h)	Deceleration (g)	Pressure (MPa)	Average power (kW)	Brake duration (s)	Total energy (MJ)
1	100	0	2.55	34.2	24	0.8
2	150 to 100	0.1	1.28	21.4	24	0.5
3	150 to 50	0.2	2.55	34.2	24	0.8
4	150 to 0	0.3	3.83	38.5	24	0.9

Since the main function of the real brake system is to decelerate the vehicle (Limpert, 2011), the simulation of the deceleration process was important for improving the understanding of hot spotting. Table 7.2 lists the models performed at various rates of braking. Due to the differences in deceleration, the corresponding brake pressures were different. The braking duration were all 24s for all four models and the total energy at the end of simulations increased with higher rates of braking except the constant speed case (reproducing the dynamometer condition).

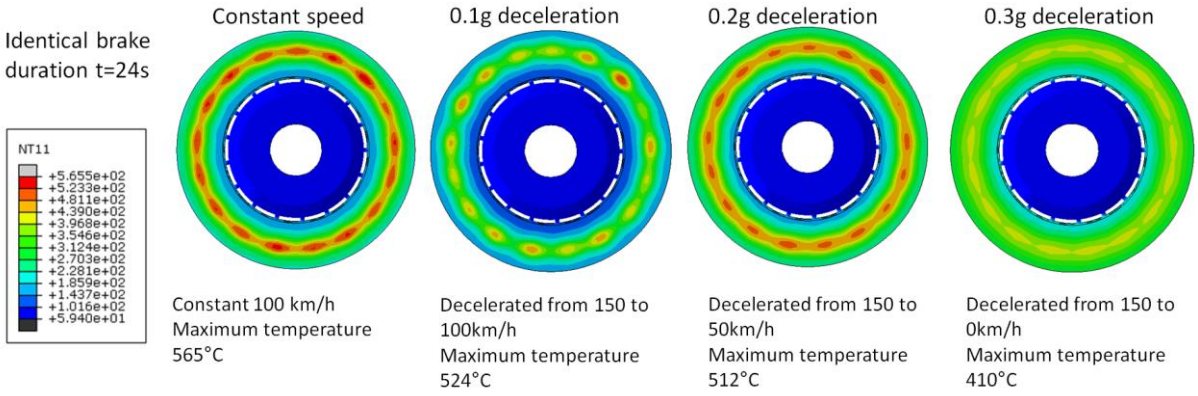

Figure 7.25 Hot spot distribution and outboard brake disc surface maximum temperature (°C) at 24s under different deceleration

The results shown in Figure 7.25 provide the temperature and hot spot distribution of the four models at 24s. First of all, the constant speed case and the 0.2g model showed similar results due to the same applied brake pressure and same equivalent speed. Then, comparing the three deceleration models, it can be found that the maximum temperature of the hot spots decreased from 524°C to 410°C when the deceleration increased from 0.1g to 0.3g. Meanwhile, the hot spots were more distinguished in the 0.1g model in terms of circumferential thermal gradients. The results showed that the pressure, braking power, and total energy of the 0.3g model was greater than the 0.2g and 0.1g models as shown by Table 7.2, but the hot spotting phenomenon was relatively insignificant when the deceleration was greater. It implied that the average speed was more significant in determining the hot spotting than pressure, power and total energy in the deceleration braking.

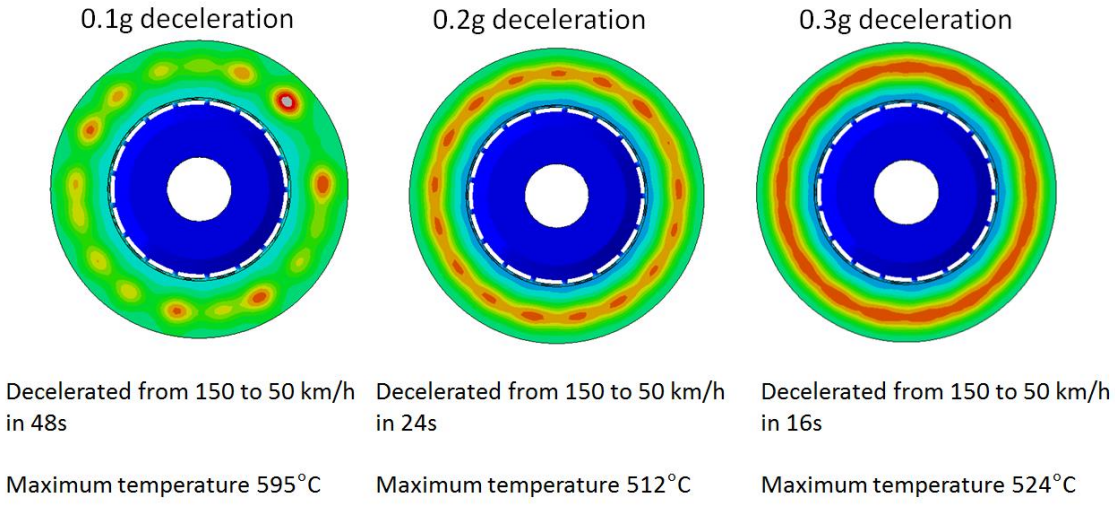

Figure 7.26 Hot spot distribution and outboard brake disc surface maximum temperature (°C) at same energy level under different deceleration

In addition, Figure 7.26 presents the results for hot spotting for different deceleration cases under different brake durations to maintain the same brake energy in the 150 to 50km/h range. The maximum temperature of the 0.1g case was 71°C greater than the 0.3g case, and the thermal gradients were greater both in the radial and circumferential directions. The results showed that at the same average speed and energy, decreasing the deceleration (brake pressure) can increase the development of hot spots. It implied that at the same energy level and same speed, increasing ratio between speed/load or time/power can promote the generation of hot spots.

7.3.6 *Influence of uneven cooling*

Due to the modelled brake disc having pins, the disc comprised 17 periodical sections with 3 different vents in each section. To investigate the effect of this, the convective heat transfer coefficients were set to zero at different vent positions to investigate the influence of uneven cooling. The vent structure and indexes of the positions are illustrated in Figure 7.27. Figure 7.28 shows the positions of the blocked vents and the corresponding hot spots. When there was no vent blocked,

the hot spots occurred at the position of vent 3. After vent position 1 was blocked the hot spot migrated toward the vent position 1. The maximum temperature increased due to the decline of the disc cooling performance. After vent position 2 was blocked, the hot spot migrated toward the vent position 2 direction and the maximum temperature significantly increased. When the vent position 3 was blocked, the hot spot position didn't change, but the maximum temperature reached 628°C, which is the highest temperature in these models. Thus it reveals that the cooling performance of vent design really does have significant contribution towards hot spotting. It should be noted that the effect of uneven cooling due to differing mass flow rate of air through each vent was not simulated. It is expected that this would contribute significantly if the actual local airflow and convective cooling coefficients were measured or predicted.

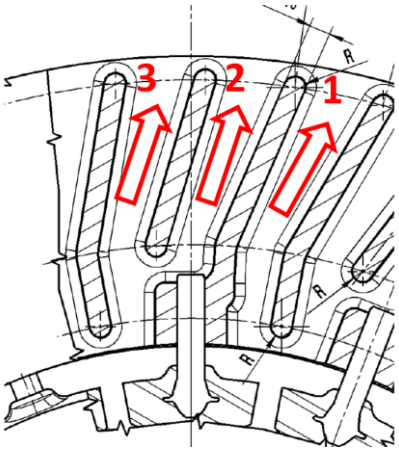

Figure 7.27 Structure of the disc and the indexes of vents at the ventilated layer

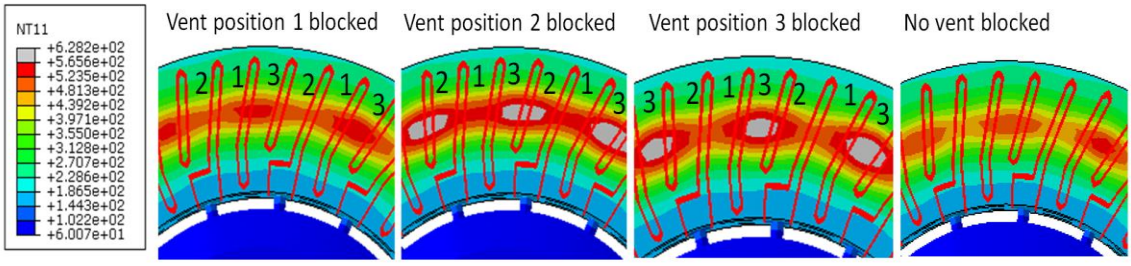

Figure 7.28 Comparison of hot spot distribution and outboard brake disc surface maximum temperature (°C) when vents were blocked at various positions

7.3.7 *Influence of pad length*

According to Sardá *et al.*, (2008) pad length is an important determinant for hot spotting. In the current study, several pad arc length (22.5°, 30° and 45°) models were simulated and compared with the standard pad length (30°) results. The pad length was reproduced numerically by modifying the scale factor discussed in section 6.4.6. The results are shown in Figure 7.29, which provides the comparison of temperature distribution for both solid and ventilated discs. It can be seen that the maximum disc temperature increased with increasing pad length. For pads shorter than 30°, no hot spots developed. This can be explained by the theory of Panier *et al*., (2005) that when the effective pad length was shorter than the minimum wavelength of the hot spot or significant geometry perturbation, it was impossible to trigger hot spots. On the contrary, for pad length models that greater than 30°, the hot stop appeared and the number decreased with increasing pad length. Moreover, the shape of hot spot transformed from ellipse to circular after the pad length exceeded 45°.

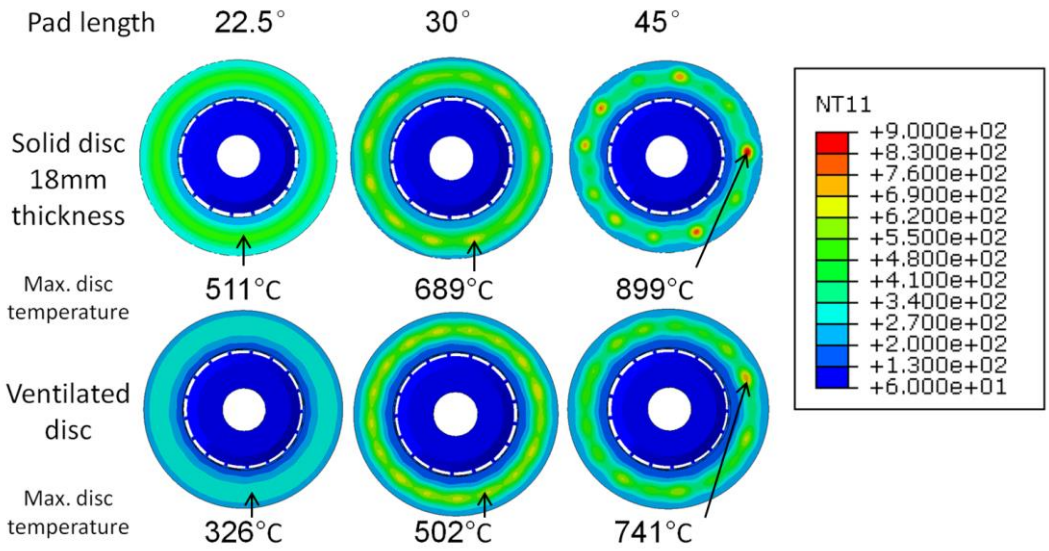

Figure 7.29 FE results showing the hot spot distribution and outboard brake disc surface maximum temperature (°C) for both solid (top) and ventilated (bottom) brake discs at 24s with differing brake pad lengths.

Regarding the solid discs; 0, 12 and 6 hot spots were developed for 22.5°, 30° and 45° pad lengths. However, for ventilated discs; 0, 17, and 15 hot spots were developed for 22.5°, 30° and 45° pad lengths respectively. It is clear that the number of hot spot of the ventilated disc was greater than the solid disc, but the maximum predicted disc temperatures were lower.

In general, the results were in agreement with both literature (Lee and Barber, 1993, Panier, Dufrénoy and Weichert, 2004, and Panier et al., 2005) and the 2D modelling results in section 6.4.6 where the argument was presented that a longer pad will develop fewer hot spots.

7.4 Summary

In this chapter, the 3D models of hot spotting were established based on the axisymmetric pad assumption. Realistic disc geometry was modelled in order to identify the hot spotting characteristics of a ventilated disc. The transient temperature and displacement field were investigated and the results were validated by experiments performed on a laboratory brake dynamometer with an array of transducers and an IR camera. The results showed an identical number of hot spots, locations and similar magnitude for both simulation and experimental measurements. The comparison between 2D and 3D hot spotting results illustrated that both 2D in-plane and out-of-plane models predicted identical distribution characteristics with the 3D model, but the magnitude of the 2D models were lower since the thermal localisation in both radial and circumferential directions could not be considered simultaneously in the 2D models.

In order to improve the understanding of the hot spotting mechanisms, the parametric studies comprised investigation into the effects of vents, pins, initial run-out, constant velocity and decelerated, uneven cooling and pad length. Initially, at same equivalent disc thickness, fewer hot spots were developed on

the solid disc surfaces than the ventilated disc which showed identical trend to the 2D results. It revealed that the periodic structure of the disc redistributed the thermal energy and affected the hot spot distribution. Then, by introducing the disc run-out, both lower order and higher order disc waviness deformations were observed. It illustrated that the magnitude of the hot spots were affected by the disc run-out by energy redistribution. Regarding the influence of braking condition, it was found that at constant speed drag braking, the hot spot distribution and magnitude were mainly determined by speed and energy respectively. When the brake energy input levels were at the same level, the hot spot distribution was predominantly affected by the ratio between speed and brake pressure. Whilst during the simulated deceleration braking, the average speed of the braking event was the most significant factor on the hot spotting. In addition, the simulations of 'blocked vents' showed that the hot spot positions can circumferentially migrate due to the cooling performance of different vent structures. It implied that optimising the vent design should be considered with regards to both convection and conduction. Furthermore, the comparison between different pad lengths by applying different scaling factors showed that the hot spots developed in fewer numbers but earlier when increasing the pad length. However, the hot spot can be prevented from appearing when the pad length was too short.

In terms of computing efficiency, since the minimal element size is a bottleneck in this 3D simulation, it should be noticed that there is an alternative method: Richardson extrapolation, which can be used to predict more accurate results through coarser mesh models rather than by refining the mesh.

Chapter 8 Discussions

8.1 Introduction

Because multiple models, experiments and parametric studies were performed in this research, a general discussion is provided in this chapter in order to evaluate the results found and improve upon the understanding of the hot spotting phenomenon.

8.2 Advantages and limitations of the axisymmetric pad assumption

8.2.1 *Advantages compared to previous models*

According to the TEI theory (Lee and Barber, 1994 and Dow and Burton, 1972), hot spotting is a thermal localisation phenomenon due to uneven contact pressure and subsequent uneven temperature and displacement distribution. Though the initial hot spotting generation mechanism has been explained by different theories, the subsequent thermal localisation process was also agreed upon in the literature (Kao and Richmond, 2000, *Panier et al.*, 2008, and Bryant, Fieldhouse and Talbot, 2011).

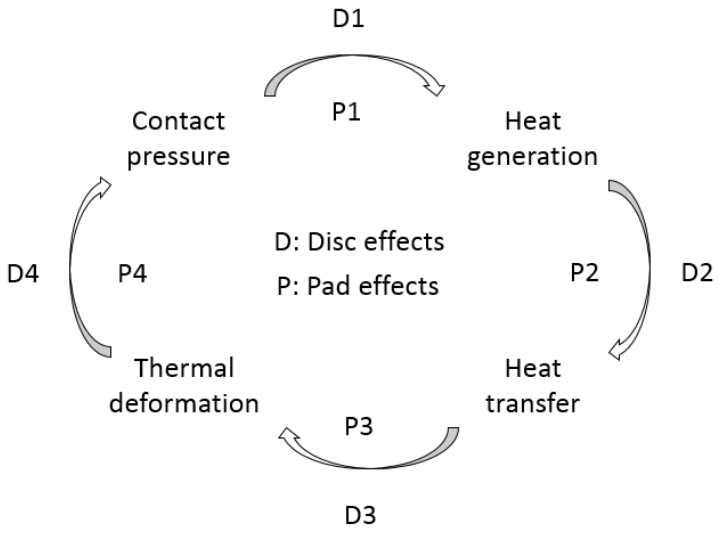

Figure 8.1 Thermo-mechanical contact cause-effect chain and the index of the effects on disc and pad

Figure 8.1 illustrates the basic thermo-mechanical contact cause-effect chain during hot spotting. The identifications D1, P1 to D4, P4 representing the effects on disc and pads. For instance, D1 means that the effects of the local disc surface heat generation were determined by the local contact pressure, and P3 refers to the effects of pad thermal deformation due to the heat transfer. In order to investigate the mechanism of hot spotting and the most efficient method to predict hot spotting, the cause-effect chain shown in Figure 8.1 was investigated in section 6.3. Table 8.1 lists the FE models under different levels of simplifications and the corresponding effects considered. Model 1 was the most commonly used simplified model to investigate the heat transfer and thermal deformation of the brake disc. Since the brake pads were not modelled, the contact pressure distribution cannot be reproduced. Therefore, the heat fluxes were calculated using analytical methods and uniformly applied on the disc surfaces. In model 2, there was an axisymmetric pad modelled but the heat flux was uniformed applied. The intention was to investigate the clamping effects of brake pads and the thermal buckling of the brake disc. The objective of model 3 was to investigate if the moving heat source was the trigger of hot spotting. Model 4 was the model which incorporated with the contact pressure dependent heat generation using a subroutine. Model 5 included the sliding effects into the axisymmetric model to investigate the effects of sliding heating.

According to the results of section 6.3, the hot spots were only observed in models 4 and 5. It verified the cause-effect chain shown in Figure 8.1 and implied that proper hot spotting models should include the contact pressure dependent heat generation.

Table 8.1 FE models under different levels of simplifications and the corresponding thermo-mechanical contact effects on disc and pad

ID	1		2		3		4		5	
Models	Uniform heat flux no pads		Uniform heat flux with asymmetric pads		Gauss distributed moving heat/load source with asymmetric pads		Pressure dependent heat source with asymmetric pads		Pressure dependent moving heat source with asymmetric pads	
Heat generation	-	-	-	-	-	-	D1	P1	D1	P1
Heat transfer	D2	-	D2	P2	D2	P2	D2	P2	D2	P2
Thermal deformation	D2	-	D3	P3	D3	P3	D3	P3	D3	P3
Contact pressure	-	-	D4	P4	D4	P4	D4	P4	D4	P4
Sliding	NO		NO		YES		NO		YES	

The established 2D in-plane and 3D models successfully predicted hot spotting of the ventilated disc since they reproduced such a thermal localisation process. Initially, as the brake pad had been modelled and thermo-mechanical contact was considered, the generation of the uneven contact pressure distribution due to uneven deformation can be achieved. Then, the frictional heat generation was defined by user-subroutine which enabled the uneven heat generation due to uneven contact pressure distribution. In addition, the uneven heat flux went into the disc with periodic structure. The implementation of the coupled thermal-displacement element enabled the uneven deformation due to the uneven temperature and disc structure characteristics. Furthermore, since the real disc geometry was modelled, it had the capability to investigate the effects of structural factors such as top-hat, pins, vents, and disc bulk deformation. Therefore, the hot spotting prediction for complex disc structures and real material properties is the most significant advantage of the demonstrated 2D and 3D FE models.

In addition, computing time reduction is a main challenge in hot spot simulations due to the nature of the transient simulation. Because of the complex rotational friction behaviour calculations, the hot spotting simulation using the traditional thermo-mechanical contact model with rotating disc and finite length pads was time consuming. Through the simplifications of axisymmetric pad and stationary disc and pad, the computing efficiency can be significantly improved according to Table 5.5. Table 8.2 shows the DOF and computing time of the three main models performed in this research under the axisymmetric pad assumption. It can be found that the computing times of the models were manageable (less than half an hour for 2D and less than 11 hours for 3D) for performing parametric studies which is a remarkable advantage over the traditional models. In terms of accuracy, the results of this research were validated with the experiments on dynamometer with identical brake condition in terms of temperature evolution and distribution and disc displacement using thermocouples, IR camera and non-contacting displacement transducers.

Table 8.2 Computing efficiency comparison of the FE models

Hot spotting models performed	DOF	Computing time
2D in-plane model	47334	10mins
2D out-of-plane model	2652	26mins
3D model	403099	11hours

In the previous experimental works (Lee and Barber, 1994, and Cho and Cho, 2008), hot spotting investigations were mainly focused on the deceleration process. It was realistic but can cause difficulties in identifying the trigger condition of hot spots due to the fact that the speed and deceleration were varying with brake pressure. Thus, there was a debate about the trigger condition of hot spotting – critical speed or energy. However, in this thesis, drag braking under

various constant speeds, pressures and durations were performed. Therefore, the effects and relationships of braking speed, pressure, power, duration and energy can be clearly distinguished and investigated independently. In addition, the deceleration process was also simulated by using the axisymmetric pad model to provide better understandings about the hot spot trigger conditions.

In summary, the hot spotting modelling method performed in this research enabled the hot spotting mechanism investigations using flexible parametric studies due to its advantages in computing time and accuracy.

8.2.2 *Limitations of the axisymmetric pad model*

There are some limitations in the axisymmetric pad hot spotting model:

1) The axisymmetric simplification cannot provide exactly identical approximation of the realistic brake system. Since the axisymmetric method was based on the probability of contact between disc and pad, the accuracy of the approximation would be decrease when disc rotation speed decreased.
2) The axisymmetric pad cannot properly simulate the relationship between the real disc and pad during the vibration of the brake system since the pad were smeared and the flexibility of the contact coupling was restricted.
3) The investigation of pad length was only based on the scaling factor method rather than actually modifying the pad length. This method cannot exactly reflect the mechanical condition of the brake pad covering one or multiple hot spots or sitting between hot spots. Therefore the problem is only addressed in a quasi-static thermo-mechanical manner.

8.3 Effects of material properties

According to the investigation performed in section 6.4.1 and 6.6.1, the effects of material properties on hot spotting and its radial migration were listed in Table 8.3

which showed the positive or negative effects on hot spotting when increasing the material properties values. The results suggested that to prevent hot spotting, increasing the specific heat capacities of the disc and pad is an effective way due to the fact that the maximum temperature of the hot spots were significantly sensitive to the heat capacity (see Figure 6.18 and Figure 6.19). Other suggestions to reduce hot spotting magnitude were lowering the other thermal property values such as back-plate, disc and pad Young's modulus, disc and pad thermal expansion coefficient, and pad thermal conductivity. Alternatively, increasing the disc thermal conductivity can also reduce the maximum hot spot temperature. Regarding the reduction of hot band migration, the recommended modifications include increasing the pad thermal conductivity and Young's modulus, and decreasing thermal expansion coefficient, specific heat capacity and wear rate. Therefore, considering both hot spotting reduction and migration reduction, it would be suggested to reduce the pad thermal expansion coefficient which was the only parameter found to be positively affecting the hot spots magnitude and radial migration simultaneously.

In addition, it was found that the interactions between material properties and hot spotting existed. Therefore, it was suggested that when considering the reduction of hot spots, the interactions (see Figure 6.18 and Figure 6.19) should be considered as well.

Table 8.3 Summary of the main effects for increasing the magnitude of material properties investigated in this project

Components	Material properties	Hot spotting amplitude	Radial migration
Back-plate	Young's modulus	Increased	Minor
Disc	Thermal conductivity	Reduced	
	Young's modulus	Increased	-
	Thermal expansion coefficient	Increased	-
	Specific heat capacity	Reduced	-
Pad	Thermal conductivity	Increased	Reduced
	Young's modulus	Increased	Reduced
	Thermal expansion coefficient	Increased	Increased
	Specific heat capacity	Reduced	Increased
	Pad wear rate	-	Increased

8.4 Effects of periodic geometry factors

As one of the main objective of this research, the effects of the periodic geometry factors were investigated in both 2D in-plane and 3D hot spotting models. The effects of vents were studied by comparing solid and ventilated discs (see section 6.4.2, and 7.3.1) with equivalent heat dissipation capabilities based on Limpert's (1975) vent factor methods and a vent DOE. The effects of pins were investigated in two directions: periodic mechanical constraints and extra thermal mass (see section 6.4.3, and 7.3.2).

The results regarding vents demonstrated that the hot spot distribution can be affected by the vents. More hot spots were developed in the ventilated disc than the solid disc with equivalent thickness in both 2D and 3D models. Besides the perturbations of the uneven geometry, another reason of the higher order hot spotting was the reduction of solid layer thickness for the ventilated disc. According to the analytical calculation (see Figure 6.14), the two solid layers of the ventilated disc were easier to be thermally buckled than the solid disc due to

the fact that the critical thermal buckling force exponentially decreased with the reduction of thickness.

Regarding the hot spot magnitudes of solid and ventilated discs, the 2D and 3D models showed similar results. The comparison performed in 2D demonstrated that the hot spot temperature variations of the solid and ventilated disc were similar (see Figure 6.21) but the maximum displacement of the solid disc was greater (Figure 6.27). Meanwhile, in the 3D simulations, the maximum thermal gradients due to hot spotting at the solid disc mean rubbing radius were greater than the ventilated disc (see Figure 7.6 and Figure 7.15). It illustrated that because the same thermal energy generated fewer hot spots on the solid disc, greater temperature at each hot spots resulted.

For the vent design, the DOE study performed in section 6.4.2 suggested that increasing the thickness of the disc and increasing the number of vents can reduce the maximum disc temperature and thermal gradient of hot spots. However, the cooling effects also significantly affected by the vent design according to section 6.4.5 and section 7.3.6. It implied that in order to optimise the thermal performance in the vent design, both conduction and convection of the disc should be properly considered. The ventilated brake disc heat transfer prediction co-simulation method used by Tang, Bryant and Qi (2014) is suggested.

With regards to the mounting pin constraint effects, the 2D results in section 6.4.3 showed that the lower order run-outs were significantly reduced by applying the rigid constraints representing the pins (see Figure 6.26 and Figure 6.27). With pins, the magnitude of the hot spots was not affected for the ventilated disc since the number of hot spots and the number of pins was identical. However, the magnitude of the solid disc's 16 hot spots was decreased since the thermal energy or stress were equalised by the 17 constraints.

The 3D simulation enabled the modelling of the real geometry and material properties of the pins. By modifying the Young's modulus and heat capacity, the effects of pins in regards to the periodic mechanical constraints and thermal mass were explored. The results in Figure 7.17 illustrated that the main effects of the Young's modulus and heat capacity on the output were non-linear, and there were significantly interactions between the constraints and thermal effects of the pins and their effects on hot spotting. It implied that for the design of pins, both factors and their interactions should be considered for hot spotting reduction.

8.5 Local thermal buckling and the initiation of hot spotting

According to the section 6.2.4, a possible mechanism of hot spotting was raised: the local thermal buckling of the disc rubbing surface. The hypothesis can be subject to a whole solid disc or just a given circumferential section of the ventilated brake disc such as a section of the friction ring between two constraints (e.g. two pins or two vents). This hypothesis is demonstrated in 3 steps shown in Figure 8.2, Figure 8.3 and Figure 8.4. As shown in Figure 8.2, the initial contact pressure between an ideal brake disc and pad can be presumed uniform. Thus the initial heat generation distribution along the disc circumference can also be regarded as uniform. However, due to considerable heat generation during a brake application, the heat flux and subsequent thermal stress distribution decrease non-linearly through the thickness of the disc.

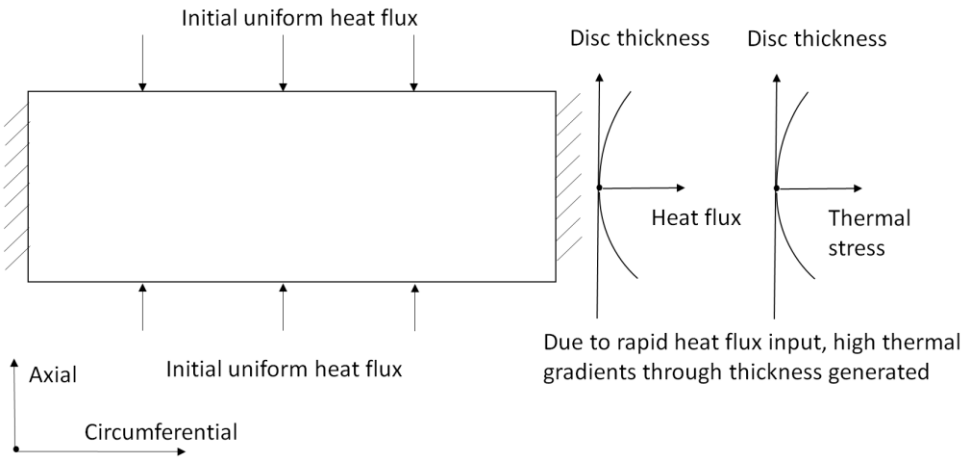

Figure 8.2 Initial uniform heat flux generation on the disc surface and the non-linear heat flux and thermal stress distribution through the disc thickness

Figure 8.3 then shows that the non-linear thermal stress distribution at different disc thickness results in bulk thermal expansion and local disc surface thermal buckling when the surface circumferential stress is sufficiently high. Such thermal buckling results in the initial surface deflections in the circumferential direction.

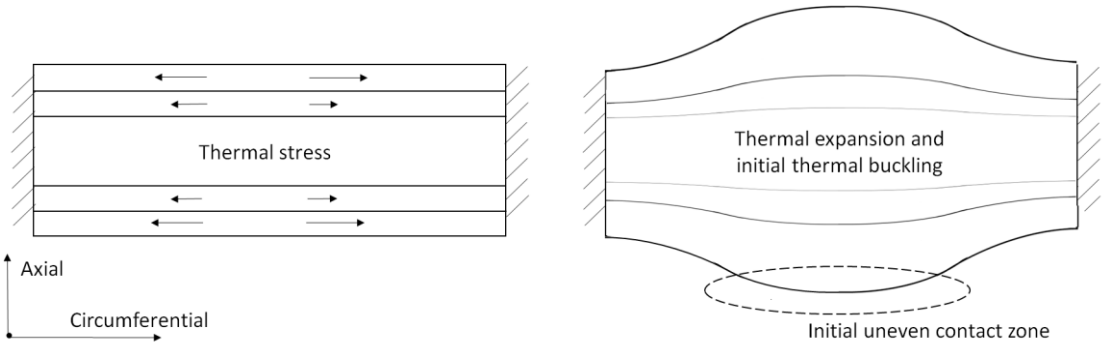

Figure 8.3 The non-linear thermal stress distribution through disc thickness and the subsequent local disc surface thermal buckling

Furthermore, the generation of initial uneven disc deformation then leads to uneven contact pressure distribution and heat generation, which will exponentially grow with time as illustrated by Figure 8.4.

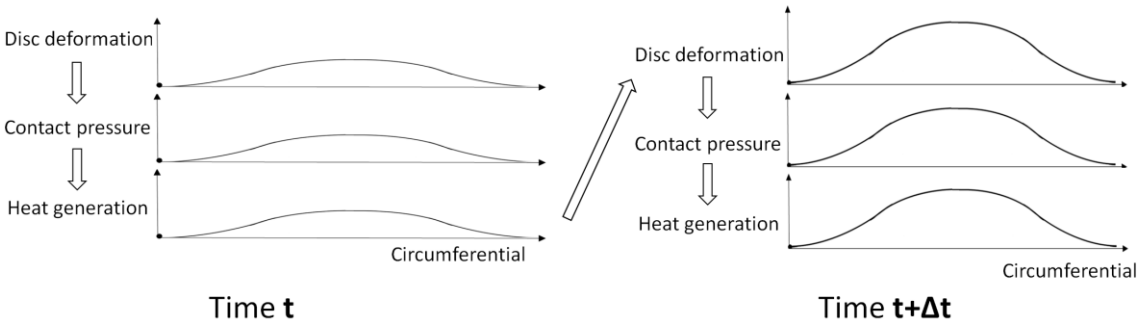

Figure 8.4 Growth of uneven displacement/contact pressure/heat generation on the disc surface along time

This hypothesis is a possible explanation of the initiation of hot spotting especially for a flat disc surface without any initial contact pressure perturbations. It is recommended that this theory is investigated in the future.

8.6 Relationship between lower order run-out and higher order hot spots

During the common hot spotting process, the disc can both thermally deform into lower order run-out and higher order hot spots. The mechanisms of lower order run-out and the subsequent hot judder have not been fully addressed (Könning and Nunes, 2016). From the observations in this research, some factors that affect the lower order run-out were found. Initially, through stress relieving of the new brake disc (identical disc to simulations and experiments), 2nd order run-out was developed with an amplitude of ~10μm to ~35μm (see Figure 4.29). It implied that the bulk disc distortions during the braking events can be regarded as being caused by partial 'in-stop' stress relieving due to the high temperatures. This triggered the subsequent lower order disc deformation. In addition, the simulation results shown in Figure 7.20, demonstrated that the bulk thermal localisations magnified the initial disc waviness which revealed that the initial disc waviness could be a determinant of lower order disc deformation. Moreover, the 2D simulations (see Figure 6.25 and Figure 6.27) illustrated that bulk disc deformation can be generated during hot spotting and that the magnitude highly

depended upon the disc geometry and constraints applied. The thermal buckling calculation of Bryant, Fieldhouse and Talbot (2011) demonstrated that circumferential thermal stress during a heavy duty stop for automotive brake was sufficient to develop lower order thermal buckling of the disc. Figure 6.27 presented that the order (1st order run-out) and magnitude of the ventilated disc run-out differed when compared with the solid disc (2nd order run-out). This can be explained from the thermal buckling point of view that the ventilated disc featured more degrees of freedom in thermal expansion at the ventilated areas, thus the circumferential thermal stresses were lower than the solid disc due to lower circumferential strain (see Figure 8.5). Therefore, according to the observations in this research, the residual stress, initial disc waviness and thermal buckling are all factors influencing the generation of lower order disc waviness.

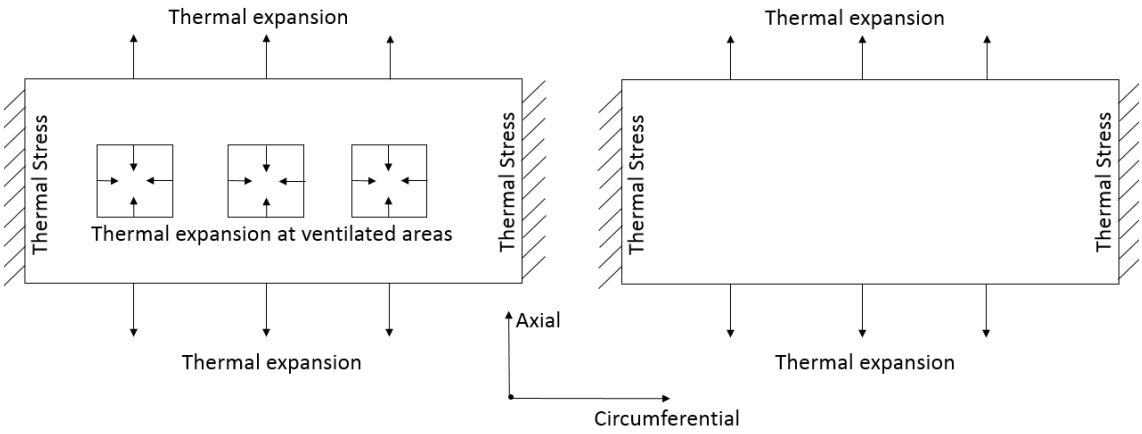

Figure 8.5 Thermal expansion directions comparison between ventilated and solid discs

Regarding the higher order disc waviness, it was clear that during hot spotting anti-symmetric waviness was an important characteristic of the hot spot distribution. The thermal buckling theory (Fan and Lippmann, 1996, Ma, 2004, Bryant, Fieldhouse, and Talbot, 2011 and Yang, 2015) explained the disc waviness as a result of the higher order disc thermal buckling, and the hot spotting as the subsequent thermal localisations on the peaks of the waviness. This is due to the fact that the disc cannot thermally expand in the circumferential

direction. When a critical temperature is reached, the circumferential thermal stress will exceed the critical buckling stress of the disc plate. However, the previous analytical higher order thermal buckling predictions (Fan and Lippmann, 1996) overestimated the bulk temperature to achieve such waviness. This is due to the fact that the hot spotting process a highly transient state and the considerable heat flux generated at the disc surface could not have enough time to uniformly heat up the entire disc. In addition, the comparison between solid and ventilated discs showed that more hot spots developed on the ventilated disc than the solid disc, which reflected that the complexity of hot spotting cannot be explained by the thermal buckling theory alone. Therefore, the actual thermal buckling is more likely to occur locally such as a thin effective buckling layer on the disc surface from a periodic section of a ventilated disc according to Figure 6.14.

In terms of the effects of bulk disc waviness on hot spotting, the results from both 2D and 3D simulations illustrated that the magnitudes of hot spots were affected by the disc bulk deformation. The temperature and displacement variations of hot spots were greater at the peaks of the run-out as shown in Figure 4.10, Figure 6.21 and Figure 7.20. This can be explained by Figure 8.6 which demonstrates the relationship between the temperature variations of hot spots and their locations on the disc run-out. The displacement field shows two hot spots (A and B) positioned at different locations along the disc run-out, and the relative coordinates of higher and lower points on the two hot spots. Thus the heights of hot spot A is Δz_A=z2-z1 and hot spot B is Δz_B=z4-z3. The corresponding thermal gradients of the two hot spots A and B are ΔT_A=T2-T1 and ΔT_B=T4-T3 respectively. Due to the fact that the temperature increases non-linearly with the displacement during thermal localisations, ΔT_B is greater than ΔT_A. In the TEI theory, the thermal localisations at each order or frequency are independent (Lee and Barber, 1993). But the results in this research showed that the higher order

hot spotting was affected by the lower order run-out due to the fact that the thermal localisations developed in a non-linear manner as illustrated by Figure 8.6.

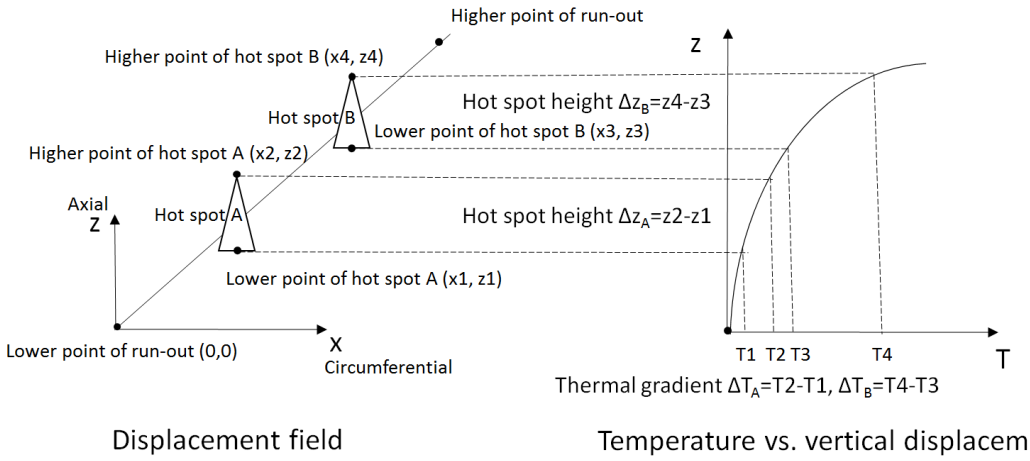

Figure 8.6 Effects of disc run-out to the thermal gradients of hot spots at different locations

8.7 Effects of pad length and pad loading

As important components of the brake system, the effects length of pad and the calliper type were investigated. Based on the experimental observations of Sardá *el al.* (2008) and numerical modelling of Panier *et al.* (2005), the longer pad length can reduce the number of hot spots and when the pad length was shorter than the minimum wavelength between possible hot spots locations, no hot spots would develop (Lee and Barber, 1993). The simulation results in this thesis were in agreement with these findings.

To be specific, as illustrated by Figure 6.35, the number of hot spots was zero when the pad lengths were smaller than ~25°. 17 hot spots were developed at ~25° and the number of hot spot decreased with the increase of pad length. This observation was similar to the 3D simulation results regarding pad length shown in Figure 7.29. In this study, the pad length was represented by the effective scaling of the material properties. Thus, the axisymmetric pad can be considered as an equivalent thermally deformable continuous homogenous friction layer. For

the pads with longer length, the effective heat capacity was greater based on the scaling factor algorithm (see Table 5.1) which gave a lower bulk pad temperature and lower local buckling stress. Since the effective modulus for longer pads was greater, the critical buckling stress increased. Therefore, it was more difficult to generate higher order pad thermal buckling for the longer pad lengths which implied longer buckling length and fewer hot spots. Since the total energy inputs were same for different pad length models, fewer hot spots received more energy into each hot spot.

Regarding the effects of pad length on hot band migration, the results in Figure 6.54 illustrated that shorter pad lengths can cause considerable migration of hot bands. In the view of equivalent material properties (i.e. the scaling factor method according to section 6.4.6), the shorter pad featured lower conductivity, lower modulus and lower specific heat capacity. Based on the parametric study results for the material properties, the reduction of thermal conductivity and modulus can facilitate the hot band migration but lower heat capacity can stabilise the hot banding. Therefore, the results revealed that the lower heat capacity cancelled some migrations effects but the influence of thermal conductivity and modulus reduction was still predominant.

In addition, the calliper type, or the piston distribution, or the mechanical loads applied on the back-plates determined the contact pressure distribution and affected the radial position of hot spots based on the observations in section 6.6.3. In the 2D and 3D models, the temperature distribution showed good correlation with each other when the same loading distribution was applied (see Figure 6.40 and Figure 7.10 respectively). The predicted maximum temperature of the 3D model was greater than the 2D models as they were able to model the circumferential temperature variations. Furthermore, according to Figure 6.42 the alternating hot bands locations between the inboard and outboard disc surfaces

implied that the wear was more important than the loading pattern to determine the hot bands locations in successive braking events.

8.8 Hot spotting operating conditions

In order to identify the influence of braking speed, load, power, duration and energy on hot spotting, parametric studies were performed using physical experiments, 2D in-plane and 3D FE models.

Initially, by comparing the disc distortions between different speed and load using the dynamometer, it was found that both the lower (2^{nd}) order and higher (17^{th}) order deformations were sensitive to the variation of speed rather than load, power and energy. Due to the limitation of motor power and the concern about causing permanent disc distortion which can reduce the repeatability between tests, the experimental tests were not performed at energy levels greater than the standard test conditions.

Then, the 2D in-plane model parametric studies of various speed and load combinations were performed in section 6.4.4. Since the computing efficiency was remarkable (~10min) according to Table 8.2, more tests were performed using the 2D FE models than in the experiments. Figure 8.7 reproduced the results of Figure 6.28 into the form of maximum hot spot temperature against energy. The temperature range was within 0 to ~5500°C which was much greater than the realistic temperature that a brake disc can reach (generally less than 1000°C). But the intention was to show the trend of the relationship between energy and maximum temperature. The fitted curve in Figure 8.7 using the 2^{nd} order least-squares method clearly shows that the temperature was growing nonlinearly with the energy input. The deviations between the simulation results samples to the fitted trend were distinguished into two zones: ‘high speed zone’ and ‘high load zone’ whose slopes were determined by the ratio between speed

and load applied. It revealed that increasing the speed/load ratio will cause a steep curve whereas decreasing the speed/load ratio will decrease the maximum temperature and cause a stable curve.

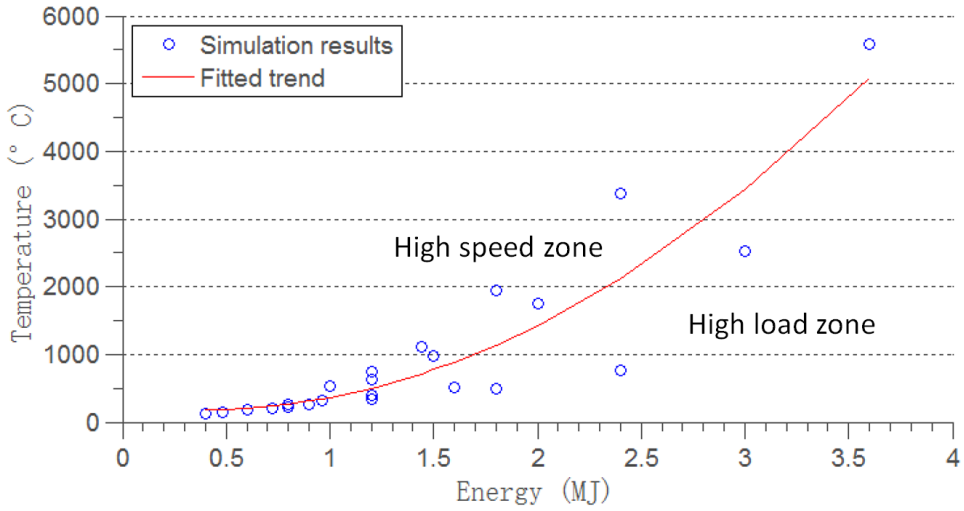

Figure 8.7 Maximum hot spot temperature varying with input energy

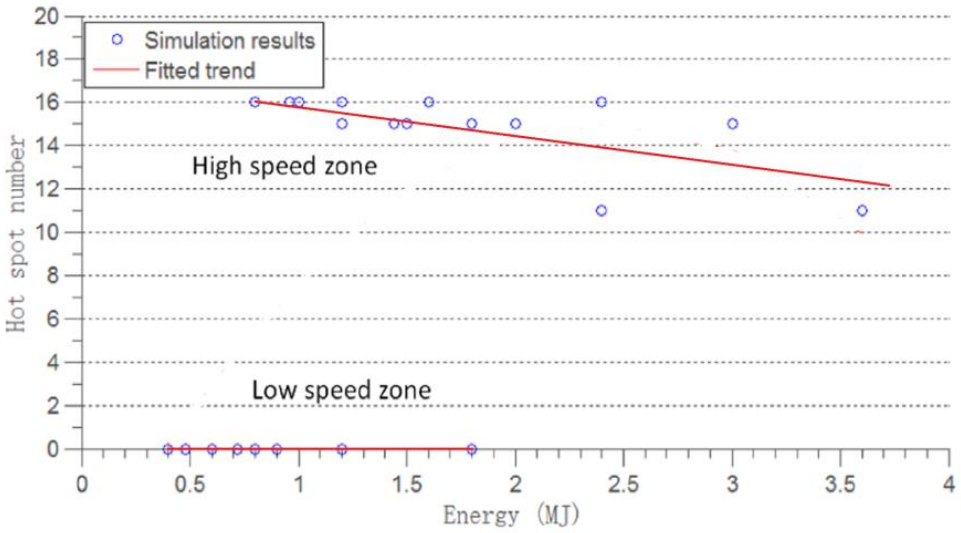

Figure 8.8 Number of hot spot varying with input energy

Regarding the relationship between number of hot spots and the energy input, Figure 6.29 was reproduced into Figure 8.8. The fitted curve shows the overall trend of the number of hot spot. The samples can be divided into 'high speed zone' and 'low speed zone' according to the number of hot spots and its direct

relationship with speed. It was clear that at the lower speed zone, no hot spots developed no matter how much energy was input. From an energy point of view, when the energy input was lower than 0.5MJ, no hot spots developed. In the range between 0.75MJ to 1.8MJ, higher order hot spots developed in the high speed zone. Eventually, when the energy was above 1.8MJ, the number of hot spots decreased with the increasing energy. Such observations implied that the number of hot spots was mainly determined by speed, and the load only affected the magnitude of hot spot temperature. The maximum temperature was mainly determined by the energy input and the deviation was affected by the ratio between speed and load.

In the 3D FE models investigation (section 7.3.4 and 7.3.5), in order to improve the understanding of the hot spotting distribution and temperature, different speed/load combinations were compared with the same energy input. In the constant speed investigations, Figure 7.22 showed that at the same brake durations under different speeds and loads, the maximum temperature manly depended upon energy input which was similar to the 2D results, and the hot spot distribution was mainly affected by the disc speed. Regarding the same energy level simulations, the temperature and hot spot distribution depended upon the ratio between speed and load as shown by Figure 7.23. In addition, Figure 7.24 illustrated that at the moment that hot spots occurred, the trigger time and hot spot distribution were identical, but the temperature was mainly attributed to the load. In the 3D deceleration case, comparing the models with different decelerations, while the average speed increased, the load, power and energy decreased. The results showed that the hot spots were affected by the speed in terms of maximum temperature and thermal gradients.

In summary, Table 8.4 listed the determinants of the hot spot characteristic with regards to amplitude, distribution and trigger condition. It shows that the disc

speed was the main determinant of all hot spotting characteristics. The input energy was the 2nd most important factor in determining the amplitude and distribution. Regarding the triggering of hot spotting, speed was the most predominant factor.

Table 8.4 Determinants of the hot spotting characteristics

Methods	Amplitude	Distribution	Trigger
Experiment constant speed	Speed, power	Speed, energy	Speed
2D constant speed	Energy, speed	Speed, energy	Speed
3D constant speed	Speed, energy, load	Speed, energy	Speed
3D deceleration	Speed	Speed	Speed/load

8.9 Effects of cooling

Since the investigation of ventilated brake disc hot spotting was the main research objective, the effects of uneven disc cooling were investigated. Two aspects of cooling performance were studied: evenly increasing the convective heat transfer coefficient of the disc and vents in the 2D models; and blocking 17 out of the 51 vents in both the 2D and 3D models. The default heat transfer coefficient was estimated from experiments based on the methods of Incropera *et al.* (2007) and Tirovic (2014) introduced in section 4.5.1.

Regarding the effects of uniform heat transfer coefficient (see section 6.4.5), the results suggest that the only the hot spot amplitude (temperature and displacement) were affected linearly. For the given geometry and braking condition, cooling did not affect the hot spot occurrence and distribution, but magnified the amplitude uniformly.

In terms of effects of uneven cooling, the heat transfer coefficients were set to zero at various vent locations in section 6.4.5 and 7.3.6. The results suggest that

the hot spot distribution was affected by the uneven cooling performance. In the 2D model, the hot spot distribution changed from anti-symmetric mode to symmetric mode as shown by Figure 6.31. In addition, the 3D model showed that blocking different vents can significantly affect the position and magnitude of the hot spots (see Figure 7.28).

8.10 Effects of uneven wear

The effects of wear on the radial migration of hot spots or hot bands were investigated by both physical experiments and simulations using the out-of-plane 2D FE model. By incorporating the subroutines FRIC, UMESHMOTION and the wear rate obtained from experiments, the interactions between thermal localisation and wear were simulated. Due to the fact that pad wear was more significant than the disc according to Jang (2004), only the pad wear was considered. The results illustrated that both 'in-stop' and 'between stops' hot band migrations were significantly affect by the wear (see Figure 6.52 and Figure 6.53).

Wear velocity was found to correlate with the temperature and contact pressure in terms of magnitude and distribution varying with time (see Figure 6.42, Figure 6.43 and Figure 6.44) which implied that the wear distribution was mainly attributed to the thermal localisation.

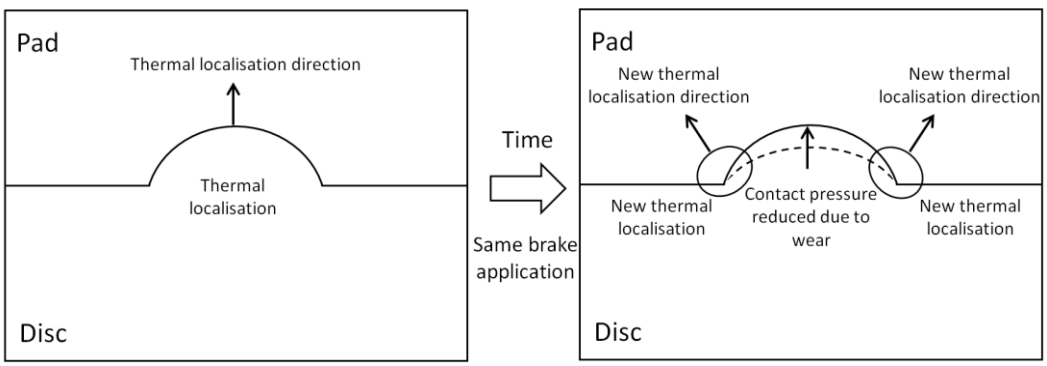

Figure 8.9 'In stop' hot band migration due to thermal localisation and wear

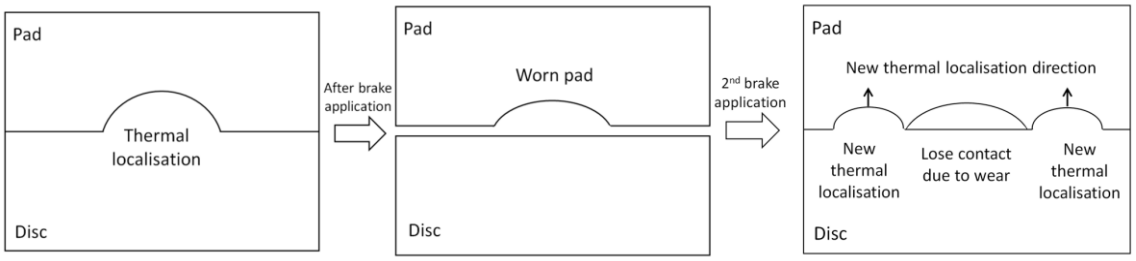

Figure 8.10 'Between stops' hot band migration due to thermal localisation and wear

The interactions between thermal localisations and wear caused both 'in-stop' and 'between stops' hot band migrations. Figure 8.9 illustrates the basic mechanism of 'in-stop' hot band migration in the out-of-plane model. It shows that the direction of the initial thermal localisation was axially toward the pad. However, due to the wear of the pad, the contact pressure was reduced. Then, the contact pressure was concentrated at the new positions, and new thermal localisations developed. The directions of the 'new' thermal localisations comprised both radial (which caused migrations) and axial componants (growth of hot bands). In terms of the 'between stops' migration, Figure 8.10 demostrates its mechanism. Initially, the thermal localisations developed in the 1st braking application. After the release of the brake, significant wear generated during braking could be observed on the pad. Then, in the 2nd braking application, the contact pressure became concentrated at the locations other than the worn zone and developed subsequent thermal localisations.

The 'between stops' migration was validated by the measuring the static contact pressure between braking tests under the identical brake pressure to the formal tests. The results (see Figure 4.23) showed that the contact pressure distribution of the interface was significantly affected by the wear caused by thermal localisations.

8.11 Cause-effect chains of hot spotting

Based on the previous results and discussions in this research, two cause-effect chains of hot spotting are proposed. One is the flowchart of Figure 8.11 that shows how each of the determinants affect the hot spotting; whilst the other, shown in Figure 8.12, illustrates the common inputs and outputs during hot spotting based on the observations of both the experiments and simulations in this research.

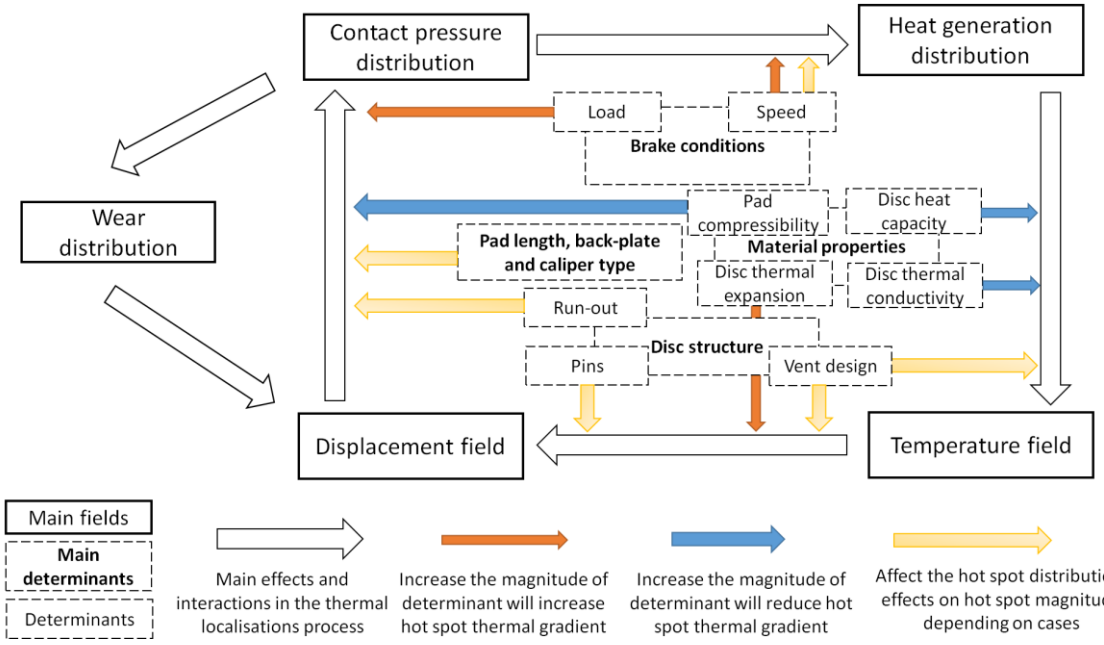

Figure 8.11 Cause-effect chain of hot spotting: effects of determinants

Figure 8.11 shows the cause-effect chain of hot spotting and the effects of determinants including braking condition, material properties, disc structure, and brake components on promoting, reducing and affecting the distribution of hot spotting. The main cause-effect chain of hot spotting was the thermo-mechanical contact process including uneven contact pressure, heat generation, temperature and displacement distributions. The determinants each affected main cause-effect chain at different stages. For instance, disc speed affected the heat generation together with contact pressure, whilst increasing speed can also increase hot spot temperature; the uneven cooling performance can influence the

hot spotting distribution by interfering with the heat transfer process (heat generation to temperature distribution); the thermal deformation was amplified by the increase of the thermal expansion coefficient; and the localised contact pressure magnitude was increased by increasing both mechanical load and Young's modulus of the materials, and the distribution was affected by the brake components such as back-plate, pad length and disc initial waviness.

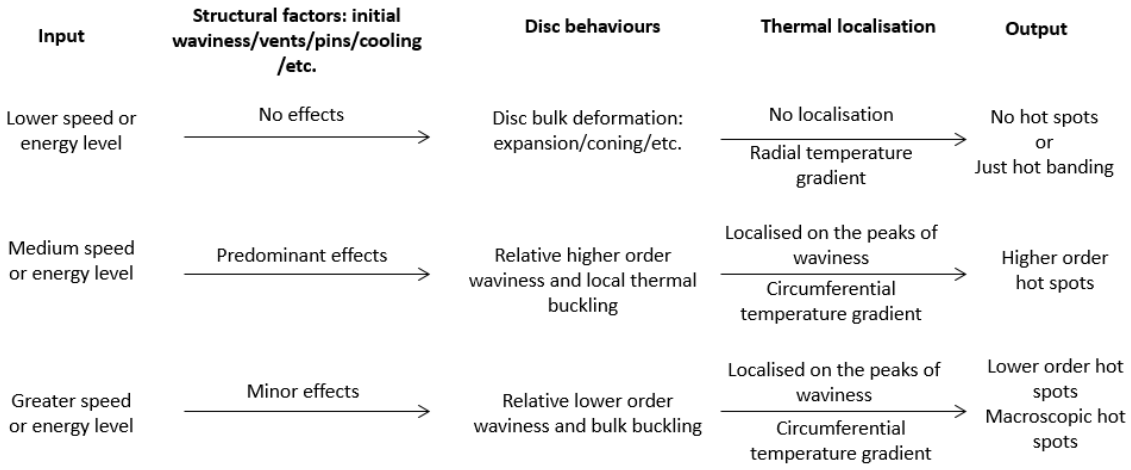

Figure 8.12 Cause-effect chain of hot spotting: input and output

Furthermore, Figure 8.12 summarises a cause-effect chain depending on the common inputs and outputs affecting hot spotting. Three input scenarios were considered: relatively low speed (or high speed but the brake duration was short and the total energy input was low); moderate speed or total energy level; and relatively high speed (or medium speed but the brake duration is relative long which gives high total energy level). The parametric studies implied that initial waviness, uneven cooling, pin and vent structure could predominantly affect the hot spot distribution when the total energy level or speed were moderate (e.g. ~1MJ or ~1000rev/min). Higher order disc waviness (17th order in this study) would be generated due to localised thermal buckling and the corresponding hot spots would develop on the peaks of the waviness. At relatively high speed/energy levels (e.g. ~2MJ or ~1500rev/min), the effects of the periodic

structural factors (vents and pins) had only minor effects due to more excessive bulk distortions and thermal stress being present. In this case, bulk disc buckling will occur and a greater wavelength will be developed in terms of the disc waviness, and the macroscopic hot spots will be formulated at the peaks of the waviness due to thermal localisation effects. Moreover, at relatively low speeds or energy levels (e.g. ~0.5MJ or ~500rev/min), no thermal buckling occur since the thermal stress is not sufficiently high to trigger the disc waviness buckling, even in a small periodic section of a ventilated disc. In this scenario, the resulting small circumferential thermal gradients will not be large enough to cause hot spotting. However, it would still be possible to develop the hot banding phenomenon. This is because of the uneven radial heat generation due to differing linear velocities at different disc radii; the subsequent thermal localisation would amplify this radial temperature gradient into hot bands.

8.12 Summary

In this chapter, the general discussions and implications for the research findings have been presented. Initially, through the comparisons between models at different levels of simplification performed in Chapter 4 and Chapter 6, it was found that the methods had several technical modelling advantages: 1) the axisymmetric pad enabled fast computing; 2) reproducing the frictional heating effect using a subroutine saved significant computing time; 3) the contact pressure dependent heat generation was the necessary condition for hot spot simulations; 4) whole disc modelling with realistic geometry enabled accurate prediction of hot spotting and consideration of disc run-out; 5) benefitting from the high computational efficiency, the parametric studies could be performed for hot spotting mechanism investigations.

The influence of the material properties on hot spotting and hot band migration were discussed as well as the main effects and interactions. It was suggested

that reducing the pad thermal expansion coefficient can reduce both hot spotting and its radial migration. The effects of interactions between material properties should also be considered during the design and selection of friction material properties.

In addition, the effects of vents and pins on hot spotting were discussed. The number of hot spots, thermal buckling tendency and maximum temperature were affected by the existence of vents due to the periodic structure. The hot spotting characteristics such as the relationship between pad length and number of hot spots, and speed and load with number of hot spots showed similar trends for solid and ventilated disc, but due to the interference of the vents, the ventilated disc was less sensitive.

Moreover, the generation of disc waviness was discussed. The effects of thermal buckling was analysed and it was proposed that it can facilitate the development of hot spots by coupling with other mechanisms. It was also revealed that the magnitude of hot spots across the disc circumference can be non-uniform due to low order disc run-out and the mechanism was shown by Figure 8.6.

Regarding the hot spotting, pad length significantly affected the number of hot spots and trigger time according to the 2D and 3D simulation results which were in agreement with literature. Regarding the effects of pad loading distribution, the radial hot spot/band migration was proven to be significantly affected.

In the aspects of trigger condition, it was found that the number of hot spots decreased with the increase of speed in both 2D and 3D models. The temperature was determined by the energetic level. For higher decelerations from the same initial speed, the results revealed that the average speed was significant with regards to the hot spotting whereas pressure was insignificant. In addition,

hot spots were less likely to appear during high deceleration braking events at same total energy levels.

In terms of the convective cooling effects, the 2D results suggest that increasing or decreasing the rotation speed can change the cooling performance uniformly but can only affect the hot spot temperature and not their distribution. The vent design was significant with regards to hot spotting reduction in order to reduce the non-uniform heat distribution.

Furthermore, wear has been verified as the main determinant of radial hot spot/band migration. It was shown that by lowering the wear rate, the migration can be reduced. The mechanisms of both ‘in-stop’ and ‘between-stops’ hot band migration phenomena were explained by Figure 8.9 and Figure 8.10 which showed the complex interactions between wear and thermal localisations.

Finally, two cause-effects chains considering the factors were given; one was based on the effects of determinants obtained in this project, the other one was summarised based on the brake conditions according to the simulation results.

Chapter 9 Conclusions

9.1 Introduction

Initially in this chapter, a summary of this thesis is presented. Then the conclusions are drawn to address the research objectives. Finally, recommendations for the future work are discussed.

9.2 Thesis summary

The aim of this research was to develop a computationally efficient model to simulate the hot spotting phenomenon for complex disc geometry and to contribute to the knowledge of the hot spotting mechanism through the analysis of parametric studies. A literature review regarding the state of art of hot spotting research was provided including the characteristics, theories, determinants and modelling methods. The research gaps were then identified. In order to reduce the computing time for the FE models, an axisymmetric pad simplification was established by applying a material scaling factor and the frictional heat generation were define by using subroutine. The computing accuracy and efficiency was verified with feasibility FE simulations. To provide a benchmark for the following hot spot simulations, experiments were performed based on a laboratory dynamometer. The hot spotting and radial hot band migration phenomena were observed and the disc waviness distortions were measured. In addition, the generation of hot spotting in ventilated discs and its radial migration were investigated by performing 2D in-plane and out-of-plane models respectively. In the 3D FE simulations, the pin-mounted ventilated disc geometry was modelled. Both 2D and 3D modelling results were validated using experiment results and showed consistency. Moreover, through parametric studies, the effects of the hot spotting determinants were examined. The further implications in hot spot mechanisms and reduction strategies were discussed.

9.3 Conclusions

- Numerical modelling innovation

The axisymmetric ‘equivalent homogenous friction material layer’ assumption of the brake pads enabled a significant improvement in computing time with similar accuracy of results. The calculation of scaling factor provided a flexible means for analysis which was only determined by the pad length. Then, the stationary disc and pad assumption based on an automatic heat generation calculation using a user-subroutine provided significant improvement in computing time with good accuracy. Thus, the model developed in this research makes the parametric studies more manageable due to higher computing efficiency than the previous methods. Regarding the proper set-up of hot spot prediction, it was found that the hot spot can only be modelled when the heat generation was related to contact pressure. It verified the TEI theory whereby the thermal localisation was mainly attributed to contact pressure variation. Moreover, it was also identified that the modelling factors such as moving heat source and load source were insignificant on the results and time consuming.

- The simulation of waviness distortions

Lower order disc waviness (run-out) was observed to occur in the 2D in-plane models due to thermal buckling effects or TEI. The introduced initial disc run-out also proved to be excessively amplified during braking applications as a result of the thermos-mechanical interactions. The disc deformation after stress reliving implied the residual stress from disc manufacturing process was another source of disc waviness distortions. Regarding the higher order disc waviness for solid discs, it was found that the thermal buckling force was not sufficient to trigger higher order disc buckling in common brake conditions. However, the highly non-linear and large thermal gradients through the disc thickness provided the

probability to trigger the surface thermal buckling which can trigger or couple with the TEI phenomenon for solid discs. This revealed that hot spotting can be caused by multiple mechanisms.

- *Effects of the geometry factors of pin-mounted ventilated discs*

For ventilated brake discs, the mechanism of hot spotting was identified to be more complicated due to the existence of periodic geometry factors which provided an uneven temperature distribution. The vents provided uneven thermal mass/cooling distribution and provided a perturbation for hot spotting distribution based on the total number, relative vane height, and cooling performance. The variation in the number of hot spots under different braking condition and pad length for ventilated discs was found to be less sensitive than the solid disc due to the significant interference from the vents. To reduce hot spotting, the design of the disc vent geometry should consider both cooling performance and solid conduction to achieve even temperature distribution. To be specific, increasing the thickness of the friction ring, vent thickness and the number of vents can reduce the maximum hot spot temperature. Similarly, the pins were observed to provide both mechanical stiffness and thermal mass contribution to the disc which significantly affected the amplitude of hot spots. The effects of stiffness and thermal mass was found to be non-linear and interacted with each other which implied that both aspects should be considered for the design of the pins. In addition, it was also found that increasing pad length can reduced the number of hot spots, but no hot spot developed when the pad length was shorter than the minimum wavelength of the main potential model shape of the hot spots. Furthermore, the investigation of the effects of lower order run-out revealed that the hot spot thermal gradient was amplified by the underlying run-out. Such variation of thermal gradients was attributed to the non-linear relationship between contact pressure and heat generation in contact surface.

- *Braking condition*

The observations from both the experiments and thermo-elastic FE simulations indicated that the number of hot spots was mainly determined by speed (or average speed for decelerations), and that the load only affected the magnitude of the hot spot temperature. Hot spots will be only triggered when the speed was high enough, whilst the occurrence time and the initial distribution were determined only by the disc speed. At constant speeds, hot spots can merge together with an increase in energy level. The maximum temperature was mainly determined by the energy input and the deviation was positively affected by the ratio between speed and load. Therefore, for deceleration events at the same energy level and same initial speed, decreasing the speed/load ratio or time/power ratio can reduce the occurrence and amplitude of hot spots.

- *Radial migration and wear*

It was found that the radial migration of hot spots and hot bands was mainly caused by the interactions between the thermal localisation and wear at the interface with some effects of disc coning and mechanical loading. For ‘in-stop’ migration, with the development of thermal localisation, the contact pressure decreased due to wear and the hot band started to migrate in the radial direction to the high contact pressure zones. For the ‘between stops’ migration, clear concave regions on the pad were developed due to the wear from thermal localisations. In the following brake application, since the pad was cooled, the initial contact zones occurred at the non-concave areas and hot bands or hot spots developed at alternative radii to the previous brake application.

- *Material selection*

To prevent hot band migrations, reducing the wear rate and thermal expansion coefficient of the friction material are recommended. Whilst to reduce the

maximum temperature of hot spots, this research has suggested increasing the disc conductivity and the disc and pad heat capacity; and decreasing the pad Young's modulus, and the thermal expansion coefficients of both disc and pad.

- *Cause effect chain*

The cause effect chain obtained in this research suggested that the thermal localisation phenomenon of ventilated brake discs was dependent upon the brake condition. At lower speeds or lower energetic level (brake duration), the main disc deformation forms are expansion, coning and hot bands. At medium speed or energetic level, higher order hot spots can occur and were significantly affected by the ventilated disc geometric factors such as vents, pins design and cooling performance. Furthermore, at even greater speed or energy, the influences from the geometric factors are reduced and hot spots can merge into macroscopic or regional hot spots.

9.4 Recommendations for future works

In order to investigate the effects and interaction of material properties on hot spotting, non-temperature dependent isotropic material properties were used in this research. It is strongly recommended that temperature dependent material properties for pad and disc should be implemented to further investigate the material selection strategies. Under realistic conditions at high energy levels, plastic yielding can be triggered which stabilises the number of hot spots rather than merging the hot spots together in the thermo-elastic model. Therefore, the disc material plasticity should also be considered. Moreover, considering the temperature dependent coefficient of friction will improve the prediction of the thermal fade phenomenon and reduce the overestimation of the maximum temperature predicted under heavy duty braking. In addition, the model can also be used to investigate other hot spot factors such as non-homogeneous material properties and uneven roughness distribution through user-subroutine UMAT.

It was clear that the vent design both affected the hot spotting by its cooling performance and thermo-mechanical deformation. Therefore, a conjugate heat transfer method (coupled FE and CFD) is suggested to provide more accurate prediction of hot spotting for ventilated discs. This would allow the disc geometry to be optimised in terms of hot spot intensity reduction.

Furthermore, thermal buckling analysis is recommended be performed by incorporating the models established in this research under different levels of simplifications regarding the load and boundary conditions, in order to investigate and distinguish the relationships between thermal buckling and hot spotting.

References

Abdelhamid, M. K., Blaschke, P., Wang, W. A., & Yang, S., 2001, An overview of brake noise and vibration problems, In *IMAC-XIX: A Conference on Structural Dynamics*, Vol. 1, pp. 57-63.

Adamowicz, A., and Grzes, P., 2011, Analysis of disc brake temperature distribution during single braking under non-axisymmetric load, *Applied thermal engineering*, 31(2011), pp. 1003-1012.

Al-Shabibi, A.M. and Barber, J.R., 2002, Transient solution of a thermo-elastic instability problem using a reduced order model, *International Journal of Mechanical Sciences*, 44(3), pp. 451-464.

Altuzarra, O., Amezua, E., and Aviles, R., 2002, Judder vibration in disc brakes excited by thermo-elastic instability, *Engineering Computations*, 19(4), pp. 411-430.

Anderson, A.E. and Knapp, R.A., 1990, Hot spotting in automotive friction systems, *Wear*, 135(2), pp. 319-337.

Barber J.R. 1967, The influence of thermal expansion on the friction and wear process, *Wear*, Vol. 10, pp. 155-159.

Barber, J.R., 1969, Thermo-elastic instabilities in the sliding of conforming solids, *Proceedings of the Royal Society of London. Series A, Mathematical and Physical Sciences*, 312, pp. 381-394.

Barber, J.R., 2010, *Elasticity 3rd edition*, London: Springer, pp. 347-363.

Barber, J. R., Dundurs, J., Comninou, M., 1980, Stability considerations in thermo-elastic contact, *Journal of applied mechanics*, vol. 47, pp. 871-874.

Barber, J.R. and Zhang R.G., 1988, Transient behaviour and stability for the thermo-elastic contact of two rods of dissimilar materials, I*nternational Journal of Mechanical Sciences*, 30(9): 691-704

Barton, D., 2014, Materials Design for Disc Brakes: Day, A.J. ed., *Braking of road vehicles 1st edition*, ISBN- 978-0-12-397314-6

Brunel, J.F., Lamure, B., Dufrénoy, P., Lamjahdy, A., and Weichert, D., 2014, *Hot-Spotting mechanisms in disc brakes: Numerical model and experiments*, EuroBrake 2014-FT-006, 13-15 May, Lille, France

Bryant, D., Fieldhouse, J.D, and Claffey, E., 2013, *Hot judder – an analysis of the development process*, In: EuroBrake 2013, 17-19 June, Dresden, Germany.

Bryant, D., Fieldhouse, J. D., and Talbot, C. J., 2011, Brake judder – an investigation of the thermo-elastic and thermoplastic effects during braking, *International journal of vehicle structures & systems*, 3(1), pp. 57-72.

Burton, R.A., Neilikar, V., Kilaparti, S.R., 1973, *Thermo-elastic instability in a seal-like configuration*, *Wear*, vol. 24, pp. 177-188.

Cho, H., Cho, C., and Kim, C. B., 2007, Thermal and mechanical performance analysis in accordance with disk stiffness changes in automotive disk brake, *SAE paper*: 2007-01-3661.

Cho, H.J. and Cho, C.D., 2008, A study of thermal and mechanical behaviour for

the optimal design of automotive disc brakes, *Proceedings of the Institution of Mechanical Engineers Part D: Journal of Automobile Engineering*, 222(D6), pp. 895-915.

Choi, J. H., and Lee, I., 2004, Finite element analysis of transient thermo-elastic behaviors in disk brakes, *Wear*, 2004(257), pp. 47-58.

Cho, M. H., Kim, D. S., Yang, S. H., Cho, Y. S., Lee, J. J., Kim, C. J., 2012, A study of the influence of pad properties and disc coning on high speed judder, *SAE paper*: 2012-01-1815.

Day, A. J., Newcomb, T. P., 1984, The dissipation of frictional energy from the interface of an annular disc brake, *Proceedings of the Institution of Mechanical Engineers, Part D: Journal of Automobile Engineering*, pp. 201-209

Day, A. J., Tirovic, M., and Newcomb, T. P., 1991, Thermal effects and pressure distributions in brakes, *Proceedings of the Institution of Mechanical Engineers, Part D: Journal of Automobile Engineering*, 205(3), pp. 199-205.

D'Cruz, A. H., 1989 Surface crack initiation in ventilated disc brakes under transient thermal loading. Paper C382/05, *Institution of Mechanical Engineers*.

Dow, T. A. and Burton, R. A., 1972, Thermo-elastic Instability of Sliding Contact in the Absence of Wear, *Wear*, vol. 19, pp. 315-328.

Du, S., Zagrodzki, P. and Barber, J.R., 1997, Finite element analysis of frictionally excited thermo-elastic instability, *Journal of Thermal Stresses*, 20(2), pp. 185-201.

Dufrénoy, P., 2004, Two-/three-dimensional hybrid model of the

thermomechanical behaviour of disc brakes, *Proceedings of the Institution of Mechanical Engineers, Part F: Journal of Rail and Rapid Transit*, 208, pp. 17-30

Eltoukhy, M. and Asfour, S., 2008, *Braking Process in Automobiles: Investigation of the Thermo-elastic Instability Phenomenon*, Department of Industrial Engineering, College of Engineering, University of Miami USA–URL: http://intechweb.org/downloadpdf.php.

Fan, X., and Lippmann, 1996, Elastic-plastic buckling of plates under residual ,*Proceeding of AEPA* 96

Fieldhouse, J.D., 2013, Brake Testing, Day, A.J. ed., *Braking of road vehicles 2013*, University of Bradford.

Fieldhouse, J.D., and Beveridge, C., 2001, An experimental investigation of hot judder, *SAE paper*: 2001-01-3135.

Fieldhouse, J.D., Bryant, D., and Crampton, A., 2008, A study of thermal judder on a laboratory dynamometer, *26th Annual Brake Colloquium & Exhibition*, San Anotonio: SAE, 2008-01-2542.

Galindo-Lopez, C.H. and Tirovic, M., 2008, Understanding and improving the convective cooling of brake discs with radial vanes, *Proceedings of the Institution of Mechanical Engineers, Part D: Journal of Automobile Engineering*, pp. 222-1211

Gourley, A. R. and Mckee, S., 1970, Hopscotch: A Fast Second-Order partial. Differential Equation Solver, *Institute of Mathematics and Applications Journal*, 6, 375-390

Graf, M., and Ostermeyer, G. P., 2014, Efficient computation of thermo elastic instabilities in the presence of wear, *Wear*, 312(2014), pp. 11-20.

Hundy, B.B., 1957, Shelling of railway wheels, *Railway Steel Topics* 4, pp. 19-35.

Incropera, F.P., DeWitt, D.P., Bergman, T.L., and Lavine A.S., 2007, *Foundations of heat transfer 6th edition*, John Wiley & Sons. pp. 260–26.

Jacobsson H., 2001, *The brake judder phenomenon: classification and problem approach*, Chalmers University of Technology

Jacobsson, H., 2003, Aspects of disc brake judder, *Proceedings of the Institution of Mechanical Engineers, Part D: Journal of Automobile Engineering*, 217(6)

Jang, H., Ko, K., Kim, S.J., Basch, R.H, and Fash, J.W., 2004, The effect of metal fibers on the friction performance of automotive brake friction material, *Wear*, 256(3-4): p. 406-414.

Jung, S. P., Park, T. W., Lee, J. H., KIM, W. H., and Chung, W. S., Finite element analysis of themalelastic instability of disc brakes, in *Proceedings of the World Congress on Engineering* 2010(3), WCE 2010, Jun 30 – July 2, 2010, London, U.K.

Kao K.T., Richmond, W.J. and Moore, W.M., 1994, The application of predictive techniques to study thermo-elastic instability in braking, *SAE paper* 942087.

Kao K.T., Richmond, W.J. and Douarre, A., 2000, Brake disc hot spotting and thermal judder: an experimental and finite element study, *International Journal of*

Vehicle Design, 23(3), pp. 276-296.

Kasem, H., Brunel, J.F., Dufrénoy, P., Siroux, M. and Desmet, B., 2011, Thermal levels and subsurface damage induced by the occurrence of hot spots during high-energy braking, *Wear*, 270(2011), PP. 355-364.

Kasem, H., and Dufrénoy, P., 2012, Relationships between surface thermal gradients and disc distortion during stop-braking with high energy dissipation, *Tribol Lett* 48(2012), pp. 169-181.

Kim, M.G., Cho, C., and Kim, C.B., 2007, Pressure change and variation of vibration in an automotive disc brake system due to hot spot, *SAE paper*: 2007-01-3663.

Kolleck, R., Loscher, J., Weiss, W., and Veit, R., 2008, *Alternative approaches for the simulation of the hot forming process*. Numisheet, Interlaken, Switzerland, pp. 621-626.

Könning, M., Nunes, R., Fischer, S., and Winner H., 2014, *Simulation of a brake system with respect to dynamic and thermal conditions during hot judder*, EuroBrake 2014-BV-010, 13-15 May, Lille, France

Könning, M. and Nunes, R., 2016, *Simulation of brake disc deformations under thermal load*, EuroBrake 2016-SVM-027, 13-15 June, Milan, Italy.

Lamjahdy, A., Brunel, J., Lamure, B., Dufrénoy, P., Weichert, D., and Markert, B., The cyclic thermomechanical coupled problem of thermal gradients in friction railway disc brakes, *Proceedings in applied mathematics and mechanics*

Lee, K., Barber, J.R., 1993, Frictionally excited thermo-elastic instability in automotive disc brakes, *Journey of tribology*, 115(4), pp. 607-614.

Lee, K.J. and Barber, J.R., 1994, An experimental investigation of frictionally-excited thermo-elastic instability in automotive disk brakes under a drag brake application, *Journal of Tribology-Transactions of the ASME*, 116(3), pp. 409-414.

Lee, K.J. and Brooks, F.Q., 2003, Hot spotting and judder phenomena in aluminum drum brakes. *Trans. ASME (J. Tribology)*, 125(1), 44-51.

Limpert, R., 1975, *Cooling analysis of disc brake rotors*, Slt Lake City: University of Utah.

Limpert, R., 2011, *Brake Design and Safety, 3rd edition*, WARRENDALE, Pa., SAE, ISBN: 978-0-7680-3438-7

Loizou, A., 2011, *Modelling and simulation of thermo-mechanical phenomena at the friction interface of a disc brake*, PhD thesis, University of Bradford.

Meng, J.D., Zhang, L.J., and Yu, Z.P., 2010, Theoretical modelling and FEA of thermos-mechanical coupling dynamics of ventilated disc brake, J*ournal of Tongji University (Natural Science)*, 38(6), pp. 800-807.

Ostermeyer, G.P., Graf, M., 2013, wear-induced migration of hot bands: models and comparison with experiments, *SAE paper*: 2013-01-2068.

Panier, S., Dufrénoy, P., Brunel, J.F., and Weichert, D., 2005, Progressive Waviness Distortion: A new Approach of Hot Spotting in Disc Brakes, *Journal of Thermal Stresses*, 28(2005), pp. 47-62.

Panier, S., Dufrénoy, P., and Weichert, D., 2004, An experimental investigation of hot spots in railway disc brakes, *Wear*, 256 (2004), pp. 764-773.

Parker, R.C., & Marshall, P.R., 1948, The measurement of the temperature of sliding surfaces with particular reference to railway blocks, *Proc. IMechE*, 158, pp.209-229.

Park, J. H., Park, T. W., Lee, J. H., Cho, M. H., 2014, Hot judder simulation of a ventilated disc and design of an improved disc using sensitivity analysis, *International Journal of Automotive Technology*, Vol. 15(1), pp. 1-6.

Podra, P., and Andersson, S., 1999 Simulating sliding wear with finite element method, *Tribology International*, 32(2), pp. 71-81.

Qi, H.S. and Day, A.J., 2007, Investigation of disc/pad interface temperature in friction braking, *Wear*, 262(5-6), pp. 505-513.

Rajkumar, A., 2013, *Contact and Convergence: Successful Strategies*, ABAQUS online training course material, Accessed on 4 December 2013.

Sardá, A., Haag, M., and Winner, H., 2008, Experimental investigation of hot spots and thermal judder, *SAE paper*: 2008-1-2544.

Shahzamanian, M.M., Shari, B.B., Bayat,. M., Ismarrubie, Z.N.and Mustapha, F., 2010, Transient and thermal contact analysis for the elastic behavior of functionally graded brake disks due to mechanical and thermal loads, *Materials and Design*, 31 (10). pp. 4655-4665. ISSN 0264-1275

Simulia, 2012, *ABAQUS theory manual*, Version 6.12, Dassault Systemes.

Steffen, T., 2006, *Hot Spot Simulation*, IMechE, Brakes 2006, pp. 199-208.

Stolarski, T., 1999, *Tribology in Machine Design. 1st Edition*, Imprint: Butterworth-Heinemann, eBook ISBN: 9780080519678.

Suryatama, D., Stewart, D.J., Meyland, S.C. and Hou, L.J., 2001, Contat mechanics simulation ofr hot spots investigation, *SAE paper*: 2001-01-0035.

Tang, J.H., and Qi, H.S., 2013, *FEM And CFD Co-simulation Study of a Ventilated Disc Brake Heat Transfe*r, EuroBrake 2013, 17-19 June, Dresden, Germany.

Tang, J.H., Bryant, D., and Qi, H.S., 2014, *Coupled CFD and FE thermal analysis of disc brake*, EuroBrake 2014, 13-15 May, Lille, France.

Thuresson, D., 2004, Influence of material properties on sliding contact braking applications, *Wear*, 257(2004), pp. 451-460

Tirovic, M. and Day, A.J., 1991, Disc brake interface pressure distribution, *Proc.I. Mech E., Part D: J. Automobile Engineering*, 205, pp. 137–146.

Tirovic, M. and Sarwar, G.A., 2004, Design synthesis of non-symmetrically loaded high-performance disc brakes Part 2: finite element modelling, *Proceedings of the Institution of Mechanical Engineers, Part F: Journal of Rail and Rapid Transit*, vol. 218, pp. 89-104.

Tirovic, M., 2013, Thermal Effects in Friction Brakes in: Day, A.J. ed., *Braking of road vehicles 2013*, University of Bradford

Tirovic, M., 2014, Thermal Effects in Friction Brakes in: Day, A.J. ed., *Braking of road vehicles 1st edition*, ISBN- 978-0-12-397314-6

Wu, H., Meng, H., Luo, X. and Xu, G., 2008, Heat transfer enhancement characteristics in nature convection along vibrant surface, *Journal of Beijing University of Aeronautics and Astronautics*, 2008(3), vol. 34, pp. 307-310.

Yang, H.Z., 2015, *Finite element analysis of thermal buckling in automotive clutch and brake discs*, Electronic Theses and Dissertations, Paper 1056.

Yi, Y.B., Barber, J.R., and Hartsock, D.L., 2002, Thermo-elastic instability in automotive disc brakes-finite element analysis and experimental verification, in J.A.C.Martins and Manuel D.P.Monteiro Marques eds., *Contact Mechanics*, Kluwer, Dordrecht, (2002), pp. 187-202.

Yi, Y.B., and Bendawi, A., 2012, Effect of convective cooling on frictionally excited thermo-elastic instability, *Wear*, 296 (2012), pp. 583-589.

Yi, Y. B., Du, S. and Barber, J. R., 1999, Effect of Geometry on Thermo-elastic Instability in Disk Brakes and Clutches, *Ann Arbor*, 1001(1999), pp. 48109-2125.

Yu, W. G., 2010, *Thermal-mechanical coupled simulation and life prediction for a ventilated disc brake*, Master degree dissertation, South China University of Technology.

Yi, Y.B., Barber, J.R. and Zagrodzki, P., 2000, Eigenvalue solution of thermo-elastic instability problems using Fourier reduction, *Proceedings of the Royal Society of London*, Series A, vol.456, pp. 2799-2821.

Yu, Z. P., Yin, D. X., Zhang, L. J., and Ning, G. B., 2005, A review on disk brake judder, *Automotive engineering*, Vol. 27, pp. 372-376.

Zagrodzki, P., Lam, K.B., Bahkall, E.A., and Barber, J.R., 2001, Nonlinear transient behaviour of a sliding system with frictionally excited thermo-elastic instability, *Journal of Tribology*, vol. 123, pp. 899-708.

Zagrodzki, P., and Truncone, S. A., 2003, Generation of hot spots in a wet multidisc clutch during short-term engagement, *Wear*, 254 (2003), pp. 474-491.

Zagrodzki, P., 2009, Thermo-elastic instability in friction clutches and brakes – transient modal analysis revealing mechanisms of excitation of unstable modes, *International journal of solids and structures*, 2009(46), pp. 2463-2476.

Appendices

Appendix 1: Examples of user subroutines-FRIC

This code is commercially sensitive

Appendix 2: Examples of user subroutines-UMESHMOTION

This code is commercially sensitive

Appendix 3: Estimation of the disc/wheel heat transfer coefficient

According to Tirovic (2014), the conductive heat transfer equation between solid parts is

$$Q_{cond} = h_{cond} A \Delta T_{cond}$$

and the convective heat transfer equation between solid and air is

$$Q_{conv} = h_{conv} A \Delta T_{conv}$$

Where *Q* is the heat dissipation; *h* is the coefficient of heat conductance or transfer; *A* is the heat transfer interface area and ΔT is the temperature differences between solid/solid or solid/air. Subscript 'cond' indicates conductive and 'conv' indicates the convective.

In the simulations performed in section 6.5 and 6.6, an estimated heat transfer coefficient was applied to the brake disc/wheel interface in order to represent the effects of heat conduction. So, the total heat dissipation should be same, gives

$$Q_{cond} = h_{cond} A \Delta T_{cond} = Q_{conv} = h_{conv} A \Delta T_{conv}$$

Therefore,

$$\frac{h_{conv}}{h_{cond}} = \frac{\Delta T_{cond}}{\Delta T_{conv}}$$

Based on the experimental measurement of the top-hat temperature (~60°) and ambient air temperature, the temperature difference $\Delta T_{conv} = 60 - 20 = 40°$. The thermal conductance of the disc/wheel interface is assumed to be 12kW/m^{2}K (Tirovic, 2014). The disc/wheel interface temperature difference ΔT_{cond} was assumed to be small (~0.1°) which gives the estimated heat transfer coefficient $h_{conv} = \frac{h_{cond} \Delta T_{cond}}{\Delta T_{conv}} = 30$W/m^{2}K.

Appendix 4: Parametric study of friction material properties to hot band migration

The first factor investigated was the modulus of the back-plate. Since the friction

material has relatively much lower thermal conductivity than the disc, the temperature raised at the back-plate can be considered insignificant according to Zagrodzki *et al.* (2009). Therefore, the effects of the thermal properties were not considered in this parameter studies. The effects of back-plate modulus on the peak temperature migration throughout 9 braking events was illustrated in Figure A.1. The results shows that 10% modifications of the modulus didn't affect the trend of hot band migrations.

Figure A.2 provided the effects of various pad moduli on hot band migration pattern. It can be observed that significant 'in-stop' migration occurred in the 0.6GPa pad modulus case. Regarding the results for moduli in range between 0.7 to 0.9GPa, the single hot bands shows increasingly significant migration with the increase of moduli. It implied that the influence of the axisymmetric loading between inboard and outboard pads to the 'in-stop' hot banding reduced due to the increase of pad moduli and more uniform contact pressure.

Figure A.3 shows the effects of pad thermal conductivities on hot band migration. It was clear that in the relatively lower conductivity case, the pattern of the migration was less repetitive between each braking event. The lower conductivity means more heat were concentrated at the contact interface which can facilitate the thermal localisation and the subsequent wear and cause more significant migrations.

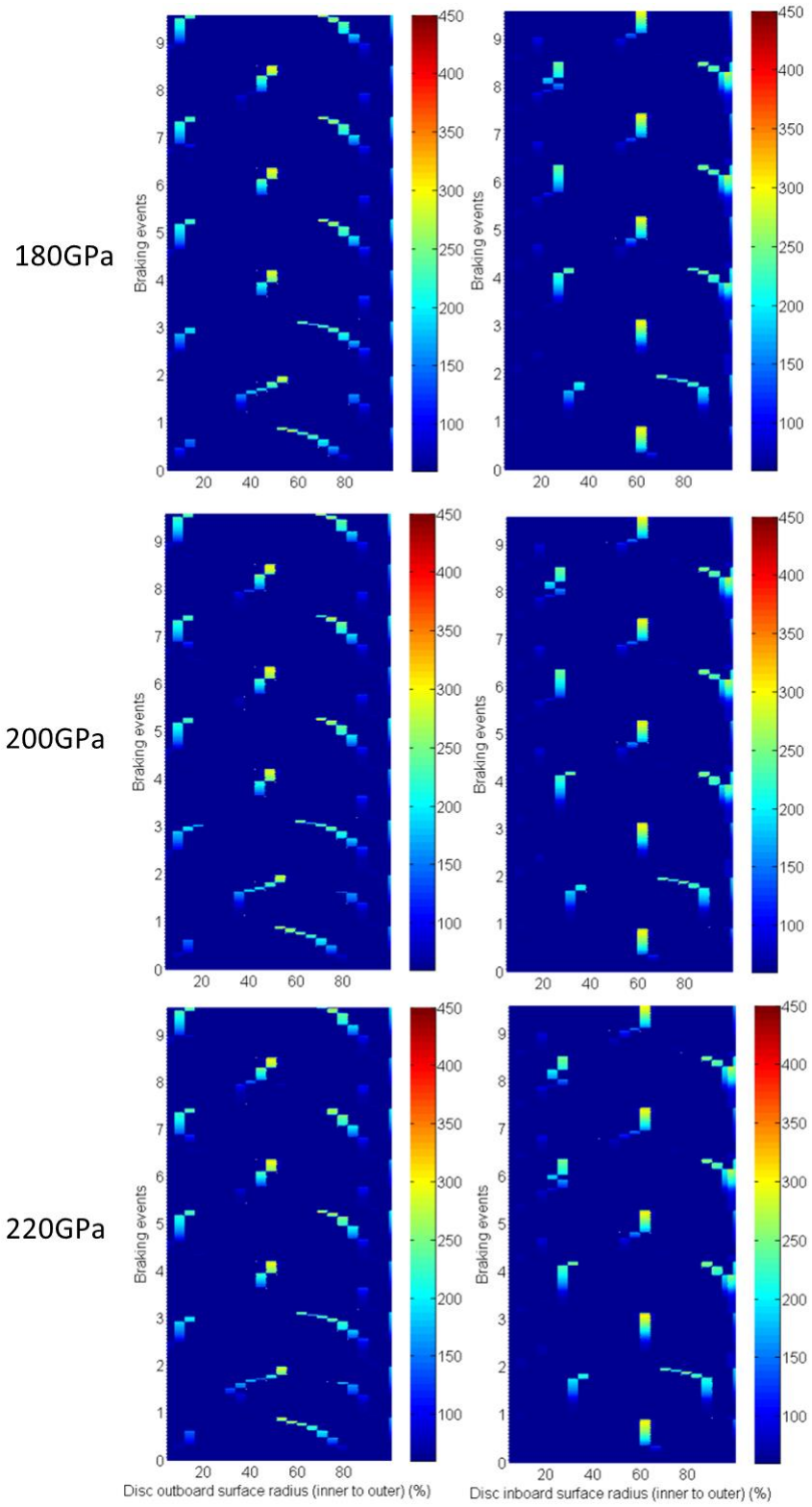

Figure A.1 Effects of back-plate modulus on peak temperature migration

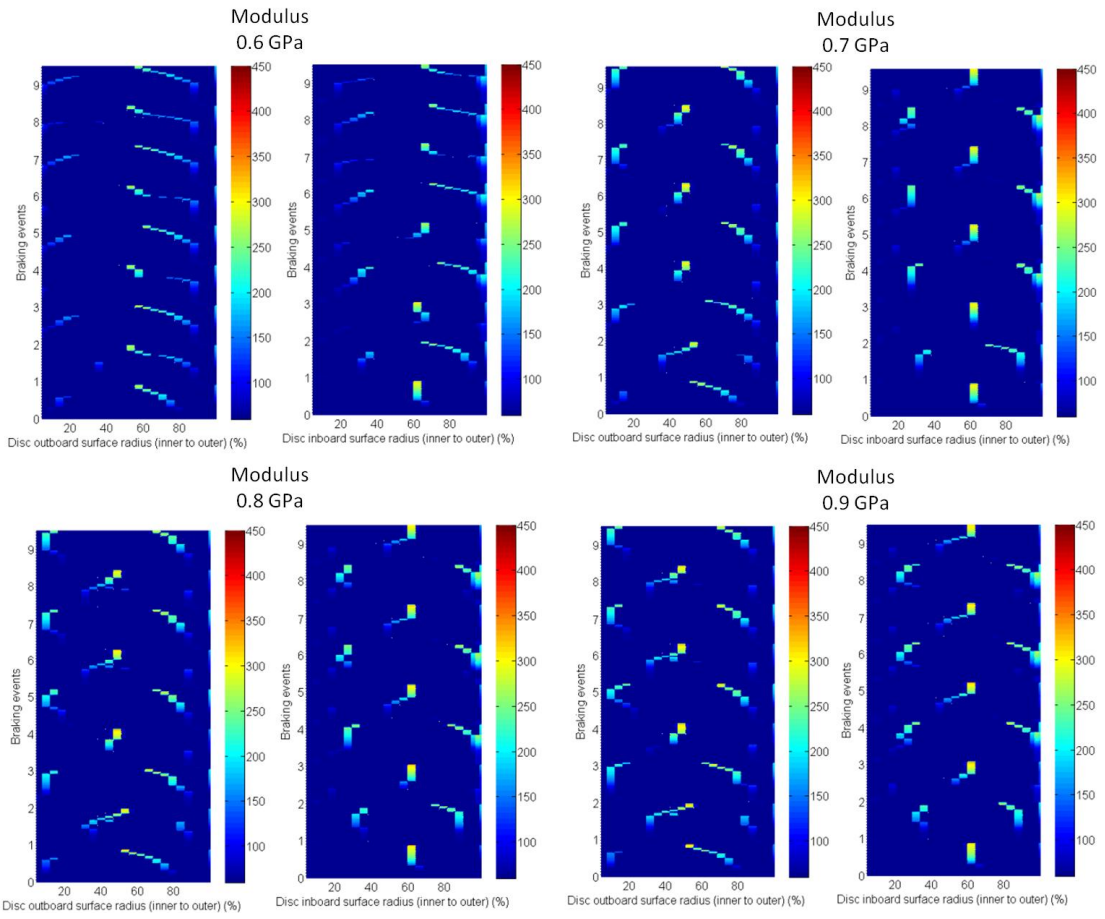

Figure A.2 Effects of pad modulus on peak temperature migration

The effects of thermal expansion coefficients were present by Figure A.4. It revealed that greater migrations were developed when the coefficient increased. Since the expansion coefficient can magnify the thermal localisation according to Lee and Barber (1993), the subsequent wear rate can be considerable when the expansion coefficient was relatively high. Therefore, the results implied that the increase of thermal expansion coefficient boost the thermal localisation-wear-contact pressure distribution variation-new thermal localisation process. In terms of the influences of increasing the pad specific heat capacity, Figure A.5 illustrated that the hot band migrations were less repeatable throughout the braking events. When the heat capacity was relatively high, the bulk temperature would be low and the heat will more concentrated at the contact interface according to the basic heat transfer Equation 3.1 through the thickness. Thus the thermal localisations and migrations would be magnified.

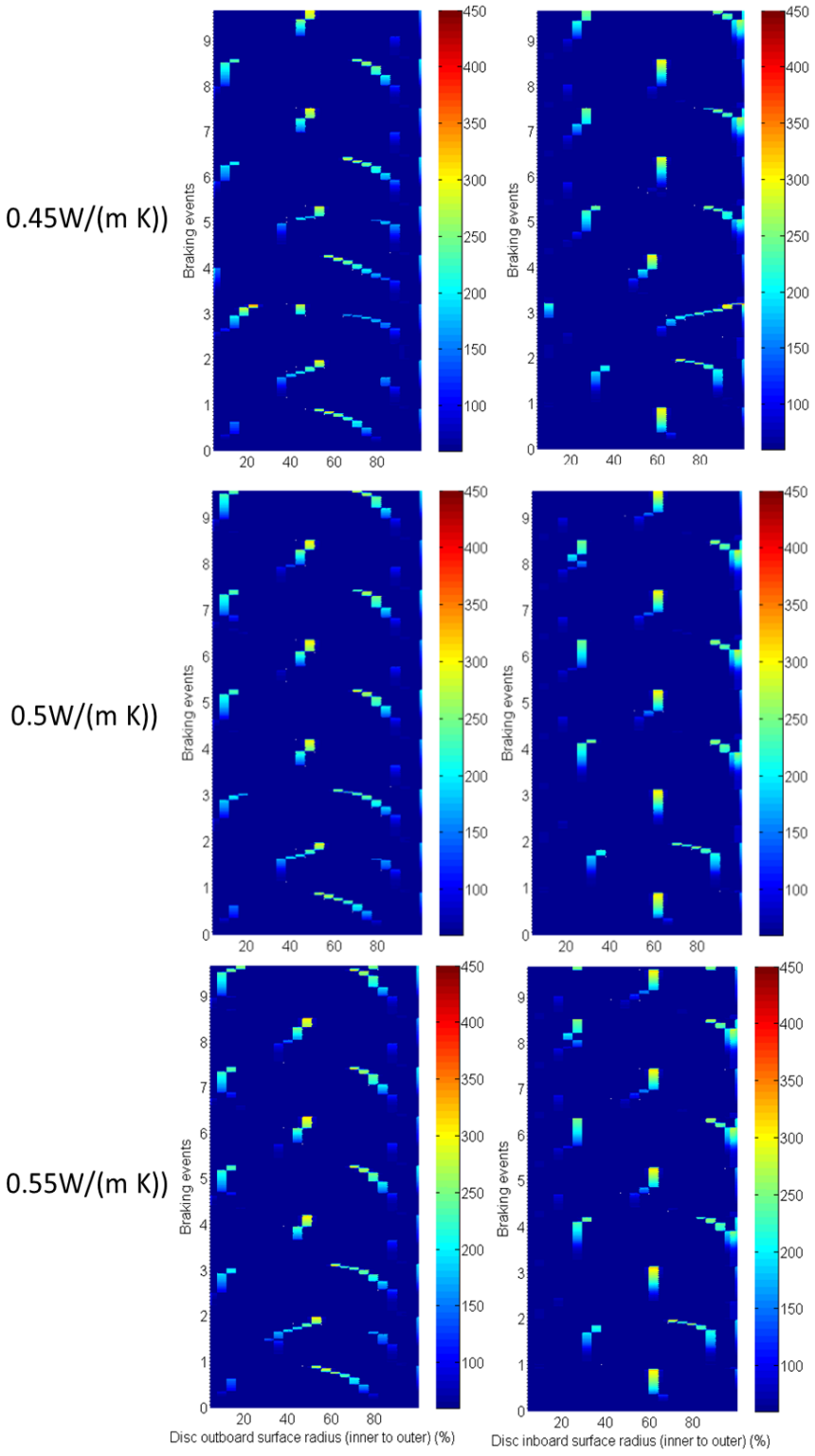

Figure A.3 Effects of pad thermal conductivity on peak temperature migration

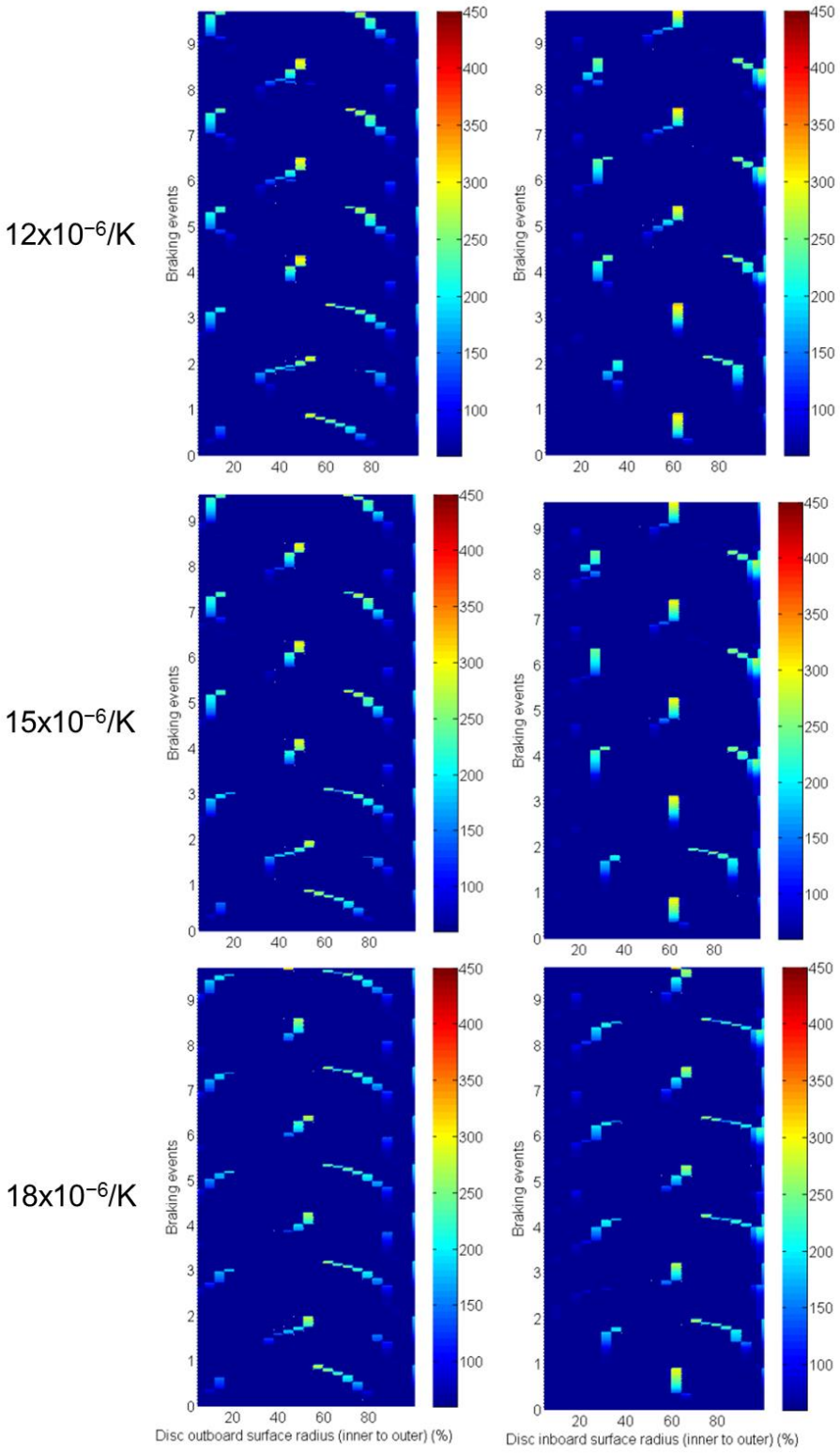

Figure A.4 Effects of pad thermal expansion coefficient on peak temperature migration

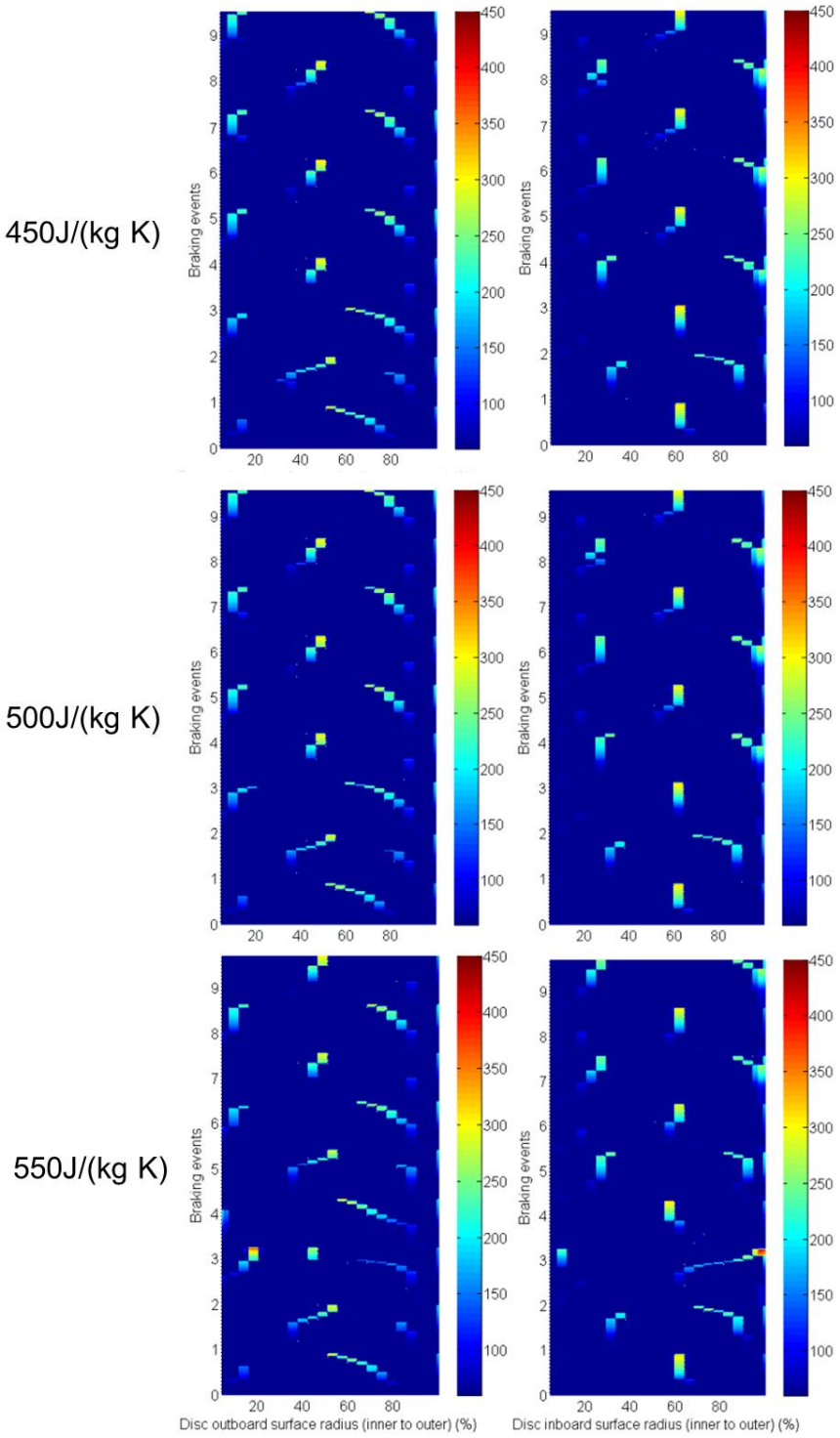

Figure A.5 Effects of pad specific heat capacity coefficient on peak temperature migration

Appendix 5: Computer specifications for the simulation and data processing

Processor	Intel Core i7-4770HQ 2.2GHz
Memory size	16GB
Operating system	Windows 8.1
Storage	250GB solid-state drive